Electronic properties of hybrid organic-inorganic perovskite films: effects of composition and environment

Dissertation

zur Erlangung des akademischen Grades
doctor rerum naturalium
(Dr. rer. nat.)
im Fach Physik
eingereicht an der

Mathematisch-Naturwissenschaftlichen Fakultät
der Humboldt-Universität zu Berlin
von

Frau M.Sc. Maryline Ralaiarisoa

Präsidentin der Humboldt-Universität zu Berlin
Prof. Dr.-Ing. Dr. Sabine Kunst

Dekan der Mathematisch-Naturwissenschaftlichen Fakultät
Prof. Dr. Elmar Kulke

Gutachter: 1. Prof. Dr. Norbert Koch
2. Prof. Dr. Emil List-Kratochvil
3. Dr. Philip Schulz

Datum der mündlichen Prüfung: 29. April 2019

Abstract

Hybrid organic-inorganic perovskites (HOIPs) have attracted tremendous attention due to their application in solar cells yielding high efficiencies on a par with conventional silicon-based solar cells. However, the long-term viability of HOIP materials is challenged by the limited understanding of HOIP structure-property relationships and by the issues of stability and reproducibility, both particularly with regard to environmental conditions. In this context, monitoring as well as understanding the evolution, and accordingly the variation of the electronic properties of HOIP film surfaces is of key importance. The surface electronic properties primarily dictate the energy level alignment (ELA) at the interfaces between the HOIP and its adjacent charge transport layers in devices. The present thesis aims at characterizing the electronic properties of solution-processed HOIP films at different stages, namely from HOIP formation to its degradation, by means of photoelectron spectroscopy (PES). The HOIP selected is the methyl ammonium (MA) lead iodide-chloride $CH_3NH_3PbI_{3-x}Cl_x$ ($MAPbI_{3-x}Cl_x$).

Firstly, the formation of $MAPbI_{3-x}Cl_x$ films upon thermal annealing is monitored by a combination of PES, time-of-flight secondary ion mass spectrometry, grazing incidence X-ray diffraction, and atomic force microscopy for disclosing changes in electronic properties, film composition, crystal structure, and morphology, respectively. Overall, the results point to the essential mediating role of chlorine in the formation of a highly textured perovskite film. The film formation is accompanied by a change of composition which leads to the film becoming more n-type. Furthermore, while the results agree with the formation of a single phase $MAPbI_3$ after complete film crystallization, they also unambiguously reveal the accumulation of chlorine at the interface between perovskite and the underlying substrate. These results propose a rationale for the predominance of $MAPbI_{3-x}Cl_x$ with regard to their chlorine-free $MAPbI_3$ counterparts.

Secondly, the separate effects of water and oxygen on the electronic properties of $MAPbI_{3-x}Cl_x$ film surfaces are investigated by PES. Already low water exposure – as encountered in high vacuum or inert conditions – appears to reversibly impact the work function (ϕ) of the film surfaces. Higher amounts of water vapor in the mbar range induce a shift of the valence band maximum (VBM) away from the Fermi level (E_F) accompanied by a decrease of ϕ. In contrast, oxygen leads to a VBM shift towards E_F and a concomitant increase of ϕ. The effect of oxygen is found to predominate in ambient air with an associated

shift of the energy levels by up to 0.6 eV. These findings emphasize the impact of least variation in the environmental conditions on the reproducibility of the electronic properties of perovskite materials.

Thirdly, PES is further employed to investigate the electronic properties of newly developed and more stable mixed cations methyl ammonium-guanidinium (Gua) lead iodide ($MA_{1-x}Gua_xPbI_3$) perovskites and those of low-cost titanium disulfide (TiS_2) nanoparticles used as hole transport materials in perovskite-based solar cells.

Finally, the thesis is concluded by additional considerations, in particular of the effect of solvents on perovskite films for over-layer deposition.

Overall, the presented PES results point out the critical impact of film composition, formation, and environment on the electronic properties of the solution-processed HOIP films.

Keywords:

Hybrid organic-inorganic perovskite, methyl ammonium lead iodide, chlorine, electronic properties, photoelectron spectroscopy, surfaces, perovskite solar cells, water, oxygen

Kurzfassung

Hybride organische-anorganische Perowskite (HOIP) genießen derzeit größte Aufmerksamkeit in der Solarzellenforschung. Grund dafür ist ihr Einsatz als Halbleitermaterial in Solarzellen, wo sie innerhalb von nur 8 Jahren den konventionellen Solarzellen ebenbürtige Wirkungsgrade erreichten. Der langfristige Einsatz dieser Materialklasse wird aber wegen Problemen hinsichtlich schlechter Stabilität und Reproduzierbarkeit in Frage gestellt, insbesondere gegenüber unterschiedlichen Umgebungsbedingungen. Deshalb ist es äußerst wichtig zu verstehen, wie die Materialeigenschaften entstehen bzw. variieren. In diesem Zusammenhang ist die Untersuchung der elektronischen Eigenschaften von HOIP von entscheidender Bedeutung, denn diese bestimmen in erster Linie die Energielevelanordung (ELA) an den Grenzflächen zwischen der HOIP-Schicht und deren angrenzenden Schichten in einer Solarzelle. Der Schwerpunkt der vorliegenden Arbeit liegt daher in der Charakterisierung der elektronischen Eigenschaften von – nach lösungsmittelbasierten Verfahren hergestellten – HOIP-Schichten während der Schichtbildung und in verschiedenen Umgebungen mittels Photoelektronenspektroskopie (PES). Insbesondere wird der Methylammonium-Blei-Iodid-Chlorid-Perowskit $CH_3NH_3PbI_{3-x}Cl_x$ ($MAPbI_{3-x}Cl_x$) untersucht.

Als erstes werden Änderungen in den elektronischen Eigenschaften, der Zusammensetzung, der Kristallstruktur, sowie der Morphologie mittels PES, Flugzeit-Sekundärionenmassenspektrometrie, Röntgendiffraktometrie mit streifendem Einfall, sowie Rasterkraftmikroskopie analysiert. Die daraus gewonnenen Informationen weisen alle auf die entscheidende Rolle von Chlor im texturierten Wachstum der Perowskitschicht hin. Die auskristallisierte Perowskitschicht weist eine stärkere n-Typ Eigenschaft auf, welche auf die Änderung der Zusammensetzung während der Schichtbildung zurückgeführt werden kann. Obwohl die auskristallisierte Schicht nur noch aus $MAPbI_3$ besteht, beweisen die Ergebnisse eindeutig die Ablagerung von Chlor an der Grenzfläche zwischen der Perowskitschicht und dem Substrat. Aus den Ergebnissen wird eine rationale Erklärung für die effizienteren Solarzellen basierend auf $MAPbI_{3-x}Cl_x$ im Vergleich zum $MAPbI_3$ nahegelegt.

Zweitens werden die separaten Einflüsse von Wasser, Sauerstoff, und Umgebungsluft auf die elektronischen Eigenschaften von $MAPbI_{3-x}Cl_x$-Schichtoberflächen untersucht. Bereits

geringste Wassermengen ähnlich wie im Hochvakuum oder in inerter Umgebung können eine reversible Reduzierung der Austrittsarbeit ϕ hervorrufen. Höherer Wasserdampf-Partialdruck führt zu einer Verschiebung des Valenzbandmaximums (VBM) weit vom Fermi-Niveau, sowie zu einer Reduzierung von ϕ. Im Gegensatz dazu führt eine Sauerstoffexposition zu einer Verschiebung des VBM in Richtung des Fermi-Niveaus und zu einer Steigerung von ϕ. Analog kommt es zu einer Verschiebung von bis zu 0.6 eV bei einer Exposition gegenüber Umgebungsluft, was den vorwiegenden Einfluss von Sauerstoff gegenüber Wasser in der Umgebungsluft demonstriert. Diese Resultate heben die Auswirkung geringer Abweichungen der Umgebungsbedingungen auf die Reproduzierbarkeit der elektronischen Eigenschaften von Perowskitmaterialien hervor.
Drittens wird im Rahmen dieser Arbeit auch die elektronische Charakterisierung von neu-entwickelten und stabileren $MA_{1-x}Gua_xPbI_3$ Perowskitmaterialien basierend auf einer Mischung von MA und Guanidinium (Gua) Kationen, sowie von kostengünstigen Titandisulfid-Nanopartikeln für den Einsatz als Lochtransportmaterial in perowskit-basierten Solarzellen, mittels PES durchgeführt.
Abschließend wird die Fragestellung untersucht, wie sich insbesondere der Einfluss von ausgewählten Lösungsmitteln für die lösungsmittelbasierte Abscheidung von Ladungträgertransportmaterial auf Perowskitschichten beurteilen lässt.

Die vorliegenden PES-basierten Untersuchungen betonen den kritischen Einfluss der Schichtbildung, der Zusammensetzung, sowie der Umgebungsbedingungen auf die elektronischen Eigenschaften von HOIP.

Schlagwörter:

Hybride organische-anorganische Perowskite, Methylammonium Blei-Iodid, Chlor, elektronische Eigenschaft, Photoelektronenspektroskopie, Oberfläche, Perowskit-Solarzellen, Wasser, Sauerstoff

Table of Content

List of Abbreviations

AFM	atomic force microscopy
ASF	atomic sensitivity factor
CB	chlorobenzene
CBM	conduction band minimum
CF	chloroform
CPD	contact potential difference
DFT	density functional theory
DOS	density of states
EA	electron affinity
E_B	binding energy/exciton binding energy
EDC	energy distribution curve
E_F	Fermi level
E_G	band gap
ELA	energy-level alignment
ETL	electron transport layer
E_{vac}	vacuum level
ϕ	work function
FA	formamidinium
FF	fill factor
FTO	fluorine-doped tin oxide
FWHM	full width at half maximum
GIXRD	grazing incidence X-ray diffraction
Gua	guanidinium
HOIP	hybrid organic-inorganic perovskite
HOMO	highest occupied molecular orbital
HTL	hole transport layer
HV	high vacuum
IE	ionization energy
IMFP	inelastic mean free path
ITO	indium-doped tin oxide
J_{sc}	short-circuit current
KP	Kelvin probe
LCAO	linear combination of atomic orbital
LUMO	lowest unoccupied molecular orbital

MA	methyl ammonium
MAI	methyl ammonium iodide
$MAPbI_3$	methyl ammonium lead iodide
$MAPbI_{3-x}Cl_x$	methyl ammonium lead iodide-chloride
MPP	maximum power point
n_{Dip}	density of adsorbed molecules
NIR	near-infrared
PCE	power conversion efficiency
PE	photoemission
PES	photoelectron spectroscopy
PSC	perovskite-based solar cell
PYS	photoelectron yield spectroscopy
RH	relative humidity
RMS	root mean square
R_S	rms roughness
SECO	secondary electron cutoff
TCO	transparent conductive oxide
ToF-SIMS	time-of-flight secondary ions mass spectrometry
μ	dipole moment
UHV	ultra high vacuum
UPS	ultraviolet photoelectron spectroscopy
UV	ultraviolet
UV-vis	ultraviolet-visible
VBM	valence band maximum
V_{oc}	open-circuit voltage
XPS	X-ray photoelectron spectroscopy

1 Introduction

The current share of solar energy in the total worldwide electricity production amounts to less than 1%. In contrast to fossil fuels, which account for about 80% of the annual global energy supply, and which are confronted with scarcity and environmental issues through greenhouse gas emissions, solar energy represents a clean and practically inexhaustible energy source that could sustain the annual energy needs of the planet in just one hour [1, 2]. The transition to renewable energy sources in general, and to photovoltaics in particular, appears to be inexorable in order to maintain the required energy supply. However, in order to be a viable alternative in such energy transition, photovoltaics must not only be clean with a durable resource, it must also be stable, efficient and cost-effective. These challenging requirements primarily depend on the solar energy conversion into electricity itself, which is achieved with a solar cell; a device typically composed of a semiconducting absorber material, where the absorbed light creates charges, embedded between a succession of other semiconductors and/or metal electrodes to facilitate charge separation and collection. To address the aforementioned challenges, intense research has been carried out to develop new and innovative materials for efficient and cost-effective photovoltaic devices. The investigated materials range from inorganic materials, with a particular emphasis on the conventional polycrystalline silicon (Si) which still dominates about 69% of the solar module production with a maximum power conversion efficiency (PCE) of 22% as for 2015 [3, 4]; to organic materials, particularly attractive due to their easy processing from solution and their properties which are largely tunable through structure-engineering [5]; to hybrid organic-inorganic materials, that combine the enhanced optoelectronic properties of inorganic materials and the low-cost and easy preparation of functional organic materials. One novel material that belongs to the latter class is the hybrid organic-inorganic perovskite (HOIP). HOIPs have attracted tremendous attention in the field of photovoltaics, primarily due to the outstanding

progression of the PCE, achieved with prototypical solar cells based on perovskite thin films, from 3.8% [6] in 2009 to 22.1% [7] in 2017, and even to 25.2% in perovskite/silicon tandem solar cells [8]. The efficiency limit of perovskite-based solar cells (PSCs) has been estimated to be about 31% [9], which is close to the theoretical Shockley-Queisser limit of 32% for single junction Si-based solar cells [10, 11]. Unfortunately, comprehension of the origin of this remarkable efficiency is not always in pace with the progression of the efficiency itself, which will eventually impede the development of the field. Moreover, the outstanding performance is unfortunately overshadowed by stability issues, mainly with regard to the environment. This thesis aims to contribute to a better understanding of these two central topics by investigating the formation of and the environmental effect on one HOIP system; the methyl ammonium lead mixed-halide $CH_3NH_3PbI_{3-x}Cl_x$ ($MAPbI_{3-x}Cl_x$) perovskite, with an emphasis on its electronic properties accessed by means of photoelectron spectroscopy (PES). PES is the most important experimental tool to explore the electronic structure of material surfaces. Notably, this tool can provide invaluable information not only about the different energy levels of a material, which is a pre-requisite for a priori guiding the choice of adjacent materials in a device, but also about the electronic properties of interfaces, essentially determining the function of interfaces as found in devices.

HOIP, which owes its name to its perovskite crystal structure, encompasses materials with the general formula ABX_3 (with a monovalent organic cation A, a divalent metal cation B, and a halide anion X), generally obtained from a mixture of organic AX and inorganic BX_2 subunits. Although all-inorganic halide perovskites (where the organic cation is replaced by an alkali metal cation) are also lately emerging in the field of perovskite-based photovoltaics [12], this work will be restricted to HOIPs. The most frequently used HOIP is the state-of-the-art methyl ammonium lead iodide $CH_3NH_3PbI_3$ ($MAPbI_3$) perovskite, obtained from methyl ammonium iodide (MAI) and lead iodide (PbI_2). Due to their versatility, the optoelectronic properties of HOIPs can largely be tuned by modifying the respective subunits or the individual compounds. Particularly, the addition of chlorine in the preparation of mixed-halide $MAPbI_{3-x}Cl_x$ perovskite film, typically obtained from a mixture of MAI and lead chloride $PbCl_2$ in a non-stoichiometric ratio of 3:1 in solution, induces long-range film crystallinity [13] and enhanced charge-transport properties [14–16] that ultimately result in enhanced solar cell performance in comparison to the single halide $MAPbI_3$ [17]. Interestingly, the final mixed-halide $MAPbI_{3-x}Cl_x$ films, which are thermally annealed to induce crystallization, mainly consist of $MAPbI_3$ [13, 18, 19], and do not exhibit any detectable traces of chlorine

[14, 20–22]. To understand the process underlying such an observation, several studies concentrated on the annealing process and they all pointed to the existence of an intermediate phase during annealing [15, 23–25], which is accompanied by chlorine release through the surface by sublimation of methyl ammonium chloride (MACl) [15, 26, 27]. A few studies suggest the presence of residual chlorine inside the perovskite film and predicted its possible impact on the electronic properties at the perovskite/substrate interface [28, 29]. Further studies suggest the role of chlorine in the nucleation [30], and growth of $MAPbI_{3-x}Cl_x$ perovskite [22]. However, the actual impact of chlorine, leading to the enhanced properties cited above is still not fully understood. A rationale that would relate the initial addition of chlorine with the final film properties can only be reached through a thorough understanding of the chlorine behavior during the annealing step. Disclosing the film's bulk composition during the annealing step will give valuable information about the location of chlorine – and accordingly its behavior – and the film evolution. Firstly, in this work, the three dimensional (3D) composition of mixed-halide $MAPbI_{3-x}Cl_x$ perovskite film before and after complete film crystallization will be reconstructed by depth-profiling the individual compounds by means of time-of-flight secondary ion mass spectrometry (ToF-SIMS). The change in composition will be correlated with the structural, morphological, and electronic properties evolution as determined by grazing-incidence X-ray diffraction, atomic force microscopy, and photoelectron spectroscopy. The results will be discussed in keeping with reported studies in order to provide a more consistent understanding of the film formation and its implication in the optoelectronic properties of $MAPbI_{3-x}Cl_x$ perovskite.

A major challenge in the long-term application of HOIPs is their reproducibility and stability which are critically influenced by light and environmental conditions. Efforts were made to avoid environment-induced degradation; for instance, solar cells retaining stable PCE of 17% for at least three months under real outdoor conditions were achieved by the application of a UV-coating to protect the devices against humidity ingress and detrimental UV-light [31]. Despite such strategies in developing external protection for the solar cells, the material's stability itself remains of paramount importance since environmental exposure occurs not only during device application but already during preparation, storage, material and/or device characterization, which can impact the determination of reliable and reproducible materials properties. In particular, exposure to water during device fabrication and operation has been often claimed to be a decisive factor for reproducibility and stability [18, 32–35]. The impact of water exposure on the properties of perovskite materials is the object of controversy in the

literature. In fact, moderate exposure to controlled humidity or ambient air has been observed to improve the crystallinity of perovskite films, the grain size, the charge carrier lifetime, and the carrier mobility, thus enhancing the performance of the perovskite-based solar cells [36–38]. Contrastingly, high exposure to water, such as high relative humidity (RH) can accelerate the degradation of the perovskite materials [39–42]. To avoid, or at least minimize the impact of water, perovskite films are typically preferentially deposited and stored in vacuum or inert gas conditions. Under these circumstances, potential changes of the materials properties from ambient air to water free and vacuum conditions must be characterized and understood for a reliable description of the phenomena observed under standard device fabrication and operating conditions. In the instance of methyl ammonium lead bromide $MAPbBr_3$ perovskite single crystals, the photoluminescence underwent drastic but reversible changes upon exposure to water and/or oxygen, and vacuum, which was attributed to the variation of the density of surface states upon exposure to water or oxygen gases [43]. Alternating exposure to air and vacuum happened to reversibly increase the photocurrent [44], and the open circuit voltage of $MAPbI_3$-based devices [45], thus pointing toward the beneficial effect of water on devices. Specifically for perovskite surfaces, the impact of the exposure to various atmospheres on their electronic structure must be investigated in order to better understand the mechanisms occurring upon such exposure. Moreover, the reliability of energy levels established from photoelectron spectroscopy measurements can be affected by the environmental conditions (i.e. high vacuum). Although some work based on X-ray photoelectron spectroscopy (XPS) were directed toward assessing the impact of water on *in situ* evaporated perovskite films [46, 47], a comprehensive understanding of the separate effects of water and oxygen exposure and of their combined effects on the electronic properties of perovskite surfaces is still lacking. Therefore, secondly, this thesis will also investigate the separate impact of water, oxygen, and air on the electronic structure of $MAPbI_{3-x}Cl_x$ perovskite films by PES. By focusing on exposure in terms of partial pressure from as low as 10^{-6} mbar up to more realistic partial pressure in the mbar range for water and oxygen, the results indicate distinct variations of the electronic structure, particularly the competing impact of water and oxygen. The critical impact of extremely low water exposure demonstrates and stresses the importance of controlled atmosphere for reliable properties assessment. The results are further discussed with regards to possible degradation pathways.

The fundamental requirements in terms of stability and cost-effectiveness for durable solar cells necessitate the development of new materials; not only of new perovskite materials but

also of compatible charge transport materials between which the perovskite active material is sandwiched. Thirdly, this thesis includes the characterization of the electronic structure of new perovskite and hole transport materials, which were investigated in the scope of collaborative works. In the former case, PES is employed to monitor the evolution of the electronic structure of $MAPbI_3$ upon gradual inclusion of the guanidinium (Gua) cation in order to stabilize the perovskite structure. In the latter case, the composition and the electronic structure of synthesized low-cost titanium disulfide (TiS_2) nanoparticles newly implemented into solar cells are assessed by PES.

The present thesis is outlined as follows: in chapter 2 the fundamental theories and concepts of the electronic structure of semiconductors will be introduced in section 2.1, then insights into the basics of HOIPs, based on the reported literature, will be discussed in section 2.2. The basic principles of solar cells in general and of perovskite-based solar cells in particular, will be discussed in section 2.3. The experimental methods employed in the scope of this thesis are described in chapter 3, with a particular emphasis on the basic principles of PES (section 3.1), which is the main experimental method used in this work. In chapter 4, details about the investigated materials and their preparation, as well as the actual experimental set-ups used to carry out the diverse materials characterization are given in section 4.1, and section 4.2, respectively. The central part of the present thesis concentrates in the results presented in chapter 5. Firstly, the formation of mixed $MAPbI_{3-x}Cl_x$ perovskite films and the role of chlorine in its formation are investigated in section 5.1. This is explored by correlating the films bulk composition with their structural, morphological, and electronic properties. Secondly, the effects of environmental exposure, namely to water, oxygen, and air, on the electronic properties of mixed $MAPbI_{3-x}Cl_x$ perovskite films are the subject of section 5.2. Thirdly, section 5.3 presents the electronic structure characterization of new perovskite systems with improved stability, and of newly developed and cost-effective hole transport materials for perovskite-based solar cells. Section 5.4 consists of two-fold preliminary test experiments conducted in the scope of this thesis. Subsection 5.4.1 presents the investigation of the structural and electronic properties of perovskite films upon exposure to selected solvents to assess the suitability of these latter for charge transport materials deposition from solution. In order to evaluate the energy level alignment at the interface between two materials in contact, the prevalent method consists in incrementally depositing thin layers of one material on top of the other and to assess the evolution of the electronic properties after each deposition. Subsection 5.4.2 shows the results of the electronic structure investigation of

films obtained from solution dilution method, which has been tested in an attempt to obtain thin enough films from solution. The results presented indicate the dependence of the electronic structure on the film preparation and provide hints on film properties improvement for future characterization of the ELA of perovskite materials prepared from solution. Finally, chapter 6 summarizes the main findings of the present thesis and finalizes it with an outlook.

2 Fundamentals

This chapter introduces to the fundamental physics of semiconductors and to hybrid organic-inorganic perovskites (HOIPs) used as semiconducting materials in photovoltaic cells. HOIPs are termed as hybrid organic-inorganic owing to the presence of organic and inorganic subunits in its crystal unit cell. Nonetheless, their electronic structure is usually discussed in the context of inorganic semiconductors. The present chapter starts with a short recall of crystal structure, and the diffraction by a crystal in section 2.1. Then, general theoretical concepts for periodic systems, necessary to describe the electronic structure in inorganic semiconductors, are presented. Following up on these basic theories, the second part (section 2.2) of the chapter begins with an introduction to the class of perovskites in general, and to the hybrid organic-inorganic perovskites (HOIPs) and their properties in particular. It then continues with the specific discussion on the existing knowledge about the electronic structure of HOIP and the still existing gap in the understanding of the function and properties of this material. In the last third part (section 2.3), the basic physics of solar cells is reviewed.

2.1 Electronic Structure of Semiconductors and their Interfaces

This first section briefly provides a general overview on the electronic structure of semiconductors. In order to do that, the section will start with a short review of the effects occurring and terms used if matter arranges in periodic structure, i.e. exhibits a crystal structure. This ordered structure is also the basis for the electronic structure determination of any solid. To illustrate this, models derived for such periodic order are employed to describe states of electrons in solids. Subsequently, the concept of density of states, which is tightly connected to the electronic states, is discussed, before finally addressing different aspects of the energy level alignment (ELA) at interfaces. The latter is of critical importance in the

description and understanding of the electronic processes, e.g. charge transport, occurring at the interfaces in electronic devices.

2.1.1 Crystal Structure and Crystal Diffraction

Crystal Structure

A solid crystal consists of atoms that are arranged in a well-defined and periodic manner. The crystal structure describes the particular arrangement of the atoms and is defined by a basis, which is an atom or a group of atoms or molecules, and the lattice. The unit cell is the basic repeating unit, which, by translation within the lattice, builds the whole 3D crystal solid. The smallest unit cell that contains only one lattice point is called a primitive unit cell. The primitive cell that encompasses a volume closest to a chosen lattice point is called the *Wigner-Seitz cell*. The *Wigner-Seitz cell* still retains the crystal symmetry and is determined by first drawing lines from the lattice point to the nearest equivalent lattice sites and second by drawing the bisector planes of these lines. 3D crystals are classified into 14 Bravais lattices (*cf.* ref. [48]); each Bravais lattice is generated by all points determined by any translational vector $\boldsymbol{R}$ such that:

$$\boldsymbol{R} = n_1\boldsymbol{a} + n_2\boldsymbol{b} + n_3\boldsymbol{c} \tag{2.1}$$

where n_1, n_2, and n_3 are integers and $\boldsymbol{a}$, $\boldsymbol{b}$, and $\boldsymbol{c}$ are the basis vectors that span the lattice. Each Bravais lattice is defined by the lattice parameters: the lengths a, b, c, and the angles α, β, γ – between b and c, between a and c, and between a and b, respectively. The reciprocal lattice in the reciprocal $\boldsymbol{k}$-space of the direct lattice in real space is defined by the reciprocal lattice vector $\boldsymbol{G}$, which is spanned by the basis vectors $\boldsymbol{a}^*$, $\boldsymbol{b}^*$, and $\boldsymbol{c}^*$ of the reciprocal lattice. These are related to the basis vectors of the direct lattice by:

$$\boldsymbol{a}^* = 2\pi\frac{\boldsymbol{b}\times\boldsymbol{c}}{\boldsymbol{a}\cdot(\boldsymbol{b}\times\boldsymbol{c})}, \qquad \boldsymbol{b}^* = 2\pi\frac{\boldsymbol{c}\times\boldsymbol{a}}{\boldsymbol{a}\cdot(\boldsymbol{b}\times\boldsymbol{c})}, \qquad \boldsymbol{c}^* = 2\pi\frac{\boldsymbol{a}\times\boldsymbol{b}}{\boldsymbol{a}\cdot(\boldsymbol{b}\times\boldsymbol{c})} \tag{2.2}$$

where the denominator $\boldsymbol{a}\cdot(\boldsymbol{b}\times\boldsymbol{c})$ corresponds to the volume of the parallelepiped spanned by the three basis vectors. It can be derived that $\boldsymbol{a}\cdot\boldsymbol{a}^* = \boldsymbol{b}\cdot\boldsymbol{b}^* = \boldsymbol{c}\cdot\boldsymbol{c}^* = 2\pi$ and $\boldsymbol{a}\cdot\boldsymbol{b}^* = \boldsymbol{a}\cdot\boldsymbol{c}^* = \boldsymbol{b}\cdot\boldsymbol{a}^* = \boldsymbol{b}\cdot\boldsymbol{c}^* = \boldsymbol{c}\cdot\boldsymbol{a}^* = \boldsymbol{c}\cdot\boldsymbol{b}^* = 0$ [49]. Thus, for the given reciprocal vector $\boldsymbol{G}_{hkl}$ given in equation (2.3), it is deduced from equations (2.2) and (2.3) that $\boldsymbol{G}_{hkl}\cdot\boldsymbol{R} = 2\pi m$, where m is an integer.

$$\boldsymbol{G}_{hkl} = h\boldsymbol{a}^* + k\boldsymbol{b}^* + l\boldsymbol{c}^* \tag{2.3}$$

The reciprocal vector $\boldsymbol{G}_{hkl}$ is perpendicular to the lattice plane denoted as (hkl). The set of integers (hkl) in (2.3) specifies the lattice planes and their orientation, and the numbers *h, k, l* are called *Miller indices.* The Miller indices are the reciprocal values of the intercepts a_1, a_2, and a_3 of the lattice plane with the direct basis vectors $\boldsymbol{a}$, $\boldsymbol{b}$, and $\boldsymbol{c}$, respectively. They are the smallest integers proportional to the inverses of the intercepts, such that: $h \propto 1/a_1$, $k \propto 1/a_2$, and $l \propto 1/a_3$. A class of planes parallel to (hkl) is denoted by $\{hkl\}$ and the related notation $[hkl]$ describes the direction of the planes. By convention, and as it is the case in this work, the notation (hkl) is adopted to also specify the set of planes parallel to (hkl) with the same lattice spacing $d_{hkl} = 1/|\boldsymbol{G}_{hkl}|$.

The *Wigner-Seitz cell* in the reciprocal $\boldsymbol{k}$-space is called the first Brillouin zone. This zone is characterized by high symmetry points and is essential for visualizing the dispersion relation $E(\boldsymbol{k})$ in $\boldsymbol{k}$-space. The high symmetry point Γ refers to the (0,0,0) point in the Brillouin zone and the band structure is often represented along the direction from this Γ point to other high symmetry points on the surface of the Brillouin zone.

Crystal Diffraction

The periodic structure of a crystal solid leads to the establishment of a band structure of the solid, as will be shown in the next subsection 2.1.2. In order to determine the crystal structure, one makes use of the scattering of light by the crystal. The present section offers a brief introduction to the fundamentals of X-ray diffraction by crystals, which is necessary to understand the results of this thesis.

A crystal can be viewed as parallel planes of atoms or molecules separated by a distance d_{hkl} as shown in Figure 2.1. In an X-ray diffraction process, incoming waves interact with the atoms, more precisely with the electrons surrounding the nucleus, and are scattered. All of the scattered waves interfere constructively if Bragg's law in equation (2.4) is satisfied; where $n\lambda$ corresponds to the path difference ΔL between two scattered waves from two successive planes, n is an integer and represents the diffraction order, and Θ is the scattering angle (Figure 2.1).

$$n\lambda = 2d_{hkl} \sin \Theta \tag{2.4}$$

This constructive interference results in intense peaks, also known as Bragg peaks. Therefrom, for each set of planes (hkl) and for a certain value of Θ, an intense diffraction peak will arise.

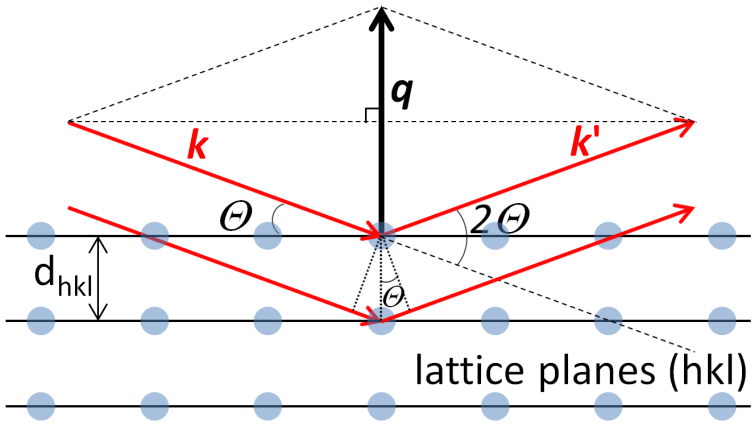

Figure 2.1 Schematic representation of Bragg's law, representing the incoming beam $\boldsymbol{k}$, the diffracted beam $\boldsymbol{k}$' at scattering angle Θ with regard to the plane (hkl), and the scattering vector $\boldsymbol{q}$. d_{hkl} denotes the lattice spacing.

The incident wave vector $\boldsymbol{k}$ and scattered wave vector $\boldsymbol{k}'$ have the same amplitude $|\boldsymbol{k}| = |\boldsymbol{k}'| = \mathrm{k} = \frac{2\pi}{\lambda}$, since the scattering process is based on elastic scattering. A change in direction from $\boldsymbol{k}$ to $\boldsymbol{k}'$ is given by the equation (2.5), such that the *scattering vector* $\boldsymbol{q}$ is a vector of the reciprocal lattice that bisects the angle between $\boldsymbol{k}$ and $\boldsymbol{k}'$ (Figure 2.1). One can deduce that the amplitude of the vector $\boldsymbol{q}$ is given by equation (2.6). For a diffraction peak – also called *Bragg reflection* – to arise, the considered set of planes must always be normal to the scattering vector $\boldsymbol{q}$.

$$\boldsymbol{q} = \boldsymbol{k}' - \boldsymbol{k} \tag{2.5}$$

$$|\boldsymbol{q}| = 2k \sin\Theta = \frac{4\pi}{\lambda} \sin\Theta \tag{2.6}$$

Hitherto, the condition for wave scattering at a fixed lattice position has been presented. In order to obtain the diffraction intensity from the whole crystal, additional interference effects originating from multiple atoms must be taken into account.

The amplitude of a wave scattered by an atom at a fixed position $\boldsymbol{r}_j$ in the unit cell will be proportional to $e^{i\boldsymbol{q}\cdot\boldsymbol{r}_j}$ [49]. In the case that the crystal has a polyatomic basis, the interference between the waves scattered from n atoms in one unit cell is described by the *structure factor*:

$$F(\boldsymbol{q}) = \sum_{j=1}^{n} f_j(\boldsymbol{q}) e^{i\boldsymbol{q}\cdot\boldsymbol{r}_j} \tag{2.7}$$

where $f_j(\boldsymbol{q})$ is the *atomic form factor* that describes the scattering amplitude by the electron density of the j-th atom in the unit cell. This quantity is specific to each chemical element and is a tabulated value that can also be calculated [50, 51]. Besides $\boldsymbol{q}$, $f_j(\boldsymbol{q})$ depends on the nuclear charge Z, and more specifically $f_j(\boldsymbol{q})$ corresponds to the Fourier transform of the atomic electron density $\rho_j(\boldsymbol{r})$:

$$f_j(\boldsymbol{q}) = \int \rho_j(\boldsymbol{r}) e^{i\boldsymbol{q}\cdot\boldsymbol{r}} d\boldsymbol{r} \tag{2.8}$$

Hence, the structure factor involves both the positions of the atoms within the cell and the electron distribution for each atom. The structure factor $F_{crystal}(\boldsymbol{q})$ of a non-infinite crystal with N unit cells and defined by a translational vector $\boldsymbol{R}_n = n_1\boldsymbol{a} + n_2\boldsymbol{b} + n_3\boldsymbol{c}$ [*c.f.* equation (2.1)] consists of the unit cell structure factor $F(\boldsymbol{q})$ and the lattice sum as given by equation (2.9) [52, 53].

$$F_{crystal}(\boldsymbol{q}) = F(\boldsymbol{q}) \sum_{n} e^{i\boldsymbol{q}\cdot\boldsymbol{R}_n} \tag{2.9}$$

In X-ray diffraction experiments, the observed intensity of diffraction $I(\boldsymbol{q})$ is proportional to the square of the amplitude, which, in turn, is proportional to the square of the structure factor:

$$I(\boldsymbol{q}) \propto |\mathrm{A}|^2 \propto |F_{crystal}(\boldsymbol{q})|^2 \tag{2.10}$$

It is noteworthy that the lattice sum in equation (2.9), and thus $I(\boldsymbol{q})$, is maximum for:

$$\boldsymbol{q} \cdot \boldsymbol{R}_n = 2\pi m, \tag{2.11}$$

where m is an integer. This is the *Laue* condition. Equivalently to equation (2.5) and as previously deduced from equations (2.2) and (2.3), the condition (2.11) is fulfilled only if $\boldsymbol{q} = \boldsymbol{G}_{hkl}$, which is the reciprocal lattice vector associated to the lattice plane (hkl).

2.1.2 Electronic States

Perovskite materials exhibit a definite crystalline structure. Since their electronic structure is generally determined in the same fashion as for inorganic semiconductors, in the present description of the electronic states, the case of inorganic semiconductors which have a periodic lattice will be essentially considered. One valence electron in such periodic system is described by the Schrödinger equation (2.12) [54, 55]:

$$H\Psi(\boldsymbol{r}) = \left(\frac{\hbar^2}{2m}\nabla^2 + U(\boldsymbol{r})\right)\Psi(\boldsymbol{r}) = E\,\Psi(\boldsymbol{r}) \tag{2.12}$$

where H is the Hamiltonian associated with the kinetic and potential energies for the particle, $U(\boldsymbol{r}) = U(\boldsymbol{r}+\boldsymbol{R})$ is the periodic potential and $\boldsymbol{R}$ is a lattice vector. Based on Bloch's theorem, the solution of the Schrödinger equation for a system in such a translationally invariant potential is a wave function $\Psi(\boldsymbol{r})$ known as Bloch function with the form:

$$\Psi_{n,k}(\boldsymbol{r}) = e^{i\boldsymbol{k}\boldsymbol{r}}u_{n,k}(\boldsymbol{r}), \tag{2.13}$$

where $u_{n,k}(\boldsymbol{r}) = u_{n,k}(\boldsymbol{r}+\boldsymbol{R})$ is a lattice periodic function, n is the band index to differentiate the different Bloch functions with the same $\boldsymbol{k}$, and $\boldsymbol{k}$ is an arbitrary wave vector which is here an index to differentiate the wave functions corresponding to the eigenvalue $E_n(\boldsymbol{k})$. The reciprocal lattice vector $\boldsymbol{G}$ is defined through $\boldsymbol{G}\cdot\boldsymbol{R} = 2\pi m$, hence $e^{i\boldsymbol{G}\boldsymbol{R}} = 1$, where m is an integer. By replacing $\boldsymbol{k}$ with $\boldsymbol{G}$, one can see that the Bloch function fulfills $\Psi_{\boldsymbol{k}+\boldsymbol{G}}(\boldsymbol{r}) = \Psi_{\boldsymbol{k}}(\boldsymbol{r})$. Consequently, wave vectors that differ by the reciprocal lattice vector $\boldsymbol{G}$ represent similar Bloch functions. Thus, it is sufficient to reduce $\boldsymbol{k}$ to its equivalent wave vector closest to the origin of the reciprocal lattice, that is, inside the Brillouin zone (the Brillouin zone being the primitive cell in the reciprocal space). The energy eigenvalues $E_n(\boldsymbol{k})$ are a periodic function of the wave vector of the Bloch wave, such that:

$$E_n(\boldsymbol{k}) = E_n(\boldsymbol{k}+\boldsymbol{G}) \tag{2.14}$$

The energy eigenvalues $E_n(\boldsymbol{k})$ describe the dispersion relation, and, taken together they form the electronic band structure of the solid. In the simplest approximation of a free electron, where the valence electron is considered free and electron-electron interactions are neglected such that U=0, the dispersion relation is given by equation (2.15).

$$E(\boldsymbol{k}) = \frac{\hbar^2}{2m}\boldsymbol{k}^2 \tag{2.15}$$

There exist several methods to calculate the band structure of semiconductors [55]. In the simple, one-dimensional Kronig-Penney model, the electrons in the crystal are assumed to be subject to a periodic potential in the form of equidistant rectangular barriers [56]. More elaborate methods such as the orthogonalized plane-wave method and pseudo-potential have been used to determine the band structure of semiconductors; where a pseudo-potential accounts for the complicated effect of core electrons that are assumed to be tightly bound to the nucleus [55, 57, 58]. In the tight-binding model, the electron is considered tightly bound to the atom. This model is related to the linear combination of atomic orbitals (LCAO), which is usually adopted to construct the band structure of organic semiconductors. In the following, the discussion is restricted to the cases of the weakly binding model, also called nearly-free-electron model, and the tight-binding model, which are two standard methods used to describe the band structure of inorganic semiconductors.

Nearly-Free-Electron Approximation

In the nearly-free-electron model, the interaction between electrons is not taken into account and a perturbation accounts for the presence of a weak periodic potential [59]. Since the potential $U(\boldsymbol{r})$ is periodic, it can be expanded in a Fourier series:

$$U(\boldsymbol{r}) = \sum_{\boldsymbol{G}} U_{\boldsymbol{G}} e^{i\boldsymbol{G}\boldsymbol{r}} \tag{2.16}$$

where $\boldsymbol{G}$ is the reciprocal lattice vector and in the one-dimensional case $G = 2\pi m/a$, m being an integer. The wave function can be expressed as a Fourier series as well:

$$\Psi(\mathbf{r}) = \sum_{\boldsymbol{k}} C_{\boldsymbol{k}} e^{i\boldsymbol{k}\boldsymbol{r}} \tag{2.17}$$

By substitution of the expressions (2.16) and (2.17) into the Schrödinger equation in (2.12), and upon translation by a reciprocal vector, one obtains a set of algebraic equations of the form [60]:

$$\left(\frac{\hbar^2}{2m}|\boldsymbol{k}-\boldsymbol{G}|^2 - E\right) C_{\boldsymbol{k}-\boldsymbol{G}} + \sum_{G\prime} U_{\boldsymbol{G}\prime-\boldsymbol{G}} C_{\boldsymbol{k}-\boldsymbol{G}\prime} = 0 \tag{2.18}$$

In order to determine the solutions for E in equation (2.18) at the zone boundaries, one has to determine the Fourier coefficients $C_{\boldsymbol{k}-\boldsymbol{G}}$ and $C_{\boldsymbol{k}}$ first. For a weak potential, it is assumed that only the first terms of the Fourier expansion are non-zero. Thus, by taking only the Fourier coefficients at G'=0 to be non-vanishing, one obtains a secular equation corresponding to $C_{\boldsymbol{k}-\boldsymbol{G}}$ and $C_{\boldsymbol{k}}$ for the energy value which results in [60]:

$$E^{\pm} = \frac{1}{2}\left(E^0_{\boldsymbol{k}-\boldsymbol{G}} + E^0_{\boldsymbol{k}}\right) \pm \left(\frac{1}{4}\left(E^0_{\boldsymbol{k}-\boldsymbol{G}} - E^0_{\boldsymbol{k}}\right)^2 + |\mathrm{U}_{\boldsymbol{G}}|^2\right)^{\frac{1}{2}} \tag{2.19}$$

where E^0 represents the energy of the free electron model [see equation (2.20)].

$$E^0_{\boldsymbol{k}} = \frac{\hbar^2 \boldsymbol{k}^2}{2m}, \qquad E^0_{\boldsymbol{k}-\boldsymbol{G}} = \frac{\hbar^2 (\boldsymbol{k}-\boldsymbol{G})^2}{2m} \tag{2.20}$$

Therefore, there exist two solutions E^+ and E^-, i.e. two branches of the dispersion relation. By restricting to the first Brillouin zone, which is limited by $+G/2 = \pi/\mathrm{a}$ and $-G/2 = -\pi/\mathrm{a}$ in the one-dimensional case, it can be deduced that if the potential is neglected ($\mathrm{U}_{\boldsymbol{G}} = 0$), the dispersion relation resembles that of the free electron case [see equation (2.20)]. At the zone boundaries, i.e. where $k = G/2$, the difference in energy between E^+ and E^- in equation (2.19) is given by $\Delta E = E^+ - E^- = 2|\mathrm{U}_{\boldsymbol{G}}|$, which corresponds to the splitting of the band parabola of the free electron case at the Brillouin zone boundary. Such energy splitting is called band gap or forbidden gap and represents a range of energy that is not covered by any band. The most relevant band gap in semiconductor physics is the one that separates occupied (valence band) from unoccupied (conduction band) states, since usually the Fermi level falls somewhere inside. The presence of this band gap is the primary condition for a solid to be denominated as a semiconductor. The equivalents of the valence and conduction bands in organic semiconductors are the highest occupied molecular orbital (HOMO), and the lowest unoccupied molecular orbital (LUMO), respectively. A semiconductor has a direct band gap if the conduction band minimum and valence band maximum occur at the same $\boldsymbol{k}$, otherwise, if they occur at different $\boldsymbol{k}$ the semiconductor is called indirect.

Tight-Binding Electron Model

The tight-binding electron model consists in the description of the electrons of the crystal by the linear superposition of the atomic orbitals. In contrast to the previously described nearly-free electron model, the electron of an isolated atom is considered tightly bound to the ionic

core, that is, the electron is localized in the atomic orbital of the free atom to which it belongs. The electron in the crystal at position $\boldsymbol{r}$ is described by a linear combination of the wave functions of the isolated atoms before they are brought together to form the crystal. The Hamiltonian is in the form:

$$H = -\frac{\hbar^2}{2m}\nabla^2 + U_{\mathrm{at}}(\boldsymbol{r} - \boldsymbol{r}_m) + \sum_{\mathrm{p}\neq\mathrm{m}} U_{\mathrm{at}}(\boldsymbol{r} - \boldsymbol{r}_{\mathrm{p}}) \tag{2.21}$$

$$= H_{\mathrm{at}} + \sum_{\mathrm{p}\neq\mathrm{m}} U_{\mathrm{at}}(\boldsymbol{r} - \boldsymbol{r}_{\mathrm{p}}) \tag{2.22}$$

Here, H_{at} is the Hamiltonian of a single atom at position $\boldsymbol{r}_m$ and the second term in (2.22) accounts for the potentials of all the atoms in the crystal except for the one at $\boldsymbol{r}_m$. The solutions of the corresponding Schrödinger equation (2.23) for a single atom are assumed to be known.

$$H_{\mathrm{at}}(\boldsymbol{r} - \boldsymbol{r}_{\mathrm{m}})\phi_{\mathrm{i}}(\boldsymbol{r} - \boldsymbol{r}_{\mathrm{m}}) = E_{\mathrm{i}}\phi_{\mathrm{i}}(\boldsymbol{r} - \boldsymbol{r}_{\mathrm{m}}) \tag{2.23}$$

In equation (2.23), $\phi_{\mathrm{i}}(\boldsymbol{r} - \boldsymbol{r}_{\mathrm{m}})$ is the atomic orbital corresponding to the wave function of the electron in the atomic energy level E_i. In order to calculate the electronic band structure, the Schrödinger equation (2.24) for the electron in the entire lattice has to be solved.

$$H\,\Psi_{\boldsymbol{k}}(\boldsymbol{r}) = E(\boldsymbol{k})\,\Psi_{\boldsymbol{k}}(\boldsymbol{r}) \tag{2.24}$$

The wave function $\Psi_{\boldsymbol{k}}$ is a Bloch function assumed to be a linear combination of the atomic orbitals $\phi_i(\boldsymbol{r} - \boldsymbol{r}_m)$, each orbital being localized at $\boldsymbol{r}_m$, as expressed in equation (2.25).

$$\Psi_{\boldsymbol{k}}(\boldsymbol{r}) = \frac{1}{\sqrt{N}}\sum_{\mathrm{m}} e^{i\boldsymbol{k}\boldsymbol{r}_m}\,\phi_{\mathrm{i}}(\boldsymbol{r} - \boldsymbol{r}_{\mathrm{m}}) \tag{2.25}$$

N is the number of atoms in the crystal. The energy eigenvalue is obtained from the diagonal elements of the Hamiltonian matrix:

$$E = E(\boldsymbol{k}) = \frac{\langle \Psi_{\boldsymbol{k}}|H|\,\Psi_{\boldsymbol{k}}\rangle}{\langle \Psi_{\boldsymbol{k}}|\,\Psi_{\boldsymbol{k}}\rangle} \tag{2.26}$$

with:

$$\langle \Psi_{\boldsymbol{k}}|H|\,\Psi_{\boldsymbol{k}}\rangle = \frac{1}{N}\sum_{\mathrm{m}}\sum_{\mathrm{p}} e^{i\boldsymbol{k}(\boldsymbol{r}_{\mathrm{p}}-\boldsymbol{r}_{\mathrm{m}})}\int d^3r\;\phi_{\mathrm{i}}^{*}(\boldsymbol{r} - \boldsymbol{r}_{\mathrm{m}})H\phi_{\mathrm{i}}(\boldsymbol{r} - \boldsymbol{r}_{\mathrm{p}}) \tag{2.27}$$

As mentioned before, the solutions of (2.23) have been assumed to be known; the energy eigenvalue of the isolated atom is E_{n}^{0}. Now, by considering only the integrals related to the isolated atom and by restricting the interaction to the nearest neighbors, the dispersion relation is in the form (*cf.* ref. [60]):

$$E(\boldsymbol{k}) \approx E_{\mathrm{i}} - \alpha - \beta \sum_{\mathrm{p}} e^{i\boldsymbol{k}(\boldsymbol{r}_{\mathrm{m}} - \boldsymbol{r}_{\mathrm{p}})} \tag{2.28}$$

The summation in equation (2.28) runs over the nearest neighbors. The terms α and β are expressed by:

$$\alpha = -\int \phi_{\mathrm{i}}^{*}(\boldsymbol{r} - \boldsymbol{r}_{\mathrm{m}}) \sum_{\mathrm{p}\neq\mathrm{m}} U_{\mathrm{at}}(\boldsymbol{r} - \boldsymbol{r}_{\mathrm{p}})\ \phi_{\mathrm{i}}(\boldsymbol{r} - \boldsymbol{r}_{\mathrm{m}})\, d\boldsymbol{r} \tag{2.29}$$

$$\beta = -\int \phi_{\mathrm{i}}^{*}(\boldsymbol{r} - \boldsymbol{r}_{\mathrm{p}}) \sum_{\mathrm{p}\neq\mathrm{m}} U_{\mathrm{at}}(\boldsymbol{r} - \boldsymbol{r}_{\mathrm{p}})\ \phi_{\mathrm{i}}(\boldsymbol{r} - \boldsymbol{r}_{\mathrm{m}})\, d\boldsymbol{r} \tag{2.30}$$

A simple application of the model is the case of a primitive cubic lattice with lattice parameter a and one atomic *s*-state per atomic site. By only taking the next nearest neighbors into account the energy dispersion based on (2.28) becomes:

$$E(\boldsymbol{k}) \approx E_{\mathrm{i}} - \alpha - 2\beta\,(\cos k_{\mathrm{x}}a + \cos k_{\mathrm{y}}a + \cos k_{\mathrm{z}}a) \tag{2.31}$$

2.1.3 Density of States

It was seen that, provided some approximations, the band structure can be derived from the states of weakly bound valence electrons interacting with the atomic core and with the other valence electrons in the solid. The band structure provides information about the bands and illustrates the dependence of the energy states $E(\boldsymbol{k})$ on the wave vector $\boldsymbol{k}$. The band structure largely contributes to the understanding of the electronic and optical properties of a solid. However, the actual distribution and transport of charges directly depends on how many empty or filled states are available at a given energy. This quantity is called density of states (DOS) and is the number of states within an energy interval [E, E+δE] denoted $D(E)$.

For an electron moving in a three-dimensional solid with a volume V (V=L^3, supposing the volume is that of a cube of edge L), the components of the wave vector $\boldsymbol{k}$ satisfy: $k_{\mathrm{i}} = \frac{2\pi}{L} n$, ($n$ is an integer, $i = x, y, z$). Each allowed wave vector, hence each possible state, in $\boldsymbol{k}$-space

occupies a volume of $\frac{(2\pi)^3}{V}$. For a known dispersion relation $E(\boldsymbol{k})$, the density of states is given by the $\boldsymbol{k}$-space volume between the energy isosurfaces $E(\boldsymbol{k})$ and $E(\boldsymbol{k})+\delta E$ divided by the $\boldsymbol{k}$-space volume per allowed state [59]:

$$D(E)dE = \frac{V}{(2\pi)^3} \int_{E}^{E+\delta E} d\boldsymbol{k} \tag{2.32}$$

The volume element $d\boldsymbol{k}$ can be separated into an element of surface area df_E of constant energy E and a component normal to this area, such that $d\boldsymbol{k} = df_E dk_\perp$. Additionally, since $dE = |\mathrm{grad}_{\boldsymbol{k}} E(\mathbf{k})|\, dk_\perp$, the DOS related to the volume V is given by:

$$D(E) = \int_{E(\boldsymbol{k})=\mathrm{E}} \frac{2}{(2\pi)^3} \frac{df_E}{|\mathrm{grad}_{\boldsymbol{k}} E(\mathbf{k})|} \tag{2.33}$$

The integrand in equation (2.33) diverges at critical points in $\boldsymbol{k}$-space corresponding to $|\mathrm{grad}_{\boldsymbol{k}} E(\mathbf{k})| = 0$, i.e. where $E(\boldsymbol{k})$ has extrema. These critical points are called van Hove singularities. Although the integrand diverges at these points, the integral itself, i.e. $D(E)$, does not necessarily and can result in a finite value. The main structures of $D(E)$ originate from these critical points. The two most important critical points are the valence band and the conduction band edges. From equation (2.33), the DOS at these band edges is given by equations (2.34) for the conduction band $[D_{\mathrm{C}}(E)]$ and the valence band $[D_{\mathrm{V}}(E)]$, where E_{C} and E_{V} are the energy offsets corresponding to the conduction band minimum and the valence band maximum, respectively. m_{e}^* and m_{h}^* are the electron and hole effective mass, respectively. Indeed, at the vicinity of the band edges the energy dispersion is parabolic and the particle mass is then replaced by the effective mass m^*. The effective mass is, mathematically, inverse proportional to the curvature of these parabolic bands $1/m^* \propto d^2E/dk^2$). Therefore, information about the effective mass can be withdrawn already from the dispersion curve.

$$D_{\mathrm{C}}(E) = \frac{(2m_{\mathrm{e}}^*)^{\frac{3}{2}}}{2\pi^2\hbar^3}\sqrt{E - E_{\mathrm{C}}} \qquad D_{\mathrm{V}}(E) = \frac{(2m_{\mathrm{h}}^*)^{\frac{3}{2}}}{2\pi^2\hbar^3}\sqrt{E_{\mathrm{V}} - E} \tag{2.34}$$

So far, the band structure and the density of states have been defined and derived. The importance of the valence band, of the conduction band, and of the forbidden region in-between has been pointed out. Whereas the band structure $E(\boldsymbol{k})$ is only defined for crystalline solids, the concept of the DOS is independent of translational invariance and is, therefore, also applicable for non-crystalline solids, provided a sufficient homogeneity regarding structure

and composition exists on a mesoscopic length scale. Due to disorder in amorphous solids, the band gap is diffuse, the band edge is indistinct, and the DOS is characterized by an exponential tail that extends into the band gap [61–63]. These band tails correspond to states classified amongst the "gap states".

Gap states

In ideal, ordered solids, the forbidden band gap corresponds to the energy region between the valence and conduction band edges, i.e $E_V < E < E_C$, where there are no states, i.e. the DOS is expected to be zero. However, in real solids, allowed states can arise in the band gap. These states are encompassed under the general term "gap states". The origin of gap states are various. The most prominent examples are the mere existence of a surface and structural or chemical defects of the solid. They may also arise, as just mentioned, from disorder. In contrast to the delocalized band states, gap states are localized in regions of the real space. These localized states can trap charges, and thus, dramatically interfere in the charge transport process.

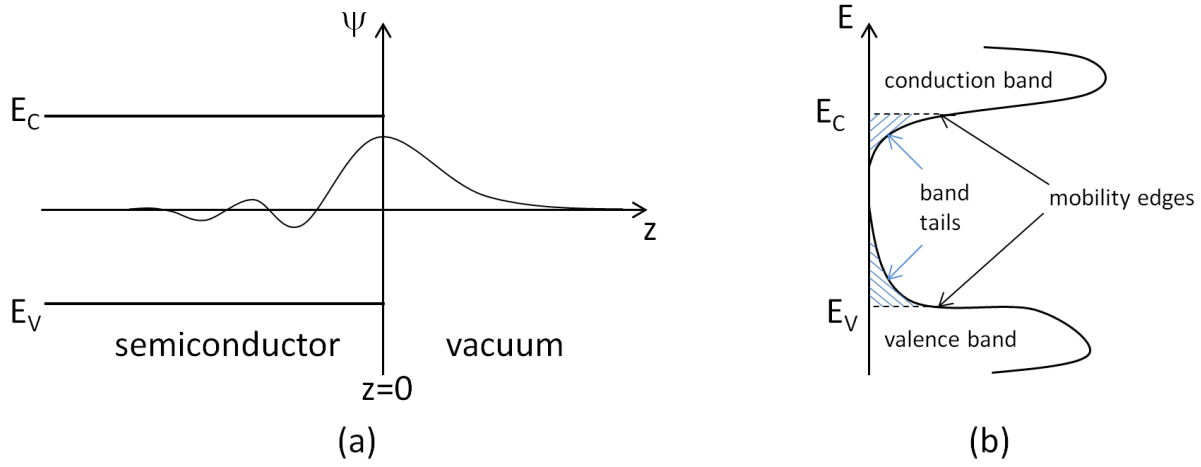

Figure 2.2 Schematic representation of **(a)** the wave function of a state localized at the surface (z=0) in one dimension and **(b)** the band tails (hatched regions) with localized states, which are separated from the band states by the mobility edges.

Surface states are electronic states that can emerge as states in the band gap of the bulk semiconductor. The corresponding wave function is localized at the surface (z=0) of the solid and decays into the bulk and into the vacuum (Figure 2.2a). These states can be due to the inherent properties of the solid surface itself, such as the abrupt termination of the bulk crystal

structure, surface reconstruction or dangling bonds. These states can also be of extrinsic origin, such as imperfections in the stoichiometry, atoms adsorbed at the surface, or new interface states arising from the interaction of two electronic materials upon interface formation. Surface states that lay deeper at mid-gap energy positions are called deep states – in contrast to shallow states which are closer to the band edges – and are particularly efficient charge recombination centers.

Surface states can be donor-like (or acceptor-like) if positively (negatively) charged when unoccupied (occupied). Such charged surface states represent a charge imbalance at the surface of the semiconductor and result in an electric field that is compensated by a charge rearrangement in the semiconductor by band bending. Thus, surface states can strongly influence the alignment of the energy levels at an interface. As mentioned, the valence and conduction bands of semiconductors with disorder exhibit band tails that extend into the band gap (Figure 2.2b). Since these band tails are localized states, the electrons in these states are not free to move, unlike electrons in Bloch states. Hopping mechanisms dominate these conducting states, the latter states are separated from the band states by the mobility edge [64, 65].

2.1.4 Energy Level Alignment

In the previous subsections 2.1.2 and 2.1.3, the electronic structure of semiconductors has been elaborated through the concepts of band structure and density of states. It has been noted that the electronic structure at the surface of a solid generally differs from its bulk properties. Electronic devices are essentially characterized by adjacent layers of electronic materials, generally semiconductors but also insulators and/or metals, with a particular relative alignment of their respective energy levels. For instance, for an optimal charge extraction at a selective interface in solar cells, the VBM of a hole transport material should lie above that of the active material and the CBM of the electron transport material should lie below that of the active material. Besides bulk electronic properties, the properties of the respective surface and interface between adjacent materials in the device are of high importance. The formation of the interface between two materials involves a rather complex electronic structure and underlies a range of possible effects, such as charge density rearrangement, bond formation, molecular hybridization, interface dipoles, or also molecular distortion [66–70]. These effects are reflected in the alignment of the energy levels at the interface between the two components in contact, which generally differs from the situation when the components are

examined individually (*cf.* vacuum level alignment at the end of the present subsection). Although there are insightful models that have been developed to describe the energy level alignment at metal/organic and organic/organic hetero-interfaces for instance [71, 72], specific device configurations often still require individual characterization on a case by case basis. Therefore, elucidating the energy level alignment at interfaces is of fundamental importance, since it determines the charge transport and accumulation or depletion in the devices.

This work investigates the surfaces of perovskites, with a particular focus on the modification of the surfaces' electronic structures by surface composition and pre-adsorbed species prior to any interface formation with usual electronic materials as found in devices. In order to grasp the complex phenomena that underlie the modifications disclosed in this work, several aspects related to energy level alignment relevant for interface formation will be presented. In the following, the Fermi level, which is a central parameter for any electronic material, will be defined first. Afterwards, adsorption on solid surfaces and the related modification of the surface dipole will be shortly discussed. Finally, the concept of band bending and Fermi level pinning is briefly introduced.

Fermi level

In the previous subsection 2.1.3, the concept of density of states was introduced, which defines the number of states in a given energy interval. The next important step is to specify the electronic charge density, i.e. the occupation of the bands. The probability for a given state at energy E to be occupied by an electron is given by the Fermi-Dirac distribution function [54]:

$$f(E) = \frac{1}{e^{\frac{(E-E_F)}{k_B T}} + 1} \tag{2.35}$$

where k_B is the Boltzmann constant and T is the absolute temperature in K. E_F is called Fermi level and denotes the electron chemical potential μ of a thermodynamic system. The probability of a state at energy $E = E_F$ to be occupied is one half. In a metal, E_F is the highest filled level that sets the boundaries between occupied and unoccupied states. In a non-degenerate semiconductor, E_F does not specify a single level and is only defined statistically as a level lying within the band gap [49]. The Fermi level should not be confused with the Fermi energy. Whereas the Fermi level E_F corresponds to the temperature-dependent chemical potential, i.e. $\mu = \mu(T) = E_F$, the Fermi energy corresponds to the chemical potential of the

electrons at a definite temperature T= 0 K, i.e. μ(T= 0 K) = E_{F}^{0}. Consequently, at T= 0 K $f(E)$ looks like a step function. The Fermi level E_{F} is an essential parameter for any electronic system since it allows determining the electron density $n(E) = D(E)f(E)$ per unit energy based on (2.35). The total concentration of electrons n, and holes p in the conduction band, and valence band, respectively, is obtained from:

$$n = \int_{E_{\mathrm{C}}}^{\infty} D_{\mathrm{C}}(E)\, f(E) dE \qquad p = \int_{-\infty}^{E_{\mathrm{V}}} D_{\mathrm{V}}(E)\, [1 - f(E)] dE \tag{2.36}$$

where $D_{\mathrm{C}}(E)$, and $D_{\mathrm{V}}(E)$ are the DOS of the conduction, and valence bands, respectively, approximated by equations (2.34). For semiconductors, assuming $|E - E_{\mathrm{F}}| \gg 2k_{\mathrm{B}}T$, the Fermi statistics in equation (2.35) can be approximated by Boltzmann statistics and the equations (2.36) become [59]:

$$n = \left(\frac{2\pi m_{\mathrm{e}}^{*} k_{\mathrm{B}} T}{h^2}\right)^{\frac{3}{2}} e^{\left(-\frac{(E_{\mathrm{C}} - E_{\mathrm{F}})}{k_{\mathrm{B}} T}\right)} \qquad p = \left(\frac{2\pi m_{\mathrm{h}}^{*} k_{\mathrm{B}} T}{h^2}\right)^{\frac{3}{2}} e^{\left(\frac{(E_{\mathrm{V}} - E_{\mathrm{F}})}{k_{\mathrm{B}} T}\right)} \tag{2.37}$$

Based on the law of mass action, which implies that the product np is fixed and depends only on temperature, and assuming an intrinsic semiconductor, equation (2.38) is obtained.

$$E_{\mathrm{F}} = \frac{1}{2} E_G + \frac{3}{4} k_B T ln\left(\frac{m_h^*}{m_e^*}\right) \tag{2.38}$$

If the effective masses m_e^* and m_h^* are equal, then the Fermi level lies at equal distance from the conduction and valence band edges, that is, in the middle of the band gap. For an intrinsic semiconductor at a temperature T > 0 K, the energy level diagram, the DOS $D(E)$, the Fermi function $f(E)$, as well as the carrier concentration $n(E)$ and $p(E)$ obtained from the product $D(E)f(E)$ and $D(E)[1 - f(E)]$, respectively, are schematically summarized in Figure 2.3a-d. The integrals giving the number of electrons n and holes p in equations (2.36) correspond to the shaded areas in Figure 2.3d. In the case of an intrinsic semiconductor $n = p = n_i$, where n_i is the intrinsic charge carrier density. The law of mass action represented by $np = n_i^2 = constant$ holds for both intrinsic and extrinsic – doped – semiconductors. The n- and p-doping of the semiconductor by addition of impurities increases the concentration of electrons and holes in the conduction, and valence bands, respectively. Correspondingly, E_{F} will adjust its position following the charge density; by shifting up towards the conduction band or down closer to the valence band, for n- or p-doping, respectively [73, 74]. Therefore, E_{F} is an essential parameter to describe the nature of dominant carrier transport and the

electronic properties of a system. It is important to point out that E_F, i.e. the chemical potential, is equal throughout any system electronically in thermodynamic equilibrium. One important surface parameter directly related to the Fermi level is the work function. The work function ϕ is defined as the energy required to remove an electron from the Fermi level E_F inside the solid to the vacuum level E_{vac} as in (2.39) and illustrated in Figure 2.3a.

$$\phi = E_{vac} - E_F \qquad \text{IE} = E_{vac} - E_V \qquad \text{EA} = E_{vac} - E_C \tag{2.39}$$

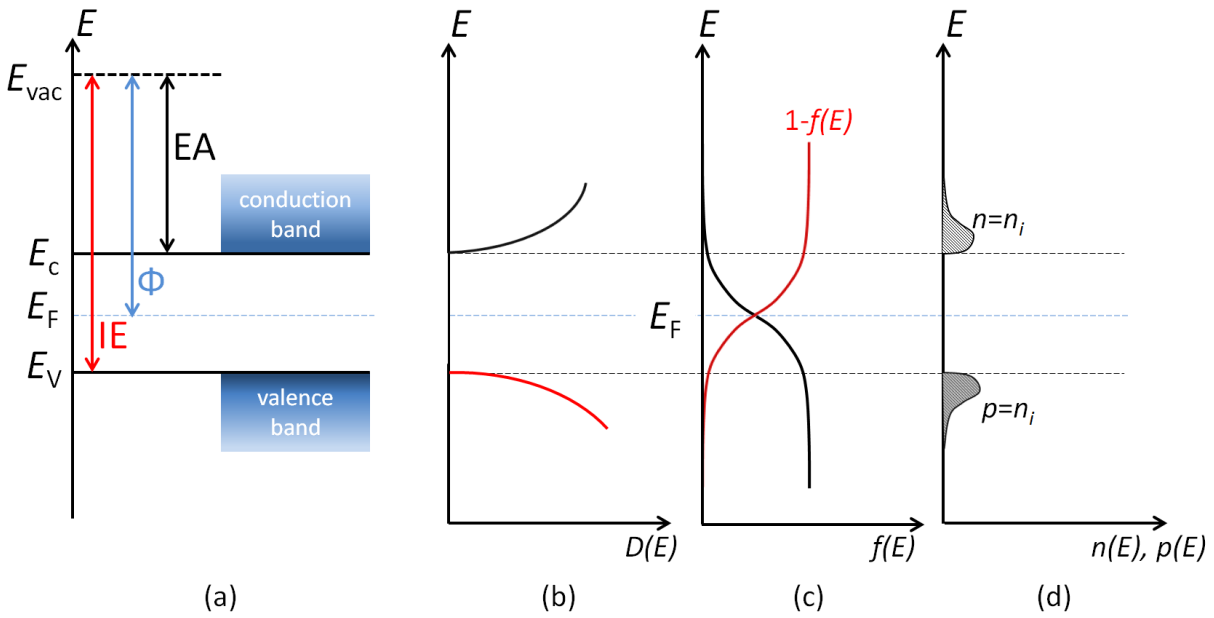

Figure 2.3 Simplified schematic of **(a)** the band diagram, **(b)** the density of states, **(c)** the Fermi distribution function, and the **(d)** electron density n(E) and hole density p(E) for an intrinsic semiconductor.

ϕ consists of a bulk contribution, that is the bulk chemical potential, and a surface contribution due to electronic charge redistribution at the surface [75, 76]. Further important parameters are derived from E_F, E_V, and E_C, as illustrated in Figure 2.3a and given in (2.39). The ionization energy (IE) is the energy difference between the vacuum level and the valence band maximum (VBM), thus designating the minimum energy required to remove an electron from the semiconductor; whereas the electron affinity (EA) refers to the energy gained when adding an electron from the vacuum level to the conduction band minimum (CBM) [75, 77]. It is clear that for a metal, the work function, the IE, and the EA are all equal.

Adsorption on solid surfaces

The interaction with adsorbed molecules from its surrounding environment generally modifies the electronic structure of an initially clean surface in many ways. According to the kinetic theory of gases, the number of particles N_{ads} adsorbed onto a surface per unit area and time is given by the adsorption rate R_{ads}:

$$R_{\mathrm{ads}} = S\frac{dN_{\mathrm{ads}}}{dt} = S\frac{p}{\sqrt{2\pi mkT}} \tag{2.40}$$

where S is the *sticking coefficient* and defines the probability that a particle impinging on a surface actually sticks on it. p denotes the gas pressure, k is the Boltzmann constant, m is the mass of the particle, and T is the temperature. Depending on the forces involved during the interaction of the adsorbed molecule with the surface, one differentiates between *physisorption* and *chemisorption*. The adsorption process is defined as physisorption when the interaction is weak and the electronic structure of both the adsorbed molecule and the solid substrate is not, or only slightly, affected. The interaction underlying this process is the van-der-Waals (vdW) bonding. By contrast, the adsorption is called chemisorption when the interaction between the surface and the adsorbed molecule is stronger and involves a chemical reaction, hence chemical bonding. For instance, the interaction of a molecular adsorbate with a metal surface can result in the hybridization of their orbitals into bonding and antibonding states [78]. Qualitatively, the potential energy curve, representing the energy of an adsorbed molecule as a function of its distance z from the solid surface can describe whether the adsorption process is physisorption or chemisorption. Simplistic one-dimensional potential energy curves are shown in Figure 2.4. From a large distance, the molecule experiences an attractive potential as it comes closer to the surface (z=0), until it reaches an equilibrium distance z_p. Then, the potential energy increases with decreasing z due to the repulsion of the electrons from the molecule and the solid surface.

This potential energy curve represents the physisorption process with the equilibrium energy E_{phys}. In contrast, the chemisorption potential energy curve is characterized by a larger potential well E_{chem}, corresponding to the strength of the molecule bonding to the surface, at a shorter equilibrium distance z_c. Note that at a large distance away from the surface, the chemisorption potential of a diatomic molecule A_2 differs from that of dissociated adatoms 2A by the dissociation energy E_{diss}, as in the case of hydrogen molecules on metal surfaces [78, 79]. Furthermore, to undergo a chemisorption, i.e. to form a chemical bond with

the solid surface, the adsorbing molecule must overcome the activation energy E_{act} at the crossing point above the reference zero energy of the physisorption and chemisorption curves.

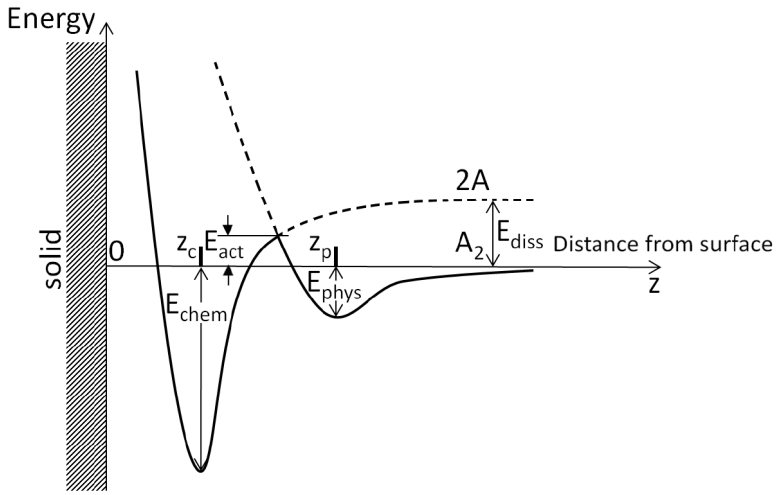

Figure 2.4 Simplified one-dimensional potential energy diagram illustrating the energetics of the adsorption process for the system formed by the adsorbed molecule and the solid surface (z=0). The adsorption potential energy curve (solid line) describes both the physisorption and the chemisorption and is characterized by a crossing point that corresponds to the activation energy E_{act}, a barrier the adsorbed molecule has to overcome in order to chemisorb on the surface. The case of dissociative adsorption is also depicted.

Upon adsorption, the electronic structure of the adsorbates and that of the surface can both be modified due to a rearrangement of the charge density. Two important examples of possible modifications of the surface are a work function change $\Delta\phi$ or a change of the band bending (*see* following section about band bending). The work function change can be due to either a dipole induced by a charge transfer between the adsorbate and the surface, or to a permanent dipole of the adsorbates. An example for the latter case is the decrease of the work function upon adsorption of molecular water on different metal surfaces that has been the topic of several case studies [80–83]. In both aforementioned cases, the interface dipole can be represented with a simple model similar to a parallel plate capacitor. The change of the potential in the vertical z direction (note that usually for symmetry reasons the x-y-components are zero) can be obtained from the Helmholtz-equation:

$$\Delta\phi = \frac{e n_{Dip} \mu_{\perp}}{\varepsilon \varepsilon_0} \tag{2.41}$$

where n_{Dip} is the surface density of the dipoles, $\mu_{\perp}$ is the dipole moment component in the direction perpendicular to the surface. ε, ε_0, and e are the relative, and vacuum dielectric

constant, and the elementary charge, respectively. It is noteworthy that in the case of monolayers formed by molecular dipoles, ε represents an effective factor that takes into account the depolarization of each molecule induced by the neighboring molecules [84, 85]. This effective factor depends on the lateral coverage n and can largely deviate from the macroscopic dielectric constant at higher coverage [84, 86].

It is also important to note that a change of the work function of a surface upon molecules adsorption can also originate from a modification of the surface dipole due to the phenomenon called "push back" effect. The wave functions of electrons in a material decay exponentially in the vacuum above the surface. This is particularly strong for metals, since electrons are highly delocalized; consequently, the spilled out electrons give rise to the formation of a surface dipole since electron density is accordingly missing inside the metal for charge neutrality. Adsorbing molecules on the surface induce a charge rearrangement due to Pauli repulsion, and thus "push" the spilled out electrons back into the material. Consequently the initial surface dipole is reduced and the work function decreases.

The present section underlines the role of adsorbates in the physics of solid surfaces. Solid surfaces are therefore investigated in ultrahigh vacuum (UHV) in order to prevent, or at least reduce, the effects of adsorbates or other contaminants for a more accurate description of their electronic properties. In this context, the impact of exposure to gases on the electronic structure of perovskite surfaces is the subject of section 5.2.

Band bending and Fermi level pinning

For a better overview, it is worth noting that in the extreme case of very weak or no interaction at the interface, the interfacial energy level alignment can be described by a simple "vacuum level alignment" (Schottky-Mott-limit), where both systems forming the interface share a common vacuum level. This simple model allows evaluating the energy level alignment at the interface directly from the energy levels of the separate systems before interface formation. Although this model can be applied, for instance, to several organic-organic interfaces [87, 88], it is not valid in most systems, particularly in the case of metal-organic interfaces [66, 67]. The primary reason for the invalidity of the vacuum level alignment is the occurrence of an interfacial interaction strong enough to induce a charge rearrangement or charge transfer at the interface, resulting in an interface dipole or band bending.

The concept of band bending was first introduced by Schottky and Mott [89–91] to describe the contact rectification at a semiconductor-metal interface due to the formation of a space-

charge region, which results in a bending of the energy bands. Upon contact, electrons are transferred from the semiconductor surface to the metal, or *vice versa*, which leads to a depletion or accumulation region at the semiconductor surface relative to the bulk. This local charge density imbalance induces an electric field at the very interface. As a result of the charge imbalance, the energy bands in the space-charge region at the semiconductor surface will bend until equilibrium is reached. The extent of the band bending can be determined based on the Poisson equation (2.42):

$$\Delta\phi(z) = \frac{\rho(z)}{\varepsilon\varepsilon_0} \tag{2.42}$$

where z is the direction from the surface into the bulk, $\rho(z)$ is the charge density, and ε and ε_0 are the relative, and vacuum dielectric constant, respectively.

Band bending, therefore, originates from a variation of charge concentration. An elementary example is the band bending observed at a p-n junction in equilibrium (see also Figure 2.10 in subsection 2.3.2), in which case the different carrier densities at both sides of the junction result in the formation of the space-charge region, and hence in the bending of the bands [49]. Estimating the extent of band bending at semiconductor interfaces can be done by means of photoelectron spectroscopy, by monitoring the energy position of the valence band and core levels upon atomic layer by atomic layer deposition of a metal or semiconductor layer on top of another semiconductor.

Also, for bare semiconductor surfaces, a surface band bending can be induced by the presence of surface defects or surface states in the semiconductor band gap. The donor- or acceptor-like surface states can have either a positive or a negative charge Q_{ss}. These charges are compensated by charges of different polarity provided by the semiconductor bulk or more precisely, the subsurfacial region, giving rise to a space charge region there. Such compensation ensures the charge neutrality such that the amount of charge in the space charge region Q_{SC} and the amount of charges from the surface states obeys equation (2.43) [79].

$$Q_{\mathrm{ss}} + Q_{\mathrm{SC}} = 0 \tag{2.43}$$

With increasing density of surface states, the bands will bend further until the density of surface states is so high that the energy position of the surface states is close to the Fermi level, at which stage the change of band bending is negligible or inexistent. This effect is termed Fermi level pinning; in other words, the surface states pin the Fermi level at a fixed energy position relative to the band edges.

2.2 Hybrid Organic-Inorganic Perovskite

The term perovskite was first used in 1839 to denominate a mineral identified as calcium titanium oxide $CaTiO_3$, which was discovered by the mineralogist Gustav Rose and named after the mineralogist Lev Perovski [92]. The $CaTiO_3$ mineral is characterized by a specific crystal structure, which has since then been referred to as the perovskite crystal structure. By extension, all materials that exhibit this particular structure are called perovskites. One differentiates between the inorganic oxide perovskites and the halide perovskites. Nowadays, the most investigated perovskite materials in the field of photovoltaics are the hybrid organic-inorganic perovskites (HOIPs), which belong to the latter group. It is noteworthy that this pronounced interest developed only within the past 9 years, although several studies focused on the investigation of these materials have been going on for decades already. Notably, the structure of HOIP methyl ammonium metal halide perovskites was firstly characterized in 1978 by Weber [93, 94], and the tunable conducting behavior of organic-based tin halide perovskites reported in 1994 by Mitzi *et.al.* [95]. It was not until 2009 that HOIP was applied in the field of photovoltaics, namely with the introduction of methyl ammonium lead bromide ($CH_3NH_3PbBr_3$) and methyl ammonium lead iodide ($CH_3NH_3PbI_3$) as light sensitizers in dye-sensitized solar cells (DSSCs), which reached a power conversion efficiency (PCE) up to 3.8% [6]. A few years later in 2012, methyl ammonium lead halides were used as the absorber in solid-state solar cells based on solution-processed thin films [96, 97]. Since then, this class of materials has attracted tremendous attention in the research field of photovoltaics and a strong focus has been put on the improvement of the PCE of perovskite-based solar cells, which evolved up to over 22% in 2017 [98], and even exceeded 23% in all-perovskite tandem solar cells in 2018 [99]. Despite this indisputable outstanding technological evolution, the understanding of the fundamental processes behind device efficiency has not kept pace with device development and still needs to be thoroughly deepened in order to establish reliable property-device functional relationships for a durable efficient material. In the present section, the perovskite structure and some important properties characterizing HOIPs are presented in subsection 2.2.1. An introduction to the electronic structure of these materials is given in subsection 2.2.2. The particular versatilities of HOIPs and the challenges faced in comprehending and improving these materials are shortly addressed in subsection 2.2.3. Although the field of photovoltaics has also recently seen the emergence of all-inorganic perovskites (e.g. $CsPbrBr_3$) [12], the present section 2.2 mainly focuses on the case of hybrid organic-inorganic perovskites (HOIPs) in general. Importantly, the main HOIP system

investigated in the sections 5.1, 5.2, and 5.4 is the methyl ammonium (MA) lead iodide-chloride $CH_3NH_3PbI_{3-x}Cl_x$ ($MAPbI_{3-x}Cl_x$). As will be discussed in section 5.1 the latter system appears to predominantly consist of the $MAPbI_3$.

2.2.1 Perovskite Structural Properties

Perovskite structure

Perovskites have a cubic crystal structure and are characterized by the general formula ABX_3, in which A is an organic or inorganic cation positioned at the corners of the lattice; B is an inorganic cation positioned in the center of the lattice; and X is an inorganic anion or poly-anion centered on the faces of the cubic lattice (Figure 2.5a).

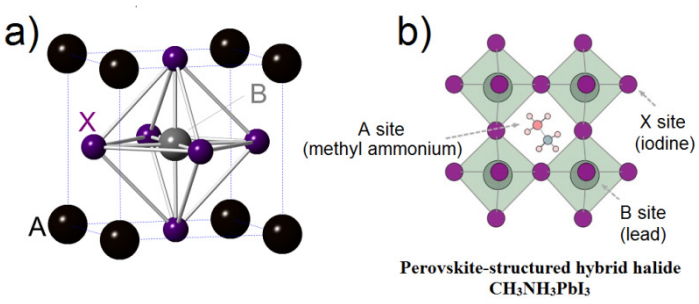

Figure 2.5 a) Schematic representation of a cubic perovskite unit cell with the general formula ABX_3. The B and X atoms are connected by grey lines to better visualize the octahedron formed by BX_6. **b)** Similar schematic representation of $MAPbI_3$ perovskite, adapted from ref. [100].

Equivalently, the cubic perovskite structure can be viewed as BX_6 octahedrons with the A cation located in the interstice. In order to form the perovskite structure, the radii of the different ions have to fulfill the condition set by the Goldschmidt tolerance factor t [101]:

$$t = \frac{r_A + r_X}{\sqrt{2}(r_B + r_X)} \tag{2.44}$$

such that t is between 0.8 and 1, and where r_A, r_X, and r_B are the radius of the respective anions. In the simplest form of a HOIP, A is an organic monovalent anion, B a divalent metal cation (Pb^{2+}, or Sn^{2+}), and X a halide anion (I^-, Br^-, Cl^-). One typical example with this simple configuration is the state-of-the art methyl ammonium (MA) lead iodide (referred to as $MAPbI_3$), which is built by the molecular A site methyl ammonium cation $CH_3NH_3^+$, the B site lead cation Pb^{2+}, and the X site iodide I^- (Figure 2.5b). In an effort to improve the stability of HOIP and to simultaneously enhance the performance of HOIP-based solar cells, alternative materials based on various combinations of different organic cations and halides,

with the final stoichiometry conforming to ABX_3, have been developed in the past few years. Of particular note are the formamidinium (FA) cation $[CH(NH_2)_2]^+$, and guanidinium (Gua) cation ($CH_6N_3^+$) for the A site, and chloride (Cl^-), and bromide (Br^-) for the X site.

For a clearer overview, except for general considerations on HOIPs and unless otherwise specified, most of the properties described in this section refers to the state-of-the-art $MAPbI_3$ perovskite. The crystal structure of the solid, three-dimensional $MAPbI_3$ is characterized by three different temperature-dependent phases, as summarized in Table 2.1 [102, 103]. At room temperature, the perovskite structure is expected to be in the tetragonal phase and undergoes a transition to a cubic perovskite phase at T>327 K (54 °C), and to the perovskite orthorhombic phase at a much lower T<165 K.

Table 2.1 The three different temperature-dependent structural phases of $MAPbI_3$ perovskite.

Temperature range (K)	**T<165**	**165<T<327**	**T>327**
Structural phase	γ-phase	β-phase	α-phase
$MAPbI_3$ crystal structure	orthorhombic	tetragonal	pseudo-cubic

These temperature-dependent phase transitions have been shown to result from the positional disorder of the MA cation relative to the orientation of the C-N axis.[104] $MAPbI_3$ is characterized by the strong orientational disorder of the MA cations due to thermal motion at high temperatures for the tetragonal and cubic phases, whereas at low temperatures, – as in the orthorhombic phase – the MA cations are ordered with a fixed orientation [102, 104–106].

HOIP as an absorber material for photovoltaic application

HOIPs are built up with organic and inorganic subunits – and therefore called hybrid –, they also feature several attractive properties that are comparable to, or even more advantageous than, those of either organic or inorganic semiconductors. A few of these properties are listed in Table 2.2; for instance, HOIPs have larger carrier mobility than organic semiconductors while exhibiting higher intrinsic carrier concentration and longer carrier lifetime in comparison to their inorganic counterparts. Two important properties of HOIP as a light absorber in a solar cell are its high absorption coefficient estimated to be 15000 cm^{-1} at 550 nm, and the tunable band gap. The optical band gap of $MAPbI_3$ is estimated to be in the range of 1.5 eV to 1.6 eV [103, 107–109], whereas the transport gap determined by means of

photoelectron spectroscopy is 1.7 eV for $MAPbI_3$ [110, 111]. As will also be discussed in subsection 2.2.3, the band gap of HOIP can vary depending on its composition. Perovskite materials are characterized by Wannier-type excitons,[1] which are delocalized over several lattice points, with reported low exciton binding energy (E_B) for $MAPbI_3$ ranging from 2 meV to 75 meV [112–114]. The high absorption coefficient of $MAPbI_3$ is generally attributed to the observation that $MAPbI_3$ behaves like a direct band gap semiconductor [97, 115, 116], in contrast to semiconductors with an indirect band gap – such as silicon. However, recent studies point towards the band gap of $MAPbI_3$ having an indirect-direct character [117, 118] This has been attributed to the Rashba-splitting of the conduction band due to strong spin-orbit coupling, which is related to the breaking of inversion symmetry, notably around the Pb site [119–121].

Table 2.2 Overview of a few properties of HOIPs – different materials taken together – and approximate reference values of solar cell parameters based on perovskite, organic, and inorganic materials. Collected and adapted from ref. [54, 107, 122–126].

Material	Perovskite	Organic material	Si	GaAs
Band gap (eV)	1.2 – 3.7	0 – 4	1.1	1.4
Absorption coefficient (cm^{-1})	10^4-10^5	~ 10^5	10^3	10^4-10^5
Carrier mobility (cm^2/Vs)	8 – 2000	~ 1	1500	8500
Intrinsic carrier concentration (cm^{-3})	10^{11}-10^{16}	~ 10^{17}	10^{10}	10^6
Carrier lifetime (ns)	> 10^8	~ 10^3	~ 10^6	~ 10^2
Solar cell – PCE (%)	~ 20	~ 10	~ 25	~ 30
Film thickness in solar cells (nm)	~ 3×10^2	$(1\text{-}2)\times10^2$	$(1\text{-}2)\times10^5$	~4×10^3

[1] An exciton is a bound state formed by an electron-hole pair (see also subsection 2.3.2). In the case of Wannier excitons, the electron-hole interaction is weak due to the screening of the Coulomb interaction by the large dielectric constant of the semiconductor.

One particularity of HOIPs is their ambipolar character, i.e. they can transport both electrons and holes [127–129]. Nevertheless, HOIPs are still commonly used in solar cells in combination with additional hole and electron transport materials for enhancing charge-transfer and reducing electron-hole recombination at the contacts [130, 131]. HOIPs are characterized by high charge carrier diffusion lengths that can exceed 1 μm [16], which is larger than the optimal thickness of a few hundred nanometers of the perovskite layer in PSCs.

HOIP materials processing

From the perspective of large-scale application, HOIPs are particularly attractive due to their solution-processability. To obtain thin films for application in prototypical solar cells, HOIPs can be deposited following a large spectrum of possible methods [132]. The four most frequently applied methods are (i) deposition by spin-coating from a perovskite precursor solution (see also section 4.1) [96, 97]; (ii) two-step sequential deposition, consisting of deposition of the lead halide solution by spin-coating followed by dipping of the obtained lead halide substrate into a methyl ammonium halide solution [133]; (iii) co-evaporation of both lead halide and methyl ammonium halide materials [134]; and (iv) vapor-assisted processing consisting of exposure of a spin-coated lead halide film to a methyl ammonium halide vapor for perovskite formation [135]. The main deposition method adopted in this work is the deposition from precursor solution by spin-coating. After the spin-coating of the perovskite precursor solution, the as-deposited yellow films are thermally annealed in order to obtain crystallized films with a dark color.

The deposition process can strongly influence the morphology of the HOIP films since it impacts the crystallization of the film, the size of the grains, and the film homogeneity. The film morphology in turn has an impact on the optoelectronic properties of the film and ultimately on device performance [134, 136–140]. Therefore, efforts have been concentrated on improving film morphology, for instance via solvent engineering, also known as anti-solvent method, as developed by Jeon et al.[141]. This developed preparation method is based on the use of two mixed solvents, namely γ-butyrolactone (GBL) and dimethyl sulfoxide (DMSO) for the perovskite solution. The additional and decisive step is the drop-casting of a non-dissolving solvent, in this case toluene, during the final stage of the spinning step. It has been asserted that GBL evaporates already in the early stage of spinning. Upon toluene drop-casting, excess of DMSO is removed and the rest of DMSO forms the MAI-PbI_2-DMSO phase, thereby slowing down the reaction between MAI and PbI_2, and hence the

formation of the final $MAPbI_3$. This freezing of the constituents has been affirmed to allow the formation of a uniform crystalline perovskite film [141]. This method is applied for thin films preparation in subsection 5.4.2.

2.2.2 Electronic Structure of Hybrid Organic-Inorganic Perovskites

Determining the electronic band structure of $MAPbBr_3$ and $MAPbI_3$ has been the object of experimental [142–145] and theoretical studies [119, 146, 147]. Band structure calculations for $MAPbI_3$ estimated that the top of the valence band consists of the antibonding state formed by the Pb 6s and I 5p atomic orbitals, whereas the conduction band minimum mainly consists of the antibonding state formed by the Pb 6p and I 5p orbitals (Figure 2.6a-b) [119, 147, 148]. The strong coupling between these orbitals yields large band dispersions for the valence and conduction band edges with particularly low DOS near/at the VBM [149, 150]. The possible presence of such a low DOS has to be taken into account while analyzing valence band spectra obtained from photoelectron spectroscopy (PES), see subsection 3.1.2.

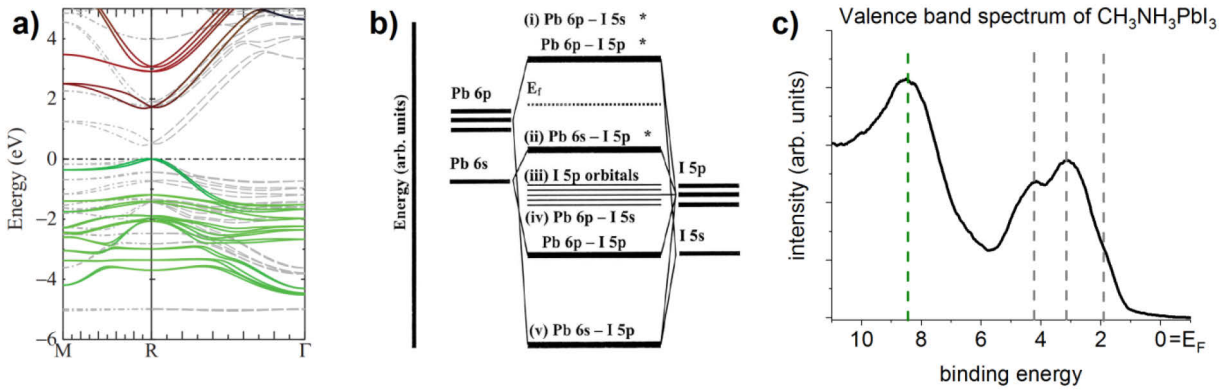

Figure 2.6 a) Calculated band structure of cubic phase $MAPbI_3$, zero on the energy scale corresponds to the valence band maximum. The M, R, and Γ points correspond to (1/2,1/2,0), (1/2,1/2,1/2), and (0,0,0). The color coding indicates a stronger contribution of I 5p (green) than Pb 6s (blue) to the VBM, and a stronger contribution from Pb 6p (red) than the other orbitals to the CBM. Bands in light grey dotted lines are calculated based on the local-density approximation, see ref. [119]. **b)** Bonding diagram of the $[PbI_6]^{-4}$ cluster to represent $MAPbI_3$. **c)** Valence band spectrum of a $MAPbI_3$ film measured by UPS. The first three peaks (grey dotted lines) closest to the Fermi level E_F correspond to states originating from the hybridizations of Pb and I orbitals, the contribution from the organic cation MA^+ are deeper in the valence band (green dotted line). a) is reprinted with permission from Brivio et al., Phys. Rev. B, 89, 155204, 2014 (ref. [119]). Copyright (2014) by the American Physical Society. b) is reprinted with permission from Umebayashi et al., Phys. Rev. B, 67, 155405, 2003 (ref. [147]). Copyright (2003) by the American Physical society.

So, the valence band features close to the band edge originate from states formed by the Pb and I orbitals and the frontier energy levels can be described by the bonding diagram of the $[PbI_6]^-$ cluster as in Figure 2.6b. In contrast, the states originating from the MA^+ cations lie energetically further in the valence band (Figure 2.6a and Figure 2.6c) and the conduction band, and therefore do not contribute to the frontier bands. Thus, the electronic properties of $MAPbI_3$ mainly depend on the inorganic lead-halide. The role of the organic cation, MA^+ in the case of $MAPbI_3$, is the subject of discussion in the field of HOIPs. The organic cation has been suggested to merely ensure charge balance and formation of the perovskite structure as long as its effective radius fulfills the Goldschmidt tolerance factor in (2.44) [119, 151]. In support of this assertion, it was shown that substituting the organic MA^+ with the inorganic Cs^+ in $MAPbBr_3$ leads to $CsPbBr_3$-based devices with performance comparable to that of $MAPbBr_3$-based devices [152]. However, a more recent resonant X-ray photoelectron spectroscopy (resPES) study reported the direct contribution of nitrogen in the organic MA to the electronic structure of $MAPbI_3$, particularly through the interaction of iodine and nitrogen valence states [153]. Moreover, it is noteworthy that the size and symmetry of the organic cation, as well as the nature of its hydrogen bond to the iodine atom can lead to the modification of the lattice parameters and thus, impact the electronic structure of the perovskite material [118, 154, 155]. A representative example of a result of such effects is the band gap narrowing by the substitution of MA^+ in $MAPbI_3$ with the formamidinium cation FA^+ [32, 156].

The electronic structure of HOIPs can be affected by the presence of defects. Earlier density functional theory (DFT) calculations proposed that donor-like or acceptor-like defects with low formation energies such as a missing I or Pb (i.e. I- or Pb-vacancy), can result in shallow donor and acceptor levels near the CBM, or VBM, respectively [157, 158]. In contrast, deep level states in perovskites can only be created by defects that have high formation energies [151]. The doping of HOIPs has been suggested to mainly consist of doping induced by native defects. It was experimentally found that the stoichiometry of $MAPbI_3$ films influences their electronic properties.[159] Films with excess of PbI_2 exhibit n-type character, whereas films with excess of MAI are p-type. This has been suggested to originate from MA^+ and I^- deficiency (i.e. MA^+ and I^- vacancies), and Pb^{2+} deficiency (i.e. Pb^{2+} vacancy), respectively [159]. It was also observed that perovskite surfaces can be n-doped by elemental Pb (Pb^0), which acts as electron donor [160]. Furthermore, the ionization energy of HOIPs depends not only on the composition but also on the preparation method [161].

Regarding the electronic structure of HOIP surfaces in particular, DFT calculations have shown that the surface termination can also impact the surface electronic properties [162, 163]. PbI-terminated $MAPbI_3$ surfaces exhibit valence and conduction band edges positioned at 1 eV energy lower, with respect to the vacuum level, than MAI-terminated surfaces, thus significantly impacting the energy level alignment at the interface between the perovskite and the charge transport material [163]. In order to assess the degradation of $MAPbI_3$ surfaces upon interaction with water, Mosconi et al. concluded from *ab initio* calculations that whilst hydration with a monolayer of water does not significantly affect the electronic structure of MAI-terminated surfaces, the band gap of PbI_2-terminated surfaces widens by 0.3 eV [164].

2.2.3 Material Versatility and Fundamental Challenges

A very important feature of HOIPs is their versatility, illustrated by the numerous physical and chemical properties that can result from the modification of their composition and preparation. This versatility offers great potential as it allows the properties of the material to be tuned. However, it also represents a critical drawback since it results in pronounced variations and large reproducibility issues from sample to sample and from laboratory to laboratory. A non-exhaustive list of these tunable properties of HOIPs, including those mentioned in subsection 2.2.1, and of the challenges in the field is given in the following:

- HOIP is obtained from a mixture of lead halides and organic cations with the condition that the Goldschmidt tolerance factor is respected. Combinations of several cations or two different halides result in different material properties, as demonstrated by the band gap tuning of the mixed halide perovskite $MAPb(I_{1-x}Br_x)_3$ ($0<x<1$) films, where the band gap of the films increases with increasing stoichiometric Br content x (Figure 2.7) [165]. Another example is the change in ionization energy upon halide substitution [166].
- The modification and optimization of the deposition method, as well as the tuning of the annealing parameters (temperature, environment or duration) in the case of solution-processed perovskite films, can improve the crystallization process and the corresponding film morphologies, which then lead to higher solar cell efficiencies (see subsection 2.2.1).
- The self-doping process in HOIPs facilitates the tuning of their electronic properties by modifying the stoichiometry of the material.

- Recently, low-dimensional (<3D) perovskites have attracted increasing attention. In particular 2D and quasi-2D (a mixture of 2D and 3D) perovskites grown from solution are promising candidates for applications in the field of nanotechnology and photovoltaics [167].
- One critical issue that has been observed in HOIP-based devices is photocurrent-voltage hysteresis, which has been suggested to be possibly related to the phenomenon of ion migration; this latter phenomenon has been and still is the focus of intense investigations [168].
- One critical disadvantage of HOIPs is the sustainability issue arising from the presence of lead in the most efficient HOIPs. Tin (Sn) was the first suggested potential, and in theory, less toxic substitute to lead. However, Sn is a harmful element and one that can lead to serious intoxication issues [169]. Although alternative solutions such as the recycling of perovskite solar cells are valuable for avoiding lead waste [170], the development of optimal lead-free perovskite materials still remains an inevitable challenge.

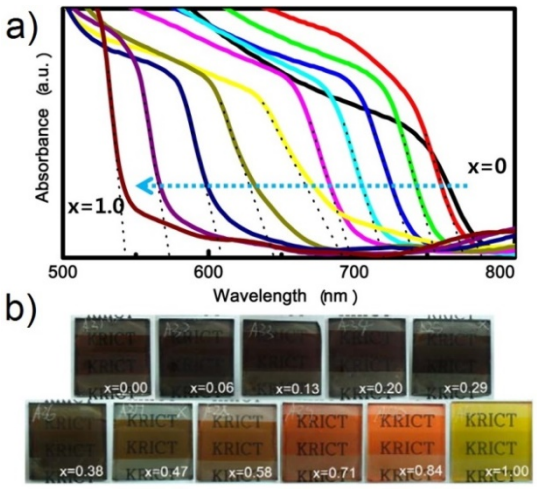

Figure 2.7 a) UV-Vis spectra of $MAPb(I_{1-x}Br_x)_3$-based solar cells, which highlight the shift of the absorption onset, hence the optical gap widening with increasing x amount of Br. Accordingly, **b)** the color of the $MAPb(I_{1-x}Br_x)_3$ nanocomposites is tuned from dark opaque to red to yellow with increasing x. a) and b) reprinted from Noh et al., Nano Lett. 2013, 13, 1764−1769. Copyright (2013) American Chemical Society.

One of the most critical challenges in the development of efficient HOIPs remains their stability, which still hinders their long-term application and commercialization. The degradation of $CH_3NH_3PbI_3$ ($MAPbI_3$) in particular is characterized by its segregation into MAI-related products and by the emergence of PbI_2 [24, 171, 172]. The latter can further segregate into Pb^0 and iodine, notably through photolysis [173–175]. Elemental lead Pb^0 in HOIPs acts as a defect that n-dopes the material and eventually pins the Fermi level close to the conduction band [160, 176]. Tremendous efforts have been made to expand the understanding of the HOIP degradation pathways, especially by addressing the effects of

different factors such as oxygen, water, light, and temperature, as will be summarized in the following. It is worth noting that a consistent description on the microscopic level of the actual processes that activate the degradation of HOIPs through the aforementioned factors often remains elusive.

Nevertheless, detailed insights have been provided in the case of oxygen [177–179]. Aristidou et al. highlighted that in dry air, oxygen rapidly diffuses through ca. 500 nm thick $MAPbI_3$ and $MAPbI_{3-x}Cl_x$ films within 10 minutes [177]. Their work also reported that the oxygen uptake is particularly eased by the presence of iodide vacancies which provide a suitable volume for the implantation of oxygen into the perovskite structure [177]. The actual oxygen-induced degradation is tightly related to the presence of light. Upon illumination, photoexcited electrons in $MAPbI_3$ are transferred to molecular oxygen, resulting in the formation of superoxide (O_2^-) [178, 179]. The superoxide species reacts with the methylammonium cation $CH_3NH_3^+$ and deprotonates this latter, resulting in the generation of methylamine CH_3NH_2, PbI_2, and iodine [178, 179]. The photo-induced degradation (1 sun illumination) of $MAPbI_3$ in presence of oxygen at level as low as 1% has been shown to start at the grain boundaries and at the surface [180]. This was suggested to be possibly due to the higher density of defects (such as iodine vacancies) [181, 182] observed at these areas [180].

Exposure to light has been also reported to induce iodide migration away from the illuminated region [183]. The driving force for this ion migration was and still is at the center of a vivid debate; it has been recently suggested that the presence of charged oxygen species, such as O_2^-, at the $MAPbI_3$ surface upon illumination can result in an electrostatic repulsion of iodide away from the surface towards the bulk before O_2^- reacts with the perovskite and eventually induces irreversible degradation [184]. These light-related issues are crucial for the reliable application of $MAPbI_3$ as light-harvester.

Whereas massive water exposure instantly dissolves the perovskite layer (see subsection 5.4.1), more moderate water vapor exposure (higher than 50% relative humidity RH) induces two significant structural changes of $MAPbI_3$ perovskite [40, 42]. Namely the reversible formation of the monohydrate phase $CH_3NH_3PbI_3{\cdot}H_2O$, and the irreversible formation of the dihydrate $(CH_3NH_3)_4PbI_6{\cdot}2H_2O$ at higher RH and/or longer exposure [see equation (2.45)][42]. The irreversibility is conditioned by the generation of an excess of water and the formation of PbI_2 [42], i.e. the second arrow in equation (2.45) will point solely towards the right direction.

$$4(CH_3CH_3)PbI_3 + 4H_2O \rightleftharpoons 4[CH_3NH_3PbI_3 \cdot H_2O] \rightleftharpoons (CH_3NH_3)_4PbI_6 \cdot 2H_2O + 3PbI_2 + 2H_2O \quad (2.45)$$

Therefore, independent of the degradation factors and processes, $MAPbI_3$ ultimately degrades when some of the primary MAI-related degradation products are irreversibly dissolved or sublimed, leaving PbI_2 behind. This is also the case for $MAPbI_3$ films which degrade into CH_3I, NH_3, and PbI_2 when exposed to heat stress [173, 185–187]. A structural investigation even suggests that such degradation of $MAPbI_3$ films can occur already at exposure to 80 °C for about one hour [188]. Such thermal instability seriously impedes the long-term application of perovskite-based solar cells, which are expected to withstand temperature up to 65 °C during their lifetime [189].

Thus, it emerges from these stability investigations that the $MAPbI_3$ structure must be stabilized in order to avoid its degradation. The main approach that has been explored is the complete or partial substitution of the organic cations and/or the halides, as mentioned in subsection 2.2.1. In the extreme case, all-inorganic perovskites such as caesium metal halide perovskites have been investigated. Whilst the inorganic iodide-based perovskites appear to be confronted with crystal phase stability issues, bromide-based $CsPbBr_3$ was reported to exhibit enhanced structural stability in comparison to its HOIP counterparts [12, 190, 191]. $MAPbI_{3-x}Br_x$-based solar cells (with x up to 0.3) exhibited enhanced stability in comparison to $MAPbI_3$-based ones [33]. This was attributed to the substitution of I by smaller Br, which leads to the shrinking of the perovskite unit cell and to the formation of a more stable cubic structure for $x>0.2$ [33]. The stronger hydrogen bonding between the NH_3^+ group of the organic cation and the halide ions in $MAPbI_{3-x}Br_x$ was suggested to play an essential role in triggering the enhanced structural stability in this case [192, 193]. However, these mixed halide $MAPbI_{3-x}Br_x$ perovskites undergo a reversible photo-induced halide phase segregation into a major bromide-rich phase and a iodide-rich phase upon illumination, where the latter constitutes a domain where carriers are trapped [194]. In an analog fashion to the halide substitution, strategies based on mixing cations have been explored in order to improve the structural and thermal stability of perovskite; these materials include the $FA_{1-x}MA_xPb(I_{1-y}Br_y)_3$ ($0<x<1$ and $0<y<1$) [195, 196], and the triple cation perovskite, in which case cesium is added to the former FA/MA mixed cations perovskite [197]. It can be seen that the rich versatility of HOIPs potentially offers a large room for stability improvement. However, the innumerable possibilities can also increase the materials complexity and generate additional issues, as shown in the example of the aforementioned phase segregation in mixed halide

perovskite. In subsection 5.3.1, newly developed $MA_{1-x}Gua_xPbI_3$ perovskites which are obtained by the partial substitution of MA by Gua will be presented. The insertion of the large Guanidinium cation into the $MAPbI_3$ structure for x up to 0.25 resulted in a more stable structure, and hence in solar cells with enhanced stability in comparison to the pure $MAPbI_3$.

2.3 Basic Principles of Solar Cells

2.3.1 The Solar Spectrum

Photovoltaic cells are devices that convert electromagnetic radiation from the sun into electrical energy. The solar spectrum striking the Earth's surface spans a wavelength range from high energy X-rays to long radio waves, although the peak of emission lies in the visible region. Since the temperature T at the surface of the sun is around 5 800 K, its spectral radiance can be approximated by the frequency-, and hence wavelength-dependent spectral radiance B_λ of a black body radiation, as described by Planck's law (2.46).

$$B_\lambda(T) = \frac{2hc^2}{\lambda^5}\frac{1}{e^{\frac{hc}{\lambda k_B T}} - 1} \tag{2.46}$$

where h is the Planck constant, c is the speed of light, and k_B the Boltzmann constant. Based on Planck's law in (2.46), the total power radiated by a black body per time and per surface area A is obtained by integrating B_λ over all wavelengths, thus resulting in the Stefan-Boltzmann law:

$$\frac{P}{A} = \sigma T^4, \qquad \sigma = \frac{2k_B^4\pi^5}{15c^2h^3} \tag{2.47}$$

where σ is the Stefan-Boltzmann constant. The spectral irradiance of the solar radiation reaching the Earth surface depends on the environmental conditions along the path between the sun and the Earth, and on the geographical position of the terrestrial surface considered. To account for these factors and ensure comparable results, the solar irradiance is defined according to the American Society for Testing and Materials (ASTM) in terms of Air Mass coefficient (AM), which defines the path length of the solar radiation through the atmosphere of the earth. Thus, AM0 corresponds to the solar spectrum outside the Earth atmosphere, which slightly deviates from that of the perfect black body spectrum due to the wavelength-dependent absorption by the sun atmosphere (Figure 2.8). When passing the Earth's

atmosphere, solar radiation is attenuated due to scattering and absorption processes, thus resulting in absorption bands in the solar irradiance. The attenuation in the infrared range is namely ascribed to water vapor and carbon dioxide, whereas oxygen contributes to the attenuation in the visible range and ozone filters out the radiation in the ultraviolet (UV) region.

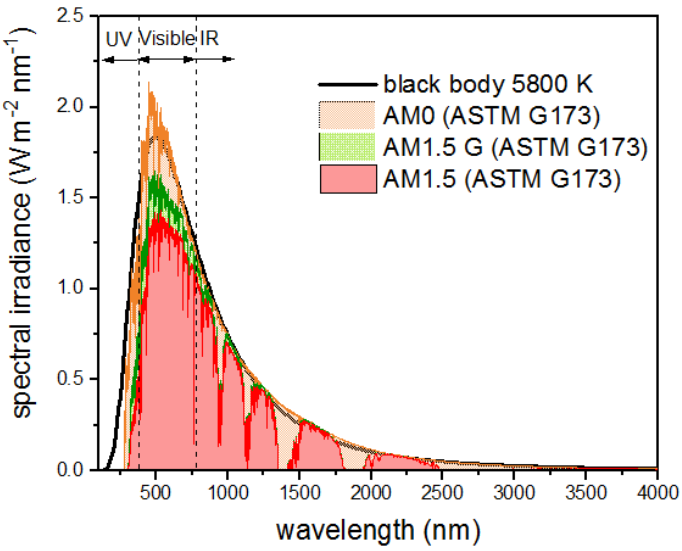

Figure 2.8 Solar spectrum outside the atmosphere (AM0, orange), global spectrum AM1.5 G (green) on Earth's surface, which consists of both direct and diffuse radiations, and the direct spectrum AM1.5 (red). Plot based on data retrieved from www.nrel.gov (ref. [198]).

The standard coefficient AM1.5 defines the solar radiation impinging at a zenith angle of 48.2° through 1.5 times the atmosphere thickness. The AM1.5 G, where G stands for global, defines the solar spectrum consisting of both direct and diffuse light reflected from the ground on a south facing surface tilted at 37° from horizontal and is shown in Figure 2.8. The corresponding total integrated irradiance is 100 mW/cm^2, which is the commonly chosen standard condition adopted in solar simulators for photovoltaic testing.

2.3.2 Physics of Solar Cells

In the following, the basic physics of solar cells is briefly summarized. A detailed derivation of the formulae shown in this section is beyond the scope of this work and can be found in the literature [54, 199–201]. The conversion of the solar radiation into electrical energy by solar cells requires three important steps to take place (Figure 2.9):

1. the light absorption and following charge generation
2. the charge separation
3. the charge transport and extraction

The first step for light conversion is obviously its absorption by the absorber material. The most important property of the selected semiconductor in this regard is an appropriate band gap to enable the optical excitation of the electrons from a low energy level, usually the valence band, to a higher energy level, usually the conduction band, and hence generate free electrons and holes that can move within the semiconductor. However, the excited electron can also still interact with the generated hole due to electrostatic Coulomb force. In that case, the electron-hole pair forms a bound state called "exciton", which corresponds to the lowest excited state of the electronic system. The exciton is characterized by the exciton binding energy (E_B) which is the energy necessary to dissociate the bound electron-hole pair into free charge carriers that can be collected. Materials with low E_B are therefore desirable for solar cell applications in order to generate a high number of free charge carriers. In inorganic semiconductors, the exciton binding energy is usually in the range of a few meV (E_B =15 meV for Si [202]), i.e. lower than the thermal energy k_BT at room temperature, whereas organic semiconductors are generally characterized by Frenkel excitons, i.e. the electron-hole pair is tightly bound and localized on the same molecule, with a higher exciton binding energy that can exceed 1 eV [203]. As mentioned in subsection 2.2.1, HOIPs are characterized by delocalized Wannier-type excitons with a few tens of meV E_B. Although the discussion about the excitonic properties of perovskite materials is still on-going, it has been conventionally agreed upon that the dominating energy conversion process in these materials is the direct free charge carrier generation [125].

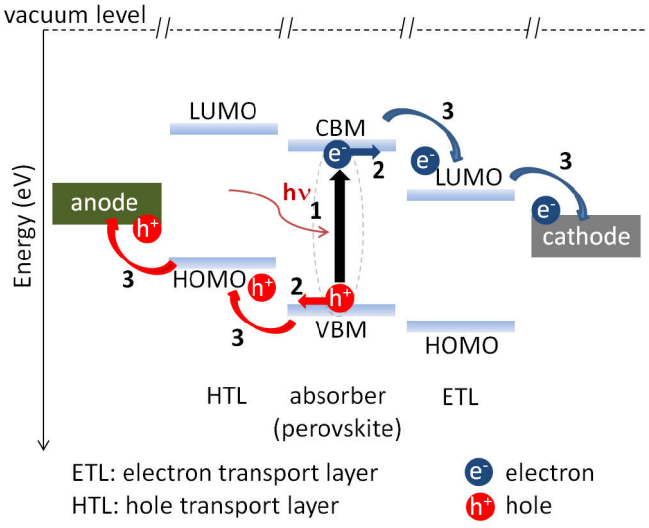

Figure 2.9 The three steps for solar radiation conversion into electrical energy in a solar cell. **1)** Light absorption and charge generation. The dotted ellipse illustrates the case of exciton generation. In the present example of a perovskite-based solar cell, free charge carrier generation pre-dominates, since the perovskite exciton binding energy is low [204]. **2)** Charge separation. **3)** Charge transport and extraction. LUMO and HOMO designate the lowest unoccupied molecular orbital and the highest occupied molecular orbital, respectively of the adjacent organic materials.

The second step is the charge separation, which, as is also the case for charge extraction, depends on the optimal alignment of the energy levels at the respective junctions, as seen in subsection 2.1.4. This second condition implies that the free charge carriers move in two opposite directions, across the interfaces and towards the respective electrodes without recombining. In the example shown in Figure 2.9, this would mean that the electron (hole) moves from the absorber layer towards the electron transport layer, ETL (hole transport layer, HTL).

The third step, which is tightly related to the charge separation and finalized with the charge extraction at the electrodes, consists of the charge transport inside the material. The transport of the charges depends on the charge carrier diffusion lengths and the electron-hole recombination that can significantly reduce the number of available free charge carriers.

Solar cells consist of several interfacial layers, thus stressing the importance of energy level alignment at the interfaces with regard to the above last two conditions. In order to further illustrate the basic physics of solar cells, the simple example of conventional solar cells based on the p-n junction is described. A p-n junction is an interface formed by a p-type semiconductor with holes as majority carriers, and n-type semiconductor with electrons as majority carriers, as shown in the one-dimensional representation in Figure 2.10.

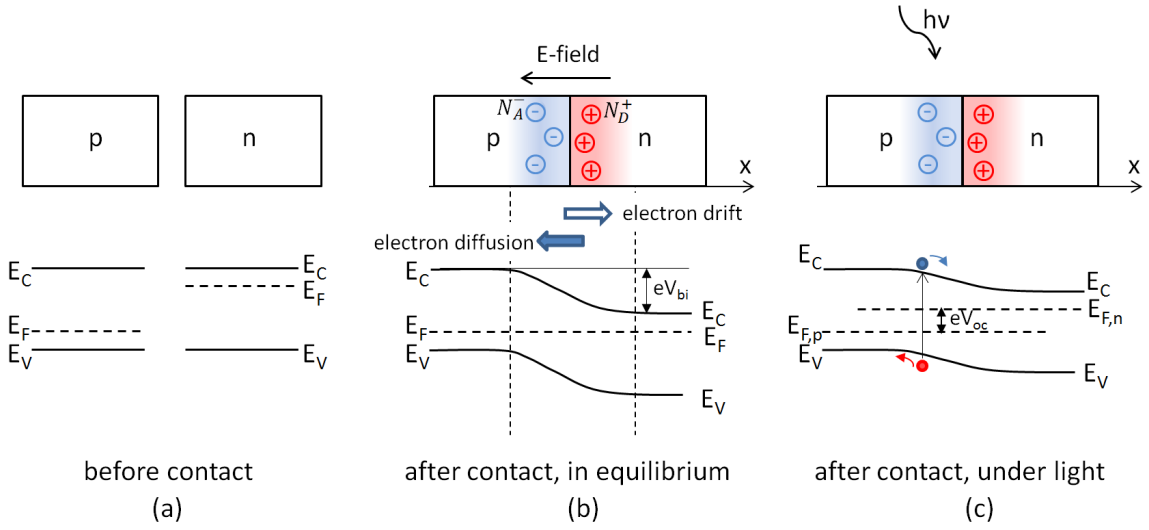

Figure 2.10 p-type and n-type semiconductors **(a)** before contact, **(b)** upon formation of the p-n junction at thermal equilibrium, and **(c)** at non-equilibrium under illumination; the red dot represents a hole and the blue dot represents an electron.

One simple example is the conventional silicon p-n junction that is formed by p- and n-doped silicon. The formation of the junction will induce carrier diffusion due to the gradient of the charge carrier concentration at the junction. Therefore, at thermal equilibrium electrons from the n-type region diffuse into the p-type region and holes from the p-type region diffuse into the n-type region. Due to these diffusion processes, the donors at the junction that contributed electrons, as well as the acceptors at the junction that contributed holes to diffusion are ionized. These ionized donors N_D^+ and ionized acceptors N_A^- are fixed in the semiconductor lattice and lead to the formation of a space charge region at the junction, thus creating an electric field (Figure 2.10b). The electrostatic potential difference across the p-n junction is the built-in potential noted V_{bi}. At thermal equilibrium, the Fermi level is constant across the junction and on both sides of the junction. Assuming a homogeneous system in the yz-plane, one can obtain the expression of the total electron current density J_n in the one-dimensional case along the x-axis normal to the surface in equation (2.48). J_n is the sum of the drift current (first term), due to the flow of charge carriers initiated by the created electric field, and the diffusion current (second term), due to diffusion of the charge carriers. In equation (2.48), μ_n represents the electron mobility, n is the electron concentration as previously given in equation (2.36), and $D_n = k_B T \mu_n / q$ is the Einstein relation.

$$J_n = q\mu_n n \frac{dE_C}{dx} + D_n \frac{dn}{dx} \tag{2.48}$$

The hole current density J_p can be analogously defined. In the steady-state, the total current J in a device based on such p-n junction, as is the case of a diode or a solar cell, is constant throughout the device and can be obtained from the sum of J_n and J_p, which finally results in:

$$J = J_S \left(e^{\frac{qV}{k_B T}} - 1 \right) \tag{2.49}$$

where J_S represents the saturation current density obtained by:

$$J_S = \frac{q D_p p_{n0}}{L_p} + \frac{q D_n n_{p0}}{L_n} \tag{2.50}$$

where D_p, and D_n are the diffusion coefficients of holes and electrons, respectively. p_{n0} is the equilibrium hole density in the n-region, and n_{p0} is the equilibrium electron density in the p-region. L_p and L_n are the hole, and electron diffusion lengths, respectively. In the dark, the current density described in equation (2.48) is also the dark current density. Upon

illumination, electrons in the valence band are excited into the conduction band; hence electron-hole pairs are generated. The electric field at the junction separates the electron-hole pairs and drives the separated carriers across the junction; accordingly, the system is no longer in equilibrium (Figure 2.10c). Due to the change of charge carrier concentration, a constant Fermi level cannot be defined anymore and the non-equilibrium condition is conceptually described by the splitting of the hole and electron quasi-Fermi levels ($E_{F,p}$, and $E_{F,n}$, respectively) in the semiconductor. The current-voltage characteristics of a solar cell can now be defined by:

$$J = J_S\left(e^{\frac{qV}{k_BT}} - 1\right) - J_{Ph} \tag{2.51}$$

where J_S is the saturation current density. J_{Ph} is the photocurrent density generated by the excess carriers upon illumination and is related to the spectral photon flux. The current density-voltage characteristic (J-V curve) of a solar cell is schematically represented in Figure 2.11 and depicts the important parameters that constitute the figures of merit of a solar cell, and which will be described in the following.

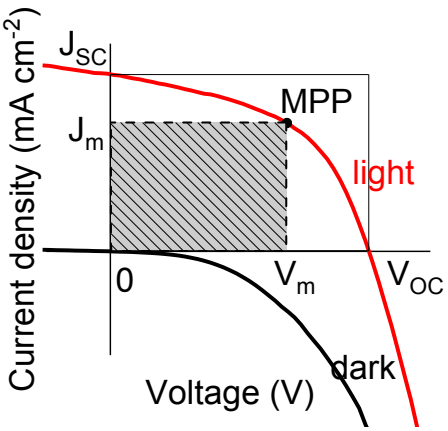

Figure 2.11 Typical J-V curves of a solar cell in dark and under illumination. The shaded rectangle represents the maximum power reached at the maximum power point (MPP) by the cell during operation.

The short-circuit current density J_{SC} corresponds to the current that flows through the cell upon illumination when no bias voltage is applied, in which case it approximately equals the photocurrent density $J_{SC} \approx -J_{Ph}$ as deduced from equation (2.51) for well-performing solar cells. The open-circuit voltage V_{OC} corresponds to the voltage across the solar cell when the contacts are electrically isolated and no net current flow is available, i.e. when the dark current and photocurrent cancel out. The maximal output power of a solar cell is reached at the maximum power point (MPP) with the corresponding J_m and V_m, the product of which

corresponds to the maximum power rectangle represented in Figure 2.11. The power density rectangle representing the product $V_{\mathrm{OC}}\,J_{\mathrm{SC}}$ is also drawn in Figure 2.11. The ratio between both rectangles results in the fill factor FF, such that $FF = V_{\mathrm{m}}\,J_{\mathrm{m}}/V_{\mathrm{OC}}\,J_{\mathrm{SC}}$. Finally, the power conversion efficiency (PCE) of a solar cell is given by:

$$\eta = \frac{FF\,V_{\mathrm{OC}}\,J_{\mathrm{SC}}}{P_{\mathrm{in}}} \tag{2.52}$$

where P_{in} is the solar input power. η, J_{SC}, V_{OC}, and FF are the figures of merit of a solar cell. The optimization of the three latter parameters is the key for increasing the PCE of a solar cell. For instance, in organic solar cells, the V_{OC} of the donor-acceptor (D-A) heterojunction mainly depends on the energy level alignment between the LUMO level of the acceptor (E_L^A) and the HOMO level of the donor ($E_{\mathrm{H}}^{\mathrm{D}}$) and can be determined by:

$$eV_{\mathrm{OC}} = E_{\mathrm{L}}^{A} - E_H^D - kT\ln\left(\frac{N_L N_H}{np}\right) \tag{2.53}$$

where N_L, and N_H are the DOS in the LUMO of the acceptor, and HOMO level donor, respectively; n is the electron density of the acceptor, and p the hole density of the donor. The last term in the right hand side of equation (2.53) has been estimated to lie in the range of 0.3…0.7 eV [205, 206].

2.3.3 Perovskite Solar Cells

The basics of solar cells has been illustrated with the standard example of a solar cell based on a p-n junction formed by two differently doped layers of the same material, hence defined as a homojunction. This standard junction can be extended to a heterojunction formed by two differently doped materials. Furthermore, a solar cell can also consist of a combination of several layers of more than two different materials with different doping character (see Figure 2.9 in previous subsection 2.3.2). A perovskite-based solar cell (PSC) mostly consists of the perovskite absorber layer sandwiched between two different carrier transport materials with differentiating p-type and n-type character. The light is absorbed in the perovskite layer and free charges carriers, instead of excitons, are dominantly created. These free charge carriers are transported through the perovskite layer and collected at the respective interface towards the corresponding charge transport layer, and finally to the respective electrode. The three most common architectures for PSCs are depicted in Figure 2.12.

In all cases, the device is constructed based on a glass substrate coated with transparent conductive oxide (TCO) which acts as a bottom electrode. The typical TCOs are fluorine-doped tin oxide (FTO), and indium-doped tin oxide (ITO). As shown in Figure 2.12a, the mesoporous structure (glass-FTO/c-TiO_2/m-TiO_2/perovskite/HTL/electrode) includes a compact layer of titania (c-TiO_2) and a mesoporous TiO_2 (m-TiO_2) layer. The TiO_2 layer acts as an electron transport layer, which is transparent to visible light thanks to its wide bandgap of ca. 3.2 eV. The perovskite is deposited onto the TiO_2 mesoporous scaffold and the device is completed with the deposition of an HTL, and the top metal electrode. The most widely used HTL in the solar cells having this structure is the organic material 2,2′,7,7′-tetrakis(N,N′-di-p-methoxyphenylamine)-9,9′-spirobifluorene, usually known as spiro-OMeTAD. In the regular planar structure (glass-FTO/ETL/perovskite/HTL/electrode), the structure differs from the mesoporous case by the absence of the mesoporous TiO_2 layer (Figure 2.12b). Often the compact TiO_2 layer is still used as an ETL. Inversely, the perovskite material in the inverted planar heterojunction structure, as in Figure 2.12c (glass-FTO/HTL/perovskite/ETL/electrode), is sandwiched between the HTL on the side of the ITO pre-coated glass substrate and the ETL on top. With the exception of the results part in section 5.3, the base structure adopted in this work is essentially the inverted structure, i.e. the investigated perovskite films have been deposited on an organic HTL, the poly(3,4-ethylenedioxythiophene)/poly(styrenesulfonate) or PEDOT:PSS, on top of an ITO-glass substrate.

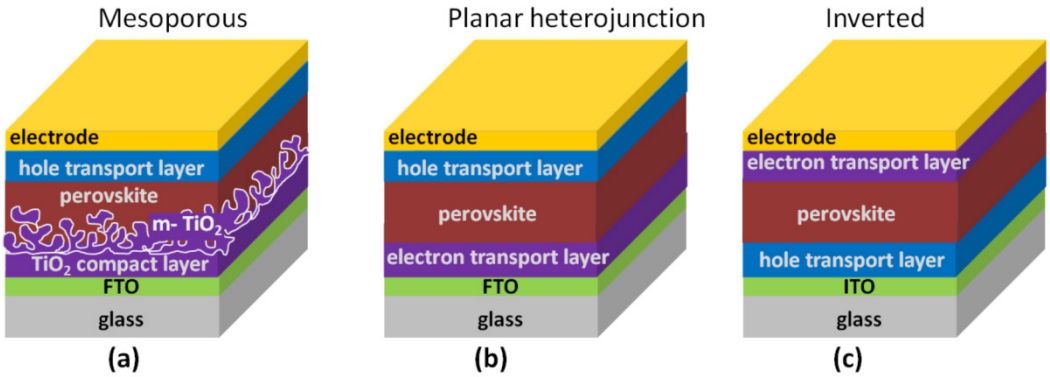

Figure 2.12 Typical device architectures of perovskite-based solar cells: **(a)** in the mesoporous structure the perovskite is embedded into a mesoporous scaffold. The planar structures can be classified into **(b)** regular, and **(c)** inverted planar heterojunctions.

The choice of the charge transport material strongly depends on the optimal position of its energy levels that must energetically match those of the perovskite layer for efficient charge transport throughout the solar cell. Moreover, charge collection and charge recombination at the respective interface tremendously depend on the defects at surfaces and interfaces, such as broken periodicities, under-coordinated lead ions or iodide, points defects, to name only a few [107, 151]. PSCs are characterized by a discrepancy between forward and reverse scan during current density-voltage characterization [207]. The origin of this hysteretic behavior is not clarified yet; the suggested explanation includes ion migration inducing band bending, charge trapping and de-trapping due to defects [168, 207, 208].

Although the classical physics of semiconductors certainly underlie the working principles of PSCs, a complete and unified picture describing the working principles of these PSCs is not well-established yet. Analogous to their inorganic and organic counterparts, the performance of perovskite-based solar cells strongly depends on the carrier transport materials and the respective interfaces formed with them. Moreover, it is important to stress that the interactions and possible chemical reactions upon formation of the interfaces between the perovskite layer and its adjacent charge transport layers can also potentially initiate degradation within the respective layers. However, the renouncement of carrier transport layers altogether can be conceivable in perovskite-based solar cells. Indeed, since perovskite has an ambipolar character, it does not behave exclusively as an n- or a p-type semiconductor but instead depends on the properties of the adjacent layers, and can conduct both electrons and holes. Without lessening the importance of HTL and ETL, it is nonetheless fair to say that the central challenge in perovskite solar cells starts with the understanding and optimization of the perovskite material itself, which ineluctably will impact on the interfaces to be formed. Indeed, variations in the perovskite surface properties – related, for instance, to chemical composition or surface termination – are inevitably to lead to variations in the above-mentioned interactions and chemical reactions occurring upon formation of the interface with the adjacent charge transport layers.

3 Experimental Methods

This chapter presents the experimental techniques employed in the scope of this thesis. The focus will be on photoelectron spectroscopy (PES), which is the main experimental tool used. Therefore, the first section 3.1 of this chapter is dedicated to the fundamentals of PES as a technique to determine the electronic structure of materials. The second section 3.2 introduces time-of-flight secondary ions mass spectrometry (ToF-SIMS), which is used in the first result part of the present thesis to elucidate the materials composition in section 5.1. Thereafter, a brief introduction to the basic principles of grazing incidence X-ray diffraction (GIXRD) as a tool for structural characterization is given in section 3.3. Ultraviolet-Visible (UV-Vis) spectroscopy, atomic force microscopy (AFM), Kelvin probe (KP), and photoelectron yield spectroscopy (PYS) are shortly introduced. These methods have been used as complementary tools and were employed to a lesser extent than PES. The actual experimental setups used are given in chapter 4.

3.1 Photoelectron Spectroscopy (PES)

Photoelectron spectroscopy (PES) is the most important experimental technique to investigate the electronic structure of materials. Based on the recorded energy distribution of electrons photoemitted from a sample, this technique allows accessing information about the band structure, the electronic states, and the chemical composition of the sample.

The working principle of PES is based on the external photoelectric effect [209, 210], which describes the emission of electrons from a sample if the sample is irradiated by an incident light with a photon energy $h\nu$ higher than the sample work function ϕ. The excess of energy left corresponds to the kinetic energy of the emitted electron. In earlier experiments, the work function of a metal was determined by measuring the retarding voltage U needed to suppress the photoelectrons liberated from the metal sample upon irradiation. Thus, the corresponding potential energy eU – where e is the elementary charge – coincides with the maximum kinetic energy $E_{kin,max}$ of the photoelectrons, such that:

$$eU = E_{kin,max} = h\nu - \phi \tag{3.1}$$

Obviously, the photoelectrons with the maximum kinetic energy determined in such experiments are only those originating from the Fermi level E_F in the metal. Yet gaining information from electrons originating from all other occupied states is essential in order to get an extendedinsight into the electronic structure of any electronic material. In present-day PES experiments, if the photon energy and the sample work function are known, the detected kinetic energy of the photoelectrons is directly related to the binding energy of the electrons in the material sample following equation (3.2), and a corresponding kinetic energy distribution can be derived as schematically illustrated in Figure 3.1.

$$E_{kin} = h\nu - E_B - \phi \tag{3.2}$$

The electron energy distribution offers a valuable qualitative representation of the density of occupied states in the sample and allows the determination of important parameters that describe its electronic structure.

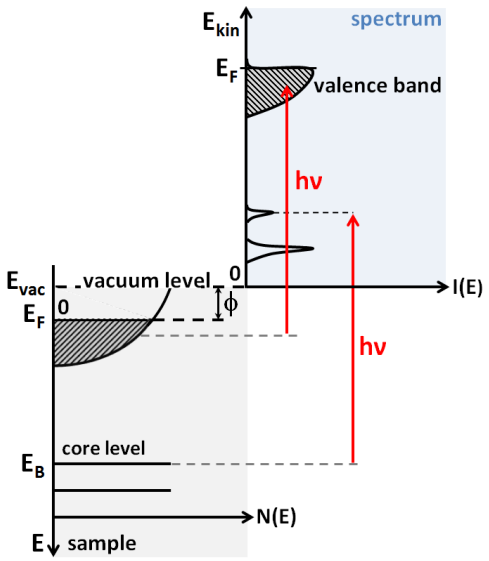

Figure 3.1 Illustration of the relation between the energy levels in a material sample and the corresponding energy distribution of the photoelectrons emitted upon excitation with photons of energy $h\nu$. The natural abscissa for the photoelectrons is the kinetic energy with its zero at the vacuum level of the sample. E_B is the binding energy of the electrons in the solid at a certain energy level and is referenced to the Fermi level E_F. Illustration inspired by ref. [211].

The intensity of the photoemitted electrons per energy interval integrated over the whole Brillouin zone is directly proportional to the DOS in the sample at the corresponding binding energy, such that $I(E_{kin}) \propto N(E)$. By varying the angle of detection, one can obtain information on the momentum distribution and therefrom resolve the electronic

dispersion $E(\boldsymbol{k})$, as mentioned at the end of subsection 3.1.1. At this point, it is important to underline that the relation established in equation (3.2) holds only for primary electrons, that is, electrons that did not undergo any inelastic scattering while traveling to the sample surface. Thus, only these primary electrons retain information about their initial state in terms of energy and momentum. In fact, since the inelastic mean free path of electrons in solids is extremely short, the primary electrons are only collected from the top surface layers. Consequently, PES has high surface sensitivity in the order of 10 Å - 50 Å (see subsection 3.1.1). These primary electrons can have kinetic energy up to the maximum energy $E_{kin,max}$ detectable in a photoemission (PE) experiment, in which case they originate from the highest occupied state [*cf.* equation (3.2)].

In contrast, secondary electrons are originally primary electrons, which have lost varying amounts of their kinetic energy due to inelastic scattering. These secondary electrons form an intensity background tail in the photoemission spectra with their lowest kinetic energy being as low as the minimum kinetic energy detected in a photoemission experiment; this minimum corresponds to the secondary electrons that had just enough energy to escape the solid and be detected. In other words, these latter electrons have just enough energy to overcome the sample work function and result in the secondary electron cutoff (SECO) energy. Therefore, the SECO can be used to determine the work function of the sample (see Figure 3.2).

The process underlying a PES experiment from electron excitation to kinetic energy detection can be explained more concretely based on the schematic representation in Figure 3.2a. The sample is irradiated either by ultraviolet light (5-100 eV) to measure the valence region (ultraviolet photoelectron spectroscopy, UPS), or by X-ray (>100 eV) to measure the core levels (X-ray photoelectron spectroscopy, XPS). Upon excitation, the photoelectron emitted from an energy level at a certain binding energy E_B has a kinetic energy E_{kin} as defined in equation (3.2). In PES experiments, the sample and the electron detector are in electronic equilibrium, i.e. the Fermi levels are aligned. However, the work functions of the sample and the detector are often different, which results in a variation of the vacuum level E_{vac} along the electron path from the sample to the spectrometer, through vacuum. In order to reach the spectrometer, the kinetic energy of the photoelectrons has to be higher than the work function difference $\left(E_{kin} > \phi - \phi_{sp}\right)$. Particularly, in order for SECO electrons to overcome this possible potential barrier, a negative bias V_{BIAS} is generally applied to the sample such that $\phi + eV_{BIAS} > \phi_{sp}$.

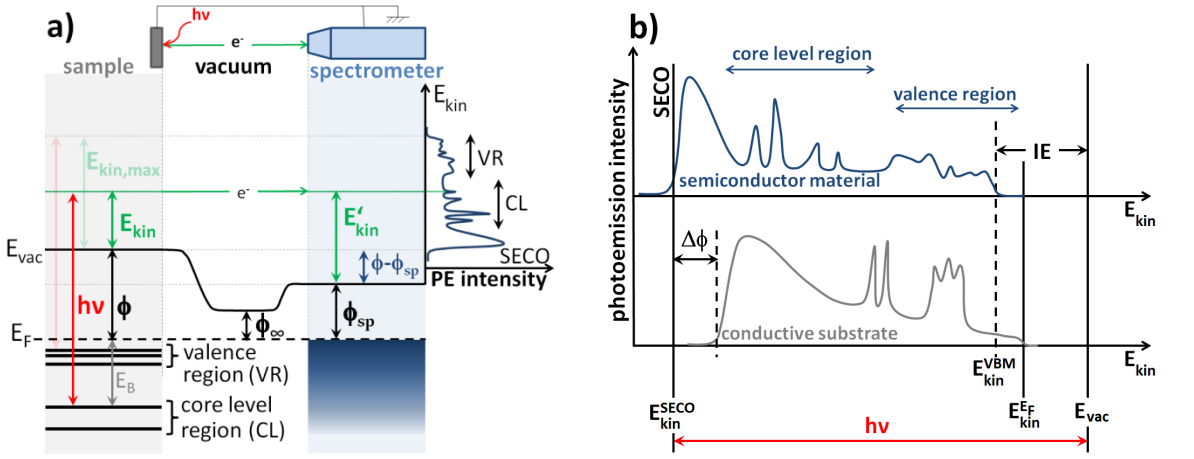

Figure 3.2 a) Schematic illustration of the photoemission process featuring the energy level diagram of the sample and the electron spectrometer in equilibrium. ϕ and ϕ_{sp} correspond to the sample, and the spectrometer work function, respectively. E_B denotes the binding energy referred to the Fermi level E_F, E_{kin} denotes the kinetic energy of the photoemitted electron, and $E_{kin,max}$ corresponds to the maximum kinetic energy of the photoelectrons originating from the highest occupied state (valence band maximum VBM) of a semiconductor. In actual PES experiments, E'_{kin} is the measured kinetic energy and depends only on the potential difference $\phi - \phi_{sp}$. The resulting hypothetical energy distribution curve (EDC) displayed on the right is described in more detail in b). **b)** Schematic of an EDC, consisting of the intensity of the emitted photoelectrons against the kinetic energy. The kinetic energy position of the SECO is determined by the secondary electron cutoff, and the VBM energy position is defined relative to E_F. b) is inspired by ref. [201, 212].

In addition, the measured kinetic energy E'_{kin} is also influenced by this work function difference, such that E'_{kin} only depends on the spectrometer work function ϕ_{sp} as deduced from Figure 3.2a and explicitly expressed in equation (3.3), where E_B denotes the binding energy referred to the Fermi level E_F of the electron in the sample. ϕ_{sp} can be determined by the Fermi edge of a metal $E_{kin}^{E_F}$ (Figure 3.2b) and mathematically calculated from (3.4).

$$E'_{kin} = h\nu - E_B - \phi_{sp} \tag{3.3}$$

$$\phi_{sp} = h\nu - E_{kin}^{E_F} \tag{3.4}$$

The energy distribution curve (EDC) resulting from the PES experiment is shown in Figure 3.2b and consists of the number of emitted photoelectrons against their kinetic energy. The main features of this typical photoemission spectrum, such as the SECO, the core level region with the electrons strongly bound to the nucleus, and the valence region are indicated. The EDC yields important parameters such as the sample work function ϕ (3.5), the valence

band maximum VBM (3.6),[2] and the ionization energy IE (3.7). These parameters are used to assess the electronic structure of the sample and their determination is a prerequisite for the establishment of the energy level alignment at interfaces. Importantly, these parameters are sensitive to changes in the sample properties such as changes in structure and in composition, as well as to the modification of the sample surface due for example to the presence of adsorbates.

$$\phi = h\upsilon - \left(E_{kin}^{E_F} - E_{kin}^{SECO}\right) - eV_{BIAS} = E_{kin}^{SECO} - V_{BIAS} + \phi_{sp} \tag{3.5}$$

$$E_{VBM} = E_{kin}^{E_F} - E_{kin}^{VBM} \tag{3.6}$$

$$\mathrm{IE} = E_{VBM} + \phi \tag{3.7}$$

As previously mentioned, to first order approximation, the photoemission spectrum provides information about the density of states in a material. However, this should be handled with great care when analyzing photoemission spectra, since these spectra can be strongly influenced by many effects such as final state effects, photoionization cross-section or selection rules for transitions between initial and final states, to name but a few. To account for the induced spectral features and/or changes in a photoemission spectrum, the photoemission process is commonly described by the phenomenological three step model as explained in the subsequent section 3.1.1. It should be noted, though, that more advanced (and complex) treatments of the photoemission (PE) process exist (e.g. the one-step model). All the experimental results presented in this work can be evaluated based on the intuitive three-step model.

3.1.1 The Three-Step model

The PE process can be considered as a one-step process in which an electron is excited from an initial occupied state into a free electron like state in vacuum where it is detected. Although this theoretical approach coherently and accurately describes the PE process, it requires rigorous calculations [211, 213]. A less accurate but simpler and acceptable theoretical approach of PE experiments is conceptually based on the three-step model restricted to the

[2] Note that the equation (3.6) for E_{VBM} can be generalized to the case of E_B, i.e. any energy level at the binding energy E_B.

one-electron picture. In this model, the PE experiment is artificially divided into three separate steps, which are considered to be independent from each other. This approach is illustrated in Figure 3.3 and consists of the following three steps:

1. The photoexcitation of an electron in the solid.
2. The travel of the electron (at this stage called photoelectron) up to the surface during which it can experience inelastic scattering.
3. The penetration of the photoelectron through the surface to escape into the vacuum where it is detected.

In the following, each step will be described separately.

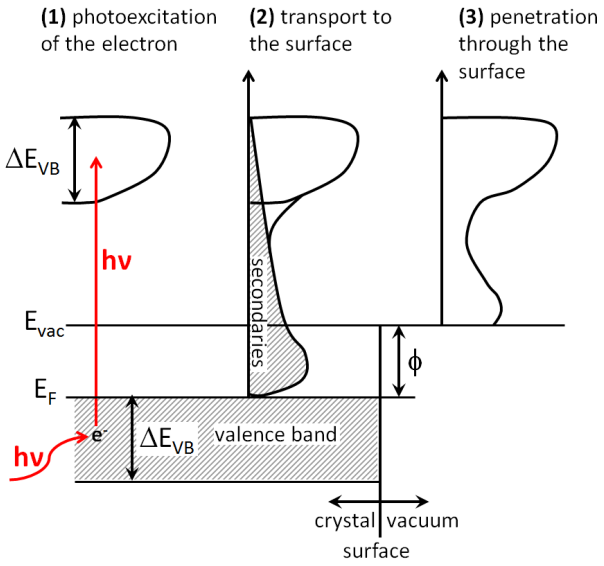

Figure 3.3 The three-step model to describe the PES process: **(1)** excitation of the electrons by the incoming photon, **(2)** travel of the photoelectron to the surface, while at the same time electrons which had lost energy due to inelastic scattering form the secondary electron background, **(3)** penetration of the photoelectron through the surface and travel into the vacuum. Illustration inspired by ref. [211].

Optical photoexcitation of an electron in the solid

In the first step, a photon is absorbed by the material and excites the electron. More specifically, the electron is considered as being in a system described by a potential $U(\boldsymbol{r})$ with the application of an external electromagnetic field, thereby resulting in the electron Hamiltonian described in equation (3.8) [213]. The first two terms in equation (3.8) correspond to the undisturbed Hamiltonian H_0, the second and third terms describe the excitation corresponding to the perturbation operator U_1, where $\hat{\boldsymbol{p}}_0$ is the momentum operator of the electron, and $\hat{\boldsymbol{A}}(\boldsymbol{r})$ is the vector potential associated with the field. By taking only first-order perturbation into account, the last term of order $\sim|\hat{\boldsymbol{A}}(\mathbf{r})|^2$ can be neglected and the

interaction operator then consists of the third term in equation (3.8), which can be rewritten as in equation (3.9).

$$H = \frac{\boldsymbol{p}_0^2}{2m} + U(\boldsymbol{r}) + \frac{e}{2mc}\left[\widehat{\boldsymbol{A}}(\boldsymbol{r}) \cdot \widehat{\boldsymbol{p}}_0 + \widehat{\boldsymbol{p}}_0 \cdot \widehat{\boldsymbol{A}}(\boldsymbol{r})\right] + \frac{e^2\left|\widehat{\boldsymbol{A}}(\mathbf{r})\right|^2}{2mc^2} \tag{3.8}$$

$$U_I \approx -\frac{e}{2mc}\left[\widehat{\boldsymbol{A}}(\boldsymbol{r}) \cdot \widehat{\boldsymbol{p}}_0 + \widehat{\boldsymbol{p}}_0 \cdot \widehat{\boldsymbol{A}}(\boldsymbol{r})\right] \approx -\frac{e}{2mc}\left(\widehat{\boldsymbol{A}}(\boldsymbol{r}) \cdot \widehat{\boldsymbol{p}}_0\right) \tag{3.9}$$

The transition probability based on Fermi's Golden Rule for optical excitation from an initial state ψ_i with N electrons to a final state ψ_f with one photoexcited electron and N-1 remaining electrons is given by equation (3.10). This transition probability is established in the dipolar approximation, i.e. a dipole that oscillates has a dependence on the distance and it is assumed that the radiation wavelength is large compared to the excitation volume. As a result, the external field $\widehat{\boldsymbol{A}}(\boldsymbol{r})$ can be reduced to the lowest order term of its Taylor expansion [213].

$$w \propto \frac{2\pi}{\hbar}\left|\langle\psi_f|U_I|\psi_i\rangle\right|^2 \delta\left(E_f - E_i - h\nu\right) \tag{3.10}$$

$\boldsymbol{\psi_i}$ and $\boldsymbol{\psi_f}$ in the matrix element $|\langle\boldsymbol{\psi_f}|\boldsymbol{U_I}|\boldsymbol{\psi_i}\rangle|$ in equation (3.10) are eigenstates of the undisturbed Hamiltonian $\boldsymbol{H_0}$ with the corresponding energy $\boldsymbol{E_i}$ and $\boldsymbol{E_f}$, respectively. Energy conservation from the initial to the final states is guaranteed by the delta function.

Photoelectron travel through the sample to the surface

After photoexcitation, the excited electron – now called photoelectron – travels through the sample, where it can lose part of or all its energy to inelastic scattering processes, towards the surface. Consequently, secondary electrons with reduced kinetic energy, which however is still enough to reach the surface and escape it, do not yield any information about their initial state anymore and only contribute to the background in the PE spectrum (Figure 3.3).

The dominating scattering process is electron-electron scattering with the corresponding cross-section σ given by:

$$\frac{d^2\sigma}{d\Omega dE} = \frac{\hbar^2}{(\pi e a_0)^2}\frac{1}{q^2} Im\left\{\frac{1}{\epsilon(\boldsymbol{q},\omega)}\right\} \tag{3.11}$$

where $\hbar q$ is the momentum transfer, E is the energy transfer, $a_0 = 0.529$ Å is the Bohr radius, Ω is the solid angle into which the electrons are scattered, and $\epsilon(\boldsymbol{q},\omega)$ represents the dielectric constant of the material. By integrating over all momentum and energy transfers, one obtains

the inverse λ^{-1} of the inelastic mean free path (IMFP) λ of the electron which is defined as the average distance a photoelectron with a given kinetic energy can travel before experiencing inelastic scattering. From equation (3.11), the IMFP is material-specific due to its dependence on the dielectric constant ϵ. However, in the energies of interest here (see Figure 3.4), the IMFP data points of different materials can be described by a "universal curve". This universal curve is obtained by approximating the electrons in the solids using the free electron gas model, such that λ^{-1} is given by equation (3.12), where R is the Rydberg constant, and r_S is the electron-electron distance. Since r_S is roughly equal for all materials, the IMFP λ for different materials results in a universal curve and thus, is material-independent (Figure 3.4).

$$\lambda^{-1} = \sqrt{3}\frac{a_0 R}{E_{kin}} r_S^{-3/2} \ln\left[\left(\frac{4}{9\pi}\right)^{2/3} \frac{E_{kin}}{R} r_s^2\right] \tag{3.12}$$

In the kinetic energy range of a few tens of eV (up to 100 eV) in the universal curve (see Figure 3.4) the IMFP λ presents a minimum that corresponds to an escape depth[3] of a few Å (up to ~1 nm). In spite of the scattering of the IMFP λ data points for different materials, the universal curve clearly indicates that in the aforementioned energy range only photoelectrons from the top few Å of the solid are able to escape without experiencing any scattering.

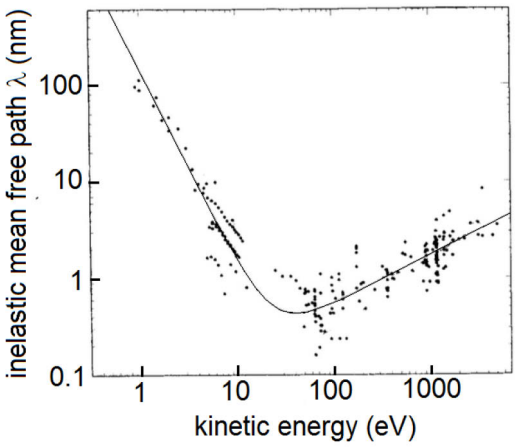

Figure 3.4 Universal curve of the inelastic mean free path IMFP λ of electrons as a function of their kinetic energy, obtained from the empirical fit of the data points, which have been compiled from several studies on different materials. Adapted from ref. [215].

[3] The escape depth is often used interchangeably with the IMFP and the information depth. Strictly speaking, according to the standard E-673 of the American Society for Testing Materials (ASTM), the electron depth designates "the distance normal to the surface at which the probability of an electron escaping without significant energy loss due to inelastic scattering processes drops to e^{-1} (36.8%) of its original value".[214]

Therefore, PES is a very surface sensitive technique. There are nevertheless strategies to probe the sample surface at different depths. Especially when running an XPS experiment, information from the top surface and deeper can be differentiated by varying the photon energy, and hence increasing the kinetic energy range, or by varying the electron emission angle. In the latter case, a measurement at near-grazing emission, i.e. at small emission angle (< 90 °) relative to the surface, is more surface-sensitive and yields information more related to the top surface than a measurement at normal emission.

As already discussed, electrons which experience inelastic scattering while traveling through the sample contribute to the secondary electron background in the PE spectrum. In order to reconstitute the primary spectrum, i.e. intensities from primary electrons, this background needs to be subtracted. Considering that the photoemission intensity $I(E)$ measured at energy E consists of the contribution from primary or secondary electrons originally from E', the background $B_g(E)$ can be expressed by [216, 217]:

$$B_g(E) \propto \lambda(E) \cdot \int_E^{\infty} K(E' - E)\, I(E') dE' \tag{3.13}$$

where $K(E' - E)$ is the inelastic energy loss cross-section function. In a first approximation, the latter scattering function $K(E' - E)$ is constant. This first approximation background correction is called Shirley background and it is the background correction used the most throughout this thesis.

Escape of the electron from the sample into the vacuum

Photoelectrons that possess enough energy to overcome the sample work function can escape from the sample surface and thereafter be detected. The final kinetic energy of the outgoing electron (outside the sample) is given by:

$$E_{kin} = \frac{\hbar}{2m}\left[\left(\boldsymbol{k}_{\parallel}^{out}\right)^2 + (k_{\perp}^{out})^2\right] \tag{3.14}$$

Because the potential at the surface changes along the direction of the surface normal, the component of the wave vector of the excited electron $k_{\perp}^{out}$, which is perpendicular to the surface, also changes during transmission through the surface. However, due to translational symmetry in the plane of the surface, the wave vector component parallel to the surface is conserved, i.e.:

$$\boldsymbol{k}_{\parallel}^{out} = \boldsymbol{k}_{\parallel}^{in} + \boldsymbol{G}_{\parallel} \tag{3.15}$$

From energy conservation, if θ is the angle between the surface normal and the electron energy analyzer, then $k_{\parallel}^{out}$ and $k_{\perp}^{out}$ can be written as in (3.16) and (3.17), respectively. E_0 represents the potential inside the solid, and ϕ the work function.

$$k_{\parallel}^{out} = \sqrt{\frac{2mE_{kin}}{h^2}} \sin\theta \tag{3.16}$$

$$k_{\perp}^{out} = \sqrt{\frac{2m}{h^2}(E_{kin}\cos\theta^2 + E_0 + \phi)} \tag{3.17}$$

Therefore, by varying the angle of emission, the associated energy distribution reflects the states indexed by $\boldsymbol{k}_{\parallel}^{out}$ and $k_{\perp}^{out}$. This forms the basis of angle-resolved photoemission spectroscopy (ARPES) for determining the dispersion of the electronic bands.

Final state effects in PES

In a *frozen-orbital approximation*, it is assumed that upon subtraction of one electron from the N-particle ground state in the PE process, the orbitals of the N-1 electrons are "frozen" in their initial state, that is, the N-1 electrons do not rearrange to screen the created photohole and their states remain the original ground states. In this approximation, the binding energy coincides with the *Koopmans' binding energy* ϵ_k, which is calculated by using the Hartree-Fock wavefunctions. By taking into account the relaxation process, i.e. electron rearrangement, the binding energy in the frozen-orbital approximation is corrected by the final state relaxation energy E_R, yielding equation (3.18).

$$E_B = -\epsilon_k - E_R \tag{3.18}$$

More generally, it is important to stress that final state effects resulting from the excitation of the N-1 remaining electrons upon photoexcitation are particularly relevant in the interpretation of PE spectra, since these effects can give rise to additional features in the spectra [216]. Two examples of such effects worth mentioning here are the Auger process and the shake-up process (Figure 3.5), which result in satellite features appearing in the PE spectrum.

In the Auger process, a core hole (usually a photohole left behind by the just departing photoelectron in a PES experiment) can be filled by an electron from a higher energy state.

This relaxation results in the emission of energy in the form of a photon, which is transferred to another electron – the Auger electron – that is then released from the atom. The resulting Auger line is identified by three indices that correspond to the initial vacant level corresponding to the core hole level, then the level from which the de-excited electron originates, and finally the level from which the Auger electron is released. Auger electrons have kinetic energies that are independent of the energy of the radiation used for photoexcitation, since they only depend on the energy difference between the described transitions, i.e. on the energy levels involved in the transition. These energy levels in turn are specific to a particular atom and its chemical environment.

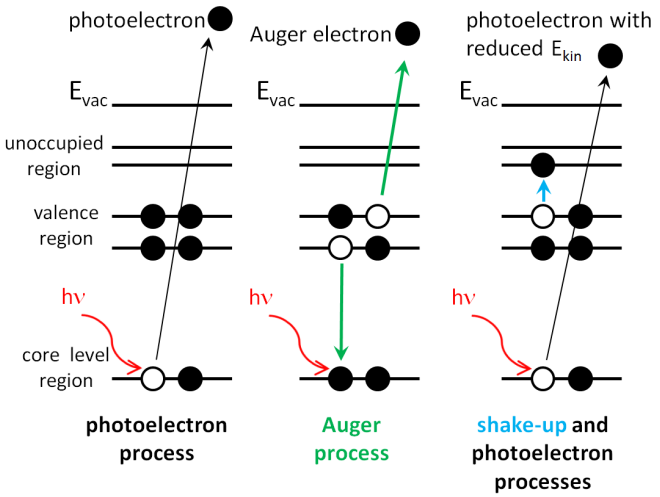

Figure 3.5 Simple schematic of the photoelectron process (left), the Auger process (middle), and the shake-up process (right).

A shake-up process is a multi-electron process characterized by the simultaneous excitation by the photoelectron of another valence electron to an unoccupied state located a few eV higher than the ground state during the photoelectron process. As a result, the kinetic energy of the photoelectron is reduced and a satellite peak is observed at higher binding energy (lower kinetic energy) than the main peak; the energy offset corresponds to the energy difference between ground and excited states.

In short, the PE spectrum is affected by a pronounced secondary electrons background resulting from inelastic scattering in the solid and final state effects. The PE spectrum is, accurately speaking, proportional to the complex matrix element in equation (3.10), which complicates the interpretation of the spectrum. The PE process is more appropriately considered in the context of a many-body system which takes relaxation processes upon photoemission and photohole creation into account. Thus, a PES experiment measures the final state energies, whereas the initial state can only be estimated theoretically.

Awareness of the electronic top surface and subsurface properties should also be raised due to the energy-dependence of the electron mean free path. Additionally, PE spectra are generally affected by the instrumental broadening originating from the excitation source or from the contribution of the analyzer. In the following section, a few specific considerations in the analysis of UPS and XPS spectra are shortly discussed.

3.1.2 Valence Band Spectra

Ultraviolet photoelectron spectroscopy (UPS)

Analyzing the valence band spectrum using an ultraviolet photon source in the energy range of 5-100 eV (higher than the sample work function) is called UPS. Consequently, UPS is a highly surface sensitive technique (5-10 Å) due to the short electron mean free path in this energy range – see Figure 3.4. Moreover, the cross-section of the valence band at these energies is large in comparison to higher photon energies in the X-ray range. The typical laboratory line source used for UPS is HeI radiation with a linewidth of 3 meV, which is two orders of magnitude smaller than the typical Al or Mg X-ray sources [216, 218]. This results in less spectral peak broadening due to the excitation source in UPS than in XPS. Important parameters describing the electronic structure of a material which can be extracted from a valence band spectrum have been given in equations (3.5), (3.6), and (3.7). The SECO, which gives the work function, is determined by the intersection of the base line and the linear slope of the SECO spectrum (Figure 3.6a). The VBM is determined by the intersection of the base line corresponding to the background intensity and the linear slope of the valence band edge from the photoemission spectra. Additional considerations for the determination of VBM for perovskites can be found at the end of the present subsection.

Care with regard to sample charging must be taken during PES experiments. Indeed, the emission of photoelectrons implies the creation of photoholes which can lead to a positive charge built-up at the surface that eventually shift the whole PE spectra or eventually damages the investigated sample [219]. This is particularly relevant for poorly conductive samples such as organic samples or insulators. One way to overcome charging or degradation effects is for example the use of a filter to reduce the intensity of the light source. Additionally, charging can be reduced by employing white light in order to excite charge carriers into the conduction band and thus increase the conductivity of the sample.

Difference spectra

One focus of this work is the study of the effect of gas exposure on the electronic properties of perovskite surfaces. In this regard, it is important to assess the actual adsorption of the gas molecules on the surface. The valence band of a substrate can be altered by the presence of adsorbates on its surface, but the induced changes can be relatively small. One method to assess more in details structures related to the adsorbates by UPS is the difference spectroscopy, which simply consists of subtracting the spectrum on a pristine substrate from the spectrum of the substrate covered with adsorbates [220–222]. The resulting difference spectrum can be compared to the reference valence spectrum of a free molecule or atom of the adsorbate in order to assess the presence of the latter. However, the resulting difference spectrum must be interpreted with care since the observed structures might, for instance, also reflect changes of the electronic structure of the substrate only, originate from interference effects between substrate and adsorbate emission [223], or might be artifact due to poor normalization of the spectra before subtraction. In this context, the substrate spectrum and the spectrum of the adsorbate on substrate are generally aligned to an appropriate level, usually the vacuum level, before subtraction. The calculation of difference spectra in this work has been carried out this way. Additionally, the selected spectra have been normalized to a common, well-distinguishable, feature before subtraction.

Determination of the valence band edge for perovskites

It is important to point out a peculiarity in the determination of the VBM from perovskite valence bands (Figure 3.6b-c). It is common practice to determine the VBM from the onset of the valence band by taking the intersection of the background intensity with the linear slope at the band edge in a representation of the photoemission intensity on a linear scale (Figure 3.6b). This standard method of determination is commonly used for inorganic and organic semiconductors and is adopted in this work. However, it has been shown that such determination from a linear scale can overestimate the VBM due to an overlooked low DOS at the VBM that originates from strong band dispersion of $MAPbI_3$, and hence the existence of non-parabolic band edges [150]. Therefore, the determination of VBM from a logarithmic plot is claimed to provide the actual value of the VBM position (Figure 3.6c) by taking into account the aforementioned low DOS. The contrast between both linear and logarithmic extraction of the VBM can be seen in the Appendix B for all perovskite spectra in the present thesis.

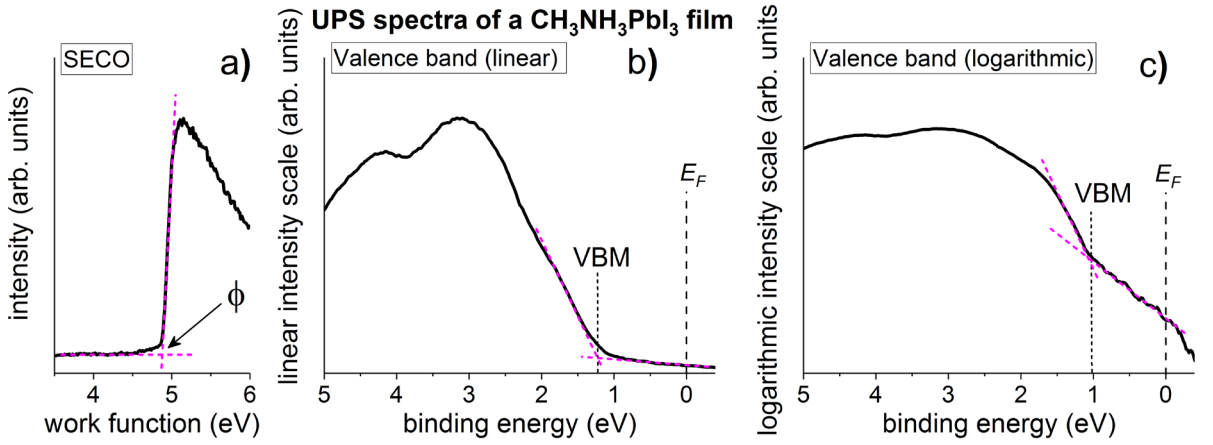

Figure 3.6 Determination of **a)** the work function ϕ from the secondary electron cutoff (SECO) spectrum; and b-c) of the valence band maximum VBM from a valence band spectrum plotted on **b)** a linear and **c)** a logarithmic intensity scale for a $CH_3NH_3PbI_3$ film. The ϕ and VBM values correspond to the intersection of the intensity slope of the respective spectrum with the background intensity (magenta dotted lines).

The VBM values extracted from the logarithmic scale are effectively lower than from the linear scale. However, except for this offset in the respective value, the logarithmic extrapolation does not affect the qualitative interpretation of results since the trends in the VBM shifts observed in the different experiments, for instance upon different exposure (Appendix B), are still observable. For consistency in the representation of the UPS data throughout this thesis, the valence band spectra are shown on a linear intensity scale.

3.1.3 Core Level Analysis

XPS allows determining the chemical composition and the electronic properties of solid surfaces. The interpretation of an XPS spectrum can be a complex process and great care should be taken during its analysis. XPS core level spectra are characterized by the main lines corresponding to the respective elements, the satellites peaks, the presence of features related to final states effects such as Auger or shake-up processes (see subsection 3.1.1), and the secondaries background. The spectral width of a core level in XPS is generally influenced by photohole lifetime, material quality and experimental broadening.

Binding energy shifts and XPS spectra shape

XPS is an efficient tool to investigate the chemical and electronic properties of solids. The electronic core levels are localized states that do not perceive the periodic potential in the

solid, in contrast to the dispersive valence states. Besides, since core electrons are in closed shells and tightly bound to the nucleus they are chemically inert. Nevertheless, when the charge state of a given chemical element differs due to a change of chemical bond or as a result of a coordination change, the electrons can be more or less bound to their nucleus, leading to a binding energy shift of the core level. This energy shift is called the chemical shift and is used to determine the chemical state of the material. Core level shifts can also give information about changes in band bending or charging of the sample.

Due to the spin-orbit coupling, the XPS spectra of the orbital levels other than the s-orbital are also characterized by two separate peaks forming a doublet. This spin-orbit splitting gives rise to two levels of total angular momentum $j = |l \pm s|$, where l and s are the orbital angular momentum and spin angular momentum, respectively. While analyzing XPS spectra, the area ratio between the two peaks resulting from the spin-orbit splitting is proportional to the ratio of the respective degeneracy $(2j + 1)$ of the spin states. The doublets are characterized by a well-documented specific energy separation between the two peak components [224], the magnitude of which increases with the atomic number Z.

The core level peak initially has a Lorentzian shape due to the core hole state lifetime broadening. From the lifetime-energy uncertainty relation $\Delta\tau\ \Delta E \sim \hbar$ [225], the lifetime τ of the core hole is related to the core-hole lifetime broadening Γ by $\tau = \hbar/\Gamma$. The natural line width $\Delta E_o = 2\Gamma$ corresponds to the full width at half maximum (FWHM) of the Lorentzian lifetime broadening. The experimental broadening from the contributions of the excitation source and the energy analyzer has a Gaussian shape. Hence, the shape of the measured XPS spectra is a convolution of Gaussian and Lorentzian functions and is characterized by a FWHM. For a Gaussian line width, FWHM can be approximated by $FWHM_{total} = \sqrt{(\Delta E_0^2 + \Delta E_A^2 + \Delta E_{h\nu}^2)}$, where ΔE_o, ΔE_A, and $\Delta E_{h\nu}$ represent the natural line width of the atomic core level, the analyzer resolution, and the natural line width of the radiation, respectively. The FWHM, the binding energy position and the peak intensity, more precisely the peak area, are the three important parameters for peak fitting.

Quantitative analysis of XPS spectra

The relative concentration of the different elemental species present in the sample can be quantitatively analyzed by means of XPS. For a homogeneous sample, the XP intensity representing the number of photoelectrons per second in the analysis volume is obtained by [224]:

$$I = nf\sigma\theta y\lambda AT \tag{3.19}$$

where n represents the number of atoms per cm^3 of the considered element, f is the incident photon flux in photons/cm^2/s, σ is the photoelectric cross-section given in cm^2 for the considered atomic orbital, θ is a factor that takes into account the angle at which the electron is detected with regard to the path of the incident photon, y is the efficiency for formation of photoelectrons of the normal photoelectron energy, λ is the mean free path of the photoelectrons in the sample, A is the sample area from which the photoelectrons are detected, and T is the detection efficiency of the emitted electrons. Most of the factors in equation (3.19) can be represented by one single factor, the atomic sensitivity factor (ASF), such that $\text{ASF} = f\sigma\theta y\lambda AT$. It follows that n in equation (3.19) for one considered element i becomes:

$$n_i = \frac{I_i}{ASF_i} \tag{3.20}$$

Accordingly, a set of ASFs for all atomic orbitals of all elements can be developed for any spectrometer and is usually given by the manufacturer. The atomic fraction of any constituent in the sample can be obtained by:

$$C_x = \frac{\frac{I_x}{ASF_x}}{\sum \frac{I_i}{ASF_i}} \tag{3.21}$$

The accuracy of XPS quantification can be in the range of 10-30% [215, 224, 226]. However, XPS quantification should be handled with care as it depends on several factors such as the accuracies of the factors included in the ASF, the accurate determination of the appropriate photoelectron intensity (influenced by peculiar features like satellites or background), or importantly the sample homogeneity.

3.2 Time-of-Flight Secondary Ion Mass Spectrometry (ToF-SIMS)

Secondary ion mass spectrometry (SIMS) is a highly sensitive technique used to obtain information about the chemical composition of a solid surface. For the analysis, the sample surface is bombarded with a focused beam of primary ions in the energy range of several keV which interact with the target atoms of the solid by transferring energy through elastic collisions [227, 228]. In this process, molecular and atomic ions are emitted at the site of

impact from the outer layers. These emitted secondary ions are collected and identified by separating their respective mass, more precisely their mass-to-charge ratio m/q. In the case of a time-of-flight (ToF) mass analyzer, before entering a flight path to the detector, the emitted secondary ions are first accelerated by applying a definite accelerating voltage, which corresponds to the electric potential difference U. Thus, if one neglects the initially small energy of the secondary ions, ions having the same charge q will also have the same kinetic energy as given in equation (3.22). However, secondary ions that have left the sample at the same time can have different velocities, depending on their respective mass, as deduced from (3.23). Since velocity $v = \frac{L}{T}$ depends on the time of flight T and the ions need to travel the path of fixed length L in order to reach the detector, it can be deduced from the rearrangement of (3.23) that the mass-to-charge ratio only depends on the time of flight (3.24) [228].

$$E_k = qU \tag{3.22}$$

$$qU = \frac{1}{2}m\left(\frac{L}{T}\right)^2 \tag{3.23}$$

$$\frac{m}{q} = \frac{2Ut^2}{L^2} \tag{3.24}$$

Therefore, the mass of the respective ion can be derived from its time of impact t at the detector. During one acquisition; the secondary ions intensity measured can be separated into their specific mass-to-charge m/q ratio, thus yielding a secondary ions spectrum (Figure 3.7). ToF-SIMS is a highly sensitive technique (up to 1 ppm) that can detect all elements [228]. Although ToF-SIMS provides valuable qualitative information about the composition of a material, this technique is limited with regard to quantitative analysis due particularly to the matrix effect. Indeed, the secondary ion yield strongly depends on the chemical matrix environment surrounding the secondary ion. Nevertheless, semi-quantitative analysis can be done by comparing relative changes between chemically similar samples, for instance. Furthermore, a depth-profiling by means of ToF-SIMS enables the 3D spatial resolution of a sample volume composition. The depth-profiling consists of the alternation of an analysis step and a sputtering step, as illustrated in Figure 3.7b and Figure 3.7c. The erosion of the top surface during the sputtering step allows the analysis of layers initially located deeper in the bulk.

In the scope of this thesis, this technique is used in order to resolve the bulk composition of perovskite samples. ToF-SIMS can provide valuable information about the depth distribution of the different compounds in single and multicomponent perovskites, provided potential artifacts originating from, for instance, sample surface morphology, possible beam damage, or the aforementioned matrix effect, are taken into account during the data analysis and interpretation [229].

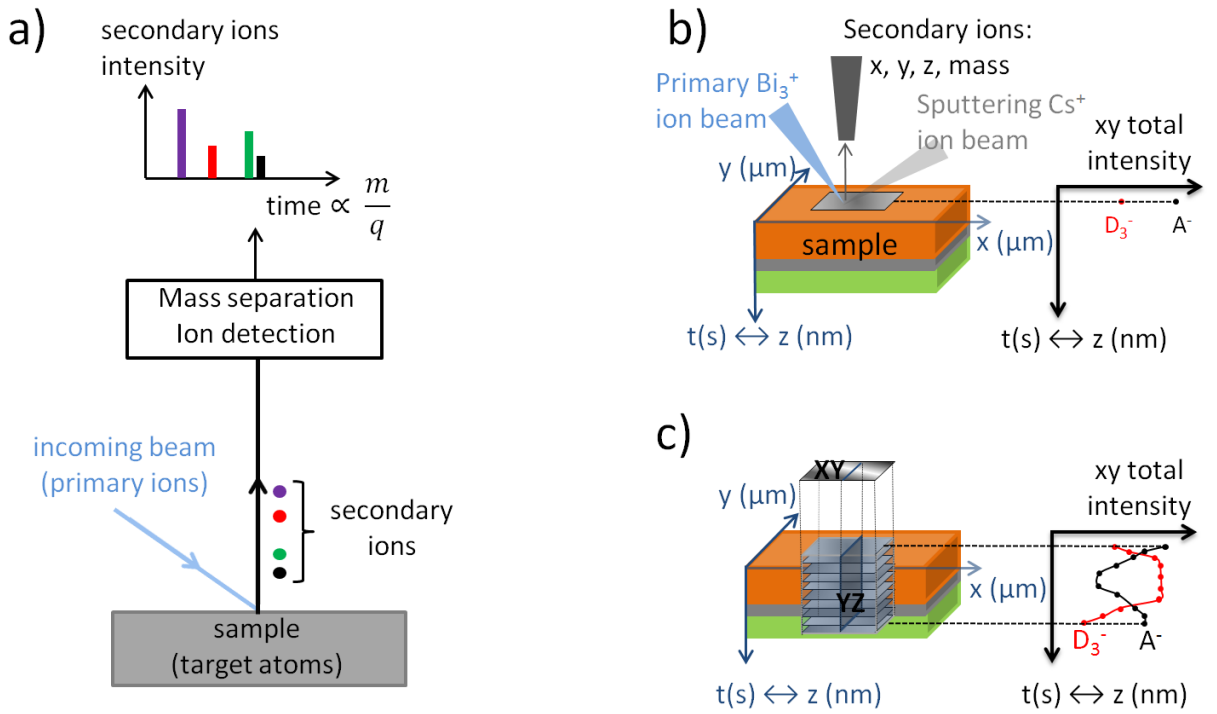

Figure 3.7 a) Simplified schematic illustration of the principles of ToF-SIMS representing the incoming primary ion that induces the generation and emission of secondary ions, which are identified by their respective mass-to-charge ratio m/q, as shown in the secondary ion spectrum on top. Extended representations of the ToF-SIMS measurement process for 3D spatial analysis of a sample consisting of several layers, as is the case in this work, are shown in b) and c) in the instance of two hypothetical ions D_3^- and A^-. **b)** The first step is the analysis of the sample's outermost layer with a Bi_3^+ primary ion beam which allows not only mapping a selected 2D surface but also obtaining the total intensity of a particular ion over this 2D surface. The second step is the sputtering of this top surface with a low energy Cs^+ ion beam for a specific sputter time t(s). **c)** The alternation of the analysis and sputtering steps in b) allows obtaining information about the composition of surfaces which were originally deeper-lying layers. Thereby, 2D depth-integrated XY map, 2D cross-section YZ map, as well as intensity depth profiles of the ions in the sample can be reconstructed. b) and c) are adapted from author's publication in ref. [230] – Published by the PCCP Owner Societies.

3.3 Grazing Incidence X-Ray Diffraction (GIXRD)

The basics of crystal diffraction have been introduced in subsection 2.1.1. In a *specular Θ/2Θ X-ray diffraction* experiment, the incident angle α and the exit angle α' of the mirror-like diffracted X-ray are equal. An X-ray diffraction pattern is obtained by varying the length of the scattering vector $\boldsymbol{q}$, i.e. by varying α, along the surface normal q_z, i.e. out-of-plane, and a Bragg peak is observed whenever a set of planes is perpendicular to $\boldsymbol{q}$ such that Bragg's law as formulated in equation (2.6) is fulfilled. In the scope of this thesis, the main diffraction method applied is grazing incidence X-ray diffraction (GIXRD). In GIXRD the incident X-ray beam impinges at a grazing angle below the critical angle of total external reflection α_c, i.e. $\alpha_i < \alpha_c$. Most of the incident intensity is reflected and importantly, a so-called evanescent wave propagates parallel to the surface and is made use of in a GIXRD experiment. The electric field corresponding to this evanescent wave is damped away from the surface, such that [231]:

$$E \propto e^{k_{t,z}z} = e^{-zk(\alpha_c^2-\alpha_i^2)^{\frac{1}{2}}} = e^{-z/\Lambda} \tag{3.25}$$

where $k_{t,z}$ is the transmitted wave vector with z being the sample depth, Λ represents the penetration depth at which the field and, by extension the amplitude of the wave, decreased by a factor of $1/e$. The penetration depth is given by [52, 232]:

$$\Lambda = \frac{\lambda}{4\pi(\alpha_c^2 - \alpha_i^2)^{1/2}} \sin\Theta \tag{3.26}$$

Consequently, in comparison to *specular Θ/2Θ X-ray diffraction*, in which case the wave penetration depth is of several micrometers, GIXRD is a more surface sensitive method since the penetration depth is much reduced – in the range of a few nanometers – due to the evanescent wave [233]. Due to this enhanced surface sensitivity, GIXRD enables the investigation of thin films while reducing contributions from the underlying substrate.

The GIXRD geometry is represented in a simplified sketch in Figure 3.8. The three-dimensional (3D) scattering vector $\boldsymbol{q}(q_x, q_y, q_z)$ is specified by two particular directions: the vertical direction $q_\perp = q_z$, which is the direction perpendicular to the sample surface; and the direction in the surface plane $q_\parallel = q_{xy} = \sqrt{q_x^2 + q_y^2}$. In comparison to the specular X-ray diffraction method, information about the in-plane structure can be gained in a GIXRD experiment. Therefore, the reciprocal space can be mapped in terms of the two scattering

vector direction q_{xy} and q_z. The resulting two-dimensional (2D) diffraction pattern can consist of diffraction rings, also referred to as Debye-Scherrer rings, centered around the beam axis. In a polycrystalline film with randomly oriented crystallites, i.e. for any set of planes there exists a number of crystallites with the proper orientation such that Bragg's law is fulfilled, the diffraction pattern is characterized by continuous Debye-Scherrer rings.

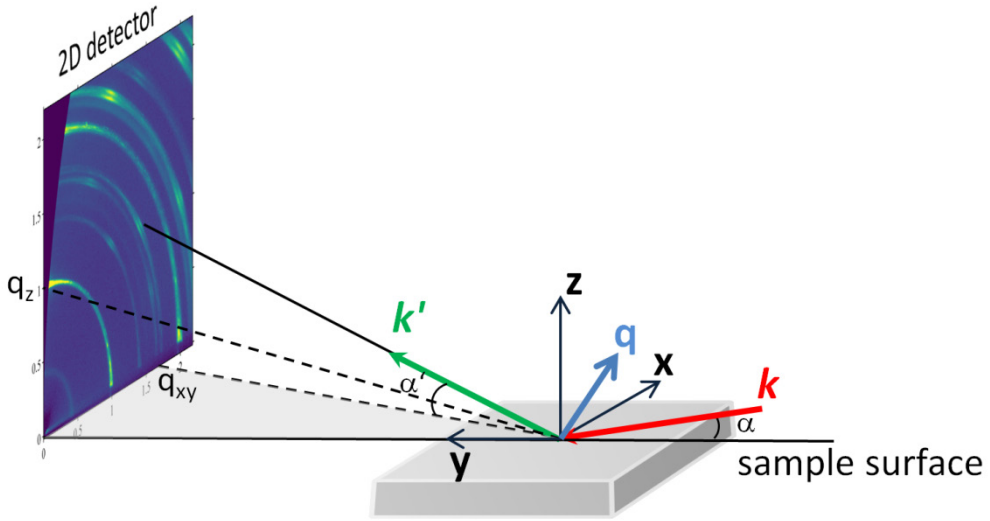

Figure 3.8 Simplified representation of the grazing incidence X-ray diffraction geometry in the sample reference system. Note that the 2D map shown in this figure has been acquired with a fixed primary beam (i.e. relative to the setup reference system), and is used here as mere representation.

However, if the crystallites present a preferred orientation along a particular direction, as it is the case for most perovskite films characterized by GIXRD in the scope of this thesis, the diffraction pattern depends on the preferred orientation and is characterized by discrete regions with enhanced intensities, since Bragg's law in this case is only fulfilled for a particular orientation.

3.4 Complementary Experimental Methods

Ultraviolet-visible-near-infrared absorption spectroscopy

Ultraviolet-visible-near-infrared (UV-vis-NIR) spectroscopy (Figure 3.9a) is a tool that yields information about the electronic transitions within a material by using light in the UV, visible, and near-infrared range. Light of definite wavelength λ is absorbed by an electronic system if the corresponding photon energy matches an electronic transition from a ground to an excited

state inside the system. As a result, absorption in the material varies over a photon energy range and the intensity I of the light transmitted through the sample is photon energy-dependent. The absorption can be evaluated by the absorbance, which measures the attenuation of the incident light intensity $I_0(\lambda)$ following (3.27). It is noteworthy that in such case the attenuation is not caused by absorption only but also by possible light reflection or other light scattering processes.

$$A(\lambda) = -\log\frac{I(\lambda)}{I_0(\lambda)} \tag{3.27}$$

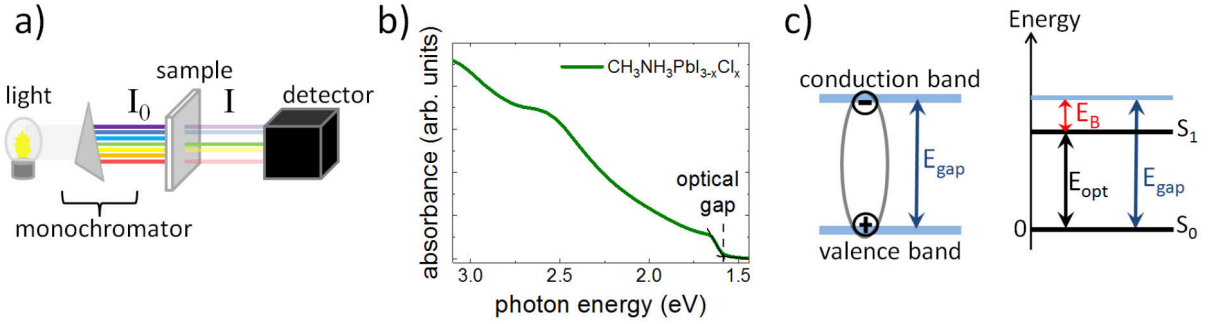

Figure 3.9 a) Simplified schematic of UV-Vis absorption spectroscopy. **b)** Typical absorption spectrum of methyl ammonium lead mixed halide $CH_3NH_3PbI_{3-x}Cl_x$ perovskite with the optical gap E_{opt} determined from the onset. **c)** Representation of an exciton as a bound electron-hole pair (left) and simplified energy state diagram (right) illustrating the difference between the optical gap E_{opt} and the transport gap E_{gap}. For a non-excitonic material (i.e. directly separated electron and hole), the exciton binding energy E_B is zero and E_{opt} and E_{gap} are equal.

For a material of uniform concentration c, the absorbance is defined based on the Lambert-Beer law:

$$A(\lambda) = \varepsilon(\lambda)\, c\, L \tag{3.28}$$

where $\varepsilon(\lambda)$ is the wavelength-dependent absorption coefficient and L is optical path length. The optical gap E_{opt} is determined from the onset of the absorption spectrum (Figure 3.9b) and corresponds to the absorbed photon energy required for the transition with lowest energy to occur, i.e. from the ground state S_0 to the first excited state S_1. If the material is excitonic, the lowest excited state corresponds to a state where the electron and hole are still attracted to each other by the electrostatic Coulomb force and are in a bound state (exciton). In this case,

the energy difference between the electronic transport gap E_{gap} and the optical gap gives the exciton binding energy E_B (Figure 3.9c). In a non-excitonic material, upon excitation the hole and electron are directly separated into the valence (or HOMO) and conduction band (or LUMO), respectively, and the optical gap reflects the transport gap.

Atomic force microscopy

Atomic force microscopy (AFM) is a type of surface probe microscopy (SPM) that renders an image of the surface topography by using a physical probe that scans the surface of the sample [234]. The probe used in an AFM experiment is a tip fixed at the end of a cantilever. The interaction between the tip and the sample on an atomic scale consists of an attraction due to Van-der-Waals forces when they are further apart, and of repulsion due to Pauli principles and to the repulsive Coulomb force between the atomic nuclei when the tip further approaches the sample surface. The overlap of both interactions can be described by the Lennard-Jones potential in (3.29), where the first term represents the short range repulsion and the second term the long range attraction; ε, r, and $r_m$are the depth of the potential well, the tip-sample distance, and the distance corresponding to the potential minimum.

$$V(r) = \varepsilon\left(\left(\frac{r_m}{r}\right)^{12} - 2\left(\frac{r_m}{r}\right)^{6}\right) \tag{3.29}$$

The tip bends depending on these interactions between the tip and the sample surface and so this displacement of the tip depends on the surface roughness. A laser which is focused on the cantilever is deflected depending on the tip displacement, and its deflection can be measured by a photodiode, as shown in Figure 3.10

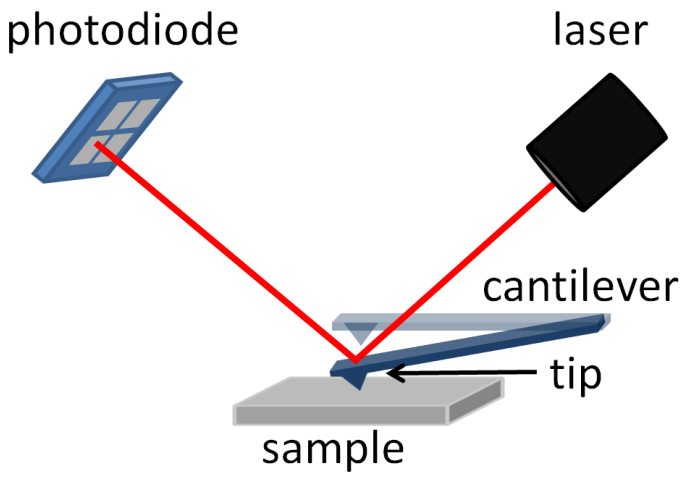

Figure 3.10 Schematic representation of the principle of AFM.

The interatomic forces are reflected in the laser deflection, which can be imaged for each definite lateral position of the sample surface. Scanning the sample surface thus results in an image that gives information about its morphology. The roughness of a selected area in an AFM image is evaluated by the mean square root (rms) parameter R_q that describes the standard deviation of the distribution of surface heights and is given by (3.30) [235].

$$R_q = \sqrt{\frac{1}{n}\sum_{i=1}^{n} y_i^2} \tag{3.30}$$

Kelvin Probe

Kelvin Probe is a contactless and non-destructive method to measure the contact potential difference (CPD) between a probe tip and the surface of an electronic material. The CPD yields the work function difference between the tip (ϕ_{tip}) and the sample (ϕ_{sample}) as given in (3.31). The work function of the sample can be determined if the tip work function is known.

$$CPD = \frac{(\phi_{sample} - \phi_{tip})}{e} \tag{3.31}$$

In a KP experiment, electrical contact is established between the tip and the sample with the respective work function ϕ_{tip} and ϕ_{sample} (Figure 3.11a-b). Upon contact, electrons from the material with lower work function, in the case of Figure 3.11 the sample, will flow to the material with higher work function, in this case the tip, in order to align their Fermi levels. This charge redistribution results in a contact potential difference which can be nullified by applying an external bias voltage V_{bi} to eliminate the surface charge (Figure 3.11c). This applied voltage thus corresponds to the work function difference in (3.31). The tip and sample surfaces are considered as the two plates of a plate capacitor separated by a distance d. For a KP measurement, the above basic principle of CPD determination is repeated several times by vibrating the tip close to the surface – still without any mechanical contact. The vibration corresponds to a periodic change of the tip-sample distance with time, and consequently to a variation of the capacitance with time. In parallel, the charge distribution Q will vary with time and the corresponding current variation $i(t)$ is given by (3.32). Hence, by measuring the change of current over a range of V_{bi}, the CPD will correspond to the applied voltage V_{bi} when the current $i(t)$ disappears.

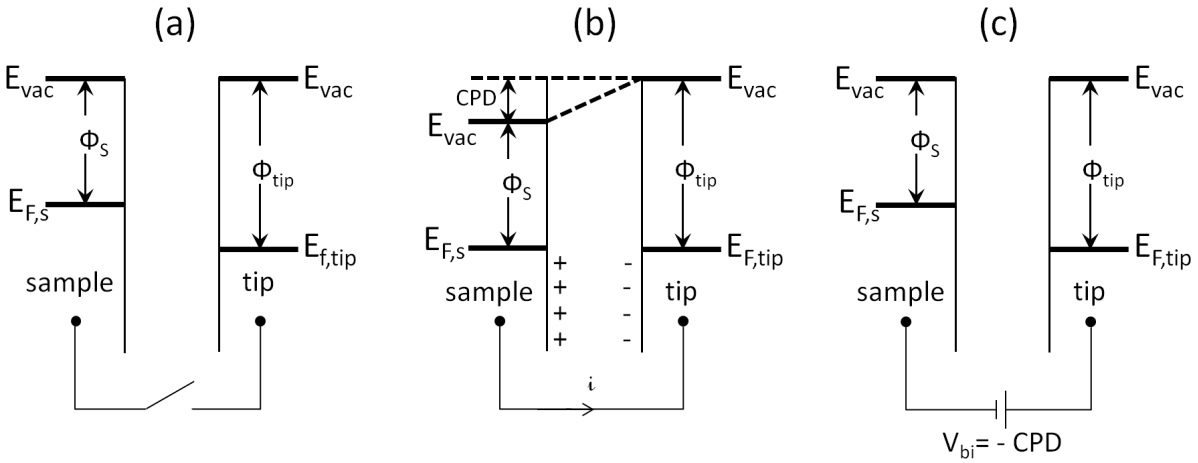

Figure 3.11 Energy and charge diagrams of a sample and Kelvin Probe tip representing the KP principle. **(a)** Sample and tip are not electrically connected and have the Fermi levels $E_{F,s}$ and $E_{F,tip}$, and the work function ϕ_s and ϕ_{tip}, respectively. **(b)** The sample and tip are electrically connected which results in electrons flowing from the sample with lower work function to the tip with higher work function, a contact potential difference (CPD) then exists between the sample and the tip. **(c)** An external bias (V_{bi}) is applied between the sample and the tip to nullify the CPD.

$$i(t) = \frac{dQ}{dt} = \frac{(CPD + V_{bi})CPD\ dC}{dt} \tag{3.32}$$

Photoelectron Yield Spectroscopy

With photoelectron yield spectroscopy (PYS) it is possible to determine the position of the highest occupied energy levels with regard to the vacuum level, in other words one can obtain the work function for a metal and the ionization energy for a semiconductor. The principle of PYS is based on the photoelectric effect similarly to the case of PES (section 3.1). But in contrast to PES, a PYS experiment is carried out in air and does not require vacuum conditions. When leaving the sample surface, the photoelectron attaches to an oxygen molecule in air and is accelerated by a system of grids (Figure 3.12a). Before reaching the anode the photoelectron detaches from the O_2^- ion and is collected there. A PYS experiment consists in collecting the electrons emitted from a sample upon exposure to UV-light over a range of photon energy usually between 3 and 6 eV. When the photon energy $h\nu$ becomes higher than the work function (ionization energy) of the metal (semiconductor) sample, photoelectrons can be and are photoemitted from the surface of the sample (Figure 3.12a-b).

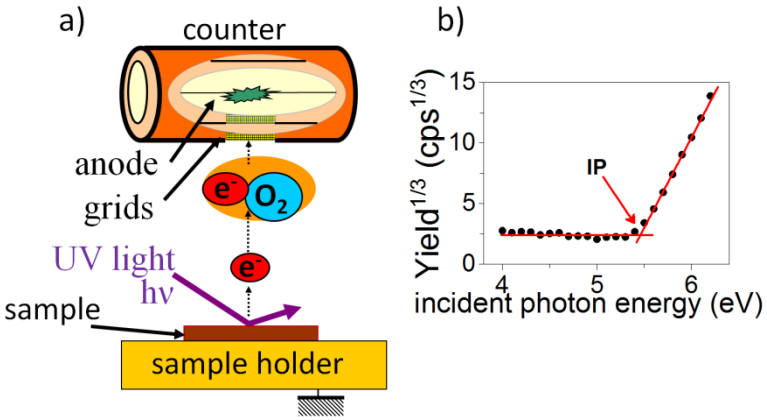

Figure 3.12 a) Simplified schematic representation of the working principle of photoelectron yield spectroscopy (PYS). **b)** Typical photoemission spectrum obtained from a PYS experiment. The photoemission threshold energy obtained from $Yield^{1/3}$ gives the ionization potential for a semiconductor. In case of a metal, the threshold energy determined from $Yield^{1/2}$ gives the metal work function. Illustration with PYS instrument from Riken Keiki CO., LTD.

Therefore, the resulting PYS spectrum is given by the sum of all emitted photoelectrons (photoelectron yield) as a function of the energy of the incident light. In fact, the yield Y is related to the incident photon energy following (3.33) [236], where I represents either the work function or the ionization energy for a metal or a semiconductor, respectively.

$$Y^{\frac{1}{n}} \propto (h\nu - I) \tag{3.33}$$

PYS spectra are usually represented following the square-root law (n=2) for a metal, and the cube-root law (n=3) for a semiconductor [236–238], yielding a linear relationship at the onset of $Y^{\frac{1}{n}}$ (Figure 3.12b). This photoemission threshold is obtained by a linear extrapolation to the baseline as shown in Figure 3.12b.

4 Materials and Experimental Setups

The present chapter details the materials investigated in the scope of this thesis and the setups employed to carry out the investigations.

4.1 Perovskite Samples and Hole Transport Materials Preparation

The samples investigated in the scope of this thesis are almost exclusively solution-processed. The main perovskite system investigated, namely in the sections 5.1, 5.2, and 5.4, is the methyl ammonium lead mixed halide $CH_3NH_3PbI_{3-x}Cl_x$ ($MAPbI_{3-x}Cl_x$) perovskite. Additionally, "single" (in contrast to "mixed" halide) methyl ammonium lead iodide ($CH_3NH_3PbI_3$, $MAPbI_3$) perovskites are investigated in subsection 5.4.2. New HOIPs based on the inclusion of guanidinium cations ($CH_6N_3^+$, Gua) into $MAPbI_3$ are the subject of subsection 5.3.1. The latter as well as the methyl ammonium (MA)-formamidinium (FA) mixed perovskite $(FAPbI_3)_{0.85}(MAPbBr_3)_{0.15}$ and the titanium disulfide TiS_2 used as HTL in subsection 5.3.2 were developed and provided by the Group for Molecular Engineering of Functional Materials (GMF) of Prof. Nazeeruddin (Ecole Polytechnique Fédérale de Lausanne, EPFL, Sion, Switzerland).

Spin-coating is the main deposition method applied for the preparation of thin films from solution in this work. Here, a certain quantity of solution is dispensed onto a substrate; the substrate is then spun at high speed around an axis normal to the substrate surface. The spinning results in the removal of most of the solution towards and off the substrate sides due to centrifugal forces, and in the evaporation of a partial amount of solvent due to the intensified air flow. In this manner, thin film with easily achieved thickness of several hundreds of nanometers remains on the substrate surface. The film thickness d is directly

related to the angular spin velocity ω and the solution concentration c by the proportionality relationship [239]:

$$d \propto \frac{c}{(1-c)^{\frac{1}{3}}} \omega^{-\frac{2}{3}} \tag{4.1}$$

In some cases, the spin coated films are annealed to further remove the solvent and/or induce crystallization, as in the case of perovskite films.

4.1.1 Methyl Ammonium Lead Mixed Halide Perovskite $MAPbI_{3-x}Cl_x$

The $MAPbI_{3-x}Cl_x$ samples consist of films obtained by spin coating of $MAPbI_{3-x}Cl_x$ precursor solution on poly(3,4.ethylenedioxythiophene)/poly(styrenesulfonate) (PEDOT:PSS) pre-covered indium tin oxide (ITO) coated glass substrates. PEDOT:PSS is a conductive polymer usually used as HTL in organic and perovskite-based solar cells. In fact, the sample configuration (ITO/PEDOT:PSS/perovskite) was adopted in order to transpose the structure of inverted planar devices as already described in subsection 2.3.3. To obtain the crystalline perovskite structure, the film was subsequently annealed. Both spin-coating and annealing steps were performed in a nitrogen N_2-filled glove box with base water and oxygen partial pressures below 0.1 ppm.

PEDOT:PSS pre-covered ITO substrates

The indium tin oxide (ITO) substrates (10 mm × 10 mm) which act as electrodes were first cleaned with a detergent. This step was followed by the sonication of the substrates successively in de-ionized water, acetone, and isopropanol for 15 min each. Subsequently, the ITO substrates were either dried by a N_2 flow or by heating in an oven at 70 °C and, if needs be, stored there before later use. Before use, the ITO substrates were UV ozone cleaned in order to remove any solvent residues and other surface contaminants, and thus to obtain a better surface quality for PEDOT:PSS deposition.

The conducting polymer PEDOT:PSS (Figure 4.1a) consists of a mixture of two polymers (PEDOT and PSS) and is characterized by a high conductivity and a good transparency, which makes it an attractive material for application in organic devices. It has been suggested that PEDOT:PSS presents a grain-like structure with the p-doped PEDOT represented as a core surrounded by a shell of charge-compensating PSS [240]. PEDOT:PSS is usually dispersed in water and is filtered before its deposition by spin-coating to remove macroscopic aggregates.

The deposition of PEDOT:PSS on ITO generally results in an improved surface roughness which can be exemplarily derived from the smoother appearance of the PEDOT:PSS covered ITO in comparison to the bare ITO as shown in Figure 4.2a-b.

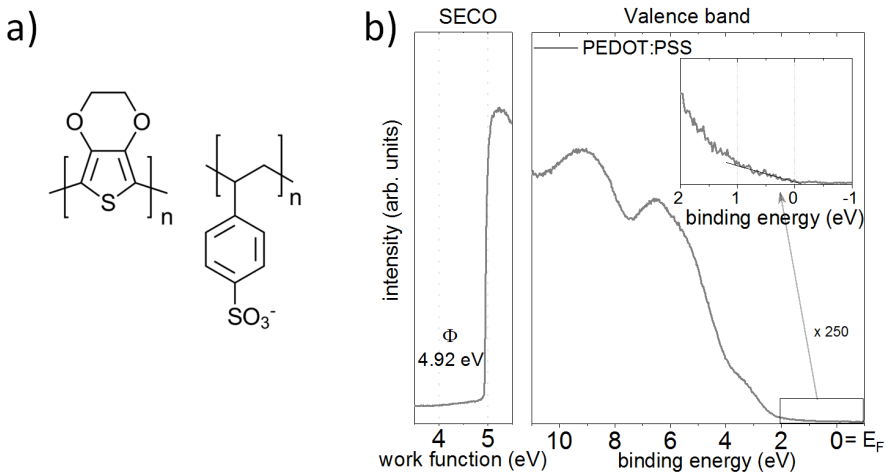

Figure 4.1 a) Chemical structure of PEDOT:PSS and **b)** UPS spectra of a PEDOT:PSS thin film.

This yields a slight reduction in rms roughness from 3.46 nm (ITO) to 1.14 nm (ITO/PEDOT:PSS). Additionally, as a reference data for comparison, the GIXRD pattern of a PEDOT:PSS covered ITO substrate is shown in Figure 4.2c, mainly exhibiting signals from the ITO substrate below the thin PEDOT:PSS layer, as derived from simulation performed by Ingo Salzmann (formerly HU Berlin). As for the electronic properties of PEDOT:PSS, note that UPS valence region spectra of PEDOT:PSS films suggest a finite density of states up to the Fermi level [201, 241].

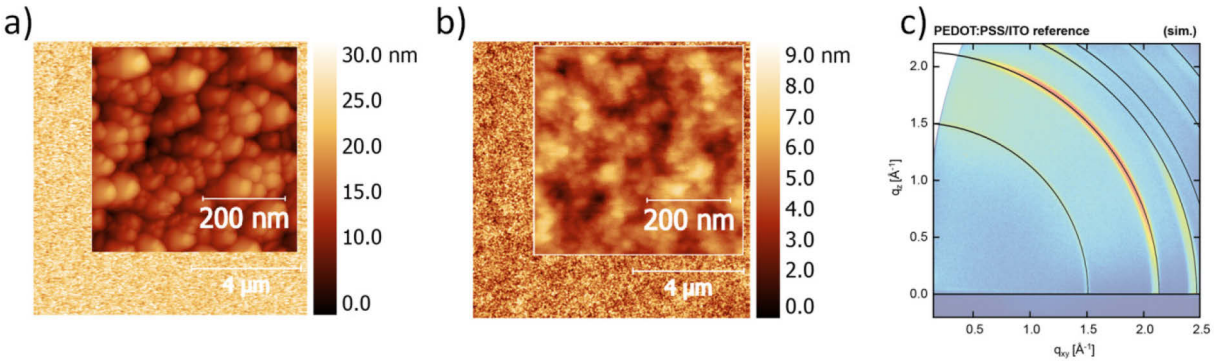

Figure 4.2 AFM micrographs of **a)** ITO-coated glass substrate, **b)** PEDOT:PSS on ITO substrate, and **c)** 2D GIXRD pattern of a PEDOT:PSS film spin-coated on a ITO glass substrate. The simulated diffraction rings (black) corresponding to the ITO are also shown. c) is adapted from author's publication in ref. [230]. c) is produced by Ingo Salzmann (formerly HU Berlin).

In fact, PEDOT:PSS has been also used as electrode owing to its high work function (~ 5 eV) [242]; as also observed for a typical PEDOT:PSS thin film used in this work, which exhibit a work function of 4.92 eV (Figure 4.1b). The PEDOT:PSS layers in this work were deposited from a filtered PEDOT:PSS (Ai4083, from Heraeus) dispersion in water, spin-coated at 40 rounds per second (rps) for 30 s under ambient conditions. To remove residual water, the PEDOT:PSS films were annealed at 180 °C for 10 min in the glove box and stored there before perovskite solution deposition.

Methyl Ammonium Lead Mixed Halide perovskite

The starting materials methyl ammonium iodide (MAI) and lead chloride ($PbCl_2$) were purchased from Lumtec. The $MAPbI_{3-x}Cl_x$ precursor solution with a material mass fraction of 40 wt% was obtained by dissolving MAI and $PbCl_2$ in a molar ratio of 3:1 in N'N-dimethylformamide (DMF) (Merck, formerly Sigma-Aldrich). Instead of designating a definite fraction of Cl, x is mostly used to stress the presence and role of chlorine in the preparation of $MAPbI_{3-x}Cl_x$ and to differentiate this perovskite from the $MAPbI_3$ obtained from a chlorine-free solution (see results section 5.1). The obtained solution was stirred at 60 °C overnight in a glove box. The precursor solution was deposited onto the PEDOT:PSS covered substrate at room temperature by spin-coating at 57 rps for 45 s before annealing at 100 °C on a hot plate for 100 min unless otherwise stated. The spin-coating and annealing steps are summarized in Figure 4.3. Note that the film properties are tightly related to its preparation, particularly to the annealing duration, a characterization in this regard will be the subject of the section 5.2.

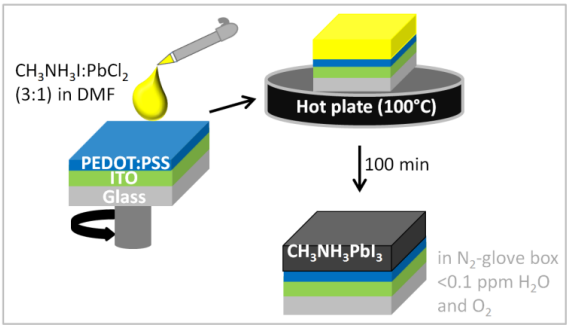

Figure 4.3 Schematic summarizing the preparation of a $MAPbI_{3-x}Cl_x$ perovskite film.

Methyl Ammonium Lead Iodide $MAPbI_3$ perovskite

$MAPbI_3$ solutions of different concentration 0.01 M, 0.05 M, 0.15 M, and 0.75 M (M=mol/L) used in subsection 5.4.2 were obtained by dissolving MAI and PbI_2 in a 1:1 ratio in a solvents mixture of γ-butyrolactone (GBL) and dimethyl sulfoxide (DMSO) in a volume (v) ratio of 7:3 v/v. The solutions were provided by Oleksandra Shargaieva from Helmholtz-Zentrum Berlin (HZB). In a glove box (HU Berlin), these solutions were deposited on PEDOT:PSS pre-covered ITO substrates by spin-coating. 5 s before the end of the spin coating process, toluene (Wako Chemicals GmbH) was dripped onto the substrate following the anti-solvent method (see subsection 2.2.1). The obtained thin films were then annealed in the glove box at 100 °C for 10 min.

4.1.2 Mixed Methyl Ammonium Guanidinium Lead Iodide Perovskite

The methyl ammonium-guanidinium lead iodide $MA_{1-x}Gua_xPbI_3$ perovskite films investigated in subsection 5.3.1 contained different ratios of MA:Gua (1-x:x, x is the percentage of Gua in decimal form). These samples were prepared by Alexander D. Jodlowski in the group of Prof. Nazeeruddin (EPFL, Sion, Switzerland). Details concerning the experimental techniques applied therein, except for PES (subsection 4.2.1), as well as about the device fabrication and film preparation can be found in ref. [243]. Here, only a brief summary of the film preparation is given in the following.

Fluorine-doped tin oxide (SnO_2) substrates were solvent-cleaned and subsequently UV ozone treated for 15 min. First, a compact hole blocking layer of TiO_2 (bl-TiO_2) was deposited by spray pyrolisis; second, a mesoporous TiO_2 (mp-TiO_2) layer was deposited on top by spin-coating, and third, tris(bis(trifluoromethylsulfonyl)imide) (Li-TFS) in acetronitrile was spin-coated onto the mp-TiO_2. A sintering step at up to 500 °C for 30 min followed each of these three steps. Stoichiometric perovskite precursor solutions were prepared by mixing MAI, GuaI, and PbI_2 in N,N'-dimethylsulfoxide (DMSO) and by varying MAI:GuaI ratio from 1:0 to 0:1 with a constant PbI_2 molarity of 1.25. The perovskite films fabrication is based on the two-steps spin-coating method developed by Seok et al. [20], consisting of a first step at 1,000 rpm for 10 s, and a second step at 4,000 rpm for 30 s, followed by the dripping of 100 µL of chlorobenzene onto the films 15 s before the end of the program. Afterwards, the substrates were annealed at 100 °C for 45 min. For solar cell fabrication, the preparation is extended to

the deposition of spiro-OMeTAD via spin-coating from a chlorobenzene solution, and the evaporation of a 70 nm thick gold electrode.

4.1.3 Titanium Disulfide Nanoparticles as Hole Transport Material

Details about the experimental techniques used to investigate the TiS_2 films used as HTM in subsection 5.4.2, except for PES (subsection 4.2.1), as well as about the TiS_2 synthesis and the corresponding devices can be found in ref. [244]. Only a short summary of the synthesis of TiS_2 powder done by Aron J. Huckaba in the GMF group of Prof. Nazeeruddin (EPFL, Sion, Switzerland) is given here. For the synthesis of the TiS_2 nanoparticles, elemental sulfur in pure oleylamine was slowly added to a preparation composed of $TiCl_4$ solution and oleylamine. The oleylamine molecules stabilize the nanoparticles [245]. The reaction that takes place was quenched by placing the flask in water. Ethanol was added to the dark suspension and the final precipitate was centrifuged. The obtained powder was dried under strong N_2 flow and stored in dark before being dispersed in toluene for solution-deposition by spin-coating. Thin TiS_2 films as used in the perovskite-based devices and thick TiS_2 films were measured by PES. Thick TiS_2 film was prepared at HU Berlin from a dispersion of 40 mg/mL of the TiS_2 powder in toluene. 50 µL of this TiS_2 dispersion was drop-casted on a UV ozone treated FTO glass substrate of ca. 1 mm × 1mm before letting it dry in a N_2-filled glove box for 45 min. The black film obtained therefrom was thicker than the spin-coated TiS_2 films used in devices. This film was transferred to the PES system without air exposure. The thin TiS_2 films were fabricated by Saba Gharibzadeh (Tarbiat Modares University, Theran) in the GMF group of Prof. Nazeeruddin (EPFL, Sion, Switzerland) and were obtained by spin-coating two and three layers of TiS_2 dispersion at 10 mg/mL in toluene on perovskite and FTO glass substrates, respectively.

The perovskite substrate the TiS_2 film was deposited on consists of $(FAPbI_3)_{0.85}(MAPbBr_3)_{0.15}$ layer on FTO/c-TiO_2/m-TiO_2. The fabrication of the FTO/c-TiO_2/m-TiO_2 substrates followed steps similar to those described in subsection 4.1.2 and can be found in detail in ref. [244]. The perovskite solution deposited on top was obtained based on the mixed composition $(FAPbI_3)_{0.85}(MAPbBr_3)_{0.15}$ (FA=formamidinium, MA=methyl ammonium) with 5% of excess in PbI_2, dissolved in DMSO:DMF solvents (1:4 v/v) at 1.25 M. After a two-steps spin-coating (first at 1000 rpm for 10 s, and second at 5000 rpm for 30 s) with chlorobenzene dripping 15 s prior to the end, the perovskite films were annealed at 100 °C for 1 h.

4.2 Experimental Setup

4.2.1 Photoelectron Spectroscopy Setups

Unless otherwise stated, all the samples prepared in the glove box were transferred to the PES setup without air exposure by using a portable transfer rod at a residual N_2 pressure $\leq 10^{-2}$ mbar. The main experimental system for PES measurements consist of an interconnected UHV system (Omicron) at the Humboldt-Universität zu Berlin (see Figure 4.4). A fast entry load-lock with a separate pumping system for achieving high vacuum (HV) allows loading samples with the portable transfer rod or at ambient pressure. Thus, samples can be transferred through a gate valve from the HV load-lock chamber to the adjacent preparation chamber (base pressure $< 10^{-9}$ mbar) without venting the latter. The preparation chamber provides facilities for annealing up to 600 °C. Moreover, the preparation chamber is equipped with evaporation sources and a quartz crystal microbalance that allow depositing materials by thermal evaporation and monitoring the nominal thickness deposited at each deposition step.

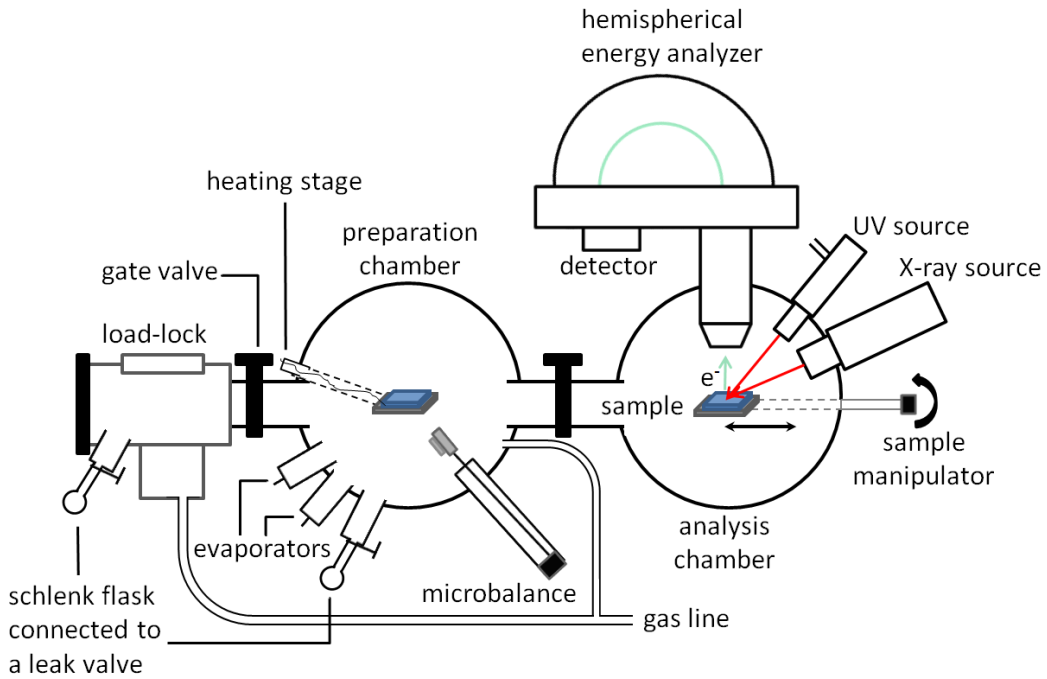

Figure 4.4 Schematic of the UHV system used in this work depicting the interconnected load-lock, preparation, and analysis chamber.

The preparation and load-lock chambers are each connected with a gas line that enables gas admission into the respective chamber. The analysis chamber (base pressure 3×10^{-10} mbar) is connected to the preparation chamber and is equipped with an X-ray source (Specs), a differentially pumped He gas discharge lamp (HIS 13, Omicron), and a Phoibos 100 (Specs) hemispherical analyzer. For the water, air, and oxygen exposure series in section 5.2, de-ionized water in a schlenk flask had been degased following a freeze-pump-thaw process; after several cycles, the water dosing into the respective chamber was performed via a leak valve. For low p_{H2O} exposure, the sample was placed in the preparation chamber before dosing water for exposure at 10^{-6} mbar for different time. For higher p_{H2O} water exposure as well as oxygen exposure, and high vacuum storage in the load-lock chamber, the base pressure used was at 10^{-6} mbar. For air exposure, the sample was exposed by taking the sample out of the vacuum system and leaving it at room temperature in the laboratory for the indicated time. For pure oxygen exposure, pure oxygen at 50 mbar was introduced into the load-lock chamber through a gas line.

The photoemission measurements were performed using a UHV apparatus (Omicron) equipped with a dual anode (Al Kα and a Mg Kα) X-ray sources giving photon excitation energy of 1486.6 eV and 1253.6 eV, respectively, with a line width of 0.85 and 0.7 eV, respectively, for XPS measurement [220]. In this work, the Al Kα radiation was mostly used. The analysis chamber is also equipped with a differentially pumped He-discharge UV source (Omicron) from which the HeI line with an energy of 21.2 eV was used for UPS investigations; the typical line width of HeI is below 10 meV. The UV light source can be operated with an Al-filter placed in the beam path to attenuate the light intensity (by a factor of 20 or 500 depending on the employed filter) when measuring sensitive samples in order to avoid irradiation damage and/or sample charging. As these X-ray and UV sources are non-monochromatic, they exhibit minor lines in addition to the respective main line, which are listed in Appendix A. Consequently, for each main photoemission peak, these minor lines give rise to satellites peaks or background intensities at definite binding energies and relative intensities (Table A1, Appendix A). Note that in the case of the UV source, these relative intensities depend on the pressure in the discharge lamp. For the UPS measurements, change of the pressure in the discharge lamp was measured only indirectly by the pressure in the main chamber. In this work, the background related to the HeI satellites is subtracted from the UPS spectra by subtracting spectra that were first multiplied by the respective relative intensity factor and then shifted by the corresponding binding energy difference with regard to the main line.

The XPS survey scans and core level spectra were recorded at pass energies of 50 and 20 eV, respectively. For the UPS data, the secondary electron cutoff (SECO) at a pass energy of 2 eV was recorded by applying a -10 V sample bias and a pass energy of 5 eV was used for the valence region spectra. The binding energies for all photoemission spectra are referenced to the Fermi level, which was calibrated by the Fermi edge of a metal.

The instrumental resolution of the UPS measurements is 170 meV. The resolution at a defined pass energy of the hemispherical electron energy analyzer can be determined by measuring the Fermi edge of a metal sample, such as polycrystalline gold sample, and by fitting the Fermi edge with a convolution of a Fermi function at room temperature, i.e. at T = 300 K (thermal energy of around 25 meV), and a Gaussian function. The width of the Gaussian function corresponds to the instrumental resolution. The detector work function was calibrated by measuring the Fermi edge by UPS and the Au $4f_{7/2}$ peak by XPS of a cleaned (annealed or sputtered) polycrystalline gold sample. Accordingly, the position of the Fermi level for UPS and XPS is corrected to match the 0 eV and 84 eV binding energy position, respectively, of the above-mentioned levels.

The XPS measurements in subsection 5.4.2 were performed with a JPS-9030 hemispherical photoelectron spectrometer (Jeol) instrument by using a monochromatic Al Kα X-ray source in the analysis chamber at a base pressure of 2×10^{-9} mbar. The overall resolution was 1.25 eV, as determined from the full-width half-maximum of the Ag $3d_{5/2}$ core level at a pass energy of 30 eV. The XPS peak fitting was performed according to a mixture of Gaussian and Lorentzian peak shape, and by subtracting a Shirley-type background.

4.2.2 ToF-SIMS Setup

Time-of-Flight Secondary Ion Mass Spectrometry (ToF-SIMS) measurements were carried out with Yan Busby in the Research Center in the Physics of Matter and Radiation (PMR) of Prof. Pireaux at the University of Namur, Belgium. The measurements were performed using a dual beam TOF.SIMS IV instrument from *IONTOF*. The dual beam depth profiling was operated in non-interlaced mode by using a 25 keV Bi_3^+ primary beam for the analysis step followed by the sputtering step with a 500 eV low-energy Cs^+ ion beam. The primary ion beam is from a liquid metal ion source with Bismuth for Bi_3^+ ions production. The depth profiles in section 5.1 are built by alternating acquisition and sputtering (for 10 s and 5 s for S-10 and S-100, respectively) steps on 250×250 μm^2 and 125×125 μm^2 analysis areas for S-10 and S-100, respectively. The lateral resolution is about 1 μm and the in-depth resolution

is about 1 nm. At each acquisition, the total secondary ions spectrum in the range of mass-to-charge ratio $1 < m/q < 800$ a.u. is collected from the sample's few topmost atomic layers. Thereafter, the molecular species present are identified by separating their respective mass-to-charge ratio. Semi-quantitative ToF-SIMS profiles representing the ions intensities as a function of sputter time (depth) can thus be reconstructed. Besides, 2D color-scaled maps can be reconstructed to depict the spatial distribution of an ion, as previously described in Figure 3.7. Thus, a 2D XY map represents the depth-integrated intensity of the ion and a 2D YZ map allows a cross-sectional visualization of the ion depth distribution along X or Y cuts.

4.2.3 GIXRD Setup

The grazing-incidence X-ray diffraction (GIXRD) measurements in the scope of this thesis were carried out with Ingo Salzmann (formerly HU Berlin). The GIXRD setup used for structure characterization was the diffraction endstation of the beamline KMC-2 at the synchrotron radiation facility BESSY II at the Helmholtz-Zentrum Berlin für Materialien und Energie GmbH (HZB, Germany). A primary beam wavelength of λ=0.1 nm and a two-dimensional Vantec 2000 area detector were used to record the diffraction intensities. The acquisition was performed under N_2 flux to reduce beam damage. The sample to detector distance was 336 mm. The setup allowed simultaneously covering a range in the reciprocal space of ca. 2 $Å^{-1}$ in both q_z and $q_{||}$ direction [246]. The acquisition time for the measurements in section 5.1 was 900 s. In the case of the *in situ* GIXRD measurements during water exposure in section 5.2, the perovskite sample was placed on a sample holder inside a closed, custom-made container, which has two windows both covered with Kapton foil for the incident and diffracted beams. A water bath of de-ionized water was around the sample holder. The change of the relative humidity (RH) over time inside the container was measured *ex-situ* by using a humidity sensor (HIH-4021) from Honeywell under similar conditions.

4.2.4 Complementary Experimental Setups

A Kelvin Probe (KP) setup from *KP Technology* was used for contact potential difference (CPD) measurements. The CPD between the Kelvin Probe tip and the sample surface is determined by measuring the current flow induced by the tip vibration, the CPD then corresponds to the applied voltage needed to nullify this current. The work function of the tip is calibrated for each measurement with a gold test sample which has a work function of ca.

4.8 eV as determined by PYS (see following paragraph). For each sample, the reported CPD value is an average of CPD measurements performed at 2 to 3 different spots of the sample surface. Note that each measurement actually consists of a measurement of several data points (over time). The measurements data are gathered in Appendix B and only the extracted CPD is given in the text.

Photoelectron Yield Spectroscopy (PYS) measurements in air were conducted using an AC-2 photoemission spectrometer by *RKI Instruments* in the photon energy range between 4 and 6 eV. The selected UV light intensity is between 5 to 50 nW for different measurement. The work function (ionization energy) of metals (semiconductors) is determined by the onset of the (photoelectron) yield$^{1/2}$ (yield$^{1/3}$) plotted as a function of the photon energy.

An Atomic Force Microscopy (AFM) setup from *Bruker* was employed to determine the morphology of film surfaces. The micrographs were acquired by selecting the ScanAsyst mode. This mode is based on the peak force tapping mode with the additional advantages of the continuous monitoring of the image quality and, accordingly, the automated adjustments of the measurement parameters. The corresponding ScanAsyst Air tip has a nominal radius of 2 nm and is integrated to a silicon nitride cantilever. The AFM data were processed by using Gwyddion 2.39. The AFM measurements corresponding to the data shown in subsection 5.4.1 were performed by Yerila Rodríguez (University of Havana, Cuba).

Optical absorption spectroscopy measurements in air were carried out using a Lambda 950 UV/Vis/NIR spectrophotometer from *Perkin Elmer Inc*. The optical band gap is determined from the absorption spectrum onset, which corresponds to the point where the baseline intersects with the linear part of the feature at the onset. The optical data shown in subsection 5.4.1 were aquired by Yerila Rodríguez (University of Havana, Cuba).

In the frame of collaborative studies, some of the results shown in the section 5.3 were collected from and in the group of Prof. Nazeeruddin (EPFL, Sion, Switzerland). These results include measurements data acquired by means of following methods by following people: Raman and photoluminescence (PL) spectroscopy by Giulia Grancini from EPFL (Sion, Switzerland), XRD by Gustavo de Miguel from the Universidad de Córdoba (Córdoba, Spain), Saba Gharibzadeh (Tarbiat Modares University, Theran) and Aron Huckaba from EPFL (Sion, Switzerland), UV-vis-IR spectroscopy by Gustavo de Miguel, scanning electron microscope (SEM) by Cristina Roldán-Carmona from EPFL (Sion, Switzerland), energy-

dispersive X-ray (EDX) spectroscopy by Emad Oveisi from EPFL (Sion, Switzerland). Moreover, device performance was established using a solar simulator. Details about the corresponding setups used can be found in refs. [243, 244].

5 Results and Discussion

As discussed in section 2.2, hybrid organic-inorganic perovskites are a very promising class of material for application in photovoltaics and related optoelectronic devices, owing to the versatility of these materials and their optoelectronic properties. These properties are based on the perovskite structure, and are, therefore, related to the formation of the perovskite material itself. The viability of perovskites as alternative materials for photovoltaics application is essentially assessed based on the lifetime of the perovskite-based solar cells. In turn, this lifetime directly depends on the stability of the perovskites in ambient environment and on the reproducibility of their properties for reliable property-function assessments. These two processes, formation and environmental effects, and particularly their impact on the electronic structure of perovskite films, are the core topic of the thesis. Additionally, the electronic properties of new perovskite materials with enhanced environmental stability and hole transport materials newly applied for low-cost application in PSCs, were investigated in the scope of the thesis.

At this point, it is noteworthy to remind the peculiarity in the determination of the valence band onset, i.e. the VBM, as already discussed in subsection 3.1.2. Due to a large dispersion at the top of the valence band, lead-halide based perovskites have been reported to likely exhibit a low DOS at the VBM [150]. Consequently, it has been suggested that the extrapolation of the VBM position from a logarithmic intensity scale more accurately reflects the actual VBM value, instead of the conventionally applied extrapolation from a linear scale. [150] Note that both methods are applied in the literature. In the present thesis, comparison between both methods was done and can be found in the Appendix B. Indeed, an offset of the absolute VBM values up to 300 meV was observed between both methods. For instance, the valence band spectrum shown in Figure 5.15, which exhibits a VBM of 1.71 eV below E_F from the linear scale – which indicates a strongly n-type property, considering a band gap of

1.70 eV [111, 247] – exhibits a VBM of 1.51 eV on a logarithmic scale (Figure B3, Appendix B). Although the absolute VBM values were different depending on the intensity scale, the trends in their respective shift throughout the different experiments on perovskite – i.e. film formation, different ambient exposures, composition, and preparation – remain the same (Appendix B). Therefore, since the present work is more importantly focused on the relative changes in the electronic properties of perovskite films, the method for valence band determination (whether linear or logarithmic) does not affect the interpretation of the results. Thus, the valence band spectra are shown on a linear intensity scale throughout this result chapter. This is also done for consistency and for optimal readability throughout all sections of the present chapter since several valence band spectra needed to be shown on a linear scale to discuss their features (e.g. sections 5.2 and 5.3) or to depict them with other materials (sections 5.3.2and 5.4). As aforementioned, the logarithmic plot of the valence spectra of all the investigated perovskite films can be found in the Appendix B.

Section 5.1 of this chapter addresses the formation of methyl ammonium lead mixed halide perovskite $MAPbI_{3-x}Cl_x$ films obtained from a mixture of MAI and $PbCl_2$ with the emphasis on the role of chlorine in the film formation. With this aim, different methods were combined to correlate the film composition with the structural, morphological and electronic properties of the perovskite films. Section 5.2 deals with the reproducibility and stability issues of perovskite films by monitoring its electronic properties in different environments, namely upon water, oxygen, and air exposure. The results are discussed regarding possible occurring interactions and phenomena at the film surface. Section 5.3 is divided in two subsections, each focused on the characterization of a new perovskite material – methyl ammonium guanidinium $MA_{1-x}Gua_xPbI_3$ perovskite – in subsection 5.3.1 and a hole transport material – titanium disulfide TiS_2 nanoparticles – in subsection 5.3.2, respectively, for application in perovskite-based solar cells. Note that in the latter section (section 5.3), the author's contribution is restricted to the PES results. The results chapter is completed by the results from additional experiments in section 5.4 that can prompt further studies. Subsection 5.4.1 investigates the effect of different solvents on perovskite film properties in order to assess their potential suitability for the deposition of hole transport materials from solution onto perovskite films. Finally, the subsection 5.4.2 shortly summarizes the results of experiments conducted to obtain films with decreasing thickness by solution dilution. This strategy was tested with the eventual aim of investigating the energy level alignment between PEDOT:PSS and perovskite.

5.1 Role of Chlorine in the Formation of Methyl Ammonium Lead Mixed Halide Perovskite

This section is based on the results published in ref. [230]. Additional considerations such as the results presented in Figure 5.1 and Figure 5.12, have been incorporated into the section. Moreover, the interpretation of the results has been enriched by more recent literature.

Beyond the high-efficiency of HOIP-based solar cells, the solution processability of HOIPs is one important feature that makes them viable candidates as active materials for large-scale application in solar cells. Commonly, in order to obtain a crystallized film, spin-coated films are thermally annealed at temperatures as low as 100 °C. Both the spin-coating and thermal annealing steps are decisive for the formation of a crystallized perovskite film with the attractive properties as enumerated in section 2.2. The standard $MAPbI_3$ is generally obtained from a mixture of the methyl ammonium iodide (MAI) and lead iodide (PbI_2). In 2012, the substitution of PbI_2 with lead chloride ($PbCl_2$) and the excess of MA in a MAI:$PbCl_2$ molar ratio of 3:1 resulted in the formation of the perovskite absorber denominated methyl ammonium lead mixed halide perovskite ($CH_3NH_3PbI_{3-x}Cl_x$ or $MAPbI_{3-x}Cl_x$) [13]. In comparison to the single halide $MAPbI_3$ perovskite, the mixed halide perovskite $MAPbI_{3-x}Cl_x$ films exhibited long-range crystallinity [13], considerably improved charge transport properties [14], and increased electron-hole diffusion lengths exceeding 1 μm, that is, differing by one order of magnitude from the electron-hole diffusion lengths of *ca.* 100 nm of $MAPbI_3$ in earlier studies [16]. These enhanced properties upon introduction of chlorine in the preparation also result in enhanced solar cell performance [14, 16]. Importantly, these earlier studies all point to two striking conclusions, namely that no or a negligible amount of chlorine was detectable in the final $MAPbI_{3-x}Cl_x$ films [14, 20–22], and that the final films actually mainly consist of $MAPbI_3$ [13, 19, 20]. One observed pathway for this "chlorine loss" is the release of Cl through the sublimation of methyl ammonium chloride (MACl) during thermal annealing, which points out the role of chlorine in the removal of the excess of MA from the non-stoichiometric precursor solution [15, 26, 27]. Unger *et. al.* directly observed a white residue deposited on a petri dish used to cover $MAPbI_{3-x}Cl_x$ samples during the thermal annealing; the white residue was characterized as MACl [27]. Similarly, an ITO-substrate fixed inside a petri dish covering $MAPbI_{3-x}Cl_x$ samples during annealing in the glove box was overlaid with a white film, which has been characterized by PES (Figure 5.1). The work function deduced from the SECO spectrum, and the valence band spectrum of the film are distinctly different from those of the underlying ITO-substrate (Figure 5.1a-b), thus

evidencing the presence of another material on the ITO-substrate, labeled as MACl in Figure 5.1. Since the Sn 3d and In 3d core level peaks from the ITO are still detected (Figure 5.1f), the white film likely covers the ITO-substrate in a rather inhomogeneous manner. The XPS core level spectra of Cl 2p, C 1s, and N 1s in Figure 5.1c-e all indicate the presence of MACl (CH_3NH_3Cl). It is noteworthy that no iodine signal was detected in the survey spectrum. The MACl removal from the film during annealing slows down the perovskite film formation and therefore allows the growth of large crystal domains [15]. However, it has been suggested and indicated that chlorine is still present not only inside the perovskite film bulk, but also at the perovskite/substrate interface, and that it modifies the electronic properties there [14, 28, 29, 248]. In short, the key role of chlorine in $MAPbI_{3-x}Cl_x$ is related to its behavior during the annealing process and to its location within the final film after crystallization. Several studies focused on the elucidation of the crystallization pathway during the annealing process reveal the occurrence of an intermediate phase during the crystallization of $MAPbI_{3-x}Cl_x$ and its impact on film formation [15, 23–25]. The nucleation and growth processes have been investigated,[30] and the influence of chlorine on the morphology of the $MAPbI_{3-x}Cl_x$ perovskite films has been analyzed [22]. Despite this, a full description of the critical role of chlorine has not been established yet. Particularly, the depth profiling of the $MAPbI_{3-x}Cl_x$ perovskite for characterizing its bulk properties has only been sparsely explored except for a few studies [249, 250].

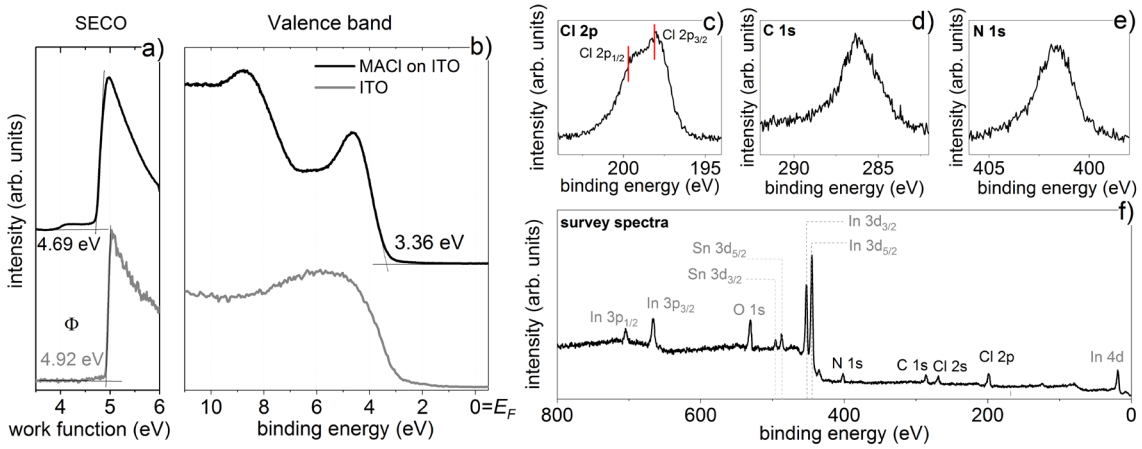

Figure 5.1 Photoemission spectra of a reference ITO sample and of a ITO sample placed above a $MAPbI_{3-x}Cl_x$ sample prepared from solution during annealing; the latter ITO sample was covered with a white film thereupon and is here designated as MACl. Although no structural characterization was done to confirm the presence of MACl, comparison with literature and the **a)** SECO and **b)** valence band spectra, as well as the **c)** Cl 2p, **d)** C 1s, and **e)** N 1s core level spectra detected by XPS support this assumption. **f)** XPS survey spectra indicate signals from the ITO substrate.

Monitoring any possible evolution of the bulk composition during annealing would not only give valuable information about the mechanisms underlying the crystallization process of $MAPbI_{3-x}Cl_x$ but would also constitute an essential contribution towards the rationalization of the role of chlorine in chlorine-based perovskites. This first part of the results chapter is dedicated to the investigation of the $MAPbI_{3-x}Cl_x$ film formation with an emphasis on the investigation of the bulk composition of the perovskite film after different annealing times, that is, before and after complete film crystallization. By means of three dimensional (3D) imaging with time-of-flight secondary ion mass spectrometry (ToF-SIMS), the lateral composition and the composition throughout the depth of the films are spatially resolved (subsection 5.1.2). The ToF-SIMS results at different stages of the crystallization process are correlated with concomitant changes in crystal structure (subsection 5.1.1), morphology (subsection 5.1.2), and electronic structure (subsection 5.1.3), as investigated by grazing incidence X-ray diffraction (GIXRD), atomic force microscopy (AFM), and ultraviolet, and X-ray photoelectron spectroscopy (UPS, and XPS). The correlation between the changes of the different properties not only reveals the location of the chlorine in the final films but also corroborates its role during crystallization and in the final film.

5.1.1 Structural Evolution Upon Crystallization

X-ray diffraction is the commonly used method to assess the formation of the perovskite structure. Perovskite films obtained from a one-step solution deposition and subsequently thermally annealed at a constant temperature of 100 °C for different times are characterized by GIXRD. The X-ray diffraction data analysis and simulations in this work have been done by Ingo Salzmann (previously from HU Berlin).

The two-dimensional (2D) GIXRD maps of a not-annealed sample, here denominated as pristine (0 min), and three other samples annealed at 100 °C for 10 min, 30 min, and 100 min, respectively, are shown in Figure 5.2. All four samples exhibit a pronounced fiber texture growth, as deduced from the discrete regions with increased intensity on the diffraction rings in the 2D patterns (Figure 5.2a-d). This type of texture means that a well-defined crystallographic plane, here the (001), of the actual crystal structure is oriented parallel to the surface of the substrate [251], in other words, the crystallites in the polycrystalline films exhibit a common plane, which is preferentially oriented along the substrate surface normal, but their azimuthal orientation is random (see section 3.3). The recorded diffraction rings have been indexed with both tetragonal and (pseudo-)cubic polymorphs of $MAPbI_3$ [32], as shown

in the simulated data in Figure 5.2e, and Figure 5.2f. The calculated positions of the (211) and (202) reflections in a tetragonal structure, as well as the peak positions expected for a tetragonal polymorph with a (001)-texture are shown in Figure 5.2e. In the case of a cubic perovskite crystal structure, no diffraction intensity is expected at the position of the observed (211) reflection [116], thus supporting the presence of a tetragonal perovskite polymorph in the samples investigated here. However, for a tetragonal perovskite crystal structure, the calculated structure factor, and hence the intensities, of the (211) and (202) reflections are identical, which is not the case here. Indeed, for the 2D patterns in Figure 5.2a-d, the diffraction intensity at the expected (211) reflection position (dotted white circles) is negligible in comparison to that at the (202) reflection position.

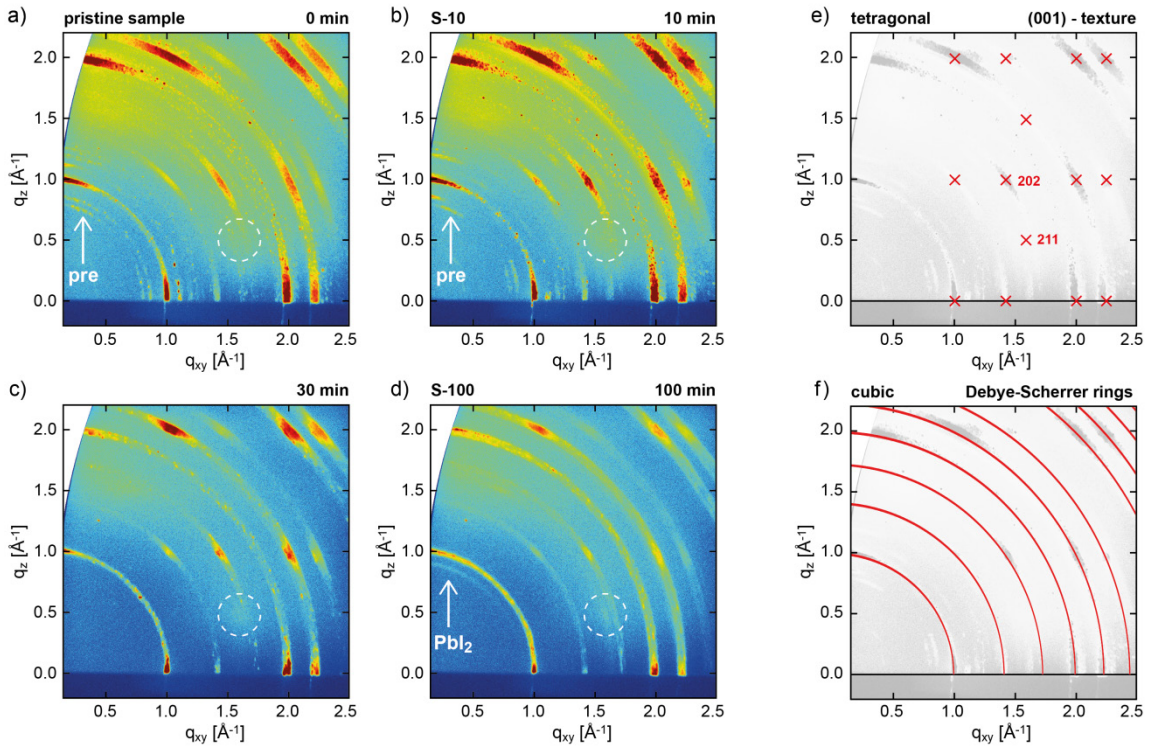

Figure 5.2 2D GIXRD patterns of $MAPbI_{3-x}Cl_x$ perovskite films after: **a)** perovskite solution deposition by spin-coating (0 min annealing time), **b)** 10 min annealing (S-10), **c)** 30 min annealing, **d)** 100 min annealing (S-100) at 100°C. **e)** Simulated diffraction pattern of tetragonal perovskite featuring the expected position of the (211) reflection [see also dotted circles in c) and d)], and the (001) fiber texture (crosses). **f)** Calculated Debye-Scherrer rings of (pseudo-)cubic perovskite. The arrows (pre) in a) and b) indicate the features assigned to the "crystalline precursor structure" still observable at short annealing time. The arrow in d) indicates the diffraction intensity corresponding to PbI_2. 2D maps processed and analyzed by Ingo Salzmann (formerly HU Berlin) and reproduced from ref. [230] – Published by the PCCP Owner Societies.

Therefore, the dominant polymorph in these investigated samples is rather the (pseudo-)cubic perovskite polymorph with a (001)-texture, which is also supported by the calculated Debye-Scherrer rings for (pseudo-)cubic perovskite, that reasonably match the experimental data, as shown in Figure 5.2f. It is noteworthy that the observed (pseudo-)cubic perovskite structure here is not the structural phase expected for $MAPbI_3$ at room temperature, since $MAPbI_3$ is commonly found to be in the tetragonal perovskite phase at room temperature and to undergo a phase transition to cubic perovskite phase only above 54 °C (see subsection 2.2.1). This observed cubic structure of $MAPbI_{3-x}Cl_x$ at room temperature has been proposed to be due to the incorporation of chloride that likely involves a lowering of the tetragonal-to-cubic transition temperature and stabilizes the cubic phase [252–255]. Further investigations are required to clarify the underlying processes.

Both the pristine and the 10 min (S-10) annealed samples already feature the $MAPbI_3$ cubic perovskite diffraction rings (Figure 5.2a-b), thus evidencing the formation of a $MAPbI_3$ perovskite phase already at room temperature, and upon short time annealing. Moreover, after comparison with the calculated diffraction rings of (pseudo-)cubic perovskite, it is evident that both samples also exhibit additional diffraction features; which have been referred to as "crystalline precursor structure" in earlier studies [24, 256]. One of these diffraction features observed at $q = 1.1\ \text{Å}^{-1}$ can actually be assigned to the methyl ammonium lead chloride ($MAPbCl_3$) perovskite, which is an intermediate phase generally observed during $MAPbI_{3-x}Cl_x$ film formation [19, 25]. The remaining additional precursor features (referred to as "pre" in Figure 5.2a-b) cannot be indexed with any of the starting materials, i.e. CH_3NH_3I and $PbCl_2$ [257, 258]. In an attempt to resolve the intermediate crystalline structure, a more recent work independent of the present study estimated the precursor features to correspond to those of a 2D perovskite structure formed by $(CH_3NH_3)_2PbI_2Cl_2{\bullet}CH_3NH_3I$ (or $MA_2PbI_2Cl_2{\bullet}MAI$) [259]. This 2D perovskite structure is crystallographically aligned along the substrate surface normal and consists of zigzagged $[PbI_4Cl_2]$ octahedra and sandwiched MAI layers.

The samples annealed for 30 min and 100 min (S-100) do not exhibit any further features related to the crystalline precursor structure and their 2D diffraction patterns mainly consist of the perovskite structure, thus, indicating the complete crystallization of the film into $MAPbI_3$ perovskite (Figure 5.2c-d). A weak diffraction ring at $q = 0.9\ \text{Å}^{-1}$ is observed for S-100, which corresponds to PbI_2 [260]. PbI_2 might originate from partial degradation of the perovskite film upon annealing [24]. It is important to note that all the mixed-halide $MAPbI_{3-x}Cl_x$ perovskite films investigated in the scope of this thesis have been prepared

following the same procedure, and films characterized by GIXRD all exhibit similar crystal structure with a fiber texture.

In the context of film formation during thermal annealing dealt with in the present section 5.1, the structure of the investigated films undergoes significant changes between 10 min annealing (S-10 sample) when $MAPbI_3$ perovskite structure and additional crystalline structures are still observed, and 100 min annealing (S-100 sample), when the $MAPbI_3$ structure is the only structure observed (except for the PbI_2 generation) and no further structural change occurs. Thus, in the following, the spatially-resolved composition, the morphology, and the electronic structure of S-10 and S100 are comparatively investigated in order to better understand the processes happening before and after complete film formation.

5.1.2 Depth Composition and Morphology Upon Annealing

In order to determine the 3D chemical composition of perovskite films upon annealing, ToF-SIMS depth profiling was performed on perovskite samples before (10 min annealing, sample S-10), and after (100 min annealing, sample S-100) complete film crystallization. The ToF-SIMS measurements were carried out with Yan Busby (University of Namur). As previously described in section 3.2, the ToF-SIMS depth profiling consists of cycles of two alternating steps; the analysis of a 2D area, i.e. in-plane resolution, to obtain a 2D mapping of the elemental composition of this area, and the sputtering for a definite time along the surface normal of this very area in order to subsequently analyze a deeper lying area, and resolve the in-depth composition. Therefore, the resulting ToF-SIMS profile consists of data points over sputter time, where each data point represents the total intensity of the selected secondary ion over each analyzed 2D area. The sputtering was carried out with a low-energy Cs^+ beam which enables the sputtering of organic and inorganic materials with comparable sputtering rates [261–263]. Thus, the sputtering rate is assumed to be constant within a probed material and the sputter time can be directly translated into the sample depth. The absolute intensities of the secondary ions acquired by ToF-SIMS here are not quantitatively comparable; however, valuable qualitative and semi-quantitative information can be obtained by this method. ToF-SIMS profiles of S-10 and S-100 are shown in Figure 5.3. In order to identify the different layers and other compounds possibly present within the samples, fragment ions have been selected accordingly while avoiding mass overlaps. For both S-10 and S-100, the organic CN^- and the inorganic PbI_3^- were selected to identify the $MAPbI_3$ perovskite phase. CN^- can also originate from other methyl ammonium-containing compounds potentially

present in the samples, such as $MAPbCl_3$ perovskite, MACl, or MAI. $C_4H_4S^-$ and $In_2O_2^-$ were selected to identify the PEDOT:PSS, and ITO layers, respectively. Additionally, the signal distribution of $PbCl_3^-$ was reconstructed to identify any compound that potentially remained or stemmed from the starting material $PbCl_2$ in S-10. In all cases, $^{37}Cl^-$ was selected to identify chlorine.

The ToF-SIMS profile of S-10 in Figure 5.3a reveals fairly constant signal intensities from PbI_3^-, $PbCl_3^-$, $^{37}Cl^-$, and CN^- (all assembled under the term "Perovskite" in Figure 5.3 for simplification) during the entire sputtering process. Hence, the top layer in S-10 is a precursor/perovskite film which consists of a $MAPbI_3$ perovskite phase, and MA- and $PbCl_2$-related compounds. Interestingly, signal intensity from $C_4H_4S^-$, i.e. from the underlying PEDOT:PSS substrate, is also detected already from the beginning of the ToF-SIMS depth profiling. The same observation was made for S-100 (Figure 5.3b), thus demonstrating the high sensitivity of ToF-SIMS (up to 1 ppm) in comparison to other surface composition characterization methods such as XPS. By means of the latter method no appreciable sulfur signal corresponding to the PEDOT:PSS layer was detected for both samples (see below in Figure 5.10d). These observations indicate that the PEDOT:PSS layer is not entirely covered by the perovskite layer, which allows detection of the signal from the underlying PEDOT:PSS from the beginning. Whereas the $C_4H_4S^-$ intensity in S-10 is flat after an initial increase, and then drops around 250 s sputter time, inversely, the $C_4H_4S^-$ intensity in S-100 is flat, then increases around 250 s sputter time.

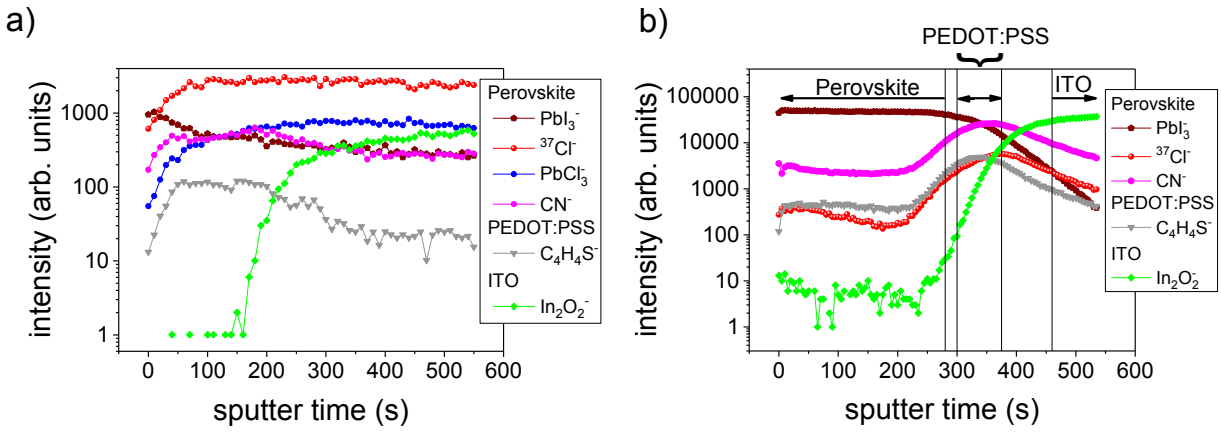

Figure 5.3 ToF-SIMS depth profiles of the samples annealed at 100°C for **a)** 10 min (S-10), and **b)** 100 min (S-100). The PbI_3^-, $C_4H_4S^-$, and $In_2O_2^-$ ions are selected to identify the perovskite, PEDOT:PSS, and ITO layers, respectively. S-10 in a) additionally features the profile of $PbCl_3^-$ indicating the presence of lead chloride-based compound. In contrast, the profiles in b) allow the distinction between the layers by setting the interfaces at the region where the intensity of the respective characteristic ion reaches 80% of its maximum value (vertical lines). Reproduced from ref. [230] – Published by the PCCP Owner Societies.

The above observations can be rationalized by analyzing the morphology of S-10 and S-100 samples evaluated with AFM (Figure 5.4). The AFM micrograph of a not-annealed sample is also shown in Figure 5.4a, which reveals needle-like structures with large voids, thus resulting in high roughness of R_S = 90 nm. It is important to stress that the film morphology and surface roughness can impact on the ToF-SIMS results through non-uniform intensity distribution, which can be misleading in the interpretation of the results [229]. Here, the roughness of the films is significantly reduced with increasing annealing time, that is to R_S = 46 nm after 10 min, and to R_S = 23 nm after 100 min (Figure 5.4b-c.). The improved surface roughness allows drawing more reliable information. Furthermore, in comparison to S-100, the AFM micrograph of S-10 confirms more inhomogeneous film coverage after 10 min annealing, as deduced from the observed pinholes and cavities (see black circles and squares in Figure 5.4b). The initial surface corrugation due to such surface irregularities is preserved throughout the sputtering process. As a result, the $C_4H_4S^-$ signal from the underlying PEDOT:PSS layer is detected from the beginning and simultaneously with the signal from the perovskite layer during the whole sputtering process. Accordingly, $In_2O_2^-$ signal from the ITO under the PEDOT:PSS layer is also detected as soon as the PEDOT:PSS layer has been sputtered.

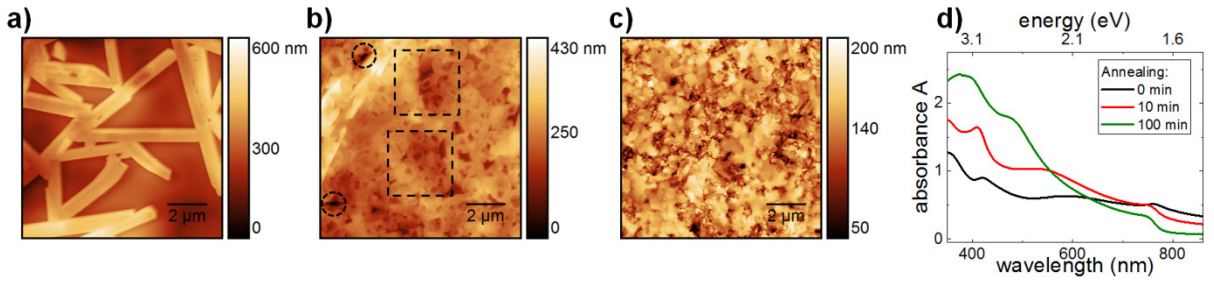

Figure 5.4 AFM micrographs of **a)** not-annealed sample (0 min annealing), and samples annealed at 100°C for **b)** 10 min (S-10), and **c)** 100 min (S-100). Squares and circles in b) point out the cavities and holes at the surface of sample S-10. **d)** UV-visible absorption spectra of $MAPbI_{3-x}Cl_x$ samples annealed for different times. a-c) are reproduced from ref. [230] – Published by the PCCP Owner Societies.

In the case of S-100, although the $C_4H_4S^-$ signal from the PEDOT:PSS is also detected from the start, the intensity plateau is reached only at ~300 s sputter time (Figure 5.3), which indicates that the PEDOT:PSS layer can be well discriminated from the perovskite layer due to the improved morphology after 100 min annealing. Indeed, by setting the respective

interfaces up to regions where the intensities from the respective layer are higher than 80% of the respective maximum value, the individual layers in the ToF-SIMS profiles (Figure 5.3b) can be much better discriminated than in the case of S-10.

It is noteworthy that the perovskite film and morphology evolution can also be perceived in the UV-Vis absorption spectra of not-annealed (0 min), 10 min, and 100 min samples shown in Figure 5.4d. The absorption capacity increases with annealing time, i.e. with the perovskite formation. Particularly at longer wavelength around 780 nm, whereas the band edge is discernable for the 100 min annealed sample, the spectrum in this wavelength region is almost flat for both 0 min and 10 min annealed samples; the pronounced non-zero background can be attributed to light scattering effects and poor surface coverage of the perovskite.

Importantly, the ToF-SIMS measurements allow information to be gleaned about the behavior of chlorine upon annealing. In the case of S-10 (Figure 5.3a), the $^{37}Cl^-$ signal follows the same trend as the detected $PbCl_3^-$ signal, indicating that both ions likely stem from the same species. In the case of S-100 (Figure 5.3b), the $^{37}Cl^-$ signal intensity is slightly above the detection limit in the perovskite region. Such low signal intensity can come either from minute amount of residual chlorine or, more likely, from contamination, since the ionization yield of Cl^- is very high in ToF-SIMS. However, around 250 s sputter time, the $^{37}Cl^-$ signal increases from the perovskite region towards the PEDOT:PSS region, where the signal reaches its maximum intensity. This $^{37}Cl^-$ distribution reveals a significant accumulation of chlorine towards and within the PEDOT:PSS layer, which is supported by the similar trends of the $^{37}Cl^-$ and $C_4H_4S^-$ signals. Moreover, it is important to stress that the high chlorine concentration detected in the PEDOT:PSS layer originates from the precursor/perovskite layer and is not inherent to the pristine PEDOT:PSS layer itself, which is demonstrated by exploiting semi-quantitative information obtained by ToF-SIMS. Indeed, the comparison in Figure 5.5 of the $^{37}Cl^-/C_4H_4S^-$ ratios within a comparably large PEDOT:PSS region in the S-100 sample and in a pristine PEDOT:PSS sample results in a 18 times higher ratio in S-100. Thus, it is confirmed that chlorine originates from the perovskite precursor and accumulates into the PEDOT:PSS layer during annealing, and finally remains there even after complete crystallization of the $MAPbI_{3-x}Cl_x$ perovskite film.

The “chlorine loss” in the final $MAPbI_{3-x}Cl_x$ perovskite film has been the focus of several studies [15, 22, 264]. It has been observed that during the annealing step, chlorine is released from the perovskite film through the sublimation of MACl [15, 27, 264], as also suggested by the PES results in Figure 5.1. Although the presence of residual chlorine within the

$MAPbI_{3-x}Cl_x$ perovskite samples have been experimentally assessed by different methods such as X-ray absorption near-edge structure (XANES) [248], or hard X-ray photoelectron spectroscopy [29], the location of chlorine within the film is still poorly described.

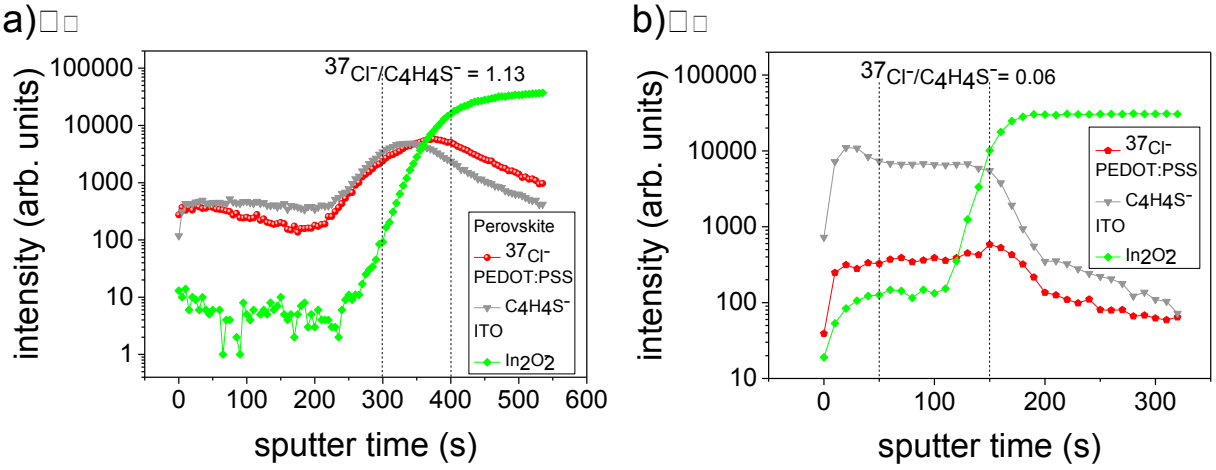

Figure 5.5 ToF-SIMS depth profiles of **a)** the S-100 sample, as extracted from Figure 5.3b, and **b)** a pristine PEDOT:PSS film on a ITO substrate. The comparison of the intensity ratios $^{37}Cl^-/C_4H_4S^-$ in the PEDOT:PSS layer, here delimited by the vertical dotted lines, for both samples yields a $^{37}Cl^-$ content 18 times higher in S-100 than in the pristine PEDOT:PSS sample. Reproduced from ref. [230] – Published by the PCCP Owner Societies.

The present ToF-SIMS study allowed tracking of the location of chlorine throughout the entire perovskite layer depth, towards and within the PEDOT:PSS hole transport layer. The presence of chlorine can strongly impact on the perovskite film properties. The presence of even a low concentration of chlorine has been reported to improve the charge-transport properties in perovskite films [14]. Additionally, the presence of chlorine at the interface between the perovskite and the TiO_2-substrate can promote the charge collection at this interface [28]. It is noteworthy that the $^{37}Cl^-$ distribution observed here resembles the chlorine diffusion observed by ToF-SIMS in mesoporous TiO_2 of a perovskite-based solar cell with a mesoporous structure [249]. Consequently, the increase of chlorine amount towards the perovskite/substrate interface and within the substrate appears to be independent of substrate and device configuration, thus providing a possible explanation for the prominence of mixed-halide $MAPbI_{3-x}Cl_x$ perovskite-based solar cells by comparison with their single halide $MAPbI_3$ perovskite counterpart. However, it is noteworthy that the exact nature of the impact of chlorine at the aforementioned interfaces likely depends on the respective substrate.

So far, the depth profiling measurements have provided information about the composition of the samples along the surface normal and about the location of the different ions. Additionally, the ToF-SIMS analysis can be extended to the analysis of the in-plane (XY) and lateral (ZY) composition for a complete 3D spatial resolution, where XY defines the plane corresponding to the sample surface, and Z refers to the axis along the surface normal and directed towards the substrate, as explained in subsection 4.2.2 and in Figure 3.7. The depth-integration of the intensity of a secondary ion over a given area results in a 2D map. 2D maps of PbI_3^-, $PbCl_3^-$, CN^-, and $CH_3NH_2I^-$ (deprotonated MAI) for S-10 are shown in Figure 5.6. In all cases, a lateral phase separation can be deduced from the existence of one region with high intensities, and another with lower intensities. Particularly for PbI_3^-, and $PbCl_3^-$ (Figure 5.6a-b), one distinguishes between two pronounced regions; a region A (red squares) with high PbI_3^- and low $PbCl_3^-$ intensities, and another region B (blue circles) with inversely high $PbCl_3^-$ and low PbI_3^- intensities.

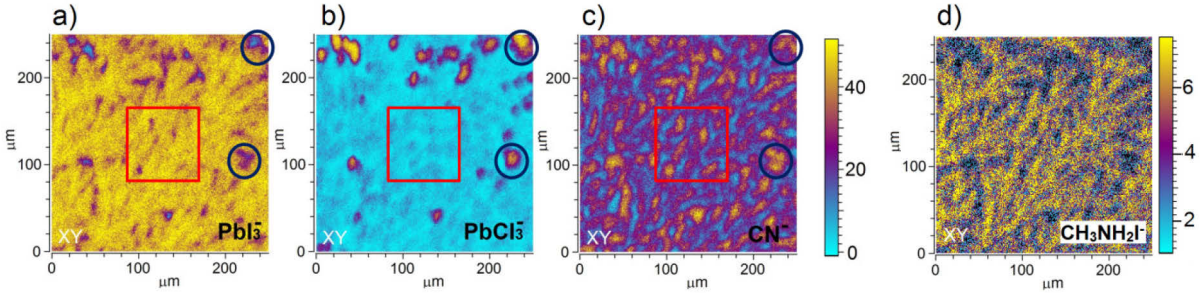

Figure 5.6 Reconstructed ToF-SIMS 2D maps for **a)** PbI_3^-, **b)** $PbCl_3^-$, **c)** CN^-, and **d)** $CH_3NH_2I^-$ ions, to identify lead iodide-, lead chloride-, methyl ammonium-, and methyl ammonium lead iodide-related compounds, respectively. The lateral resolution is ca. 1 µm. Regions A (red squares) indicate regions with high PbI_3^- and CN^- intensities and low $PbCl_3^-$ intensity; and inversely, regions B (blue circles) indicate regions with high $PbCl_3^-$ and CN^- intensities and low PbI_3^- intensity. The same color scale is adopted for the 2D maps of PbI_3^-, $PbCl_3^-$, and CN^-, and a different one for the 2D map of $CH_3NH_2I^-$. Illustration by Yan Busby (University of Namur), adapted by the author and reproduced from ref. [230] – Published by the PCCP Owner Societies.

Therefore, one can deduce a phase separation between a region A that corresponds to the formed $MAPbI_3$ perovskite phase, as determined by GIXRD in subsection 5.1.1; and a region B that corresponds to a $PbCl_3^-$-related phase. This latter phase likely originates from the fragmentation of the intermediate $MAPbCl_3$, as established for S-10 by GIXRD in the previous subsection 5.1.1. Although $PbCl_2$ was not detected by GIXRD, it is not completely ruled out that the $PbCl_3^-$ ions partially derive from minute amounts of $PbCl_2$ remaining from

the original organic compound in the precursor/perovskite film. Indeed, $PbCl_2$-based perovskite precursor solution was found to contain a certain amount of un-dissolved $PbCl_2$ as nanoparticles [30], which then act as nucleation centers, promoting the growth along a preferred orientation and the formation of perovskite films with large crystalline domains upon annealing.

The 2D map of CN^- in Figure 5.6c displays high CN^- signal intensities in both previously described regions A and B, thus indicating that CN^- is present in both regions. In region A where the $MAPbI_3$ phase predominates, CN^- can be assigned to the fragmentation of MA in $MAPbI_3$. CN^- in this region might also originate from traces of MAI (compound in excess in the original precursor solution), as supported by the 2D map of the reconstructed $CH_3NH_2I^-$ (de-protonated MAI) in Figure 5.6d, which indicates a similar spatial distribution of MAI to the one of PbI_3^-. In region B where the $PbCl_3^-$-related phase predominates, CN^- is assigned to the intermediate $MAPbCl_3$ in S-10 (see subsection 5.1.1). Thus, the precursor/perovskite film in S-10 is characterized by two phase-separated regions; a region A with mainly the formed $MAPbI_3$ perovskite phase, and possibly unconverted MAI; and a region B dominated by the intermediate $MAPbCl_3$ phase with possible traces of $PbCl_2$. This conclusion is consistent with the topotactic transformation occurring during $MAPbI_{3-x}Cl_x$ film formation suggested by Williams et al.[22] and Moore et al. [26]. The described transformation presupposes the presence of a chloride-rich phase and a peripheral iodide-rich phase at the early stage of the annealing. During annealing, MA^+ and I^- from the iodide-rich phase diffuse to the chloride-rich phase, where I^- replaces Cl^- at its position, and Cl^- is released from the film as MACl. Subsequently, a more stabilized iodide-rich phase evolves with enhanced film crystallization, in comparison to $MAPbI_3$ perovskite obtained from chlorine-free synthesis. Therefore, the intermediate chloride-rich phase – correspondingly the intermediate $MAPbCl_3$ in the ToF-SIMS results – acts as a preceding structural template for the final $MAPbI_3$ perovskite. In contrast to these previous studies, the particular outcome of the present ToF-SIMS analysis is the resolution of the spatial distribution of the perovskite film composition, which points out the lateral coexistence of the chloride-rich and lead iodide-rich phases right throughout the film depth before complete crystallization, as also evidenced by the YZ cross section maps of PbI_3^-, $PbCl_3^-$, and CN^- of S-10 in Figure 5.7.

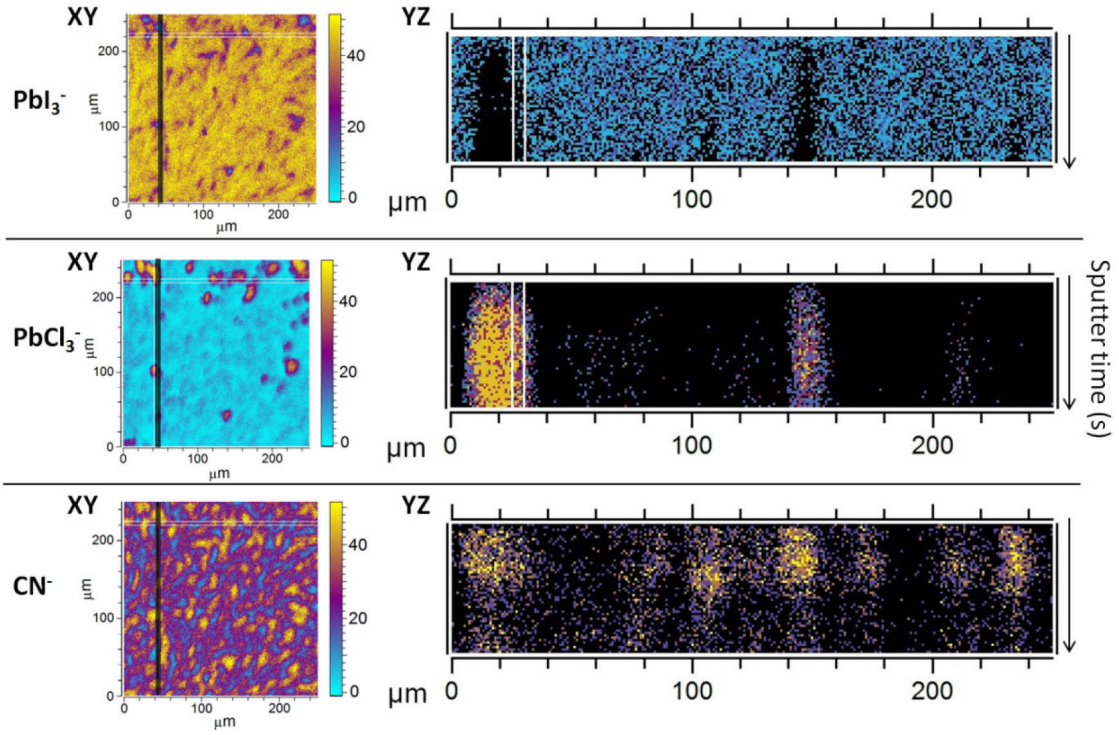

Figure 5.7 ToF-SIMS XY maps (from Figure 5.6), and the respective cross section reconstruction maps along YZ sections, each defined by the black line in the corresponding XY map, for PbI_3^-, $PbCl_3^-$, and CN^- in S-10. The YZ maps evidence the extension of the phase separation throughout the entire film depth. Illustration by Yan Busby (University of Namur), adapted by the author and reproduced from ref. [230] – Published by the PCCP Owner Societies.

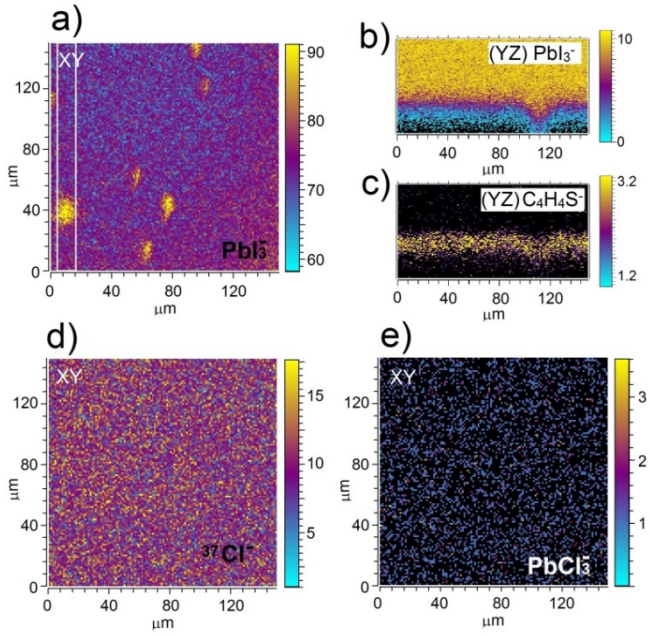

Figure 5.8 ToF-SIMS maps from S-100. **a)** XY map of PbI_3^-, YZ maps of **b)** PbI_3^-, and **c)** $C_4H_4S^-$, these last two maps correspond to the section delimited by the two white lines in a). XY maps of **d)** $^{37}Cl^-$, and **e)** $PbCl_3^-$ are also shown. The spots with high intensities in the 2D map of PbI_3^- in a) are attributed to increased signal due to the diffusion of $MAPbI_3$ into defects in the underlying PEDOT:PSS layer, as observed around 100 µm breadth in b) and c). Illustration by Yan Busby (University of Namur), adapted by the author and reproduced from ref. [230] – Published by the PCCP Owner Societies.

During annealing, while chlorine is either released as MACl or migrates towards the interface into the PEDOT:PSS layer, MA^+ and I^- recombines with Pb to form $MAPbI_3$ perovskite. Therefore, the complete crystallization is characterized by a single $MAPbI_3$ perovskite phase, as evidenced by the 2D maps of S-100 in Figure 5.8, where no phase separation is observed anymore from the maps of PbI_3^- and $^{37}Cl^-$ (Figure 5.8a-b). No $PbCl_3^-$ signal was detected either (Figure 5.8a), thus, no lead chloride-related compound is present. The detected $^{37}Cl^-$ signal displayed in Figure 5.8b comes from chlorine accumulated towards and within the PEDOT:PSS layer as established in Figure 5.3b.

5.1.3 Electronic Property Evolution Upon Annealing

So far, the changes in composition within the entire perovskite films has been correlated with a change of morphology and the evolution of the crystal structure from an intermediate templating structure to the single $MAPbI_3$ perovskite phase with a preferred orientation. These changes shed light on the role of chlorine within the $MAPbI_{3-x}Cl_x$ film and during its formation. Hereafter, to gain additional information about the film formation, the influence of the above-mentioned changes on the electronic properties of the perovskite film surface is investigated by UPS and XPS. No chlorine was detected for both S-10 and S-100, as deduced from the Cl 2p core level spectra in Figure 5.9.

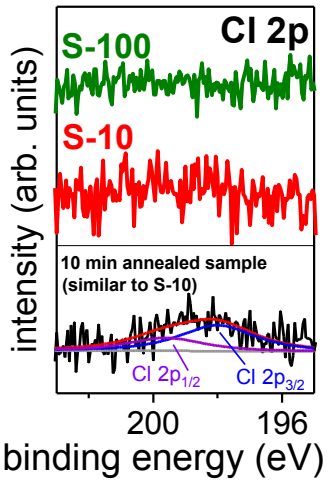

Figure 5.9 XPS core level spectra of Cl 2p for S-100 (green, top), S-10 (red, middle), and another perovskite sample (black, bottom) similar to S-10, i.e. annealed for 10 min at 100 °C, which exhibits – in contrast to S-10 and S-100 – some intensity. By applying a Shirley background (grey), the bottom spectrum can be fitted (red curve) with two peaks representing the Cl $2p_{1/2}$ (violet), and $Cl2p_{3/2}$ (blue) doublets. The detected signal for this latter sample can be explained by the longer acquisition time (twice as long as for S-10) and/or shorter exposure to X-ray irradiation (5 vs 60 min for S-10) before actual acquisition of the Cl 2p spectrum, which might have induced chlorine loss. Adapted from ref. [230] – Published by the PCCP Owner Societies.

However, it is noteworthy that the XPS measurement on a similarly prepared sample, annealed for 10 min at 100 °C, features a weak but perceptible Cl 2p intensity, as shown in

Figure 5.9. In the latter case, the acquisition time was longer (20 scans) in contrast to S-10 (10 scans), which can account for the improved signal-to-noise ratio. Another difference between this sample and S-10 is also the acquisition order of Cl 2p spectrum during measurement. Whereas the Cl 2p spectrum has been acquired after the sample has been exposed to X-ray for only 5 min in the former case, in the case of S-10, the Cl 2p spectrum has been acquired after several other elemental regions, which resulted in a longer exposure to X-ray irradiation of 60 min before actually acquiring the Cl 2p spectrum. Therefore, the absence of chlorine in the case of S-10 might therefore also be related to the release of chlorine through X-ray irradiation, as has been reported for halogenated compounds [265].

The core level spectra of Pb 4f, I 3d, N 1s, and S 2p for S-10 and S-100 are shown in Figure 5.10a-d, respectively. No definite signal from S 2p related to PEDOT:PSS is detected (Figure 5.10d). Upon annealing from 10 min (S-10) to 100 min (S-100), the core levels shift to higher binding energy by 0.6 eV for Pb 4f, and by 0.7 eV for both I 3d and N 1s Figure 5.10a-c. Concomitant shift of the valence band maximum (VBM) by 0.5 eV to higher binding energy (Figure 5.10f), and of the work function (ϕ) to 0.4 eV lower value (Figure 5.10e) are also observed.

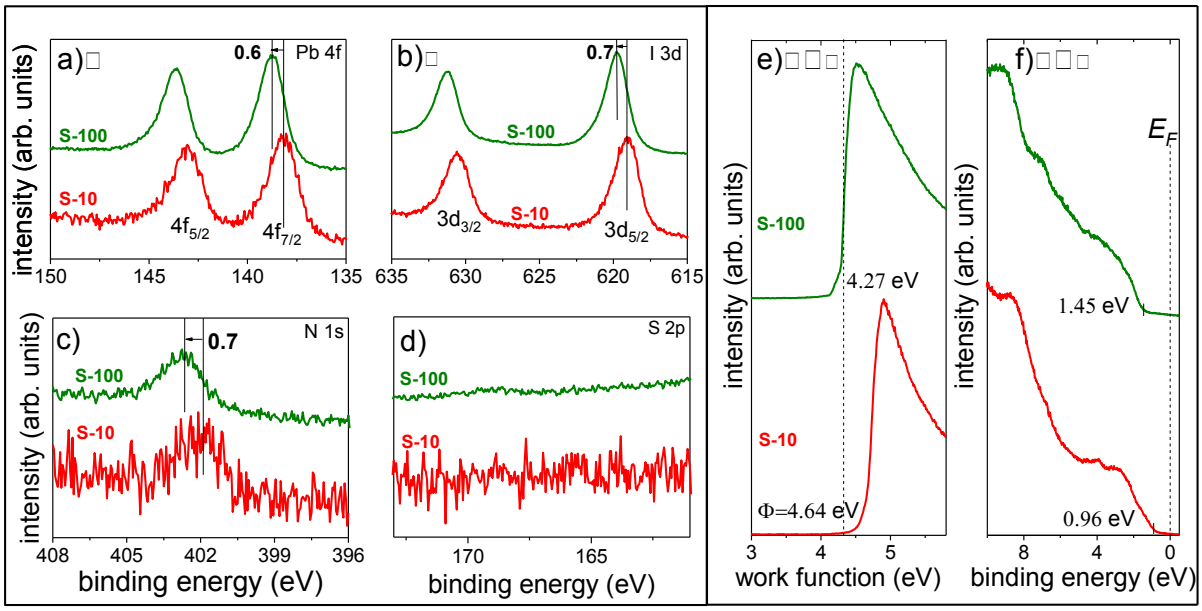

Figure 5.10 Photoemission spectra of samples annealed at 100 °C for 10 min (S-10, red lines), and for 100 min (S-100, green lines). XPS spectra of the **a)** Pb4f, **b)** I3d, **c)** N1s, and **d)** S2p core levels, and UPS spectra showing **e)** SECO, and **f)** valence band. Reproduced from ref. [230] – Published by the PCCP Owner Societies.

The shift towards higher binding energies, by approximately the same amount of all electronic levels (core and valence), indicates that the shift is most likely of an electrostatic nature. Since these electronic levels shift away from the Fermi level, the material becomes more n-type upon complete crystallization to perovskite. This is in agreement with the transition from p- to n-type doping of perovskite upon annealing, which has been accounted for by an evolution of the phase composition [25]. Particularly, as also mentioned in section 2.2.2, due to MA^+ and I^- deficiency associated with the reduction of MAI content upon thermal annealing, $MAPbI_3$ perovskite films undergo a conversion into a more n-doped electronic property [159]. It has also been reported that the ionization energy of perovskite films is sensitive to the film composition. In particular, films with deficient MAI content (translated in MA^+ deficiency) have been observed to exhibit higher IE than films with PbI_2 deficiency [161]. This possibly explains the slight IE increase by +0.12 eV observed from S-10 to S-100 here. This possibility is corroborated by the reconstructed ToF-SIMS XY maps representing the CN^- to PbI_3^- ratio (CN^-/PbI_3^-) for S-10 and S-100 in Figure 5.11. The XY map of S-100 indicates a nicely uniform low-intensity ratio distribution. In contrast, the XY map of S-10 features an inhomogeneous intensity distribution with regions that exhibit higher intensity ratios, i.e. higher MA concentration. This indicates that S-10 has a higher relative MA concentration in comparison to S-100.

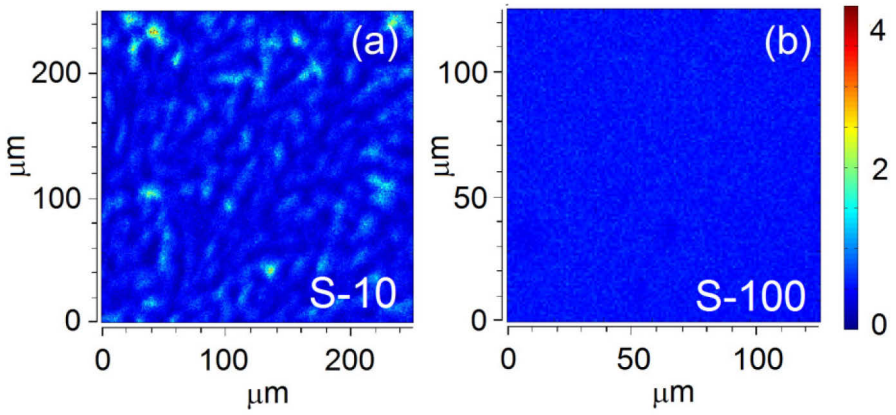

Figure 5.11 ToF-SIMS XY maps representing the CN^-/PbI_3^- intensity ratio calculated for **a)** S-10 and **b)** S-100. S-10 is characterized by an inhomogeneous intensity ratio distribution, emphasized by regions with distinctly higher intensity ratio, that is, higher concentration of organic MA compound, whereas S-100 exhibits a homogeneous intensity ratio distribution. Reproduced from ref. [230] – Published by the PCCP Owner Societies.

However, since the IE increase from S-10 to S-100 is tantamount to the 0.1 eV smaller work function shift in comparison to the shift of the valence level, it can also be explained by a change in the surface electrostatic potential due to structural changes in addition to the observed change of the doping level. Likewise, the small difference in the shift between the valence and core levels can be explained by the overall change of the valence electronic structure. It is noteworthy that this latter shift difference can also be attributed to the change of the chemical environment of the respective atoms. Indeed, a shift to higher binding energy of the Pb 4f and I 3d core levels has been also recently observed during the crystallization of $MAPbI_{3-x}Cl_x$ film and has been suggested to result from the different chemical environment of lead and iodine in the aforementioned 2D perovskite phase and in the final single $MAPbI_3$ phase [259].

As an aside, since monitoring the change in electronic structure *in-situ* during annealing would give a more accurate insight into the formation process, a not-annealed perovskite film has been tentatively annealed in ultra-high vacuum. The evolution of the electronic structure upon two different annealing steps has been monitored by means of UPS and XPS measurements at room temperature as shown in Figure 5.12.

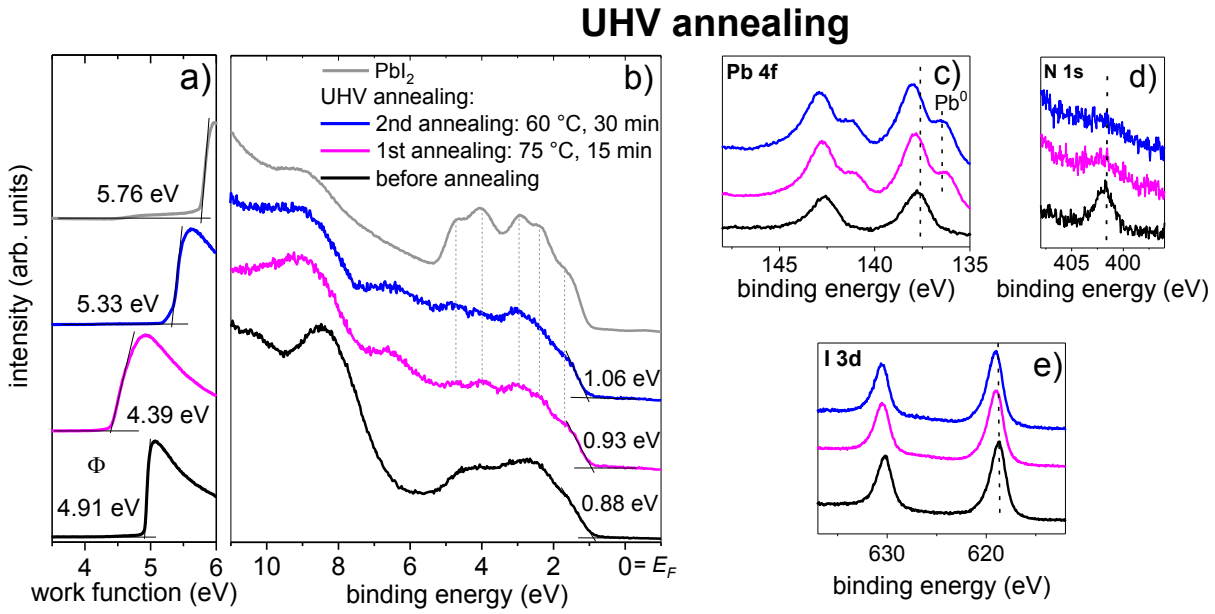

Figure 5.12 Photoemission spectra of a not-annealed perovskite sample (black), first annealed in UHV at 75 °C for 15 min (magenta), and subsequently annealed a second time in UHV at 60 °C for 30 min (blue). **a)** SECO, and **b)** valence band spectra, as well as XPS core level spectra of **c)** Pb 4f, **d)** N 1s, and **e)** I 3d. Comparison with the SECO and valence band spectra of PbI_2 shown in a) and b) highlights the formation of PbI_2 at the surface upon annealing in UHV.

The pristine perovskite sample freshly deposited from solution, i.e. not-annealed, exhibits a valence band spectrum similar to that of S-10 as shown in Figure 5.12b. The work function value of 4.91 eV (Figure 5.12a) and the VBM at 0.88 eV BE are in line with the trend observed at different annealing time observed with S-10 and S-100, namely the higher ϕ and the VBM and the main core levels (Figure 5.12c-e) closer to the Fermi level at lower annealing time. Although the direction of the shift upon first annealing in UHV (at 75 °C for 15 min) is the same as for samples annealed in a N_2-filled glove box, the chemical composition is different, as demonstrated by the appearance of a second Pb 4f peak at lower binding energy which corresponds to elemental lead Pb^0 and which indicates degradation at the film surface. The formation of PbI_2 is evidenced by the characteristic features of PbI_2 discernible in the valence band spectrum of the sample upon annealing as shown in Figure 5.12b. A second annealing step (at 60 °C for 30 min) induces more pronounced degradation into PbI_2 with even more apparent features of PbI_2 in the corresponding valence band spectrum. The presence of a PbI_2 layer at the perovskite film surface can seriously impede the charge carrier transport at the interface between the perovskite film and the transport overlayer [266]. Thus, the N_2-filled glove box is more recommendable as a more optimal and easily controlled environment than UHV for thermal annealing.

In summary, the results presented in this section reveal that during the $MAPbI_{3-x}Cl_x$ films crystallization by thermal annealing, chlorine from the precursor solution is not only released as MACl, as commonly known, but also diffuses towards the back interface between perovskite and the underlying hole transport material PEDOT:PSS, where it remains even after complete crystallization. This behavior of chlorine during crystallization is successfully derived from the evolution of the composition of $MAPbI_{3-x}Cl_x$ films throughout the bulk, which has been correlated with the evolution of the structure, the morphology, and the electronic structure upon annealing. Before complete crystallization, i.e. at short annealing time, $MAPbI_{3-x}Cl_x$ films are characterized by an inhomogeneous composition with a lateral phase separation between single $MAPbI_3$ perovskite and lead chloride-rich domains. These latter domains are dominated by the presence of $MAPbCl_3$, which is an intermediate phase that acts as a preceding structural template directing the film growth following a preferred orientation. After complete crystallization upon a longer annealing time, the $MAPbI_{3-x}Cl_x$ films exhibit a fiber texture growth with a preferred orientation of the crystallites along the surface normal and are characterized by a highly uniform single $MAPbI_3$ phase. Furthermore, the phase evolution is accompanied by a change of the films' electronic structure to a more

n-type character, which is related to relative deficiencies in MA content upon increasing annealing time. These results emphasize not only the role of chlorine in the formation of highly oriented films during annealing, but also its influence on the charge transport within the film and at the interface to the respective underlying substrate. Both outcomes have been reported in literature to likely impact on the performance of photovoltaic devices.

It is important to stress that the final "mixed halide $MAPbI_{3-x}Cl_x$ perovskite" film actually consists of the single $MAPbI_3$ perovskite phase, with chlorine having left the film, either by sublimation of MACl or by diffusion towards the underlying transport layer. Therefore, later experimental results obtained for $MAPbI_{3-x}Cl_x$ can be fairly analyzed in the light of existing reports on $MAPbI_3$. However, the wording is retained – particularly throughout this thesis – in order to highlight the relevance of chlorine in the formation process of $MAPbI_{3-x}Cl_x$ perovskite obtained from chlorine-based precursor solution. One remaining question is the implication of chlorine in the formation of the stabilized (pseudo-)cubic $MAPbI_3$ structure at room temperature, as also reported in literature for $MAPbI_{3-x}Cl_x$, instead of the expected tetragonal perovskite structure. Understanding the origins of the decreased cubic-to-tetragonal transition temperature can enable the selective design of perovskite materials with enhanced stability.

5.2 Environmental Effects on the Electronic Property of Perovskite Films

The previous section 5.1 explored the importance of thermal annealing in the formation of crystallized $MAPbI_{3-x}Cl_x$ perovskite films and pointed out how the effective properties of $MAPbI_{3-x}Cl_x$ films are strongly related to their formation. The present section now turns to the less effective aspect of poor reproducibility and stability of the films with regard to environmental conditions, which inhibit the applicability of perovskite materials as a lasting alternative to established photovoltaic materials. The present section aims at assessing the separate effects of water vapor and oxygen exposure, and their combined effect in air, on the electronic structure of $MAPbI_{3-x}Cl_x$ perovskite films by using photoelectron spectroscopy (PES) before obvious degradation sets in. Most of the results shown in this section have been published in ref. [267], which includes the investigation of the effect of the exposure to water at different partial pressure in subsection 5.2.2, the exposure to oxygen in subsection 5.2.3, and the exposure to high vacuum and to air in subsection 5.2.4. Additionally, the first subsection 5.2.1 presents additional preliminary characterizations of the electronic structure of $MAPbI_{3-x}Cl_x$ perovskite films in air by using Kelvin probe (KP) and photoelectron yield spectroscopy (PYS).

At this stage, it is important to note that all pristine samples transferred from a N_2-filled glove box to the UHV system for UPS measurement without air exposure (see subsection 4.2.1), exhibited a n-type surface property, i.e. the energy position of E_F in the band gap is closer to the conduction band than to the valence band. This n-type character has been often observed for $MAPbI_3$ perovskites and has been related to the presence of Pb^0 defects at the $MAPbI_3$ surface [160, 176]. Consequently, variation of the density of Pb^0-induced surface states can lead to variation of the n-type character, as observed on the pristine samples in the present work, which exhibit a variation of the E_F position by up to 0.4 eV. However, the ionization energy values extracted from the UPS measurements were comparable within the error margin of the experiment [(5.85 ± 0.07) eV][4].

5.2.1 Preliminary Characterizations

[4] (5.60 ± 0.07) eV with VBM determined from logarithmic intensity scale.

In order to evaluate the electronic structure of $MAPbI_{3-x}Cl_x$ perovskite films in ambient air and in vacuum, three similarly prepared samples P1, P2, and P3 were directly transferred from the inert box to the UHV system for first UPS measurements without any exposure to air. After UPS measurements, the samples were brought to air for KP and PYS measurements, before finally being characterized in UHV by UPS again. The UPS results are shown in Figure 5.13a-b. The PYS spectra are shown in Figure 5.13c and the values of the parameters extracted from the UPS, PYS and KP (KP data in Appendix B) measurements are summarized in Table 5.1.

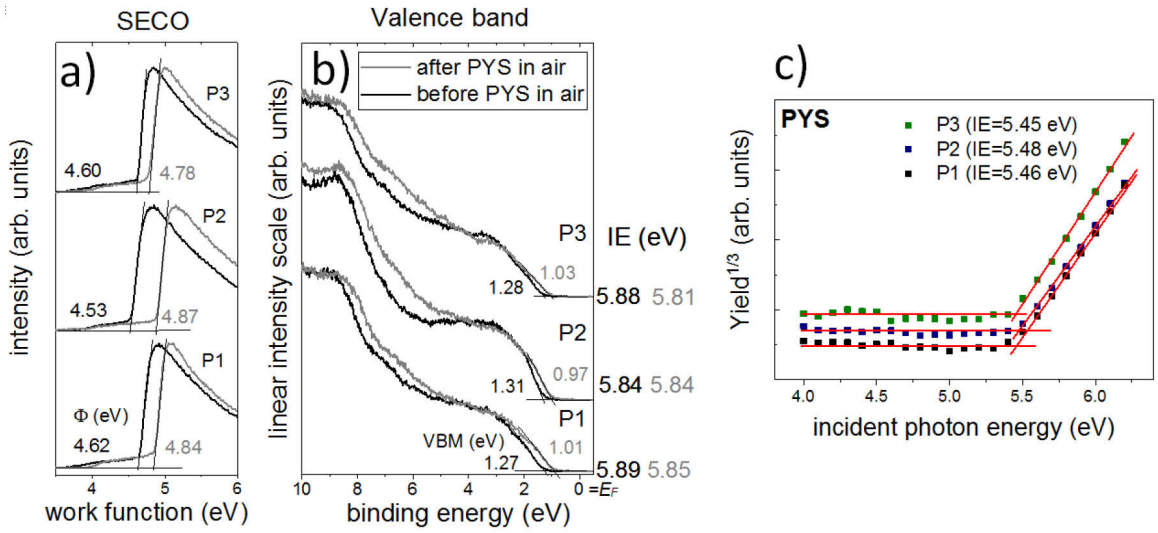

Figure 5.13 UPS and PYS spectra of $MAPbI_{3-x}Cl_x$ films P1, P2, and P3. **a)** SECO and **b)** valence band spectra measured by UPS in UHV before and after PYS and KP measurements in air. The corresponding IEs are shown on the right side of each graph. **c)** PYS spectrum recorded for all samples P1, P2, and P3. The threshold energy that yields the IE is determined as the onset of the PYS spectrum by assuming a linear background.

Table 5.1 Parameters obtained from UPS measurements (ϕ_{UPS}, IE_{UPS}, and VBM_{UPS}) before and after KP (ϕ_{KP}) and PYS (IE_{PYS}) measurements on $MAPbI_{3-x}Cl_x$ films in air; the given errors are estimated from a set of 3 samples P1, P2, and P3 (see Figure 5.13). VBM* is estimated from the difference between ϕ_{KP} and IE_{PYS} in the table. Corresponding KP and PYS data are gathered in the Appendix C.

	UHV before air			air			UHV after air		
(eV)	ϕ_{UPS}	IE_{UPS}	VBM_{UPS}	ϕ_{KP}	IE_{PYS}	VBM*	ϕ_{UPS}	IE_{UPS}	ϕ_{UPS}
Lin. (UPS)	4.58 ±0.04	5.87 ±0.04	1.29 ±0.02	4.83 ±0.03	5.47 ±0.01	0.64	4.83 ±0.04	5.83 ±0.04	1.00 ±0.02

Before air exposure, the as-prepared samples exhibit average work function and VBM values of ϕ_{UPS}=(4.58±0.04) eV and VBM_{UPS}=1.29 eV, respectively. By taking a band gap of 1.70 eV into account [111, 247], these values imply that the samples have a n-type property like the fully crystallized perovskite film in section 5.1.3. When comparing the UPS results before and after air exposure (i.e. KP and PYS measurements in air), an increase of the work function ϕ_{UPS} by ca. 0.3 eV is observed, whereas the ionization energy IE_{UPS} does not change. The $MAPbI_{3-x}Cl_x$ surfaces therefore became less n-type, i.e. E_F shifts towards mid-gap upon air exposure. Interestingly, the work function ϕ_{KP} measured in air by KP is the same as ϕ_{UPS} measured by UPS after air exposure.[5] The results imply that air exposure induces a change of the surface electronic properties with the E_F shifting from a position closer to the CBM towards mid-gap. The observed changes are likely related to ambient conditions, notably to oxygen or water present in air or possibly the combined effect of both. In the following subsections, the conducted experiments were restricted to PES measurements in UHV in order to investigate the effect of water and oxygen separately. After exposure to different gases (water vapor, oxygen, residual gases in HV at 10^{-6} mbar) in a chamber initially with at least HV conditions, the electronic structures of perovskite films are monitored.

5.2.2 Effect of Water

As mentioned at the end of the introduction part of the present section, this section deals among others with the investigation of the impact of water on the electronic structure of $MAPbI_{3-x}Cl_x$ before any apparent structural degradation sets in. Indeed, upon longer exposure to higher RH, $MAPbI_3$ perovskites undergo a structural change into monohydrates followed by a conversion into PbI_2 [40, 42]. To monitor such structural changes and estimate the timescale on which they are detectable for $MAPbI_{3-x}Cl_x$, GIXRD measurements have been conducted *in situ* on perovskite films exposed to high RH beyond 80%, as shown in Figure 5.14. The first 2D GIXRD reciprocal space map acquired (Figure 5.14a) exhibits regions with enhanced intensities which show that the $MAPbI_{3-x}Cl_x$ film has a certain fiber texture as already seen in section 5.1. In contrast, the last 2D GIXRD map after 1000 min exposure to RH above 80% (Figure 5.14b) exhibits additional features at $q = 0.6$ Å^{-1} and

[5] Note that the VBM_{UPS} extracted from a logarithmic intensity scale (Figure B2, Appendix B) yield IE_{UPS} values of (5.57±0.06)eV, which differ only by 0.1 eV from the IE_{PYS} values.

$q = 0.75$ Å^{-1} assigned to $MAPbI_3 \cdot H_2O$ monohydrate that forms reversibly during perovskite hydration [42]. Besides, PbI_2 is identified by the diffraction feature at $q = 0.9$ Å^{-1}.

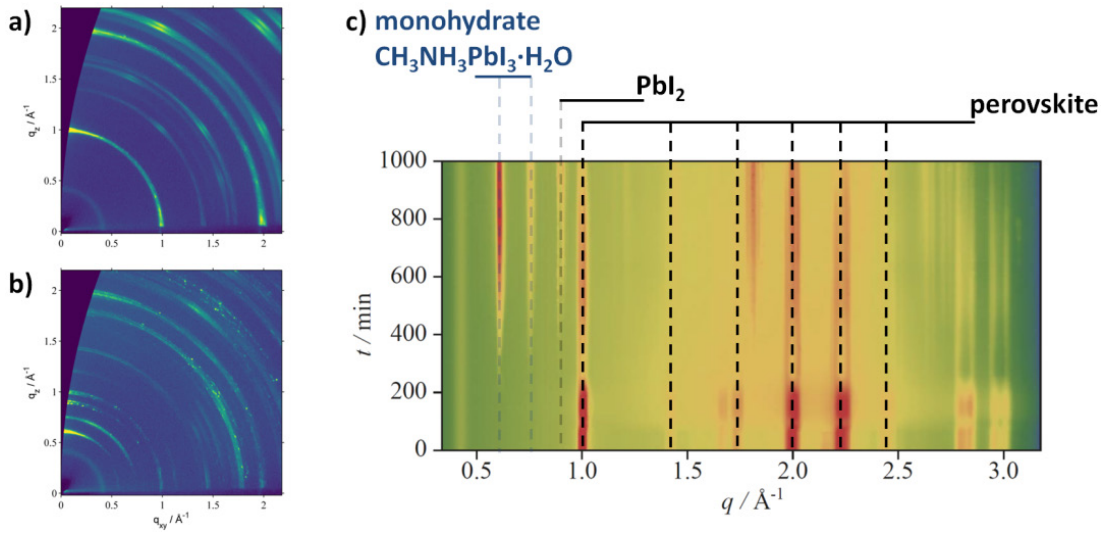

Figure 5.14 2D GIXRD patterns of a $MAPbI_{3-x}Cl_x$ film **a)** before and **b)** after exposure to high relative humidity (RH) beyond 80% for 1000 min; the broad ring around $q = 0.4$ Å^{-1} is due to the Kapton foil of the humidity container. **c)** Integrated diffraction intensities over 1000 min time *in situ* exposure to RH beyond 80% of the $MAPbI_{3-x}Cl_x$ film in a) and b), showing features corresponding to the monohydrate $MAPbI_3 \cdot H_2O$ phase that appear after 170 min, followed by the detection of PbI_2-related signal after over 200 min. 2D maps and integrated intensities map processed and analyzed by Ingo Salzmann (formerly HU Berlin) and reproduced from ref. [267].

The integrated diffraction intensities for constant q over time shown in Figure 5.14c point out that the features related to the monohydrate and to the PbI_2 can only be detected after ca. 170 min, and 200 min, respectively. It is to be noted that since the structural evolution upon exposure to high RH observed for the $MAPbI_{3-x}Cl_x$ film here is similar to that of $MAPbI_3$ single crystal reported in literature [42], $MAPbI_{3-x}Cl_x$ and $MAPbI_3$ perovskites both follow the same degradation pathway. Importantly, these results indicate that a priori no relevant hydrate species formation or significant water-induced degradation into PbI_2 is to be expected below the indicated exposure times (<170 min) to 80% RH (i.e. $p_{H2O} \approx 20$ mbar at 20 °C). Consequently, this also applied at the exposure times chosen in the following PES studies, which have been restricted to conditions comparable to those typical during device fabrication, i.e. 10^{-6} mbar < p_{H2O} < 4 mbar, where p_{H2O}=4 mbar corresponds to water partial pressure in ambient air at 17% RH.

Low water exposure (p_{H2O} = 10^{-6} mbar)

The electronic structure of a pristine $MAPbI_{3-x}Cl_x$ perovskite film was monitored after alternating storage in UHV, exposure to low p_{H2O} = 10^{-6} mbar, and mild heating in UHV at 50 °C (Figure 5.15).

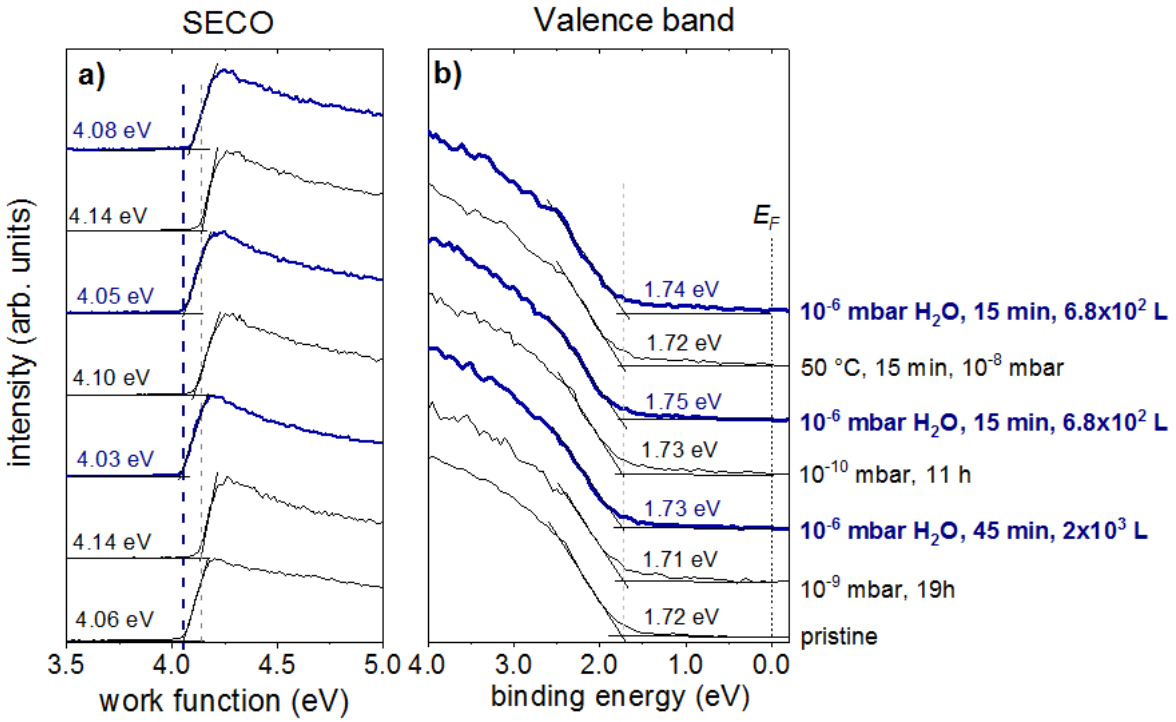

Figure 5.15 UPS spectra of $MAPbI_{3-x}Cl_x$ upon H_2O exposure to p_{H2O} = 10^{-6} mbar for different duration – dosage is also given in Langmuir (L) – with subsequent storage or heating in UHV. **a)** SECO and **b)** the corresponding valence band spectra with the respective VBM. Reproduced from ref. [267].

The SECO spectra (Figure 5.15a) and valence band spectra (Figure 5.15b) show the strong n-type character of the pristine film with a work function of 4.06 eV and a VBM of 1.72 eV[6]. Storing this sample in UHV (10^{-9} mbar residual gas pressure) for 19 h resulted in an increase of the work function to 4.14 eV. Following exposure of the sample to p_{H2O} = 10^{-6} mbar for 45 min decreased the work function from 4.14 to 4.03 eV. Subsequent alternation of UHV storage for several hours, p_{H2O} exposure, and mild annealing in UHV at 50 °C shows a systematic and reversible decrease of the work function by up to ca. 100 meV upon exposure

[6] As already mentioned at the beginning of the results chapter 5 the pristine sample shown in Figure 5.15b exhibits a VBM of 1.51 eV when the onset is determined from a logarithmic intensity scale (Figure B3, Appendix B).

to $p_{H2O} = 10^{-6}$ mbar. In all cases, whereas the work function changed at each alternating step, the valence region remained unaffected within the error margin of the measurement. Therefore, the reversible work function decrease upon exposure to p_{H2O} as low as 10^{-6} mbar is likely due to the adsorption of water molecules on the surface, which desorb again when the sample is stored in UHV for several hours at room temperature or mildly heated at 50 °C. Interestingly, the work function of the pristine sample transferred from the glove box also increases upon UHV storage for several hours. Since $p_{H2O} = 10^{-6}$ mbar corresponds to a water partial pressure 100 times lower than the p_{H2O} in standard glove box (water content of 0.1 ppm), this work function change suggests the adsorption of water on the perovskite film surfaces already under typical glove box conditions. The reversible shifts indicate that at low p_{H2O} water only physisorbs on the perovskite surface.

One possible phenomenon occurring upon water molecules adsorption could be the reduction of some charge spill-out at the perovskite surface by the Pauli repulsion from the electron density of the water molecules. Such "push-back" effect would result in a reduction of the initial surface dipole, and hence, in a decrease of the work function (subsection 2.1.4). In order to assess if this phenomenon actually occurs for perovskite surface, the work function and the VBM of a $MAPbI_{3-x}Cl_x$ perovskite film upon sequential deposition of the saturated hydrocarbon tetratetracontane $C_{44}H_{90}$ (TTC) is monitored. This inert wide energy gap molecule ($E_{G,TTC}$ = 9 eV) can evidence the isolated "push-back" effect due to the sole molecule physisorption without inducing any other mechanisms such as charge transfer or chemisorption [268]. Similarly to the sample in Figure 5.15, a pristine $MAPbI_{3-x}Cl_x$ sample (Figure 5.16) is stored in UHV for several hours, which also results in a work function increase by 0.14 eV that was assigned to the desorption of residual water from the preparation in the glove box during UHV storage. Figure 5.16a shows that the work function of the perovskite surface did not decrease even after deposition of a 2 nm thick TTC layer, and no shift of the VBM is observed in Figure 5.16b either. At a large thickness of 240 Å, the SECO shift during successive measurements in Figure 5.16a and the shift of the whole valence band spectra in the inset of Figure 5.16b illustrate the sample charging due to the thick TTC layer on top. Therefore, the push-back effect is not operative for $MAPbI_{3-x}Cl_x$ perovskite and does not explain the work function decrease upon exposure to low p_{H2O}. A more plausible explanation for this reversible work function decrease shown in Figure 5.15 is the vertical arrangement of water molecules and thus of their dipole moments at the film surface with a net vertical contribution, which induces a ϕ decrease by $\Delta\phi$ as given by the Helmholtz

equation in (2.41) and previously discussed in subsection 2.1.4. Thus, $\Delta\phi$ is proportional to the density of adsorbed dipoles n_{Dip} and to the dipole moment $\mu_{\perp}$ in the direction of the surface normal, implying that the water molecules are, on average, preferentially oriented at the perovskite surface with the negative oxygen end directed towards the perovskite surface.

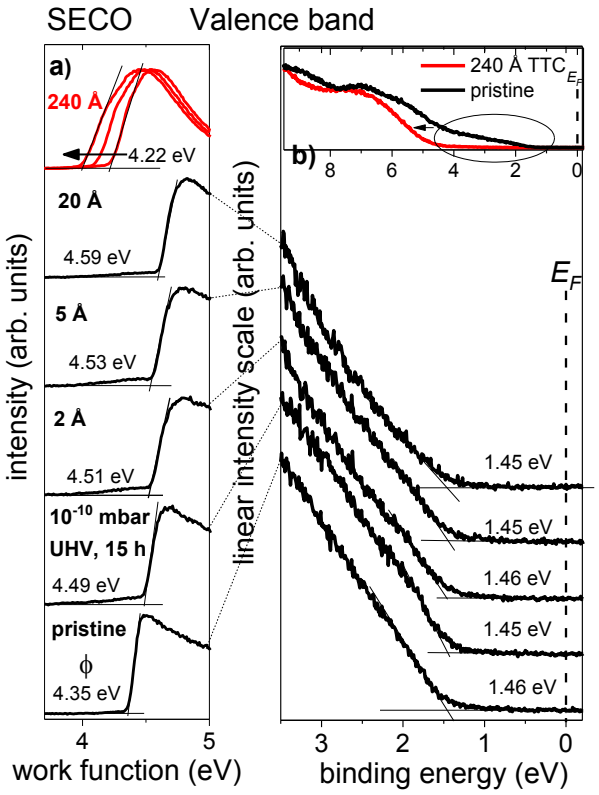

Figure 5.16 UPS spectra of $MAPbI_{3-x}Cl_x$ films upon incremental deposition of TTC layers of different nominal thicknesses. **a)** SECO and **b)** valence band spectra with the respective VBM. The three spectra in the top of a) and the inset in b) show the work function and valence band spectrum shifts at a nominal thickness as large as 240 Å and are due to sample charging at large thicknesses. Reproduced from ref. [267].

Since the $MAPbI_{3-x}Cl_x$ films in this work generally exhibit a fiber texture (*see* the beginning of the present section or previous section 5.1), the preferential orientation of the crystallites along the direction of the substrate normal is propitious for this preferential orientation of the adsorbed water molecules. However, it is noteworthy that the water adsorption on $MAPbI_3$ surface additionally depends on the surface termination and the orientation of the MA cation and the Pb–I bond [164, 269].

Higher water exposure (p_{H2O} = 4 mbar)

The electronic structure of another $MAPbI_{3-x}Cl_x$ perovskite film is monitored upon exposure to higher p_{H2O} = 4 mbar which is comparable to a p_{H2O} in air at 20 °C and at a RH of 17%. After exposure to p_{H2O} of 4 mbar for one hour, the work function of perovskite film decreased by ca. 0.3 eV (Figure 5.17a) and the VBM concomitantly shifted to higher binding energy by

basically the same amount (Figure 5.17a). The shift suggests that the perovskite surface has an even more pronounced n-type character and water acts as a donor.

Like previously proceeded to assess the reversibility of the changes assigned to water, the films were mildly heated at 50 °C for 15 min, which similarly resulted in an increased work function and decreased VBM.

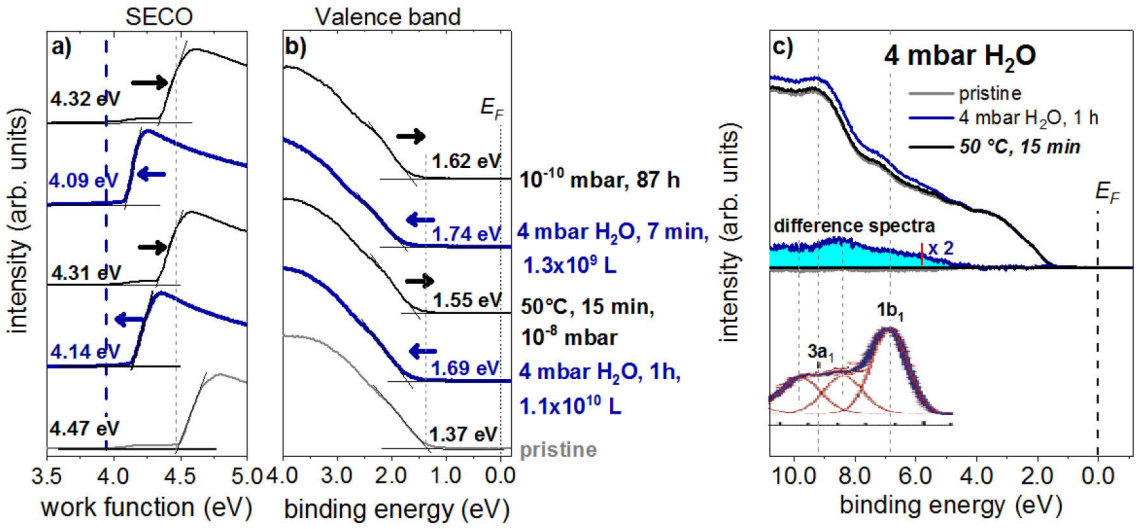

Figure 5.17 UPS spectra of $MAPbI_{3-x}Cl_x$ after alternating H_2O exposure to p_{H2O} = 10^{-6} mbar for different duration – dosage is also given in Langmuir (L) – and subsequent storage or heating in UHV. **a)** SECO and **b)** the corresponding valence band with the respective VBM. **c)** Top: wide binding energy range valence band spectra and difference spectra resulting from the subtraction of the spectrum after heating (*50 °C, 15 min*, black curve), i.e. with assumed less water content, from the spectra before (grey curve) and after (blue curve) water exposure. The valence spectra are shifted to align the VBMs to that after *50 °C, 15 min* heating and normalized to the feature at 3.1 eV which results from Pb and I atomic orbitals for $MAPbI_3$ perovskite. Bottom: valence spectrum of liquid water showing the $1b_1$ and $3a_1$ orbitals, adapted from ref [270]. Reproduced from ref. [267]. The spectrum of liquid water reproduced from ref. [270] is aligned to a common vacuum level as that of perovskite (see text).

Subsequent exposure to p_{H2O} = 4 mbar and storage in UHV for over three days also supported the reversibility of the work function and VBM shifts upon exposure to higher p_{H2O}. The work function and VBM values obtained for the consecutive water exposure and annealing/UHV storage indicate that the changes induced by water is only partially reversible, at least within the time frame chosen here. Note that no shift in the core levels was observed that would indicate a band bending, as deduced for a similarly prepared sample exposed to 5 mbar water for 13 h and shown in Figure C3 (Appendix C). However, a relative increase of the O 1s signal intensity from oxygen at ca. 533 eV is consistent with the presence of molecular water

on the surface (Figure C3, Appendix C). The shift $\Delta\phi$ of the work function here is larger compared to $p_{H2O} = 10^{-6}$ mbar and can be due to the increased density of adsorbed water molecules n_{Dip} [*see* Helmholtz equation in (2.41)] at higher water partial pressure, in analogy to the previously discussed results. However, upon $p_{H2O} = 4$ mbar exposure, in addition a VBM increase by up to 0.33 eV towards higher binding energy values is observed. Interestingly, this shift is consistent with the theoretically estimated 0.3 eV downshift of the VBM with regards to E_F upon hydration of a $MAPbI_3$ surface with a water monolayer. This effect has been assigned to a local band gap widening predicted for PbI_2-terminated surfaces only [164]. Nevertheless, further studies reported that the incorporation of water only slightly (by up to 50 meV), impact the band gap of bulk $MAPbI_3$ [44, 164, 271, 272]. In any case, such band gap widening might contribute partially or entirely to the VBM shift upon $p_{H2O} = 4$ mbar exposure. The parallel shift of both ϕ and VBM also indicates stronger interactions of the water molecules with the perovskite surface than simple physisorption. This shift suggests that the perovskite surface becomes more n-type upon higher p_{H2O} exposure, possibly as a result of the generation of Pb^0 which has been reported to arise along with a shift of the Pb 4f core level to higher binding energy upon exposure to water [46]. Indeed, the generation of this defect species has been suggested to first start with the conversion of $MAPbI_3$ into PbI_2 before the decomposition of this latter into Pb^0 and gaseous I_2 via photolysis [46]. The possible amount of Pb^0 at the surface of the samples investigated here is too low to be detected. Nonetheless, minute amount of Pb^0 has been suggested to be present at the surface of even freshly prepared films, which creates surface states that pin E_F at the conduction band, explaining the pronounced n-type surface character of freshly prepared $MAPbI_3$ films [160, 176]. Following this rationale, the observed reversibility characterized by the film becoming less n-type upon mild annealing would indicate a reduction of the Pb^0 content. Although mildly heating perovskite films in air has been reported to decrease the Pb^0 content due to the reinclusion of lead into the perovskite structure [273], which might be the case here, the partial reversibility deduced from the results in Figure 5.17a-b implies that overall the density of Pb^0-related surface states irreversibly increases.

The results in Figure 5.17a-b are further processed to support the adsorption of water on the perovskite film surface. The difference spectra in Figure 5.17c were obtained by subtracting the properly scaled valence spectrum after annealing in UHV (black curve, less adsorbed water molecules) from the spectra before (gray) and after (blue) exposure to $p_{H2O} = 4$ mbar, as also described in subsection 3.1.2 and in the caption of Figure 5.17c. The difference spectrum

of the sample after p_{H2O} exposure yields a residuum spectrum that can be attributed to adsorbed water. The valence spectrum of pure liquid water is characterized by the 1 b_1 and 3 a_1 valence states at 11.16 and 13.50 eV BE below the vacuum level, respectively [270]. In order to align the valence spectrum of liquid water to a common vacuum level, the work function of the perovskite substrate is taken into account, which places the 1 b_1 and 3 a_1 features at 6.85 and 9.19 eV BE, respectively, with respect to E_F. This is in fairly good agreement with the features observed in the difference spectrum after water exposure in Figure 5.17c (blue). It is notable that the 3 a_1 signal is split and its peak position is an average of two overlapping peaks [270], which originate from the hydrogen-bond interaction between neighboring water molecules in the liquid phase [270, 274]. These water-related features disappear upon annealing, as evidenced by the corresponding difference spectrum (gray) that resembles well the pristine spectrum. Interestingly, a finite DOS in the blue difference spectrum is additionally observable at lower BE (red mark at ≈5.50 eV in Figure 5.17c) and this DOS also vanishes with the water-related features upon heating. This DOS is tentatively attributed to the 1π-orbital of dissociated OH-groups [83, 275]. It is important to stress that complementary methods, such as surface vibrational spectroscopy or metastable impact electron spectroscopy [276], are necessary to unambiguously make such an attribution, which goes beyond the scope of the present investigation. The dissociation of water on solid surfaces is the subject of several studies [83, 277], although this phenomenon has not been explored in the case of HOIPs in particular. And yet the presence of dissociated OH-groups can constitute a degradation pathway for $MAPbI_3$. Ab initio studies on MAI-terminated $MAPbI_3$ surfaces predicted that unlike water molecules that only form hydrogen bonds with the MA cations upon adsorption, hydroxyl radicals can initiate the deprotonation of the MA cation, the resulting formation of CH_3NH_2 molecules and its desorption [278, 279]. This latter step is generally the first step in the degradation of $MAPbI_3$ perovskite. Further studies exploring the mechanisms of water dissociation could be beneficial for a deeper understanding of the impact of water on the degradation of perovskite surfaces.

5.2.3 Effect of Oxygen

The UPS spectra of a $MAPbI_{3-x}Cl_x$ perovskite film before and after exposure to increasing oxygen dosage are shown in Figure 5.18a-b. A gradual work function increase by up to 0.3 eV is observed, accompanied by a gradual VBM shift to lower BE. The magnitude of the shift over time in the present experiment indicates that after 12 h exposure to 50 mbar oxygen, the

effect of oxygen has reached (or has been close to) saturation. In contrary to the case of water exposure, the direction of the shift here indicates that the pristine perovskite surface is less n-type upon exposure to oxygen. Furthermore, the valence spectra did not show any particular difference upon increasing oxygen exposure, as shown by the respective difference spectra in Figure 5.18c that do not exhibit any definite feature.

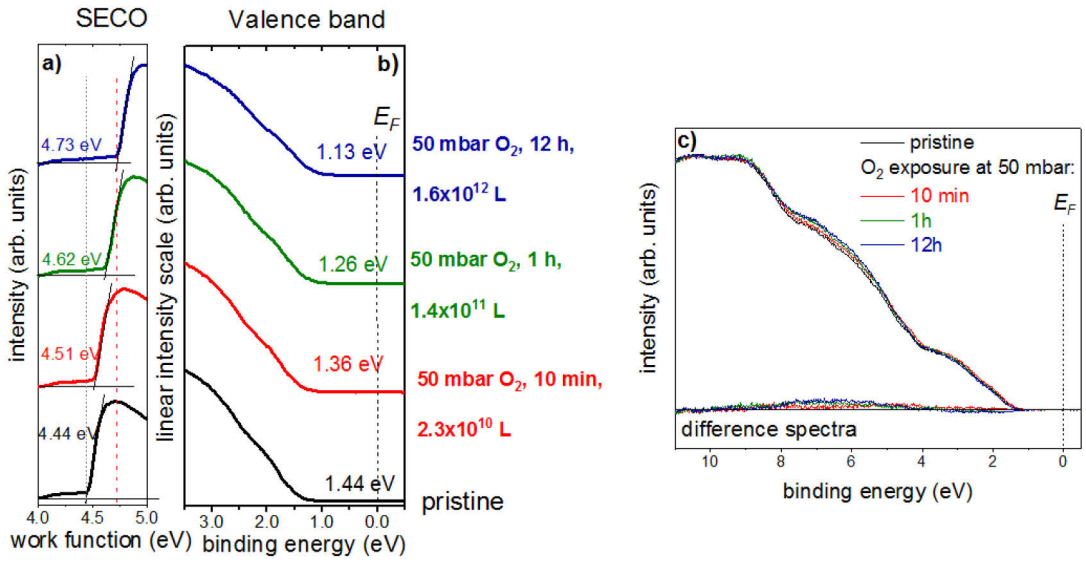

Figure 5.18 UPS spectra of a $MAPbI_{3-x}I_x$ perovskite film before (black curve) and after (red, green, and blue curves) oxygen exposure to 50 mbar for different time – dosage is also given in Langmuir (L). **a)** SECO and **b)** corresponding valence band spectra plotted with the respective VBM. **c)** Wide range valence spectra and difference spectra obtained by subtracting the spectrum after O_2 exposure (black curve) from those after 10 min (red), 1h (green), and 12h (blue) O_2 exposure. The valence spectra were shifted to align the respective VBM to that before exposure. Adapted from ref. [267]

The electronic property change observed here is in line with previous suggestion that oxygen on perovskite films acts as an acceptor. The incorporated oxygen captures electrons that are generated in the perovskite layer upon illumination; thus resulting in the formation of superoxide (O_2^-) species [178]. This superoxide species readily reacts with $MAPbI_3$ by deprotonating the MA cation, thus initiating the degradation of $MAPbI_3$ through the formation of degradation products like PbI_2 [177]. The electronic property change observed can also be assigned to the reduction of Pb^0-related surface states through the oxidation of the elemental lead upon oxygen exposure. Consequently, the n-type surface property is reduced and E_F shifts toward midgap.

5.2.4 Effect of Residual Gas in High Vacuum and Air

After discussing the isolated effect of water and oxygen exposure on perovskite film surfaces, it is now valuable to assess the impact of more realistic environmental conditions on the electronic properties of perovskite surfaces.

High vacuum (10^{-6} mbar)

First, the influence of storage under HV at 10^{-6} mbar on pristine perovskite films is monitored by alternating mild heating and HV storage. The residual gas in the HV essentially consists of water [280, 281] as evidenced by a residual gas analysis (RGA) in a chamber under HV at 10^{-7} mbar (Figure 5.19).

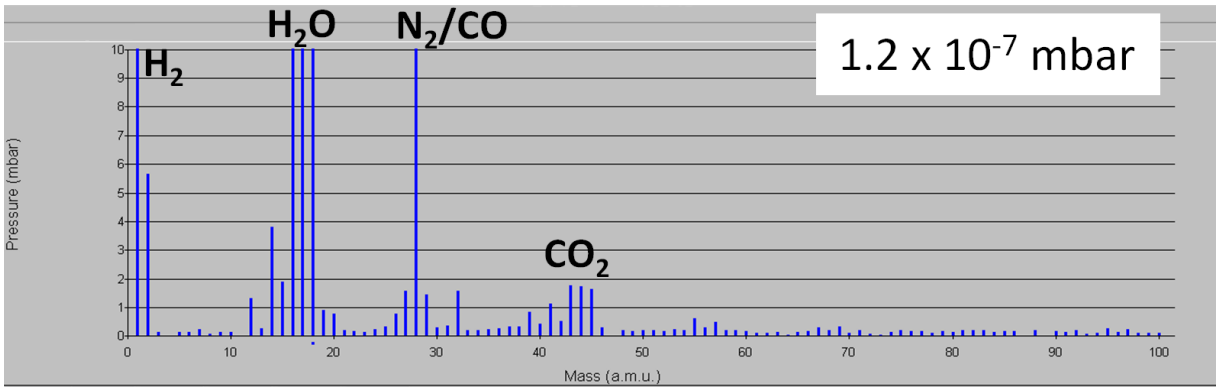

Figure 5.19 Extract of a residual gas analysis (RGA) conducted in a vacuum chamber with a total residual pressure of 1.2×10^{-7} mbar. Data acquired by Raphael Schlesinger (formerly HU Berlin).

After a first measurement (Figure 5.20a-b), the pristine sample is mildly heated in UHV (10^{-8} mbar) at 50 °C for 10 min in order to obtain an initial water-free surface, as suggested by the results of the previous subsection 5.2.2. Accordingly, the work function ϕ increased from 4.22 to 4.35 eV whereas the VBM remained unchanged. Subsequently, after storing the sample in HV for one hour, ϕ decreased again by ca. 0.2 eV without any VBM shift. Further alternation of heating steps and HV storage led to reversible change of ϕ with only minor variations of the VBM (up to 60 meV, see Figure 5.20b).

Subtraction of the scaled valence spectrum of the sample after the second heating step (black curve) from the spectrum after 17 h HV storage (blue curve) in Figure 5.20c yields a difference spectrum that exhibits the same water-related features and the finite DOS around ca. 5.5 eV previously observed after exposure to p_{H2O} = 4 mbar in subsection 5.2.2. These

similar features and the reversible work function change similar to the behavior observed at low p_{H2O} = 10^{-6} mbar in subsection 5.2.2 both point out the presence of water on the perovskite surface already under HV conditions. Therefore, the discussion developed in subsection 5.2.2 also holds here, suggesting that modification of the surface electronic properties due to water-related processes can occur already at moderate and very low levels of water exposure, i.e. at early stages before hydrate species can even be observed.

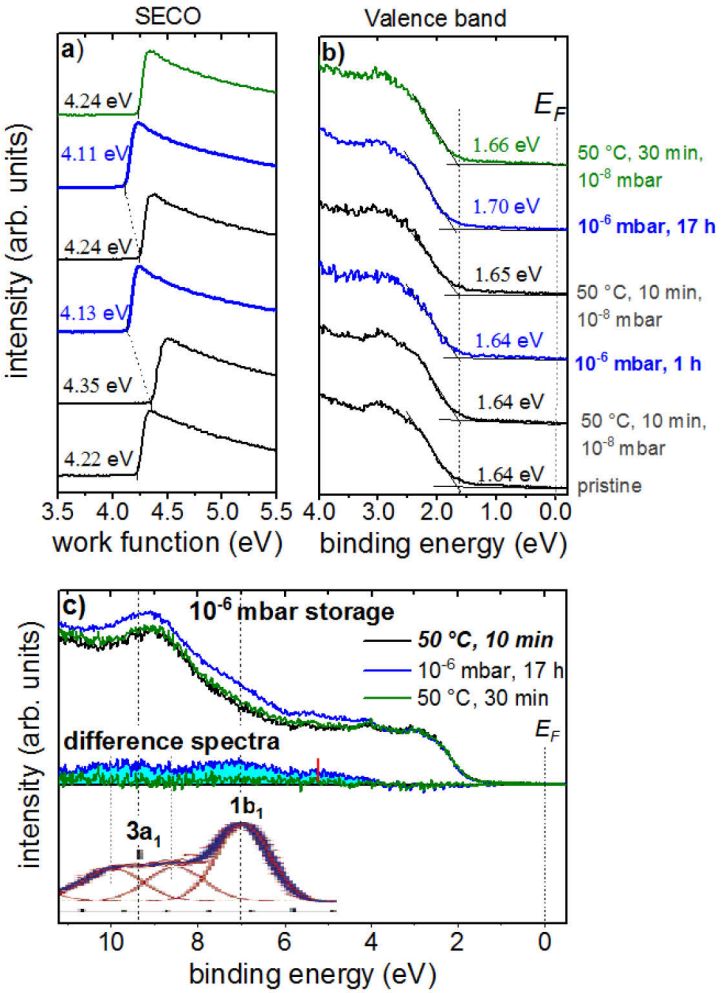

Figure 5.20 UPS spectra of a $MAPbI_{3-x}Cl_x$ perovskite film after alternating storage in the HV at 10^{-6} mbar (blue curves) and heating (black and green curves): **a)** SECO and **b)** the corresponding valence band spectra with the respective VBM. **c)** Wide range valence and difference spectra obtained by subtraction of the spectrum after *10 min, 50 °C* heating (black curve) from the spectra after storage at 10^{-6} mbar (blue curve) and subsequent heating (green curve). Illustration reproduced from ref. [267]. The valence band spectra of liquid water displaying the $1b_1$ and $3a_1$ orbitals is shown in c) for comparison (extracted and adapted with permission from ref. [270]).

Air exposure

Now, the effect of ambient air on another $MAPbI_{3-x}Cl_x$ perovskite sample is evaluated. Ambient air primarily consists of 21% O_2 and 78% N_2; the water partial pressure p_{H2O} contained in ambient air is proportional to the relative humidity RH at a given temperature. In

the present experiment, RH was ≈ 40% (p_{H2O} ≈ 0.9%) at room temperature. The experiment is similar to the preliminary experiment conducted in subsection 5.2.1, except for the shorter exposure time of 15 min[7]. The results in Figure 5.21a-b are also in accordance with the UPS results shown in Figure 5.13.

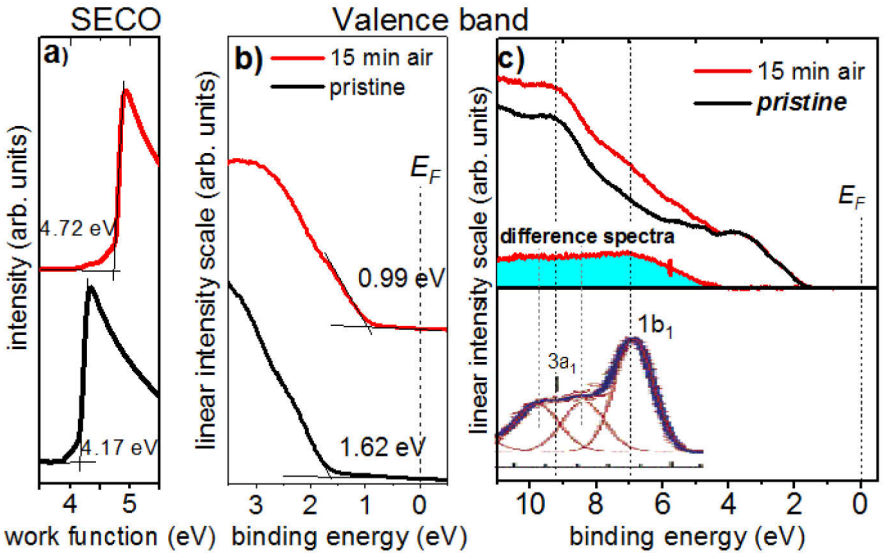

Figure 5.21 UPS spectra of a $MAPbI_{3-x}Cl_x$ perovskite film before (black curve) and after ambient air exposure (red curve): **a)** SECO and **b)** the corresponding valence band spectra. **c)** Wide range valence and difference spectra. The valence spectrum after *15 min air* exposure is shifted to align its VBM to that before air, and then normalized to the feature at 3.1 eV binding energy. Illustration reproduced from ref. [267]. The valence spectrum of liquid water is depicted and shows the $1b_1$ and $3a_1$ orbitals for comparison, adapted with permission from ref. [270].

After air exposure, the sample became less n-type, as evidenced by the concomitant increase of the work function and BE decrease of the VBM by 0.6 eV (Figure 5.21a-b). The observed change follow the same trend observed upon exposure to pure oxygen, thus, points out the dominating effect of oxygen over that of water. This can be explained by the fact that the partial pressure of oxygen in air is higher than that of water. More than half of the BE shift observed here originates from the band bending due to the charge transfer from perovskite to O_2 as deduced from the 0.4 eV BE core level shifts in Figure 5.22. The difference spectrum from the subtraction of the scaled spectra before and after ambient air exposure in Figure 5.21c yields a residuum with weak features still relatable to those of the water valence spectra.

[7] In contrast to the air exposure time of one to two hours due to the KP and PYS measurements between the UPS measurements in subsection 5.2.1.

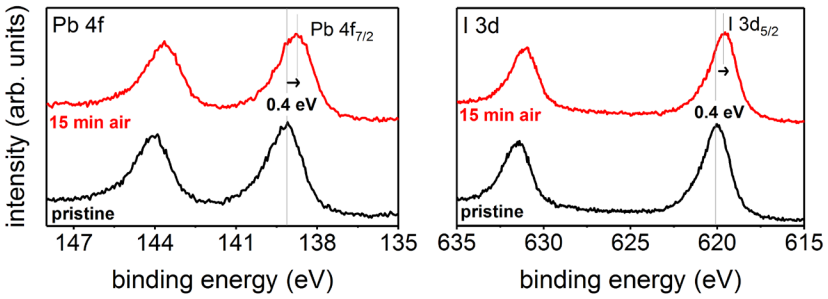

Figure 5.22 XPS spectra of Pb 4f and I 3d core levels of $MAPbI_{3-x}Cl_x$ perovskite film in Figure 5.21 before (black curve) and after ambient air exposure (red curve). Reproduced from ref. [267].

The present work reveals how water, oxygen and air at various levels of exposure impact on the electronic structure of $MAPbI_{3-x}Cl_x$ perovskite film surfaces. Pure water exposure induces concomitant decrease of the work function and shift of the VBM away from E_F, both by 0.3 eV in the above experiments, suggesting that the surface becomes more n-type. In contrast, oxygen exposure results in a work function increase and a parallel VBM shift closer to E_F, thus reducing the initial n-type character of the pristine $MAPbI_{3-x}Cl_x$ perovskite surfaces. This can be attributed to the adsorbed O_2 acting as an acceptor and/or to the reduction of Pb^0 surface states by oxidation. In light of these two distinct trends the effect of ambient air, characterized by E_F almost at midgap position owing to a 0.6 eV energy shift, is dominated by the effect of oxygen. Additionally, low water exposure comparable to water content under high vacuum and inert gas conditions already prompts a work function decrease, indicating that water already adsorbs at these typical conditions for device fabrication. The present work raises awareness of the critical importance of the environment on the electronic properties of perovskite and the need of its control in order to reliably disclose and compare the actual intrinsic properties of perovskite materials. Variations of the electronic properties will necessarily influence the energy level alignment at the interfaces in devices, and consequently impact device performances.

Besides, the discussion in the present work has been extended to the possibility of water dissociation that might precede material degradation and thus affect the material stability. However, it is important to point out the need for more detailed investigations of the water adsorption in order to assess the occurrence of such phenomenon on perovskite surfaces.

5.3 New Materials for Perovskite Solar Cells

The previous sections 5.1 and 5.2 dealt with the investigation of the formation process of mixed halide $MAPbI_{3-x}Cl_x$ perovskite films and the impact of environmental conditions on its electronic structure. In the following subsection 5.3.1, the investigation of a new perovskite material $MA_{1-x}Gua_xPbI_3$ ($0<x<1$) is presented, which is based on a mixture of methyl ammonium (MA) and guanidinium (Gua) cations. The use of this material resulted in solar cells with enhanced stability in comparison to single halide $MAPbI_3$. Subsection 5.3.2 deals with the characterization of the composition and of the electronic properties of titanium disulfide (TiS_2) nanoparticles developed for its first application as a low-cost hole transport material in perovskite-based solar cells. Note that the author's contribution in the results presented in the present section 5.3 mainly consists of the PES measurements and analysis.

5.3.1 Mixed Methyl Ammonium Guanidinium Lead Iodide Perovskite

The versatility of HOIPs has been pointed out in section 2.2; particularly, their structural and optoelectronic properties can be tuned by combining different cations and/or halides. In the present work, perovskite films obtained from the combination of the organic cation guanidinium ($[C(NH_2)_3]^+$, Gua) with the organic cation methyl ammonium ($CH_3NH_3^+$, MA) in lead iodide-based perovskite are investigated. The results shown here are part of a published article [243], but with an extended interpretation of the PES data.

One peculiarity of Gua is its large ionic radius of ~278 pm [282], which is slightly above the upper limit of the tolerance factor (t ~1.03) defined in equation (2.44). As a result, Gua forms low-dimensional perovskites when mixed with PbI_2 [283, 284]. Here, perovskite films, referred to as $MA_{1-x}Gua_xPbI_3$, with different relative percentages of Gua cation ($0 < x < 1$, x corresponds to the Gua percentage in decimal form) are characterized by PES in order to assess the chemical environments of the different constituents and to monitor the electronic properties of the perovskite films upon addition of different Gua amounts. In combination with additional methods, the results suggest that for $x < 0.25$, the Gua cation is inserted into the crystal unit, forming a 3D perovskite with improved thermal and environmental stability in comparison to the single cation $MAPbI_3$ perovskite. This is supported by the highly efficient solar cells (PCE over 19%) with enhanced stability obtained from this mixed cations-approach.

Composition and structure of mixed cations $MA_{1-x}Gua_xPbI_3$ perovskite films

Since the approach developed in the scope of this work is based on the variation of the relative ratio of two cations, it is essential to assess the actual composition of the $MA_{1-x}Gua_xPbI_3$ films obtained with different relative Gua content x ($0 \leq x \leq 1$). It is to be noted that the Gua/MA ratio x/1-x first refers to the materials stoichiometry in the precursor solution (see subsection 4.1.2). In order to determine whether this stoichiometry is preserved in the films and to assess the chemical environment of the different elements constituting the materials, X-ray photoelectron spectroscopy (XPS) measurements (Figure 5.23) were carried out on $MA_{1-x}Gua_xPbI_3$ films with increasing Gua content from x=0 (i.e. 0%, $MAPbI_3$ only) to x=1 (i.e. 100%, $GuaPbI_3$ only). In order to compare the XPS data of the different samples, the XPS core level spectra were referenced to the C 1s carbon at 285 eV detected for all samples.

All the XPS spectra of the N 1s core levels shown in Figure 5.23a for different Gua percentages can be fitted with two peaks, except for $MAPbI_3$ (x=0) and $GuaPbI_3$ (x=1), which exhibit only one peak each, centered at 402.3 eV and 400.3 eV, respectively. These peaks can be assigned to the NH_3^+ group in MA ($CH_3NH_3^+$), and to the NH_2^+ group in Gua ($[C(NH_2)_3]^+$) [285]. It is noteworthy that in the former case the positive charge is localized on one N atom, whereas in the latter case the positive charge is delocalized across the molecule, i.e. distributed between the three N atoms, which results in the characteristic resonance structure of guanidinium cations [286, 287]. Therefore, the fraction of positive charge on each N atom in Gua is lower in comparison to MA, and the N 1s peak in Gua shifts accordingly to lower binding energies [285]. Based on the literature [285], and on the reference measurements on the pure $MAPbI_3$ and $GuaPbI_3$ films in Figure 5.23a, the two contributions in the N 1s spectra observed for the other samples ($0 < x < 1$) in Figure 5.23a can be assigned to MA and Gua. Note that the respective peak does not exhibit any significant binding energy shift between the different samples. Indeed, only a slight variation below 100 meV in the peak position was observed for Gua, and no shift was noticed for MA (see vertical dotted lines in Figure 5.23a). This indicates that the same nitrogen species are present in all samples. Clearly, the relative intensity of the two N 1s peaks gradually changes with the increasing Gua percentage. The analysis of the respective peak area in Figure 5.23a confirmed the preservation of the initial Gua percentage, i.e. of the Gua/MA ratio, within the final structure. This is illustrated by the linear correlation of the relative Gua ratios determined experimentally (Gua_R) and theoretically (Gua_T), i.e. based on the initial stoichiometry of the materials in the precursor solution (see inset in Figure 5.23a).

The Pb 4f spectra with the doublets Pb $4f_{5/2}$ and Pb $4f_{7/2}$, as well as the I 3d with the doublets I $3d_{3/2}$ and I $3d_{5/2}$ are shown in Figure 5.23a and Figure 5.23b, respectively. All the samples exhibit one main Pb $4f_{7/2}$ peak centered at 138.5 eV, which corresponds to Pb^{2+}, as well as only one I $3d_{5/2}$ peak centered at 619.4 eV, in agreement with values previously reported in literature for perovskites [285, 288], therefore confirming the formation of Pb-I bonds. The Pb/I ratio is also fairly comparable (with only ca. 5% variation) from sample to sample as deduced from the fits in Figure 5.23b-c.

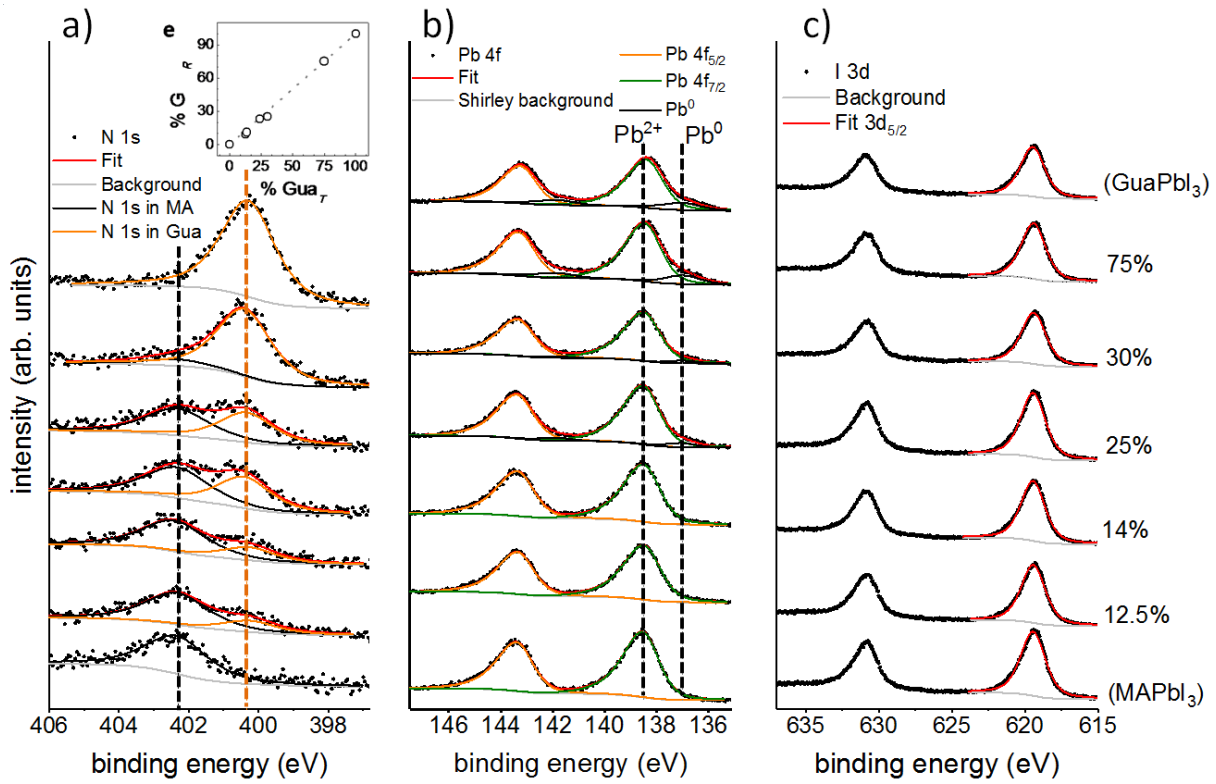

Figure 5.23 XPS spectra of **a)** N 1s, **b)** Pb 4f, and **c)** I 3d core levels for $MA_{1-x}Gua_xPbI_3$ films with different percentages of Gua (x:1-x represents the Gua:MA ratio where x is the percentage in decimal form). In a), vertical dotted lines differentiate the N 1s peaks corresponding to the NH_3^+ group in MA (black line) and to the NH_2^+ group in Gua (orange line) at high and lower binding energy, respectively. The **inset** in a) depicts the quantification of the relative percentage of Gua, where Gua_R corresponds to the experimental values obtained from the N 1s XPS results and Gua_T corresponds to the theoretical values, i.e. the initial stoichiometry of the materials in the precursor solution. b) The doublets Pb $4f_{5/2}$ and Pb $4f_{7/2}$ of the Pb 4f spectra were fitted with two separate peaks (orange, and green curves, respectively). Vertical dotted lines differentiate the Pb species corresponding to Pb^{2+} in perovskite and Pb^0 corresponding to traces of reduced lead detected in some of the samples. c) Doublets corresponding to I $3d_{3/2}$ and I $3d_{5/2}$; the red curves are the fits applied to I $3d_{5/2}$ only. Illustration based on data in ref. [243]

The Pb 4f spectra additionally reveal traces of reduced lead Pb^0, as deduced from the Pb $4f_{7/2}$ peaks at lower binding energies. As already mentioned in the previous section 5.2, Pb^0 defects are reported to affect the electronic property of the perovskite surface [160, 289], as is also the case in the UPS analysis here (*vide infra*).

The preservation of the Gua/MA ratio in the film as confirmed by XPS is particularly indispensable for the interpretation of the XRD data acquired by Gustavo de Miguel (Universidad de Córdoba) in Figure 5.24a-c. Indeed, it primarily indicates that no new amine-derivatives have formed, that both Gua and MA cations are present in the film, and that they are possibly embedded in the existing crystal structure. Importantly, the XRD data indicate that with increasing Gua content up to x=0.25, the MA in the perovskite unit cell is gradually substituted by Gua. This is supported by the overall gradual decrease in the intensity of the reflection peaks corresponding to $MAPbI_3$ in Figure 5.24a, as well as by the gradual shift and broadening of the diffraction peaks corresponding to the (110) and (220) lattice planes for the other $MA_{1-x}Gua_xPbI_3$ perovskite films with $x \leq 0.5$ in Figure 5.24b.

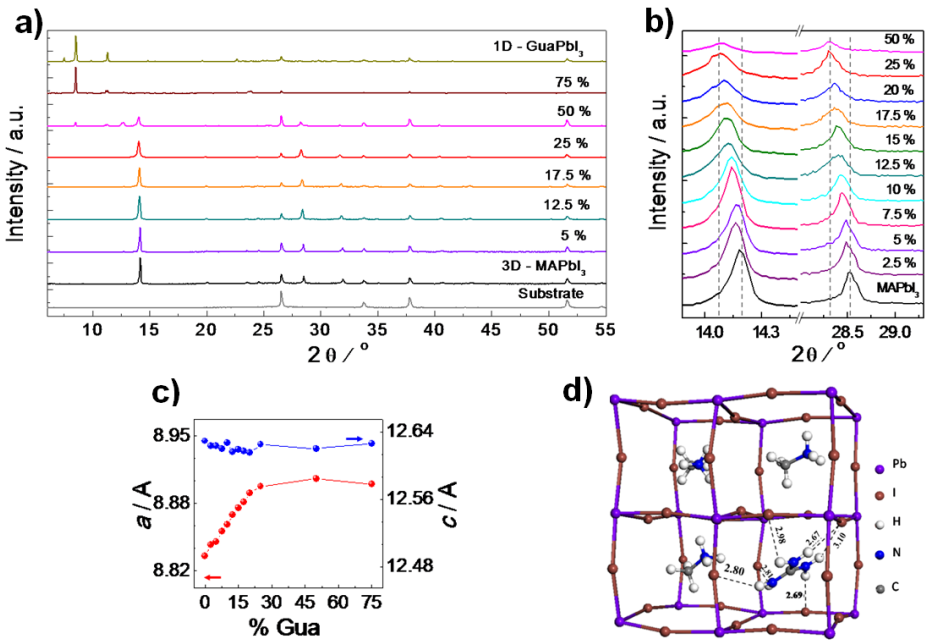

Figure 5.24 a) Normalized XRD data for mixed $MA_{1-x}Gua_xPbI_3$ perovskite films with different percentages of Gua (x:1-x represents the Gua:MA ratio where x is the percentage in decimal form). **b)** Magnification of the XRD peaks in a) for (110) (left) and (220) (right) for several $MA_{1-x}Gua_xPbI_3$ perovskite films with $x \leq 0.5$. **c)** Variation of the lattice parameters *a* and *c* of the $MA_{1-x}Gua_xPbI_3$ unit cell with increasing Gua percentage, obtained from the crystallographic analysis of the experimental XRD data. **d)** Optimized simulated structure of the unit cell of $MA_{0.75}Gua_{0.25}PbI_3$ with the six H-bond distances relative to I atoms. All XRD-data and figures are from Gustavo de Miguel (Universidad de Córdoba) and all figures are reproduced with permission from ref. [243].

The peaks shift is likely related to the expansion of the unit cell while accommodating the large Gua and is similar to shifts observed upon sequential substitution of formamidinium (FA) cations with Cs in $FAPbI_3$ [290], or in the case of $MA_xEA_{1-x}PbBr_3$ perovskite (EA=ethylammonium) [291]. The cell expansion is corroborated by the progressive increase of the value of the lattice parameter *a* from 8.838 Å to 8.902 Å for $x \leq 0.25$, whereas the *c* value remained constant at 12.625 Å for all Gua percentages (Figure 5.24c). For higher Gua content ($x>0.25$), the value of *a* is constant. Moreover, for $x>0.25$ the diffraction signal corresponding to $MA_{1-x}Gua_xPbI_3$ decreases significantly and new diffraction peaks at 8.54° and 11.31° 2θ angles appear, both indicating the formation of 1D $GuaPbI_3$ phase [285]. These observations imply that at Gua percentage higher than 25%, Gua cations are no longer incorporated into the crystalline network and form phase-separated 1D $GuaPbI_3$. It is noteworthy that these observations are in contradiction to previous work, which suggested that Gua would only act as a passivating agent and is not incorporated into the perovskite structure due to its larger size [292]. A recent structural characterization of perovskites based on guanidinium and methyl ammonium cations, with the general formula $(C(NH_2)_3)$-$(CH_3NH_3)_nPb_nI_{3n+1}$ (n = 1, 2, 3), also suggested the formation of 2D perovskites with alternating Gua and MA cations in the interlayer space [293]. However, significant variations in the preparation method could explain variations in the crystallization dynamics. In the present work, different percentages of Gua were incorporated within the precursor solution and were preserved during crystallization, as assessed by the XPS data (inset, Figure 5.23a).

At this point the formation enthalpies of $MA_{1-x}Gua_xPbI_3$ shall be briefly discussed, which were calculated by Luis Camacho (Universidad de Córdoba) based on density functional theory (DFT) in order to evaluate the stability of the $MA_{1-x}Gua_xPbI_3$ structures. The DFT calculations confirm that the formation enthalpy becomes highly negative with the incorporation of Gua, hence pointing out the enhanced stability of the $MA_{1-x}Gua_xPbI_3$ systems with $x>0$.[243, 294] This is in contrast to the pure $MAPbI_3$ ($x=0$), which features a value close to zero, in line with other literature values.[295, 296] Moreover, the formation of the 3D $MA_{0.75}Gu_{0.25}PbI_3$ perovskite appears to be thermodynamically favored in comparison to its phase separation into pure $MAPbI_3$ or $GuaPbI_3$ (detailed discussion about the thermodynamics of formation can be found in ref. [243] and in its supplementary information). However, at larger $x \geq 0.25$, both $MA_{0.75}Gu_{0.25}PbI_3$ and $GuaPbI_3$ crystalline phases appear because the 3D octahedral $[PbI_6]$ network cannot accommodate additional Gua cations. The optimized unit cell for $MA_{0.75}Gu_{0.25}PbI_3$ is presented in Figure 5.24d, in which

the main H-I interactions with the Gua cation are depicted. It is important to stress that the formation of hydrogen bonds is essential for the structural stabilization. In comparison to the 1-2 H bonds per MA molecule in pure $MAPbI_3$, the insertion of Gua implies six H bonds while reducing the H-I distance, which appears to be the cause for the superior $MA_{0.75}Gu_{0.25}PbI_3$ stability.

Electronic properties of $MA_{1-x}Gua_xPbI_3$ perovskite films

To gain further insight into the electronic properties of the different $MA_{1-x}Gua_xPbI_3$ perovskite films, UPS measurements were performed and the corresponding results are shown in Figure 5.25. Before discussing the UPS results, it has to be noted beforehand that for x<0.2 a tiny (below 0.02 eV) but continuous band gap widening with increasing Gua content was deduced from the optical and photoluminescence (PL) spectroscopies data, whereas for x>0.2 the band gap widening is more apparent (Figure D1 and Figure D2, Appendix D).

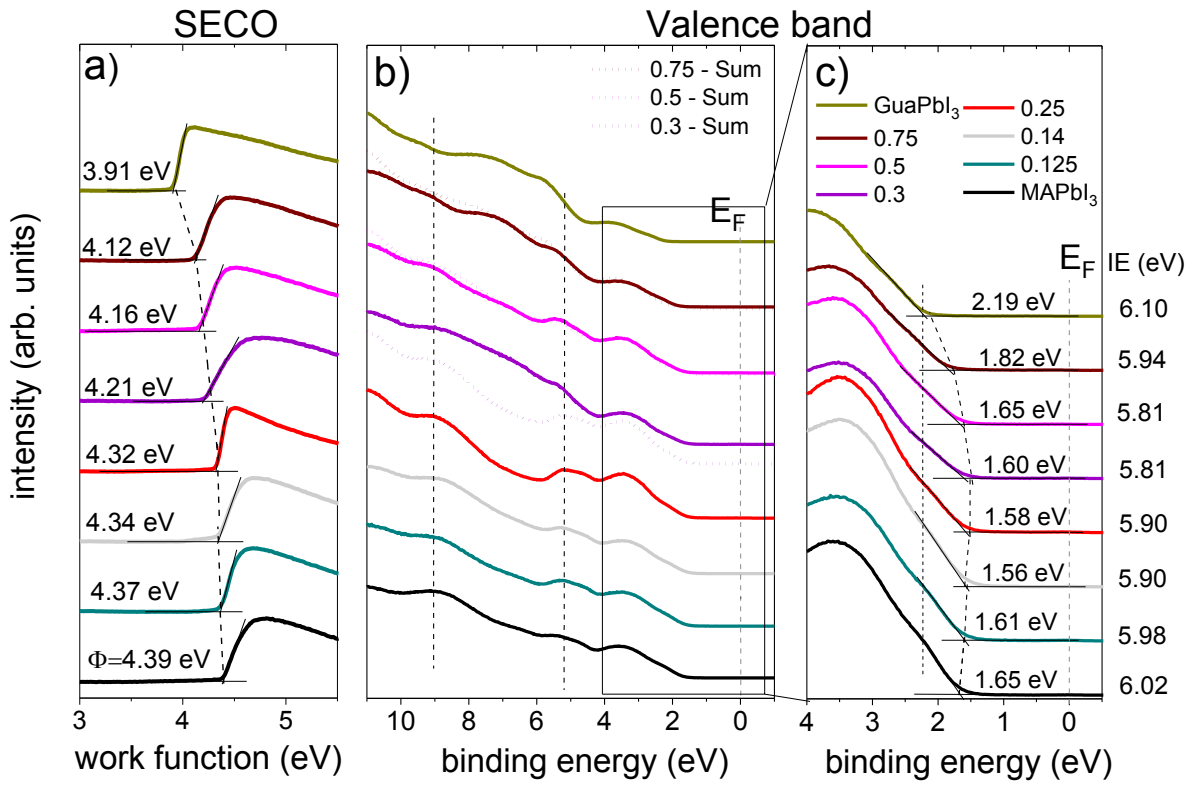

Figure 5.25 a-c) UPS spectra of $MA_{1-x}Gua_xPbI_3$ films with different percentages of Gua (x:1-x represents the Gua:MA ratio where x is the percentage in decimal form) with: **a)** SECO and **b)** wide, and **c)** narrow binding energy range valence spectra of the different samples. a-c) are illustration reproduced from the data in ref. [243]. The dotted curves in b) are spectra obtained by the simple sum of the weighted contributions from $MA_{0.75}Gu_{0.25}PbI_3$ spectrum (red) and the $GuaPbI_3$ spectrum (dark yellow) for x>0.25. Illustration adapted with permission from ref. [243].

The SECO spectra in Figure 5.25a show a gradual decrease of the work function ϕ with increasing Gua percentage. The ϕ values obtained in Figure 5.25a, and the VBM values determined from the narrow range valence band spectra in Figure 5.25c reveal a slight reduction of the ionization energy (IE=ϕ+VBM) by up to 0.14 eV for increasing Gua content up to x=0.25. Additionally, a small variation (within 0.1 eV) of the valence band maximum for $x \leq 0.25$ (Figure 5.25c) is observed, which can be associated with the variation in the density of surface states due to varying Pb^0 content assessed from the XPS data in Figure 5.23b. As already discussed in section 5.2 and subsection 2.2.3, even inconspicuous amount of Pb^0 induces surface states which pin E_F close to the conduction band, thus explaining the characteristic n-type of perovskite surfaces [160, 176]. This can also explain the n-type property observed here. Particularly, at larger Gua content, the number of Pb^0-related surface states distinctly increased (Figure 5.23b). The density of Pb^0 of the samples here is of 10 atom% for pure $GuaPbI_3$, below 5 atom% for the mixed cations perovskites with $x \geq 0.25$, and below 0.5 atom% for $MAPbI_3$ and for mixed cations perovskites with low x ($x < 0.25$), as derived from the XPS spectra in Figure 5.23b. For x>0.25 the VBM in Figure 5.25 shifts to higher binding energy with increasing x, concomitantly with the band gap widening indicated by the optical data (Figure D1, and Figure D2 in Appendix D). This implies that in all cases the Fermi level is close to the conduction band and is likely pinned there. For instance, $GuaPbI_3$ has an optical band gap of ca. 2.5 eV and exhibits a VBM at 2.2 eV below the Fermi level, which suggests a pronounced n-type property.

Importantly, while the valence band spectra in Figure 5.25c retain the valence band features of $MAPbI_3$ up to x = 0.25, the valence band features distinctly change at larger Gua content and gradually resemble those corresponding to pure $GuaPbI_3$. The co-existence of $MA_{0.75}Gu_{0.25}PbI_3$ and $GuaPbI_3$ for x>0.25 is supported by the spectra obtained by simple additive re-composition of the weighted contributions from $MA_{0.75}Gu_{0.25}PbI_3$ and $GuaPbI_3$ spectra, as shown by the dotted curves in Figure 5.25b. Indeed, except for x=0.30, these spectra obtained by summation fairly resemble those of the measured samples. Interestingly, most of the changes in the valence band features occur in the binding energy region between 5.5 eV and 8.7 eV. This would be consistent with the suggestion that the states which originate from the organic cation in HOIP typically lie deeper in the valence band with respect to the Fermi level (see also subsection 2.2.2), whereas the frontier edges are generally associated with contributions from Pb and I [119, 150]. In accordance with these observations, the valence band edge of $MA_{1-x}Gua_xPbI_3$ is dominated by the states which originate from the

Pb and I atomic orbitals, as derived from DFT calculations performed by Luis Camacho (Universidad de Córdoba) and shown in Figure 5.26.

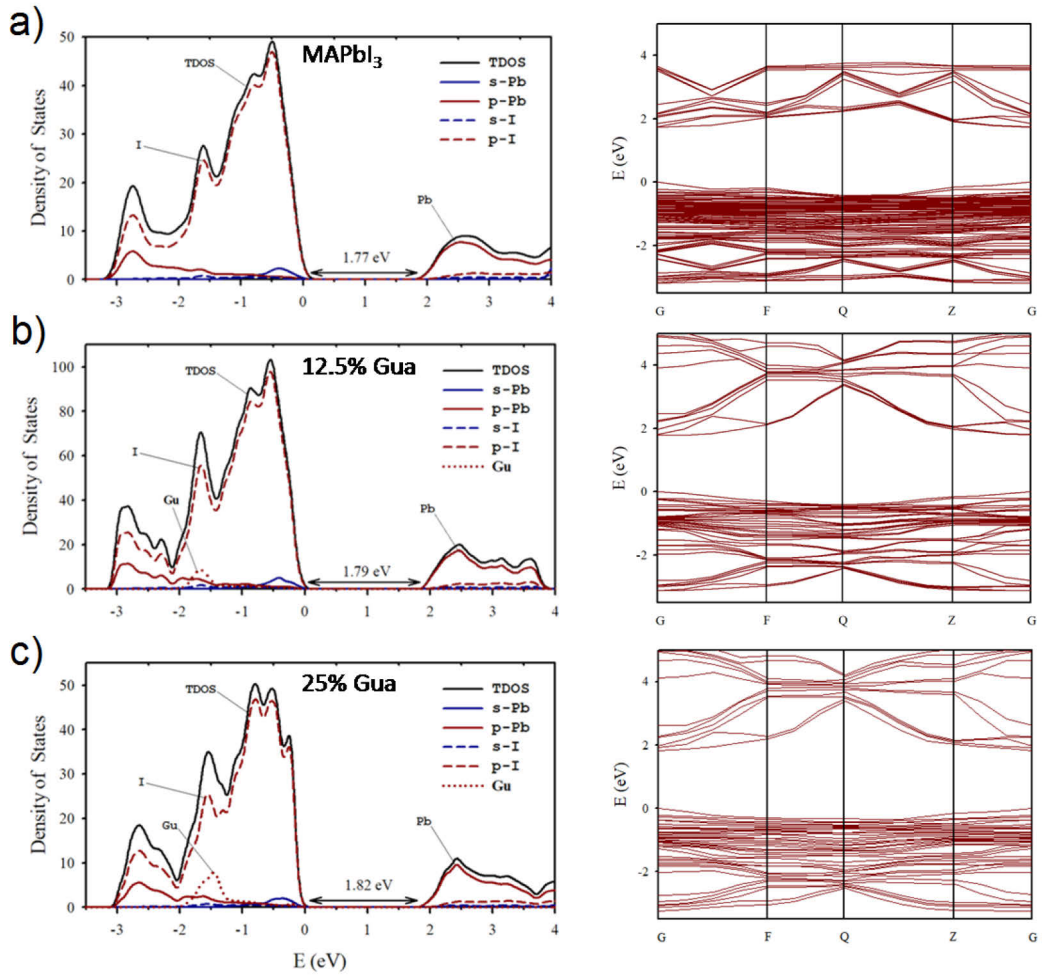

Figure 5.26 Calculated density of states (left) and electronic band structure (right) of **a)** pure $MAPbI_3$, **b)** mixed $MA_{0.875}Gua_{0.125}PbI_3$, and **c)** mixed $MA_{0.75}Gua_{0.25}PbI_3$. Left: the total density of states (solid black line), as well as the calculated separate contribution from the Pb 6s states (s-Pb, blue solid line), the Pb 6p states (p-Pb, red solid line), the I 5s states (s-I, blue dashed line), the I 5p (p-I, red dashed line), and from Gua (red dotted line) are shown. Theoretical calculations from Luis Camacho (Universidad de Córdoba), reproduced with permission from ref. [243].

The calculated electronic band structures and density of states of $MAPbI_3$ (x = 0) and two other representative mixtures (x = 0.125, and x = 0.25) do not exhibit any relevant differences; the top valence band and the bottom conduction band are dominated by the contribution from the I 5p and Pb 6p states, respectively (Figure 5.26), as also described in subsection 2.2.2 and in ref. [119]. Nevertheless, a small but gradual band gap energy increase with the Gua insertion is observed, yielding values of 1.77 eV, 1.79 eV, and 1.82 eV

for x = 0 ($MAPbI_3$), x = 0.125, and x = 0.25, respectively. This is attributed to the effect of lattice expansion. The two mixtures conserve the direct band gap at the Γ symmetry point of $MAPbI_3$ and all three systems display similar dispersion of the valence and conduction bands, which ensures low carrier effective masses [243].

The coexistence of pure $GuaPbI_3$ with the mixed $MA_{0.75}Gua_{0.25}PbI_3$ phase for x>0.25 suggested by the UPS data is corroborated by scanning electron microscopy (SEM) measurements performed by Cristina Roldán-Carmona (EPFL Sion). The SEM images in Figure 5.27a-d and Figure D3 in Appendix D show that with increasing Gua content up to 0.25, the $MA_{1-x}Gua_xPbI_3$ morphology is characterized by micrometer-large crystal domains with increasing size. In contrast, for x>0.25 elongated rod-like morphology is also discernable, which is characteristic of 1D $GuaPbI_3$ (Figure 5.27d). This is associated with the occurrence of a phase segregation between regions with the 3D $MA_{0.75}Gua_{0.25}PbI_3$ phase and regions with the 1D $GuaPbI_3$ phase for x>0.25.

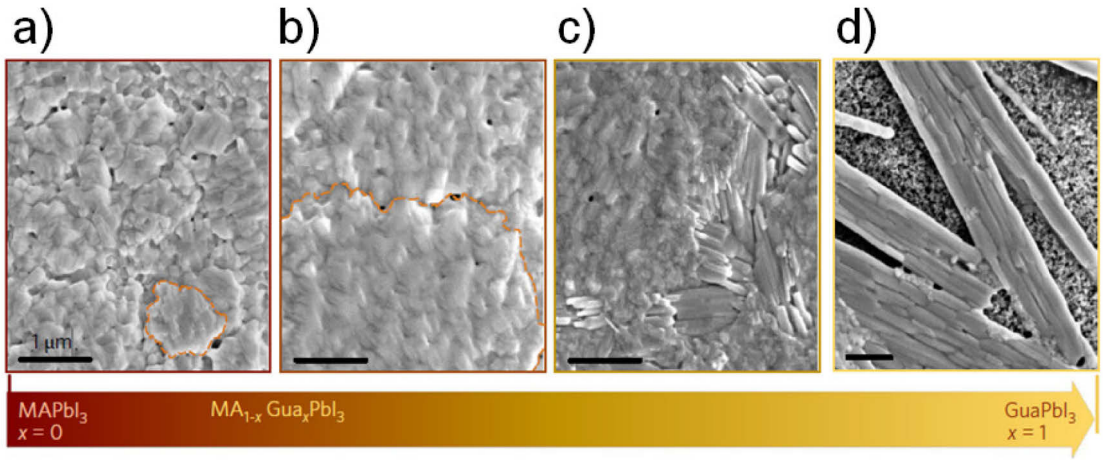

Figure 5.27 a-d) SEM images of four representative samples: **a)** $MAPbI_3$, $MA_{1-x}Gua_xPbI_3$ with **b)** x = 0.14, **c)** x = 0.30, and **d)** $GuaPbI_3$. Scale bars correspond to 1 µm. Orange lines delimit the crystal domains. SEM measurements by Cristina Roldán-Carmona (EPFL Sion), adapted and reproduced with permission from ref. [243].

The phase segregation at x>0.25 is further supported by micro-PL and micro-Raman measurements (Figure D4a and Figure D4b in Appendix D, respectively), done by Giulia Grancini (EPFL Sion). The results suggest a spatial distribution of the band gap over microscopic sample areas and a correlated position-dependent variation in the Raman spectra,

both related to a change of composition [297], more specifically, to the formation of low-dimensional perovskite, as for the pure 1D $GuaPbI_3$ [243, 298].

Solar cells with the FTO/b-TiO_2/mp-TiO_2/perovskite/Spiro-OMeTAD/Au architecture (Figure 5.28a) have been fabricated and characterized by Alexander D. Jodlowski (EPFL Sion and Universidad de Córdoba) based on the $MA_{1-x}Gua_xPbI_3$ perovskite film with x≤0.25, i.e. before the aforementioned phase segregation occurs. The average photovoltaic parameters are briefly summarized in Figure 5.28b. The short-circuit current density J_{sc} and the fill factor FF does not change with the incorporation of Gua content up to x = 0.14, whereas the open-circuit voltage V_{oc} increases progressively, which can be associated with the optical band gap widening.

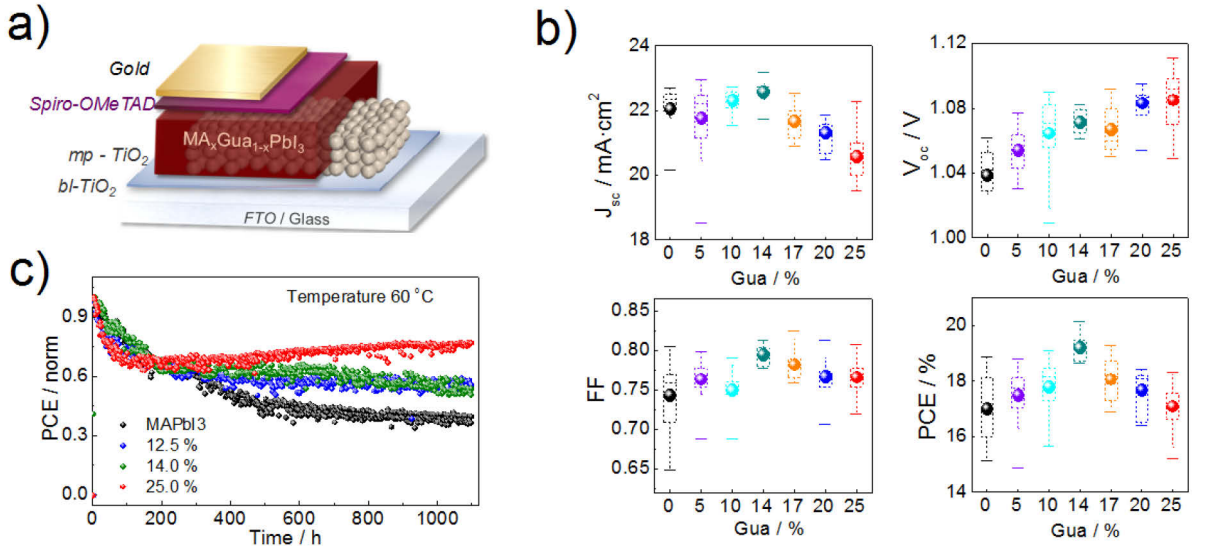

Figure 5.28 a) Device architecture of the perovskite solar cells integrating $MA_{1-x}Gua_xPbI_3$ perovskite films (Glass/FTO/bl-TiO_2/mp-TiO_2/Perovskite/Spiro-OMeTAD/Au). **b)** Clockwise: Plots of J_{sc}, V_{oc}, PCE, and FF of $MA_{1-x}Gua_xPbI_3$ perovskite-based devices with increasing x up to 0.25 (25%). The data shown are averaged values from more than 191 devices. **c)** Thermal stability test for $MA_{1-x}Gua_xPbI_3$ perovskite-based solar cells with x=0, 0.125, 0.15, 0.25 at 60 °C under continuous illumination and MPP tracking under Argon atmosphere. The initial PCE of the respective cells are 18.77%, 18.97%, 18.11%, and 17.14%. Solar cell characterizations by Alexander D. Jodlowski and corresponding figures adapted from ref. [243].

As a result, solar cells with a PCE = (19.2±0.4)% are obtained for x = 0.14. It is noteworthy that the IE values of the $MA_{1-x}Gua_xPbI_3$ films with x≤0.25 are higher than 5.90 eV. Considering the 5 eV IE of spiro-OMeTAD [299, 300], the IEs yield an optimal relative positioning of the respective perovskite VBM for hole extraction towards the spiro-OMeTAD

layer. To assess the device stability, a test under continuous AM1.5 G Sun illumination at maximum power point (MPP) tracking at 60 °C and under an Ar atmosphere for more than 1,000 hours was conducted. In comparison to devices based on pure $MAPbI_3$, those obtained with mixed $MA_{1-x}Gua_xPbI_3$ perovskites of different x exhibit enhanced stability, as evidenced in Figure 5.28c. After an initial decrease, that has been associated with the inter-penetration of spiro-OMeTAD and the gold electrode [301], the performance gradually stabilizes and recuperates, which correlated with Gua incorporation.

In conclusion, a new $MA_{1-x}Gua_xPbI_3$ perovskite composition consisting of a combination of Gua and MA cations has been presented. With the support of additional techniques, PES and XRD analysis suggested that the incorporation of Gua content up to x = 0.25 leads to the formation of a highly stable 3D crystalline structure, likely mediated by the increased number of H bonds within the inorganic framework, in comparison to the state-of-the-art $MAPbI_3$. As a result, solar cells based on such composition exhibit enhanced device stability and photovoltaic performance in comparison to $MAPbI_3$, with a high PCE exceeding 20% for a Gua content x = 0.14. These results further underline the versatility of HOIPs and motivate the exploration of organic cations with sizes at/beyond the limit of the tolerance factor.

5.3.2 Titanium Disulphide TiS_2 as Hole Transport Material

The work presented in the present subsection are based on results published in ref. [244]. As previously described in section 2.3, perovskite-based solar cells (PSC) consist of several layers where the perovskite layer is generally sandwiched between an electron- [302] and a hole-transport layer [303, 304] (ETL and HTL, respectively). Organic materials such as octakis(4-methoxyphenyl)-9,9′-spirobi[9H-fluorene]-2,2′,7,7′-tetramine (Spiro-OMeTAD) or poly[bis(4-phenyl)(2,4,6-trimethylphenyl)amine (PTAA) are among the most common HTLs employed in the highest efficiency solar cells. [305] However, the implementation of both materials in solar cells hinders the low-cost commercialization and durable application of the latter due to the expensive purification processes of both organic materials [306], and their poor long-term stability.[307] Alternatively, inorganic p-type semiconductors such as CuSCN,[308] CuI,[309, 310] NiO,[311] Cu_xO [312], and FeS_2 [313, 314] have been employed due to their low-cost and ease of synthesis, their stability, and high carrier mobility. Still, the number of candidates is restricted by the difficulty in meeting criteria such as high electrical conductivity, appropriate energy level matching, and structure stability in one

material. The choice is further limited by the array of applicable deposition methods since the deposition of these inorganic materials often requires: first, solvents, such as di-n-propylsulfide for CuSCN and CuI, that can partially degrade the perovskite layer (see also subsection 5.4.1) or second, high-temperature treatments that hinder their application in PSC, and yet also increase their fabrication costs. Therefore, the design of a new low-cost, stable, and efficient material as HTL is imperative to fully exploit the potential of PSCs.
In the present subsection, results from the characterization of novel TiS_2 nanoparticles as an efficient and low-cost HTL in PSCs are presented. TiS_2 is an earth abundant material that is mostly known for its application as an electrode in lithium-ion batteries [315] and hydrogen-production catalysis [316]. Considering its good electrical conductivity ($\approx 10^3\ \Omega^{-1}\ cm^{-1}$)[317] and an ionization energy of 5.46 eV [318], TiS_2 represents a potential candidate as an HTL in PSCs. In the following, the implementation of the synthesized TiS_2 nanoparticles as a HTL in devices bearing the structure FTO/c-TiO_2/m-TiO_2/$(FAPbI_3)_{0.85}(MAPbBr_3)_{0.15}$/$TiS_2$ is described. Here, the glass substrate is coated with the fluorine-doped tin oxide (FTO) electrode, titanium dioxide TiO_2 acts as a scaffold and ETL. Methyl ammonium (MA)-formamidinium (FA) mixed perovskite $(FAPbI_3)_{0.85}(MAPbBr_3)_{0.15}$ is used as absorber material, and TiS_2 is spin-coated on top. These HOIP-based solar cells yield a high PCE above 13.5%. PES analysis provides information about the chemical species formed upon material synthesis, and describes the electronic properties and the energy levels of the new material.

Upon spin-coating of the TiS_2 dispersion on transparent FTO pre-covered substrates, the originally black dispersion results in a thin film with high transparency. Three main transitions at ≈480, ≈550, and ≈620 nm can be derived from the transmittance spectrum of TiS_2 in Figure 5.29a, as acquired by Saba Gharibzadeh (Tarbiat Modares University, Theran), which possibly indicate the existence of different nanoparticle size regimes [319]. The onset of the absorption spectrum in the inset in Figure 5.29a yields an optical band gap E_g of about 1.8 eV. Powder X-ray diffraction (XRD) measurements performed by Saba Gharibzadeh (Tarbiat Modares University, Theran) and Aron Huckaba (EPFL Sion) and shown in Figure 5.29b reveal that the nanoparticles are amorphous, as also previously reported [320]. Scanning electron microscopy (SEM) images, obtained by Cristina Roldán-Carmona (EPFL Sion), of the top surface in Figure 5.29c (top) reveal a wide distribution of the particle size. It is noteworthy that the spin-coating speed impacts this size distribution; films at low spin-coating speed < 5000 rpm exhibited both small and large TiS_2 nanoparticles, whereas spin-coating at 5000 rpm resulted in significantly reduced distribution and an overall nanoparticle

size below 100 nm (Figure E1, Appendix E). A possible explanation for this difference might be the higher centrifugal force at a spin speed > 5000 rpm that results in larger particles being ejected from the substrate surface during spin-coating. The maps obtained by energy-dispersive X-ray (EDX) spectroscopy by Emad Oveisi (EPFL Sion) in Figure 5.29c show that the elements Ti and S are present over the whole material surface, implying the formation of a homogeneous film after the spin-coating of the TiS_2 dispersion. However, the actual species constituting the films cannot be unequivocally determined by these data.

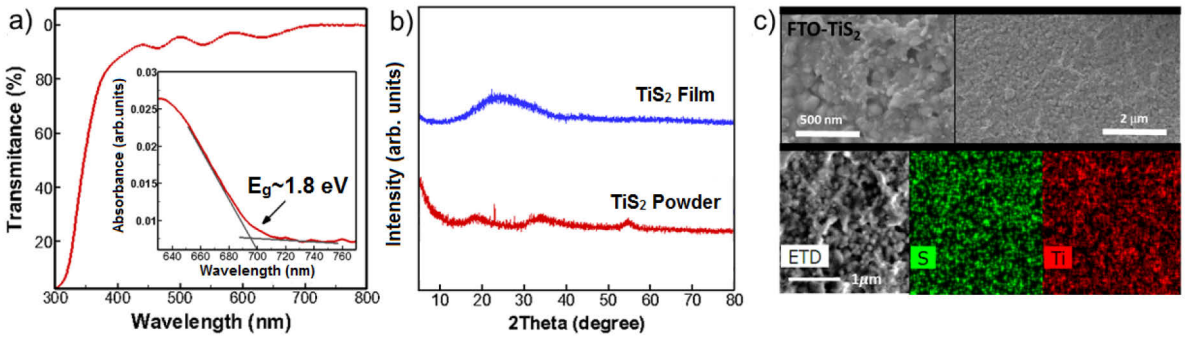

Figure 5.29 a) UV-visible transmittance spectra of a TiS_2 film on FTO substrate. **Inset**: corresponding absorption spectrum yielding an optical band gap of TiS_2 of ca. 1.8 eV. **b)** XRD diffraction pattern of the as-synthesized TiS_2 powder and a TiS_2 film on a glass substrate. **c)** Top: SEM images of TiS_2 nanoparticles deposited on FTO. Bottom (from left to right): SEM images of TiS_2 film, and EDX maps for Ti and S. Optical data in a) are from Saba Gharibzadeh (Tarbiat Modares University), XRD-data in b) are from Saba Gharibzadeh (Tarbiat Modares University) and Aron Huckaba (EPFL), SEM data in c) are from Cristina Roldán-Carmona (EPFL Sion), and EDX-data in c) are from Emad Oveisi (EPFL Sion), all figures are adapted and reproduced with permission from ref. [244].

To assess the actual composition and the chemical state of the different constituents of the TiS_2 materials, XPS measurements were carried out on a thick TiS_2 film (powder) obtained by drop-casting TiS_2 dispersion on FTO glass substrate (preparation at HU Berlin). The recorded core-level spectra and the corresponding spectral fits are shown in Figure 5.30. The Ti 2p and S 2p spectra consist of several doublets corresponding to different chemical states. Spin-orbit levels typically feature similar FWHM. Here, it can be observed that the Ti $2p_{1/2}$ peak is broader than the Ti $2p_{3/2}$ peak, which is attributed to the shorter lifetime of the core hole in Ti $2p_{1/2}$ in comparison to Ti $2p_{3/2}$. This is due to the Coster-Kronig transition [289, 321], which is a particular case of the Auger process (see subsection 3.1.1), where the initial core hole (photohole) is filled by an electron from the same shell, thus representing an additional

decay channel for the core hole. Therefore, the core hole has a shorter lifetime, and hence the lifetime broadening is enhanced. The low-binding-energy contributions of Ti 2p (Ti $2p_{3/2}$ at 457.1 eV and Ti $2p_{1/2}$ at 463.8 eV) and S 2p (S $2p_{3/2}$ at 161.3 eV and S $2p_{1/2}$ at 162.5 eV) can be assigned to the titanium and sulfur as in TiS_2, respectively. Still, additional peaks at 458.8 eV (Ti $2p_{3/2}$) and 464.5 eV (Ti $2p_{1/2}$) are derived from the Ti 2p spectrum, which exhibit lower intensities in comparison to the main Ti 2p contribution from TiS_2. This additional Ti 2p contribution is attributed to TiO_2, with the corresponding O 1s peak found at 530.4 eV. The partial oxidation of TiS_2 into TiO_2 has been already reported [322] and can be induced by trace amounts of oxygen and/or ambient moisture during the synthesizing process.

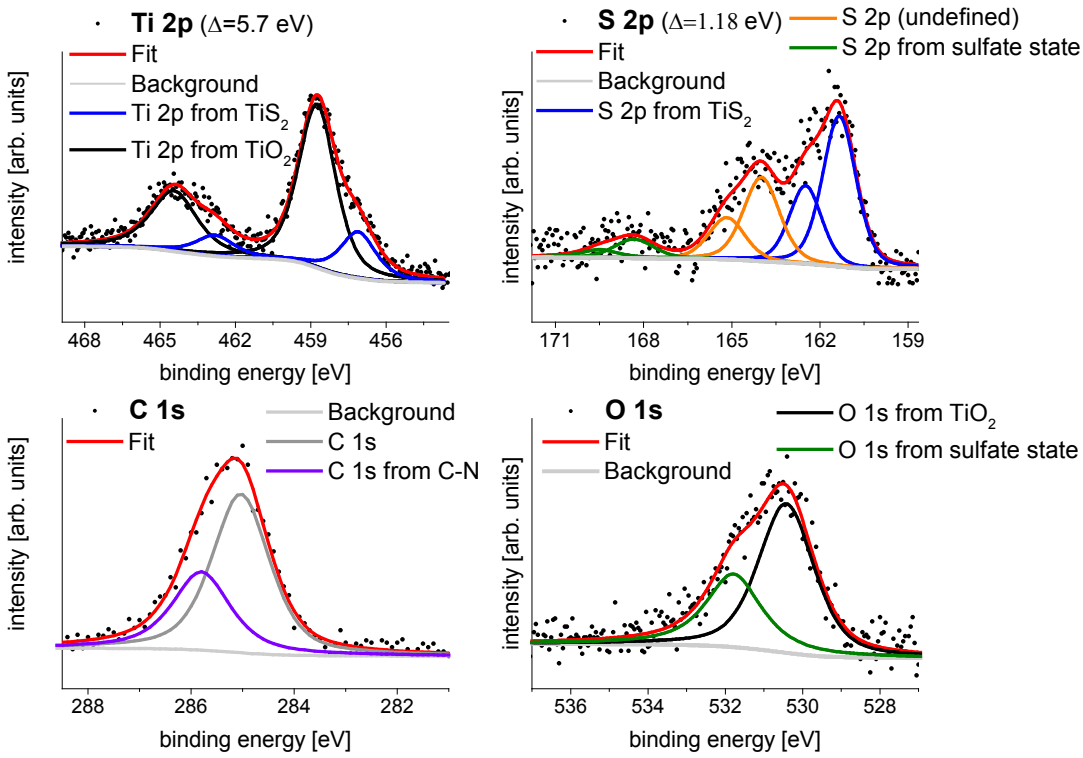

Figure 5.30 XPS core level spectra of Ti 2p, S 2p, C 1s, and O 1s for TiS_2 powder deposited on FTO substrate by drop-casting. The spin-orbit splitting for the doublets is each given by Δ for Ti 2p and S 2p. Illustration reproduced with permission from ref. [244].

It is worth mentioning that this partial oxidation of TiS_2 can possibly be at the origin of a built-up of ions/charges at the perovskite/TiS_2 interface, which can promote recombination and impacts the charge transport [244]. The S 2p spectrum exhibits two additional features as well. The S $2p_{3/2}$ and S $2p_{1/2}$ states at 164 and 165.18 eV, respectively, correspond to an undefined sulfur species as previously reported in literature [323]. However, these binding

energy positions interestingly coincide with that of S 2p in the S-S bond as found in CuS, which can be assigned to the presence of S_2 dimers [324, 325]. A third contribution, which consists of the peaks at 168.3 and 169.5 eV, exhibits relatively low intensity and corresponds to sulfur as in sulfate, which can be associated with the presence of the O 1s peak at 531.8 eV as in sulfate and hydroxyl groups [224]. Finally, the C 1s core level spectrum consists of a peak at 285 eV attributed to adventitious carbon, and of a peak at 285.8 eV corresponding to C-N bonding in the organic oleylamine ($C_{18}H_{35}NH_2$) ligand.

The results of the UPS measurements performed on a thick film obtained from drop-casting of the TiS_2 dispersion are shown in Figure 5.31a. The work function $\phi_{(TiS2)}$ and valence band maximum position $VBM_{(TiS2)}$ of TiS_2 extracted from the SECO and valence spectra are 4.13 eV and 1.53 eV, respectively, thus yielding an ionization energy of 5.66 eV. Curiously, the determined $VBM_{(TiS2)}$ represents a high value, which is inconsistent with some previous works that report a TiS_2 band gap of 0.7 eV or lower [318]. Nevertheless, as suggested by theoretical and experimental reports, the band gap of nanostructured TiS_2 can be tuned by modifying its morphology, for instance, from nanotubes to single-sheet monolayers, thereby prompting semimetal-to-semiconductor transition [326–328]. In the present case, the determination of the VBM is quite involved as disclosed in the inset in Figure 5.31a, where some tailing intensity detected up to the Fermi level would agree with the suggested semimetallic character of bulk TiS_2 [329]. Nonetheless, the identified defect-rich TiO_2 can also account for this density of states close to E_F. Furthermore, although background subtraction was carefully applied to the UPS spectra, it is not completely ruled out that these intensities are related to some satellites tailing caused by the non-monochromatic UV source.
It is important to note that TiS_2 thin films deposited by spin-coating on FTO and on $(FAPbI_3)_{0.85}(MAPbBr_3)_{0.15}$ mixed perovskite (Figure 5.31b) also exhibit valence band features similar to those of the TiS_2 thick film (powder). Besides, the determined work function of ≈4 eV and VBM of ≈1.5 eV are comparable to those of the TiS_2 thick film. This implies that the thick and thin films both exhibit similar electronic properties. However, due to the low amount of material deposited by spin-coating for the thin film fabrication, as previously assessed by SEM in Figure 5.29c (top), the tailing intensity up to E_F could not be detected, in contrast to the case of the thicker film. The SECO and valence spectra of a reference mixed perovskite film, as used in a device, is also shown in Figure 5.31b and result in $\phi_{(perovskite)}$ = 4.23 eV and $VBM_{(perovskite)}$ = 1.67 eV.

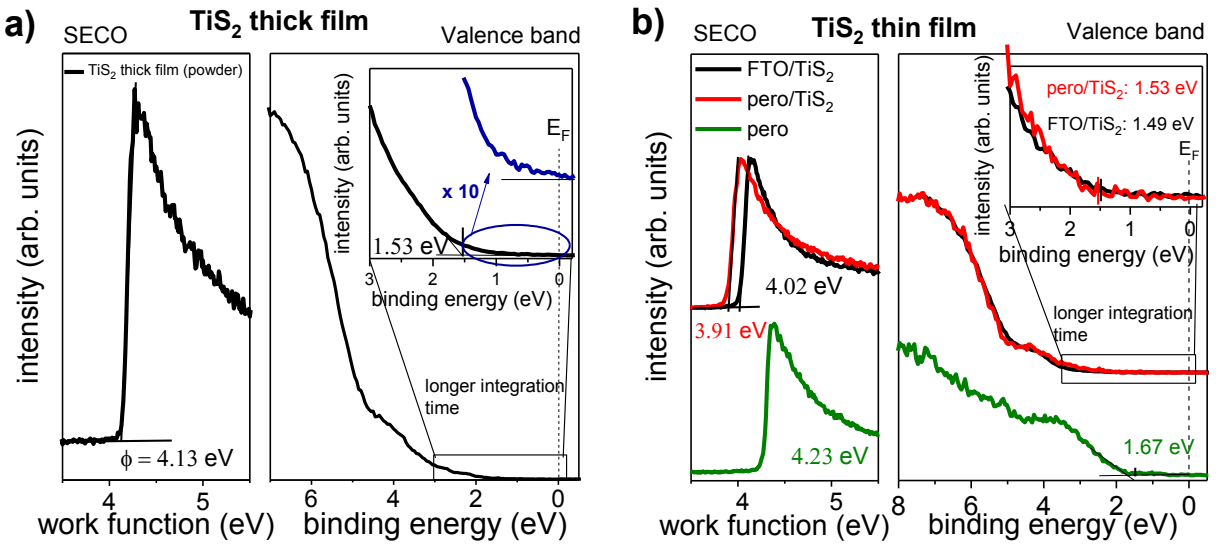

Figure 5.31 a) UPS spectra of TiS_2 powder deposited on FTO by drop-casting: SECO (left) and valence band spectrum (right) with the **inset** displaying the magnified spectrum in the lower binding energy region. **b)** UPS spectra of $(FAPbI_3)_{0.85}(MAPbBr_3)_{0.15}$ mixed perovskite (pero, green) deposited on FTO/c-TiO_2/m-TiO_2-substrate, of TiS_2 thin film on FTO/c-TiO_2/m-TiO_2/$(FAPbI_3)_{0.85}(MAPbBr_3)_{0.15}$ (pero/TiS_2, red), and of TiS_2 thin film on FTO (FTO/TiS_2, black). Illustration adapted with permission from ref. [244].

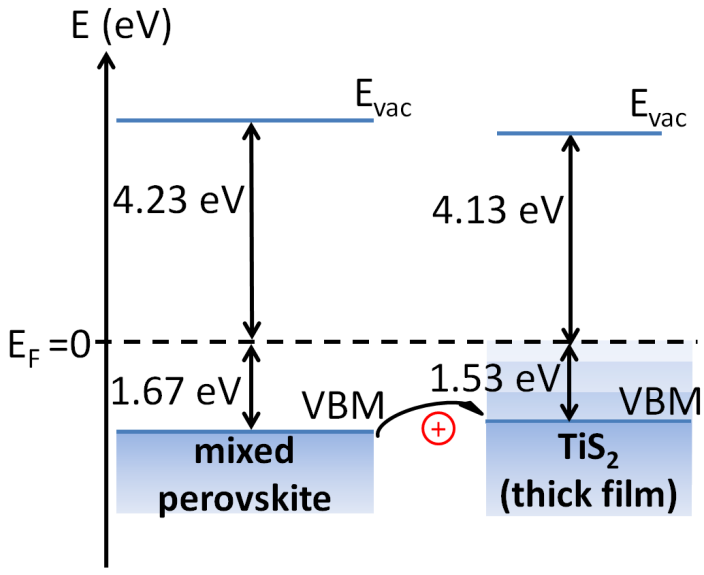

Figure 5.32 Energy level diagram of the $(FAPbI_3)_{0.85}(MAPbBr_3)_{0.15}/TiS_2$ structure, based on the work function and VBM values of $(FAPbI_3)_{0.85}(MAPbBr_3)_{0.15}$ (pero) and the TiS_2 thick film extracted from the UPS spectra in Figure 5.32. Illustration reproduced with permission from ref. [244].

Based on these parameters and the UPS results in Figure 5.31a, an energy level band diagram can be drawn (Figure 5.32), where the 0.15 eV lower $VBM_{(TiS2)}$ of TiS_2 points out a suitable energy level alignment for hole extraction from the mixed perovskite layer to the TiS_2 layer, as well as a favorable conduction band energy position for blocking electrons, as estimated from the 1.8 eV optical gap. This predicted effective charge extraction between the mixed perovskite and the TiS_2 layer is actually confirmed by the high current density reached by PSCs with the investigated perovskite/TiS_2 structure. Indeed, the solar cells with n-i-p configuration, as illustrated in Figure 5.33a (characterized by Saba Gharibzadeh, Tarbiat Modares University), exhibit a J_{sc} comparable to that of PSCs with spiro-OMeTAD, as interpreted from the J-V curves in Figure 5.33b. However, the open circuit voltage V_{oc} and FF obtained with TiS_2 are distinctly lower than in the case of solar cells containing spiro-OMeTAD. As a result, a lower PCE of ≈13.5% for the champion cell (averaged PCE value of 12%) was obtained with TiS_2 in comparison to ≈18.1% with spiro-OMeTAD. These lower V_{oc} and FF suggest an increase of charge recombination and shunt-resistance losses at the perovskite/HTL interface, likely mediated by the very small particle size and the ultrathin film (Figure 5.33c), that can possibly induce shunting pathways in the device. It is noteworthy that devices fabricated without HTL exhibit a reasonable performance with a PCE ≈ 8.4%; however, the deformation of the J-V curve in Figure 5.33b indicates an uncompensated charge accumulation within the device, thus hindering the estimation of the real photovoltaic values.

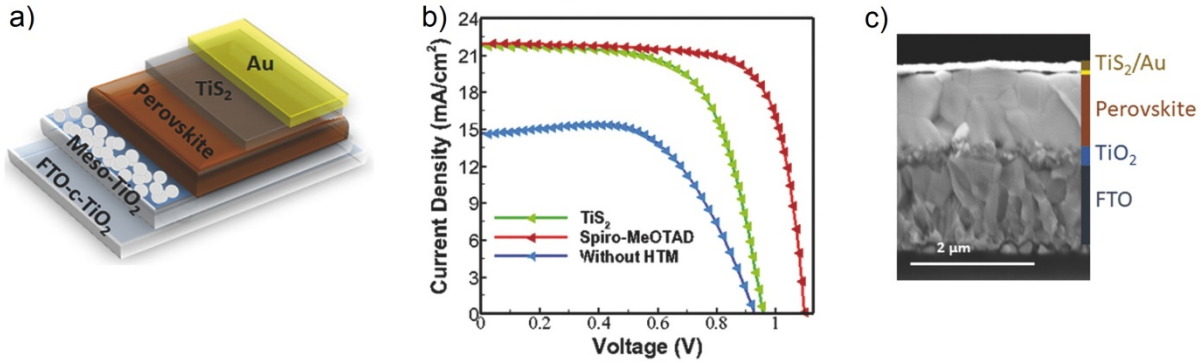

Figure 5.33 a) Schematic of the device configuration. **b)** J-V curve of the champion cells employing TiS_2 and spiro-OMeTAD as HTLs, and without HTL for comparison. **c)** Typical cross-section SEM image of a complete perovskite-based device. Solar cells characterization by Saba Gharibzadeh (Tarbiat Modares University), SEM data from Cristina Roldán-Carmona from (EPFL Sion); all figures reproduced with permission from ref. [244].

A comparative analysis (Table E1, Appendix E) assessing the cost per m^2 of TiS_2 and spiro-OMeTAD was also performed by Aron Huckaba (EPFL, Sion). In contrast to the costly multiple purification steps and synthesis of spiro-OMeTAD, the here introduced TiS_2 nanoparticles were prepared following one single synthesis step. Consequently, the cost analysis resulted in cost per gram and cost per m^2 44 times and 30 times, respectively, higher for spiro-OMeTAD in comparison to TiS_2.

In summary, inorganic TiS_2 nanoparticles synthesized following a simple two-step hot injection method have been characterized and implemented as HTL in perovskite solar cells. TiS_2 films deposited from solution dispersion by simple spin-coating exhibit intense absorption. However, limitations with regard to the achievable film thickness and partial oxidation of the deposited films have been observed by XPS measurements, which can potentially affect the working mechanism of the solar cells. Nonetheless, devices with TiS_2 as HTL exhibit remarkable current density comparable to the case of the commonly used spiro-OMeTAD, which can be explained by an effective charge extraction at the perovskite/TiS_2 interface, as supported by the suggested favorable alignment of the respective energy levels. Although the solar cell efficiency of 13.5% attained with TiS_2 is lower than the 18.1% PCE attained with spiro-OMeTAD, the significant price difference makes TiS_2 a suitable candidate for low-cost solar cell production. The introduction of this novel material for low-cost, durable, and efficient perovskite solar cells represents an important path towards scaling up the perovskite technology.

5.4 Additional Experiments

Alongside the core topic of mixed $MAPbI_{3-x}Cl_x$ perovskite formation and its electronic properties variation upon exposure to different environments as discussed in sections 5.1 and 5.2, respectively, work directed towards an investigation of the interfaces between perovskite and charge transport materials was initiated. To orient the choice of solvents for charge transport material deposition from solution on top of a perovskite layer, the effect of selected solvents on the structural and electronic properties of $MAPbI_{3-x}Cl_x$ perovskite films was investigated. The results are presented in subsection 5.4.1. In an attempt to obtain solution-processed perovskite thin films with varying thicknesses, for future investigations of the ELA between perovskite and their substrates (e.g. PEDOT:PSS) and film thickness dependent electronic structure, the effectiveness of solution dilution for thickness variation was tested (subsection 5.4.2) by monitoring the electronic structure and structural properties of different films obtained with different preparation methods.

5.4.1 Characterization of the Effect of Solvents on Perovskite films

The results presented in the present subsection 5.4.1 are the subject of a manuscript in preparation [330]. Organic electron- and hole-transport materials are commonly deposited either by thermal evaporation or from solution. The latter method necessitates the use of a suitable solvent that not only dissolves the material but also preserves the underlying perovskite layer upon deposition. Accordingly, the present subsection aims at assessing the effect of four candidate solvents on the structural and electronic properties of $MAPbI_{3-x}Cl_x$ films. Chlorobenzene (CB), and chloroform (CF) are usually used to deposit charge transport layers such as spiro-MeOTAD or 6,6-phenyl C_{61} butyric acid methylester (PCBM) from solution [331–333]. Contrastingly, dimethylformamide (DMF) and water (H_2O) are good polar solvents for perovskite. In all cases, the as-prepared $MAPbI_{3-x}Cl_x$ films were characterized before and after solvent exposure by GIXRD, AFM, UV-vis spectroscopy, and PES in order to assess the impact of the solvents on the structure, morphology, optical, and electronic properties of the films, respectively. The solvent exposure consists of depositing about 25 µL of CB, CF, or DMF or ca. 80 µL of water onto the perovskite films. After each exposure, the perovskite films were left in ambient air at room temperature for 2 to 5 min

(CB, CF) or 1 to 2 h (DMF, H_2O) until they appear dry. Thereafter, the films were characterized again.

Structural and morphology characterization

The 2D GIXRD patterns of $MAPbI_{3-x}Cl_x$ films before and after exposure to the respective solvent are shown in Figure 5.34. The analysis was performed by Ingo Salzmann (formerly HU Berlin). Before exposure, all the films exhibited the diffraction rings associated with the perovskite structure, with the typical ring at q = 1 $Å^{-1}$ assigned to the (110) crystal plane [13, 24, 230]. This observation confirms that the as-prepared films all fully crystallized into perovskite. The 2D GIXRD patterns before and after CB and CF exposure in Figure 5.34a and Figure 5.34b, respectively, do not display any particular differences in the error margin of the measurements. All the diffraction rings corresponding to the perovskite structure are still observable with comparable intensities and new features that might indicate degradation, for instance into PbI_2, were not detected. Therefore, CB and CF do not induce any noticeable structural changes in the perovskite films. In contrast, DMF and particularly H_2O exposure significantly impacted the structural properties of the as-prepared perovskite films, as assessed by the 2D GIXRD patterns in Figure 5.34c and Figure 5.34d, respectively.

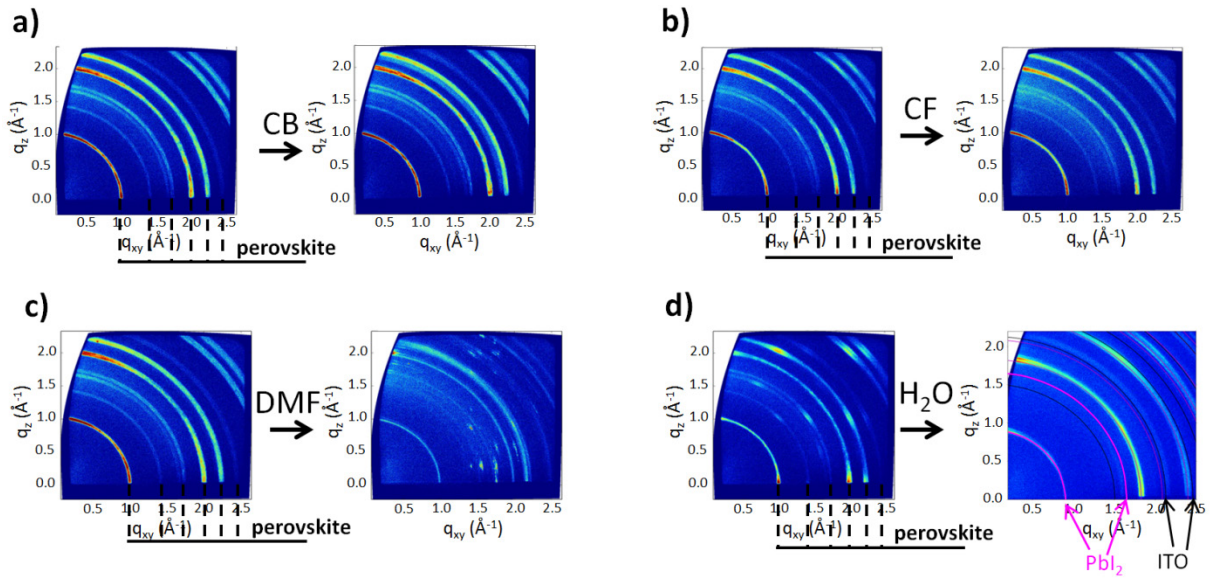

Figure 5.34 2D GIXRD patterns of $CH_3NH_3PbI_{3-x}Cl_x$ perovskite films before (left) and after (right) exposure to **a)** chlorobenzene (CB), **b)** chloroform (CF), **c)** dimethylformamide (DMF), and **d)** water (H_2O). Calculated diffraction rings assigned to PbI_2 (pink), and to the ITO substrate (black) are shown in d). 2D GIXRD maps processed by Ingo Salzmann (HU Berlin) and reproduced from ref. [330].

Interestingly, after DMF exposure, the characteristic diffraction features related to perovskite were still observed (Figure 5.34c). However, these features exhibited an overall reduced intensity as compared to before exposure. It is worth noting that upon exposure to DMF, the dark opaque $MAPbI_{3-x}Cl_x$ film (photographs in Figure 5.36 below) was instantaneously dissolved and turned into a visually transparent film. When the film was apparently dry, though mostly transparent it exhibited regions of darker tones, which, in the light of the 2D GIXRD results, can be associated with partially re-crystallized perovskite. Indeed, the GIXRD results after DMF exposure indicate that the dissolved film partially reconverted to perovskite again while drying in ambient air at room temperature. In the case of H_2O exposure, the film was instantaneously dissolved into a yellow solution. The 2D GIXRD pattern of the dry – and still yellow – film in Figure 5.34d display a diffraction ring at $q = 0.9$ Å^{-1}, which corresponds to the (001) plane of PbI_2 [24]. No diffraction features were present at $q = 0.6$ Å^{-1} and $q = 0.75$ Å^{-1} (*cf.* Figure 5.14 in subsection 5.2.2), which would be indicative of the presence of a monohydrate phase. Therefore, massive exposure to water, leads to direct and irreversible degradation of $MAPbI_{3-x}Cl_x$ perovskite into PbI_2, in line with previous observations [21, 42]. Additionally, diffraction rings corresponding to the ITO substrate are observed in Figure 5.34d, suggesting that the ITO substrate was poorly covered after water exposure. To confirm interpretation from the GIXRD measurements, the morphology of perovskite films before and after solvent exposure was assessed by AFM measurements (by Yerila Rodríguez, University of Havana), as shown in Figure 5.35. First, the AFM micrographs of $MAPbi_{3-x}Cl_x$ films before and after H_2O exposure are inspected. Whereas the as-prepared film exhibited a uniform morphology, the film after water exposure was characterized by large grains with width up to a few micrometers. These large grains appear as isolated aggregates, as also previously reported in literature [21], and result in a film with lower coverage and much higher roughness in comparison to the initial perovskite film (rms roughness of 237 nm for the former and 55 nm for the latter). This confirms the poor coverage suggested by the GIXRD results. The AFM micrographs of films exposed to CB, CF, and DMF are also displayed in Figure 5.35. No apparent change in morphology is observed after exposure to CB and CF, as corroborated by the comparable rms roughness of the films. In the case of DMF, the exposure resulted in a film morphology characterized by randomly spread needle-like crystallites with large voids in-between, implying large film inhomogeneity on a micrometer scale. The formation of clusters in the case of water and DMF exposure are likely induced by the presence of solvent and its gradual evaporation.

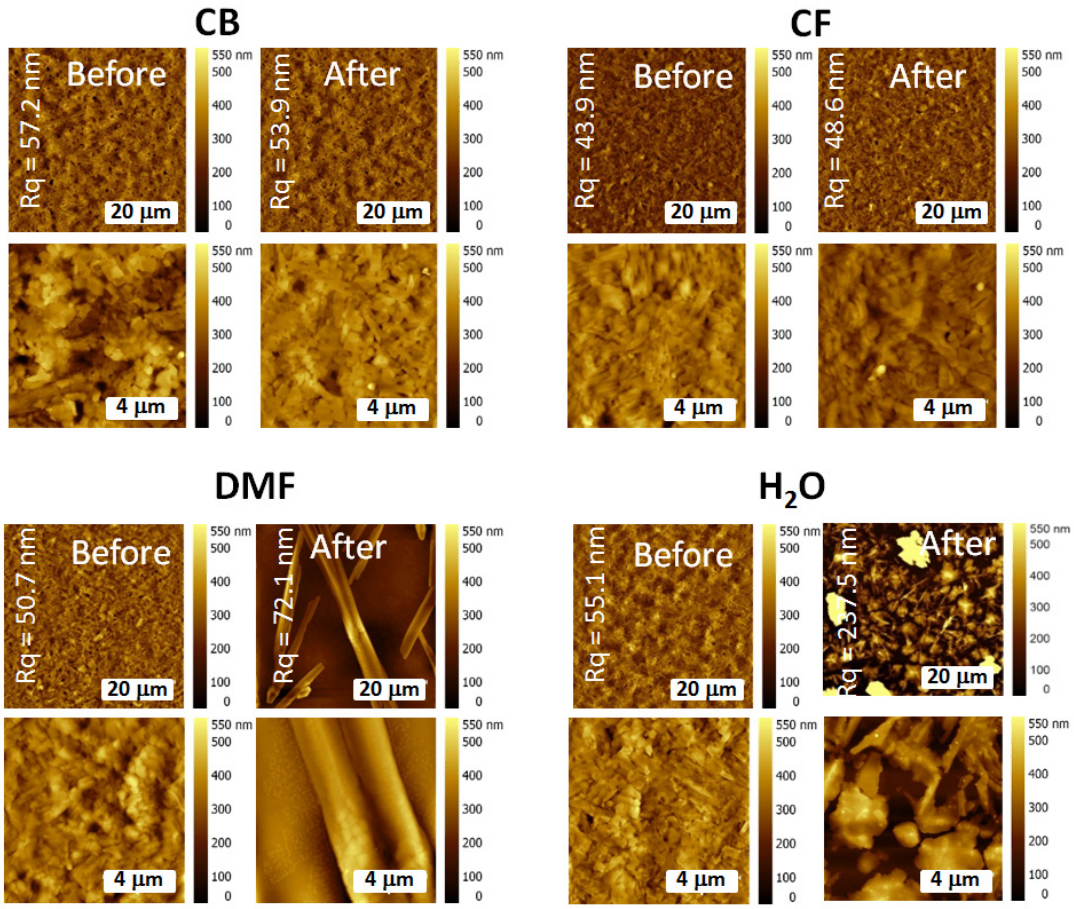

Figure 5.35 AFM micrographs of $CH_3NH_3PbI_{3-x}Cl_x$ perovskite films before and after exposure to chlorobenzene (CB), chloroform (CF), dimethylformamide (DMF), and water (H_2O). Adapted from data and figures provided by Yerila Rodríguez (University of Havana) from ref. [330].

Therefore, in line with the GIXRD results, the AFM measurements point out that CB and CF do not affect the morphology the perovskite film, whereas DMF and H_2O distinctly deteriorate the film quality.

Optical and electronic structure characterization

In agreement with the GIXRD and AFM results, the UV-vis spectra, performed by Yerila Rodríguez (University of Havana), before and after CB and CF exposure in Figure 5.36 indicate that these solvents did not affect the absorption properties of the films either, as suggested by the very similar absorption spectra. Therefore, the bulk properties of the perovskite films are likely preserved after exposure to CB and CF, indicating that these solvents are a priori suitable for depositing organic transport layers from solution on top of the perovskite film. Foreseeably, the absorption spectra of the films after DMF and H_2O exposure

in Figure 5.36 are distinctly different from those of the as-prepared films. After DMF exposure, a distinct decrease of the absorbance over the whole visible region is observed and a weak signal yielding an onset around 787 nm can be associated with the absorption edge of $MAPbI_3$. This latter observation is consistent with the perovskite-related features identified by GIXRD in Figure 5.36, therefore corroborating the partial re-crystallization into perovskite already at room temperature. Furthermore, the decreased absorbance can be explained by the incomplete film re-conversion into perovskite.

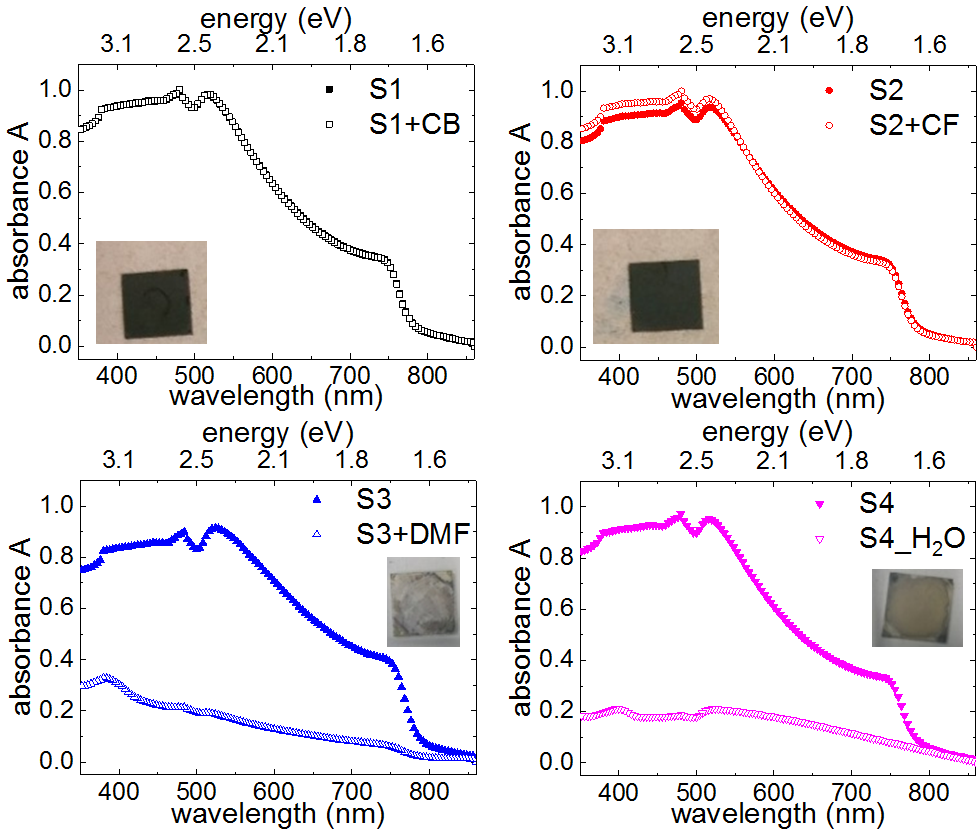

Figure 5.36 UV-vis absorption spectra of $MAPbI_{3-x}Cl_x$ films before and after exposure to chlorobenzene (S1), chloroform (S2), dimethylformamide (S3), and water (S4). **Insets**: photographs of the respective sample (10 × 10 mm^2) after solvent exposure. Data acquired by Yerila Rodríguez (University of Havana) and reproduced from [330].

In the case of H_2O exposure, a featureless absorption spectrum with drastically decreased intensity is observed in Figure 5.36 (S4+H_2O). The yellowish appearance of the sample after H_2O exposure shown in the photograph in the latter figure supports the presence of PbI_2 interpreted from the GIXRD data. However, no absorption feature related to PbI_2, with a characteristic absorption onset expected at 2.3 eV (539 nm), was observed, since only a broad

spectrum was recorded. This lack of structure in the broad spectrum can be related to scattering effects, which are caused by the film inhomogeneity and the large and isolated aggregates evidenced by the AFM micrographs (*cf.* Figure 5.36).

To evaluate the impact of the different solvents on the electronic properties of the perovskite films, PES measurements have been conducted (Figure 5.37 and Figure 5.38). The UPS data in Figure 5.37 show that all samples exhibited a work function increase upon exposure to the respective solvent, as deduced from the SECO spectra in Figure 5.37a. Besides, all valence band spectra featured pronounced changes after the respective solvent exposure (Figure 5.37b). All the results obtained so far indicated that CB and CF exposures do not alter the film bulk properties. Strikingly, the electronic structure of the film surface was, on the contrary, significantly affected by exposure to CB and CF. This is evidenced by the shape of the valence band spectra in Figure 5.37b, which is markedly different from those of the as-prepared films. Additionally, magnification of the lower binding energy region close to E_F in Figure 5.37c and Figure 5.37d discloses low but finite intensities which yield VBM onsets shifted by 0.5 and 0.2 eV to lower binding energy for CB and CF, respectively, in comparison to the respective as-prepared film. These VBM energy shifts are in the same direction and of the same amount as the respective work function change, thus indicating that the surface became less n-type after exposure to CB and CF. This is further supported by the core levels shift to lower binding energy, as representatively shown for the Pb 4f core level spectra in Figure 5.38a.

The appearance of the new features in the valence band spectrum in Figure 5.37c at about 6 and 8 eV, as well as a strong attenuation of the feature around 2.7 eV after CB and CF exposure indicate the modification of the surface electronic property. This might originate from the segregation – at least at the surface – into degradation products such as PbI_2 or CH_3NH_3I (MAI). However, none of the features observed in the valence band spectra of PbI_2 and MAI layers spin-coated on ITO substrates (Figure 5.39) can be identified in the valence band spectra after CB and CF exposures in Figure 5.37. It is also possible that the pronounced changes are a result of mere surface contamination due to solvent residues. In such case, the contaminants did not affect the morphology or the absorption properties of the film but were revealed by the surface-sensitive UPS measurements. Nevertheless, the change of valence band shape and the adoption of a less n-type character imply a surface electronic modification.

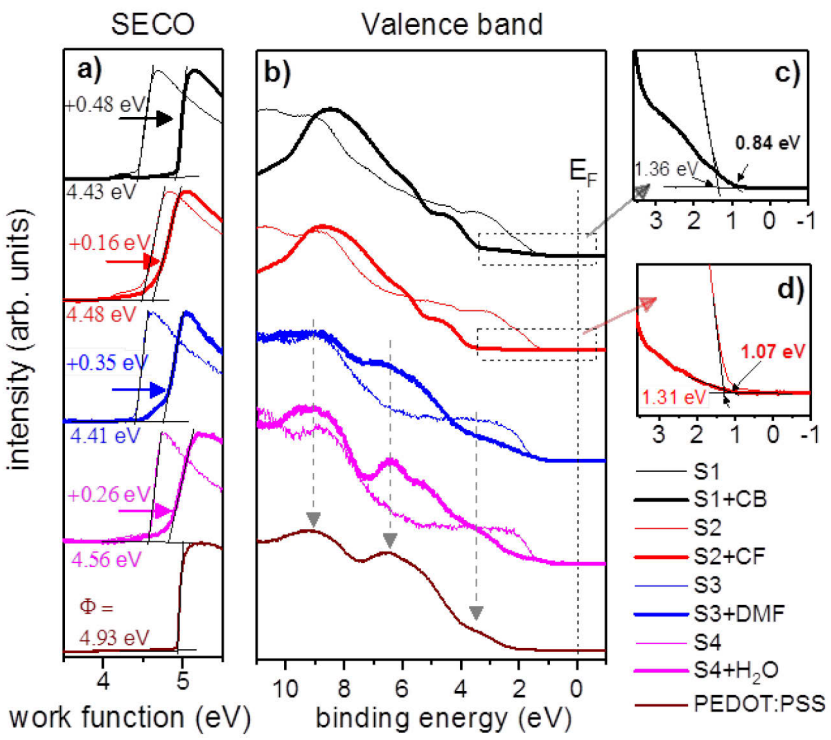

Figure 5.37 a) SECO and **b)** valence region spectra of $MAPbI_{3-x}Cl_x$ films before (normal) and after (bold) exposure to CB (S1), CF (S2), DMF (S3), and H_2O (S4). The SECO and valence band spectra of PEDOT:PSS are shown for comparison (brown curves). Magnification of the valence band spectrum in the binding energy region close to E_F for **c)** S1 and **d)** S2 before and after exposure to CB and CF, respectively. Reproduced from ref. [330].

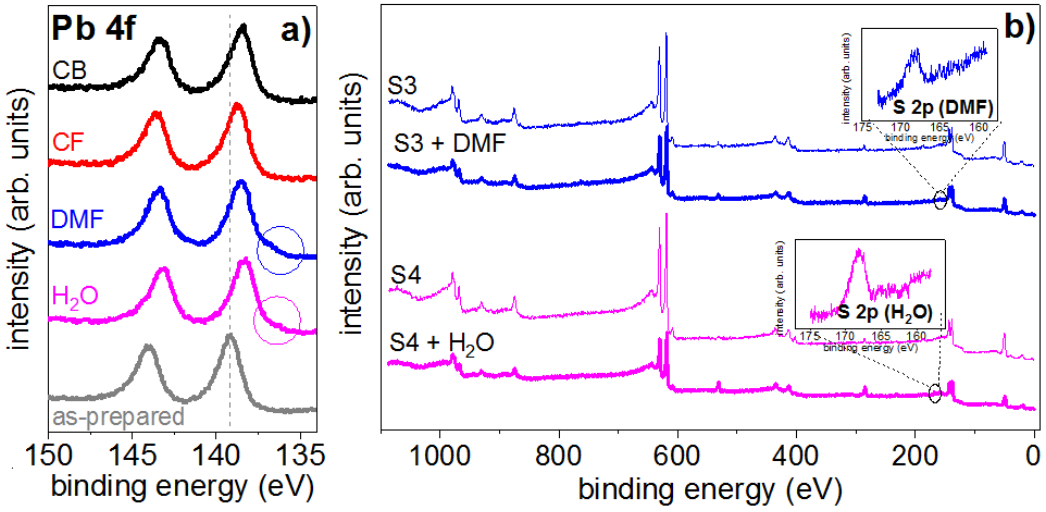

Figure 5.38 a) Normalized XPS spectra of Pb 4f core level after solvents exposure for $MAPbI_{3-x}Cl_x$ films, showing a shift to lower binding energy of all the spectra in comparison to the spectrum for an as-prepared sample (grey). The Pb 4f spectra for samples exposed to DMF and H_2O exhibit a density of states at lower binding energy (blue and magenta circles, respectively) corresponding to Pb^0 defects. **b)** XPS survey spectra for $MAPbI_{3-x}Cl_x$ films before and after exposure to DMF (S3) and water (S4). **Insets**: high-resolution XPS spectra of S 2p core level after solvent exposure evidencing the detection of signal related to the PEDOT:PSS substrate. Illustration reproduced from ref. [330].

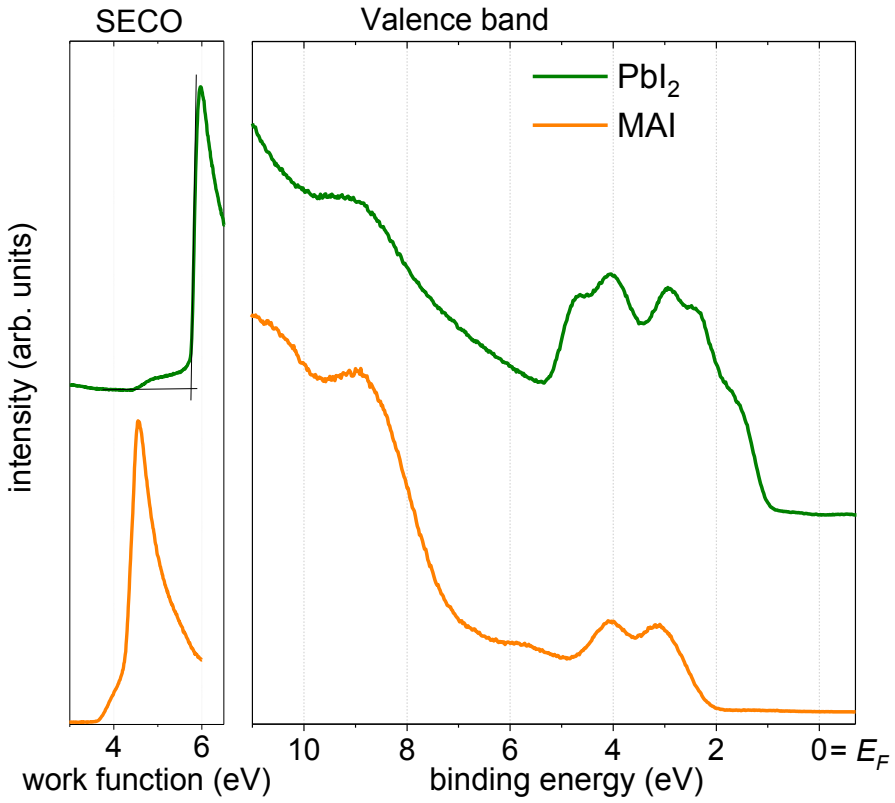

Figure 5.39 SECO (left) and valence region (right) spectra of methyl ammonium iodide (MAI) and lead iodide (PbI_2) layers. Illustration reproduced from ref. [330].

Although the origin of such modifications was not fully determined from the present data, it is possible that they were induced by a reduction of the surface states density induced by the solvent exposure, for instance related to a reduction of the amount of Pb^0-defects. The valence band spectra of the samples exposed to DMF and H_2O are clearly dominated by features that can be assigned to the respective PEDOT:PSS substrate, as evidenced by the comparison with the valence band spectrum of a bare PEDOT:PSS layer in Figure 5.37a and corroborated by the signal from the S 2p core level detected by XPS measurements for the samples exposed to DMF and water in Figure 5.38b. The detection of these signals corresponding to the underlying substrate is consistent with the poor coverage concluded from the GIXRD and AFM characterizations. Noteworthy, upon DMF and H_2O exposure, Pb^0 species are detected as shown by increased density of states at lower binding energy in the Pb 4f XPS spectra in Figure 5.38a.

In summary, chlorobenzene and chloroform preserve the morphology, as well as the structural and optical bulk properties of $MAPbI_{3-x}Cl_x$ perovskite films, suggesting that these solvents are likely suitable for the solution-deposition of organic transport layers on perovskite. However, both solvents strikingly induce significant changes in the electronic properties of the film

surface, namely a pronounced change in the spectral shape of the valence band and the adoption of a less n-type character. Such changes, which are proposed to be related to a modification of the surface states, certainly impact on the interface formation when these solvents are used for depositing the charge transport layers. The exposure to massive amounts of DMF and H_2O leads to the instantaneous dissolution of the perovskite films, which, once dried, exhibit inhomogeneous morphologies. While the films exposed to DMF partially re-crystallize into perovskite already in ambient air at room temperature, the films exposed to water degrade irreversibly into PbI_2. The latter degradation is certainly accounted for by the large amount of water used for the exposure. As previously shown in subsection 5.2.2, no such instantaneous and pronounced degradation is expected at lower water exposure, for instance in ambient air at 80% RH. However, minute amount of water as encountered in glove boxes or in high vacuum conditions can already impact on the electronic structure of perovskites. Accordingly, the results presented in this section also motivate the question of the potential effects on the electronic and morphological properties of perovskites of reduced or residual amounts of solvents present in typical preparation and storage environments, particularly in glove boxes.

5.4.2 Solution Dilution for Thin Film Fabrication in View of ELA Analysis at the Interface between PEDOT:PSS and Perovskite

In order to establish the ELA between adjacent materials in a device, knowledge of the energy levels of the individual materials is essential and can aid in the choice of the electronic materials. As already discussed in subsection 2.1.4, interface formation is often accompanied by effects such as formation of an interface dipole, charge distribution resulting in band bending, or bond formation. In order to assess these effects, the ELA at the interface between two materials can be established by monitoring the evolution of the energy levels as one material is deposited in a stepwise manner onto another (usually referred to as “substrate”). The main challenge in this approach is the production of layers that are ultrathin (typically in the Å to nm range) and homogeneous enough so that they can reflect the actual situation as encountered in buried layers in a device. Two of the rare studies addressing the aspect of ELA between $MAPbI_3$ layers and different substrates (in contrast to transport materials onto a $MAPbI_3$ substrate), including ZnO(0001) [334], and PEDOT:PSS substrates [288], investigated the respective energetic interface by *in situ* co-evaporating PbI_2 and CH_3NH_3I onto the substrate to obtain $MAPbI_3$ layers of nominal thickness ranging from 0.2 to about

200 nm. Although these studies provide valuable information about the ELA between selected substrates and the perovskite materials on top, additional and comparable studies are still needed for a deeper insight into the complexity of interface formation and for putting the contrasting conclusions of these studies into perspective. Preliminary measurements on thin $MAPbI_3$ films obtained by co-evaporation indicating variation of the DOS in the first few nm up to 8 nm are shown in Figure F1 in Appendix F. Importantly, studies adopting the same approach on perovskite films obtained by solution deposition, which is still the most prevalent deposition method applied in the field of perovskite solar cells, are still missing. One possible manner of achieving thin layers from solution consists in serial dilution of an original solution of definite concentration, e.g. c0, assuming that the higher the dilution factor is – i.e. the lower the concentration is – the thinner the spin-coated film will be for fixed spin-coating parameters [see equation (4.1)].

In the scope of the present thesis, this solution dilution approach has been experimented in order to test its applicability for obtaining very thin solution-processed perovskite films. The aim of such experiment is the eventual investigation of the interface between solution-processed perovskite and the underlying hole transport material PEDOT:PSS. In the present subsection, the results of such experiments are shown for three series of samples. The first series consists of samples obtained by dilution of a $MAPbI_{3-x}Cl_x$ precursor solution of concentration c0 (40 wt%), a reference concentration already used for all perovskite samples reported previously in sections 5.1, 5.2, and subsection 5.4.1. The second series is based on the same $MAPbI_{3-x}Cl_x$ solution c0 and its 1:10, 1:5, and 1:2 dilutions. Additionally, in an attempt to improve film morphology, the anti-solvent method was applied. This method consists of toluene dripping at the end of the spin-coating process. This latter step has been suggested to slow down the $MAPbI_3$ formation, promoting the nucleation and growth of a homogeneous perovskite film [141, 335]. For the third series, based on the solvent engineering developed by Jeon et al. [141], the same procedure involving the toluene dripping was followed, however, the solutions (of decreasing concentration 0.75 M, 0.15 M, 0.05 M and 0.01 M.) used were obtained by mixing MAI and PbI_2, hence without chlorine, in a mixture of γ-butyrolactone (GBL) and dimethyl sulfoxide (DMSO) solvents. Although the fabrication of very thin films from the solution dilution approach still remains a challenge, the following results show that the electronic properties of the films are indeed influenced by the different preparation methods (solution and deposition).

The UPS spectra of the first series of samples obtained by dilution of the reference $MAPbI_{3-x}Cl_x$ solution c0 (40 wt%) are shown in Figure 5.40 (see Figure F3 for corresponding XPS spectra). The PEDOT:PSS substrate work function of 4.88 eV was reduced to 4.60 eV upon deposition of the dilution 1:100. Thereafter, a gradual decrease of the work function by up to 0.50 eV is observed for samples with increasing concentration from 1:100, 1:10 to 1:5 and c0 (Figure 5.40a). Concomitantly, the corresponding valence band spectra of 1:100 and of 1:10 gradually shifted to higher binding energy (BE), as shown by the shift of the feature at ca. 6.3 eV BE in Figure 5.40b. It is worth noting that the shape of the valence band spectra for 1:100 and 1:10 resembles the spectrum of PEDOT:PSS, although a slight evolution in the lower BE region is perceptible (inset in Figure 5.40b). For 1:5, the valence band spectrum in Figure 5.40b is dominated by the typical $MAPbI_3$ features with an onset at 1.47 eV BE. Both SECO and valence band spectra of 1:5 and c0 indicate that no more change takes place at concentrations above 1:5, since both samples exhibit similar work function and VBM values, implying that the film obtained with this concentration is already too thick for probing the interface.

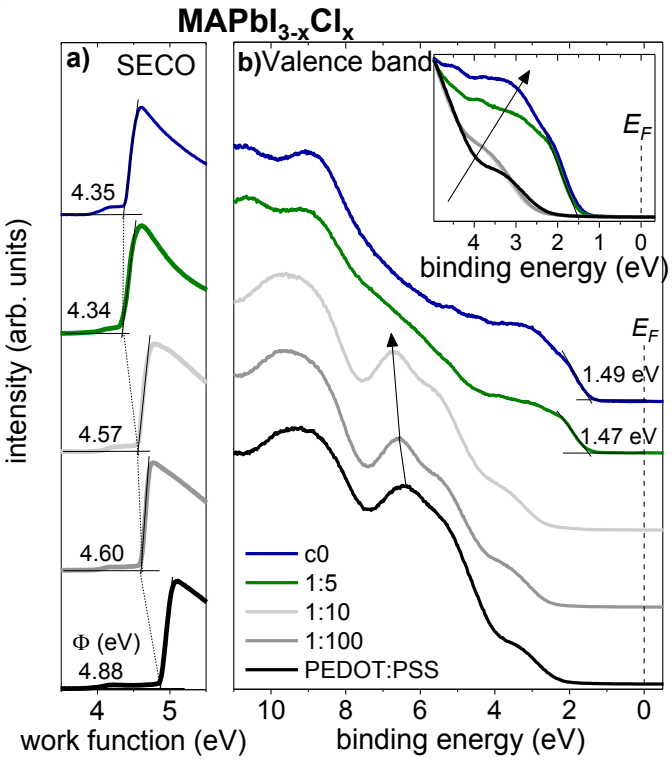

Figure 5.40 a) SECO and **b)** valence region spectra of PEDOT:PSS films, and $MAPbI_{3-x}Cl_x$ films obtained from precursor solutions of different concentration prepared by dilution of a reference concentration c0 (40 wt%) with the dilution factors 5, 10, and 100, respectively. The inset in b) shows the narrow range valence band spectra to allow comparison of the features.

Indeed, assuming a film thickness directly proportional to the solution concentration [239], and a film thickness of ca. 260 nm obtained from the reference solution c0 (Figure F4, Appendix F), the 1:5 dilution likely resulted in a several tens of nm thick film. The distinct attenuation of the intensities of the O 1s and S 2p core level spectra related to the PEDOT:PSS substrate in Figure F3 (Appendix F), supported by the large coverage derived from the AFM micrographs in Figure F5 (Appendix F) suggests that a thick film has formed. In contrast, the morphologies of the 1:10 and 1:100 samples as determined by AFM (Figure F5, Appendix F) are comparable to that of PEDOT:PSS (see Figure 4.2b), in line with the prevalent signal from PEDOT:PSS observed by UPS. This also suggests that the low amount of material deposited imitate the morphology of the PEDOT:PSS substrate. Nevertheless, on a micrometer scale, clustering grains forming isolated islands of 200 nm width are observed on the AFM micrograph of 1:10, which can be associated with formed perovskite (Figure F5, Appendix F). Indeed, the 2D GIXRD pattern of 1:10 (Figure F6, Appendix F) is evidence of the formation of perovskite at this concentration and its growth in a fiber texture. In addition, the GIXRD patterns demonstrate the presence of perovskite already at concentrations as low as 1:100, although strong and dominant signal from the underlying ITO was detected. No perovskite-related signal was observed for a lower dilution of 1:1000, and so no further studies were performed at this dilution ratio. Since perovskite can already form at concentrations as low as 1:10 and 1:100, though with poor surface coverage, it is likely that very thin films are also obtainable in this concentration range, provided the morphology can be improved. In an effort to improve film morphology, the solution deposition method with toluene as anti-solvent was applied. Although the coverage was improved for the 1:10 dilution, as indicated by more densily spread grains, the film was still not continuous (Figure F5, Appendix F). UPS measurements show that all four samples (1:10, 1:5, 1:2, and c0) exhibited the similar features that can be associated with $MAPbI_3$ perovskite (Figure 5.41), likely as a result of the improved morphology which led to a strong attenuation of the signal from the PEDOT:PSS substrate. The 6.17 eV high IE of 1:10, in comparison to that of the samples corresponding to higher concentrations (IE~5.88 eV), indicates that the materials formed with 1:10 exhibit pronounced variations, possibly in composition, with regard to the other samples. The assessments of the origins of the changes in electronic properties necessitate XPS analysis and GIXRD measurements, which have not been performed for this series of samples.

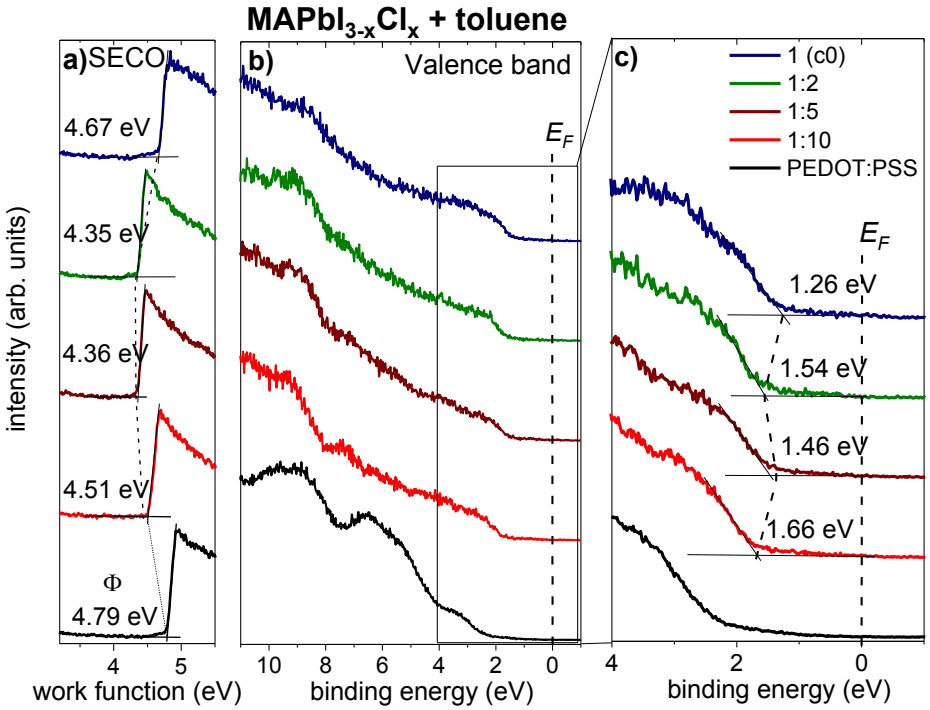

Figure 5.41 a) SECO, **b)** wide and **c)** narrow binding energy range valence region spectra of PEDOT:PSS and $MAPbI_{3-x}Cl_x$ films obtained from precursor solutions of different concentration prepared by dilution of a reference concentration c0 (40 wt%) with the dilution factors 2, 5, and 10, respectively. The respective solution was deposited following the anti-solvent method, that is, the dripping of toluene before the end of the spin-coating process.

Based on the solvent engineering developed by Jeon et al. [141], a solution of the single halide $MAPbI_3$ in a mixture of DMSO and GBL, with toluene dripping was also tested. As already described at the end of the subsection 2.2.1, this method has been proven to induce the formation of dense and uniform perovskite layers due to slower crystallization induced by the use of DMSO and GBL and the toluene dripping [141]. Four $MAPbI_3$ precursor solutions with different concentration were prepared, namely 0.01 M, 0.05 M, 0.15 M and 0.75 M. Note that the concentration of the previous mixed halide $MAPbI_{3-x}Cl_x$ perovskite solution c0 would correspond to a concentration of 1.7 M, which is about the double of the highest $MAPbI_3$ solution concentration used here. The UPS spectra of these samples are shown in Figure 5.42. The valence band spectrum of 0.01 M is very similar to that of PEDOT:PSS. The work function of the 0.01 M sample is, however, lower than that of PEDOT:PSS, which is similar to the trend that have been observed for the case of $MAPbI_{3-x}Cl_x$. It should be noted, that the whole valence band spectrum shifts in parallel with the work function.

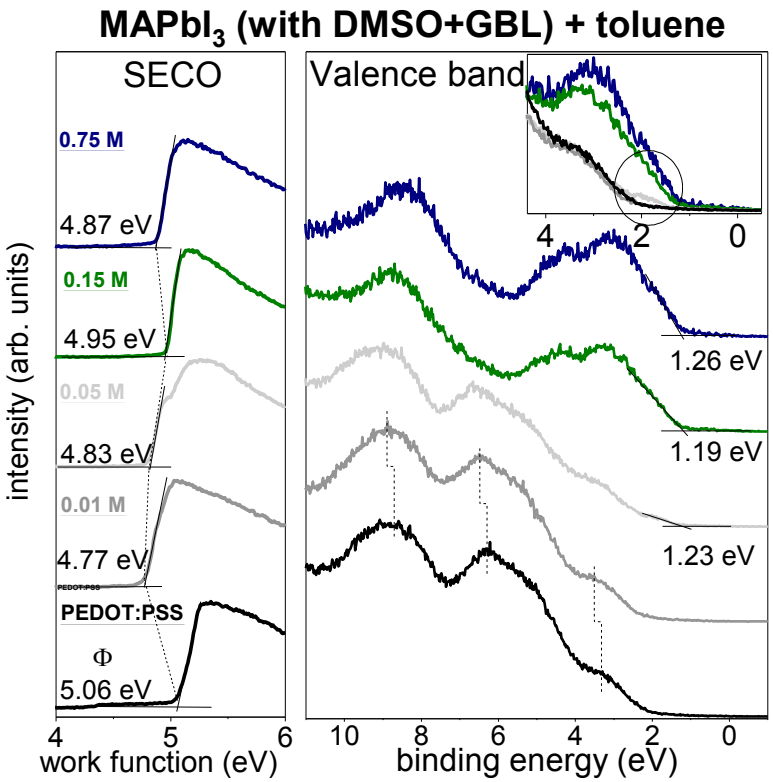

Figure 5.42 SECO (left) and valence region spectra (right) of PEDOT:PSS, and $MAPbI_3$ films obtained from precursor solutions of different concentrations; 0.75 M, 0.15 M, 0.05 M, and 0.01 M. The precursor solution was obtained from $MAI:PbI_2$ in a mixture of DMSO and GBL . The inset in the figure on the right shows the narrow range valence band spectra to allow comparison of features.

Although the shape of the valence band spectrum of 0.05 M still resembles that of PEDOT:PSS (see also S 2p signal from PEDOT:PSS in Figure 5.43), a finite density of states can be distinguished in the BE region between 2.5 and ca. 0.7 eV (inset, Figure 5.42), which can be associated with the formation of perovskite. The distinct change of the valence band spectral shape occurs from 0.05 M to 0.15 M and points toward a significant evolution of the electronic properties between both concentrations. This is consistent with the GIXRD data in Figure F7, Appendix F, which pinpoint that perovskite can be identified at concentration above 0.05 M. Note that the GIXRD patterns of $MAPbI_3$ do not feature any indication of a particular texture, in contrast to the fiber texture of $MAPbI_{3-x}Cl_x$. Also, the AFM micrograph of 0.01 M indicates the formation of clusters with only small gaps in-between and a much denser distribution, hence a better coverage, than in the case of, for instance, 1:10 in the first $MAPbI_{3-x}Cl_x$ series.

Based on XPS measurements, additional information about the film composition can be drawn for the first ($MAPbI_{3-x}Cl_x$ without toluene) and third ($MAPbI_3$ in DMSO-GBL and with toluene) series. Since the XPS data for both series yield comparable information, the results for the $MAPbI_3$ series are shown in Figure 5.43, whereas those corresponding to $MAPbI_{3-x}Cl_x$

can be found in Figure F3, Appendix F. The XPS spectra in Figure 5.43 are indicative of the presence of additional constituents for the two lowest concentrations (i.e. 0.01 M and 0.05 M). These contributions are compared to those identified or suggested in the work by Olthof *et. al*. [288], which investigated the case of very thin $MAPbI_3$ films obtained by thermal deposition on PEDOT:PSS substrate. The peaks fitted in black in Figure 5.43 are labeled as perovskite since they are centered at binding energies expected for $MAPbI_3$ perovskite.[8] The Pb $4f_{7/2}$ of both samples exhibit two peaks: one peak centered at 138.7 eV corresponding to perovskite and a second peak at higher binding energy. The high BE Pb 4f contribution has been suggested to represent lead in $PbSO_4$, as a product of a chemical reaction between lead in the deposited material and sulfur in PEDOT:PSS [288].

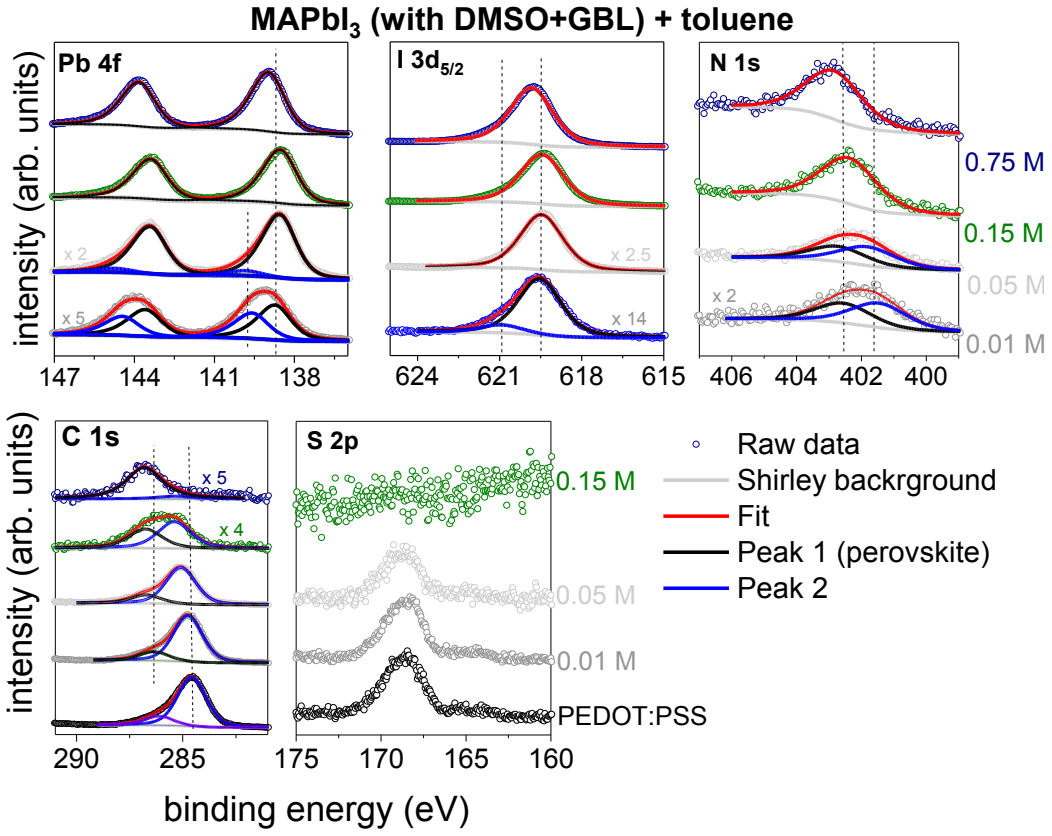

Figure 5.43 XPS spectra of Pb 4f, I $3d_{5/2}$, N 1s, C 1s, and S 2p core levels for $MAPbI_3$ films and of C 1s and S 2p core levels for a bare PEDOT:PSS layer (*cf.* Figure 5.42 for UPS spectra). The $MAPbI_3$ films are obtained from precursor solutions of different concentrations 0.75 M, 0.15 M, 0.05 M, and 0.01 M. For optimal representation, the signal intensity of some core levels is magnified.

[8] As aforementioned, no signal from perovskite could have been measured by GIXRD for these lowest concentrations.

These additional products have been observed for thickness up to 3 nm, before the DOS specific to $MAPbI_3$ arose [288]. The I 3d spectrum of 0.01 M also exhibits two contributions; the high BE peak has been associated with degradation products such as I_2 or methyl iodide CH_3I [288]. A N 1s peak distinct from the N 1s peak related to perovskite can also be observed at lower BE and could be related to decomposition products such as methylamine CH_3NH_2 or ammonia NH_3. The presence of these organic products containing a methyl group is supported by the strong C 1s peak signal at around 284.8 eV. Therefore, the films obtained from concentrations as low as 0.01 M and 0.05M can more easily degrade, likely due to the poorer morphology and the lack of crystalline order, especially in the case of 0.01 M. The same explanation would apply also for 1:10 and 1:100 for $MAPbI_{3-x}Cl_x$, since all the described peak contributions are observed for these samples as well (Figure F3, Appendix F).

The PES results indicate that the electronic structure of the films is correlated to the morphology, particularly to the film coverage. On the one hand, low concentration results in films with poor coverage and more prone to degradation, thus impeding a reliable ELA assessment. It should be noted that the degradation mentioned here describes the decomposition of the precursor materials or that of the perovskite and it cannot be ruled out that such degradation actually also occurs at the interface in the case of thicker films grown from solution. On the other hand, films obtained with higher solution concentrations exhibit electronic structure already comparable to that of thick perovskite films, which likely does not reflect the electronic structure evolution close to the interface anymore. The main electronic structure changes are found between the 1:10 and 1:5, PEDOT:PSS and 1:10, and 0.01 and 0.15 M for the first, second, and third series, respectively. Controlling the film morphology between these concentrations would be a recommended strategy to obtain uniform films with thicknesses of just a few nm. The application of the anti-solvent method during spin-coating distinctly improved the film morphology. Other methods such as time-temperature dependent annealing treatments, where ramp temperature control allowed obtaining highly oriented films with almost full coverage, are possible alternatives [336].

6 Summary and Conclusions

The main focus of this thesis was the characterization of the electronic properties of HOIP film surfaces, in particular those of the $MAPbI_{3-x}Cl_x$ perovskite upon formation and upon environmental exposure. The characterization not only provided insights into property-function relationships, pertaining to the perovskite film preparation, but also highlighted the close dependence of the material's electronic property on the environmental conditions. This work is particularly relevant for a better understanding of the prominence of HOIPs in solar cells and their major drawbacks – stability and reproducibility. Furthermore, the characterization of film surfaces in the present work represents a basis point to reckon with for future ELA investigation since variations of the surface electronic properties prior to interface formation will necessarily impact the ELA. The electronic properties of the surfaces were characterized by UPS to access the valence electronic structure including the frontier energy levels, and the work function. XPS was employed to monitor the materials' composition and the core level shifts related to electrostatic effects or varying chemical environment. Additional techniques were employed to correlate the electronic properties of the films with the structure (GIXRD), the morphology (AFM) and the bulk composition (ToF-SIMS). It is noteworthy that the latter technique holds a prevailing role in the first part of this work. Thus, first (ad 1), a multi-technique characterization allowed to delineate the role of chlorine in the formation of $MAPbI_{3-x}Cl_x$ perovskite films during thermal annealing, namely by monitoring property changes before and after complete crystallization. Second (ad 2), the effects of water vapor, oxygen, as well as air on the electronic properties of $MAPbI_{3-x}Cl_x$ surfaces were investigated to assess the film reproducibility and the potential degradation pathways in different environmental conditions. Third (ad 3), the electronic characterization was further extended to new perovskite materials for enhanced stability and new hole transport materials for more cost-effective perovskite-based solar cells. Finally,

preliminary test experiments relative to solvents effects on $MAPbI_{3-x}Cl_x$ and to HOIP thin film preparation from solution were performed (ad 4).

Ad 1) During thermal annealing, the formation of solution-processed $MAPbI_{3-x}Cl_x$ films, obtained from a mixture of $PbCl_2$ and MAI in a 1:3 ratio, was found to be mediated by an intermediate phase that likely acts as a structural template for the formation of textured perovskite films. Before complete film crystallization, this intermediate lead chloride-rich phase coexisted with the already formed $MAPbI_3$ perovskite phase and both phases were spatially well-separated throughout the depth of the films. The complete film crystallization was characterized by the full conversion into a single $MAPbI_3$ phase. The absence of chlorine in the final film was explained by its eventual release through the surface and by its accumulation at the perovskite/substrate interface during thermal annealing. The change in composition and structure associated with this phase evolution during $MAPbI_{3-x}Cl_x$ film formation resulted in a modification of the film's electronic properties. Particularly, shifts of the electronic levels by ca. 0.4 eV indicated that the material became more n-type upon annealing. This change was correlated with relatively lower MA content after annealing, illustrating how the excess or the deficiency of a compound can act as electronic defects. Furthermore, the present findings unequivocally clarify the debated presence and location of chlorine, which was found to mostly accumulate at the perovskite/substrate interface, possibly modifying the interfacial optoelectronic properties there. Importantly, the presence of chlorine through $PbCl_2$ in the precursor solution and the associated formation of an intermediate phase critically impact the film growth following a preferential orientation along the surface normal, which is particularly essential for enhanced charge transport in devices. These conclusions emphasize the predominant properties of $MAPbI_{3-x}Cl_x$ prepared from chlorine-based precursor in comparison to $MAPbI_3$ and can justify the preservation of the denomination $MAPbI_{3-x}Cl_x$. Nevertheless, the predominantly (pseudo-) cubic phase exhibited by the $MAPbI_{3-x}Cl_x$ films is in contrast with the generally claimed tetragonal phase of $MAPbI_3$. Such disagreement, which is likely related to the presence of chlorine, requires additional studies and a more thorough investigation of the structural phase transition around room temperature. The observations in this work also inspire new approaches for the fabrication of textured perovskite films through the controlled formation of a preceding structural template.

Ad 2) Exposure to water, oxygen, and air affected the electronic properties of $MAPbI_{3-x}Cl_x$ perovskite film surfaces with initially n-type character in contrasting manners. On one hand,

exposure to 4 mbar water partial pressure (p_{H2O}) induced concomitant shift of the work function and the VBM corresponding to a more n-type surface character. This phenomenon was partially reversible and was suggested to originate from either an increase in the density of defects states, possibly related to Pb^0-generation which eventually pins the E_F, or by a previously predicted local band gap widening upon hydration of the perovskite surface. It was also shown that exposure to p_{H2O} as low as 10^{-6} mbar, as encountered in HV or inert gas glove boxes, readily induced a reversible work function decrease, which was assigned to the water dipole moment. On the other hand, oxygen exposure (50 mbar partial pressure) led to work function and VBM shifts in reverse direction, that is the perovskite surface became less n-type. This latter trend was also systematically observed upon air exposure, thereby demonstrating the prevailing effect of oxygen over that of water in air. In line with previous work, these results suggest that oxygen acts as an acceptor that can capture electrons and form the highly reactive superoxide (O_2^-), the latter can readily react with the organic MA of the perovskite and thereby induce degradation. Consequently, the results seemingly point towards a more detrimental effect of oxygen than water in air. Difference spectra from the UPS data suggest not only the effective water adsorption but also the possibility of water dissociation into adsorbed hydroxyl. This latter species can be critical for initiating the perovskite material degradation. Still, the suggested water dissociation here remains at the stage of speculation and therefore requires more detailed studies before delivering any unambiguous statement. Besides, a more precise description of the water interaction at the perovskite surface is still challenged by difficulties in the production of well-defined surfaces with definite surface termination. Beyond the importance of the present findings in the context of perovskite degradation; they particularly emphasize the relevance of even seemingly negligible variations in the environment conditions that can significantly account for the reproducibility of the film electronic properties.

Ad 3) Based on $MAPbI_3$, new $MA_{1-x}Gua_xPbI_3$ perovskite systems stabilized by the introduction of the large guanidinium (Gua) cations were characterized by means of several methods, including PES. The XPS data confirmed that the initial MA/Gua ratio is preserved for all x values. UPS data indicated that $MA_{1-x}Gua_xPbI_3$ films with Gua amount up to x = 0.25 exhibited comparable electronic properties. At higher x values, the films exhibited gradually larger VBM in accordance with the gradual band gap widening, and a change in the electronic valence spectra, especially in the region associated with the organic moiety. The PES data support the suggested inclusion of the large Gua into the $MAPbI_3$ structure at lower x

percentage and the additional formation of lower dimensionality perovskite at higher x values (>0.25). Consequently, $MA_{1-x}Gua_xPbI_3$ films with x<0.25 exhibited enhanced stability in comparison to $MAPbI_3$, which is possibly due to the presence of increased number of hydrogen bonds within the structure. This work motivates new path for designing perovskite materials with improved stability.

Additionally, XPS and UPS were used to characterize synthesized TiS_2 nanoparticles which have been applied as novel low-cost hole transport materials (HTMs) in perovskite-based solar cells. The valence electronic structure of the material suggested an optimal ELA with the underlying perovskite substrate, which is reflected in the effective charge extraction at this interface, ultimately leading to enhanced solar cells efficiency in comparison to reference solar cells with no HTM. Nevertheless, the oxidation of the TiS_2 layer identified by XPS was suggested to mediate the accumulation of charges at the perovskite/TiS_2 interface.

Ad 4) The effects of selected solvents on the properties of $MAPbI_{3-x}Cl_x$ perovskite films were investigated in order to assess their potential suitability for deposition of charge transport layer on top of the perovskite films. Upon exposure to chlorobenzene (CB) and chloroform (CF), whilst the morphological, structural and optical properties were preserved, the electronic properties were strongly affected. A significant change in the valence band features was accompanied by a concomitant shift of the work function and VBM that correspond to a film becoming less n-type, possibly indicating the reduction of surface defects. These observations motivate the question of the possible influence of minute amount of solvents, present for instance in glove boxes, on the electronic properties of perovskite during preparation, analogous to the case of gases in Ad 2. Liquid water – in contrast to the lower water vapour exposure in Ad 2 – and dimethyl formamide (DMF) both instantly dissolved the perovskite films. Whereas the complete degradation into PbI_2 was demonstrated in the former case, a partial perovskite re-crystallization was observed upon ambient air drying at room temperature for the latter case. This illustrates both the easy formation and degradation of the perovskite film.

In preparation for an investigation of the ELA at the interface between solution-processed perovskite and a PEDOT:PSS substrate, the suitability of a solution dilution method was tested. This would, in theory, allow for the production of very (a few nm) thin perovskite layers which are required to access the electronic structure at the very interface and its evolution with increasing thickness, i.e. further away from the substrate. Instead of the establishment of any definite ELA, the electronic characterization rather highlighted the

dependence of the electronic properties on the preparation method and the film composition. This dependence was partly explained by varying morphology, notably by inhomogeneous film coverage.

The findings in this work highlight how the electronic properties of HOIPs can be influenced by their preparation, composition, and environmental conditions. The changes in structure, composition, and electronic properties during $MAPbI_{3-x}Cl_x$ film formation were successfully correlated and all converged to the importance of the added chlorine in the film growth with a preferred orientation along the substrate normal. Since such growth modes are particularly relevant for device performance, this work, therefore, provides improved understanding of the material's structure-property-function relationship. This work also stresses the critical impact of the environmental conditions on the electronic properties of $MAPbI_{3-x}Cl_x$ perovskite and calls for a particular care when assessing these electronic properties. Within the framework of multi-technique analysis, PES was also used to assess the impact of a mixture of cations in the stabilization of newly developed perovskite materials.

The findings in this work can serve as reference point for the characterization and design of HOIP materials in future studies. Such basis points are particularly valuable for the development of this complex class of materials, not only with regard to their stability but also for the deliberate exploitation of their immense potential.

Bibliography

[1] Lewis NS, Nocera DG. Powering the planet: Chemical challenges in solar energy utilization. *Proc Natl Acad Sci* 2006; 103: 15729–15735.

[2] Chen CJ. *Physics of Solar Energy*. John Wiley & Sons, 2011.

[3] Benick J. Approaching 22% efficiency with multicrystalline n-type silicon solar cells. *33rd Eur PV Sol Energy Conf Exhib 25-29 Sept 2017 Amst Neth* 2017; 5.

[4] Chu S, Cui Y, Liu N. The path towards sustainable energy. *Nat Mater* 2017; 16: 16–22.

[5] Heimel G, Salzmann I, Duhm S, et al. Design of Organic Semiconductors from Molecular Electrostatics. *Chem Mater* 2011; 23: 359–377.

[6] Kojima A, Teshima K, Shirai Y, et al. Organometal Halide Perovskites as Visible-Light Sensitizers for Photovoltaic Cells. *J Am Chem Soc* 2009; 131: 6050–6051.

[7] Yang WS, Park B-W, Jung EH, et al. Iodide management in formamidinium-lead-halide-based perovskite layers for efficient solar cells. *Science* 2017; 356: 1376–1379.

[8] Sahli F, Werner J, Kamino BA, et al. Fully textured monolithic perovskite/silicon tandem solar cells with 25.2% power conversion efficiency. *Nat Mater* 2018; 17: 820–826.

[9] Sha WEI, Ren X, Chen L, et al. The efficiency limit of $CH_3NH_3PbI_3$ perovskite solar cells. *Appl Phys Lett* 2015; 106: 221104.

[10] Shockley W, Queisser HJ. Detailed Balance Limit of Efficiency of p-n Junction Solar Cells. *J Appl Phys* 1961; 32: 510–519.

[11] Rühle S. Tabulated values of the Shockley–Queisser limit for single junction solar cells. *Sol Energy* 2016; 130: 139–147.

[12] Liang J, Wang C, Wang Y, et al. All-Inorganic Perovskite Solar Cells. *J Am Chem Soc* 2016; 138: 15829–15832.

[13] Lee MM, Teuscher J, Miyasaka T, et al. Efficient Hybrid Solar Cells Based on Meso-Superstructured Organometal Halide Perovskites. *Science* 2012; 1228604.

[14] Colella S, Mosconi E, Fedeli P, et al. $MAPbI_{3-x}Cl_x$ Mixed Halide Perovskite for Hybrid Solar Cells: The Role of Chloride as Dopant on the Transport and Structural Properties. *Chem Mater* 2013; 25: 4613–4618.

[15] Yu H, Wang F, Xie F, et al. The Role of Chlorine in the Formation Process of "$CH_3NH_3PbI_{3-x}Cl_x$" Perovskite. *Adv Funct Mater* 2014; 24: 7102–7108.

[16] Stranks SD, Eperon GE, Grancini G, et al. Electron-Hole Diffusion Lengths Exceeding 1 Micrometer in an Organometal Trihalide Perovskite Absorber. *Science* 2013; 342: 341–344.

[17] Song D, Heo JH, Han HJ, et al. Reproducible formation of uniform $CH_3NH_3PbI_{3-x}Cl_x$ mixed halide perovskite film by separation of the powder formation and spin-coating process. *J Power Sources* 2016; 310: 130–136.

[18] Zhou H, Chen Q, Li G, et al. Interface engineering of highly efficient perovskite solar cells. *Science* 2014; 345: 542–546.

[19] Park B, Philippe B, Gustafsson T, et al. Enhanced Crystallinity in Organic–Inorganic Lead Halide Perovskites on Mesoporous TiO2 via Disorder–Order Phase Transition. *Chem Mater* 2014; 26: 4466–4471.

[20] You J, Hong Z, Yang YM, et al. Low-temperature solution-processed perovskite solar cells with high efficiency and flexibility. *ACS Nano* 2014; 8: 1674–1680.

[21] Philippe B, Park B-W, Lindblad R, et al. Chemical and Electronic Structure Characterization of Lead Halide Perovskites and Stability Behavior under Different Exposures—A Photoelectron Spectroscopy Investigation. *Chem Mater* 2015; 27: 1720–1731.
[22] Williams ST, Zuo F, Chueh C-C, et al. Role of Chloride in the Morphological Evolution of Organo-Lead Halide Perovskite Thin Films. *ACS Nano* 2014; 8: 10640–10654.
[23] Saliba M, Tan KW, Sai H, et al. Influence of Thermal Processing Protocol upon the Crystallization and Photovoltaic Performance of Organic–Inorganic Lead Trihalide Perovskites. *J Phys Chem C* 2014; 118: 17171–17177.
[24] Tan KW, Moore DT, Saliba M, et al. Thermally Induced Structural Evolution and Performance of Mesoporous Block Copolymer-Directed Alumina Perovskite Solar Cells. *ACS Nano* 2014; 8: 4730–4739.
[25] Atittaya Naikaew PP. Role of phase composition for electronic states in $CH_3NH_3PbI_3$ prepared from $CH_3NH_3I/PbCl_2$ solution. *Appl Phys Lett* 2015; 106: 232104.
[26] Moore DT, Sai H, Tan KW, et al. Impact of the organic halide salt on final perovskite composition for photovoltaic applications. *APL Mater* 2014; 2: 081802.
[27] Unger EL, Bowring AR, Tassone CJ, et al. Chloride in Lead Chloride-Derived Organo-Metal Halides for Perovskite-Absorber Solar Cells. *Chem Mater* 2014; 26: 7158–7165.
[28] Colella S, Mosconi E, Pellegrino G, et al. Elusive Presence of Chloride in Mixed Halide Perovskite Solar Cells. *J Phys Chem Lett* 2014; 5: 3532–3538.
[29] Starr DE, Sadoughi G, Handick E, et al. Direct observation of an inhomogeneous chlorine distribution in $CH_3NH_3PbI_{3-x}Cl_x$ layers: surface depletion and interface enrichment. *Energy Environ Sci* 2015; 8: 1609–1615.
[30] Tidhar Y, Edri E, Weissman H, et al. Crystallization of methyl ammonium lead halide perovskites: implications for photovoltaic applications. *J Am Chem Soc* 2014; 136: 13249–13256.
[31] Bella F, Griffini G, Correa-Baena J-P, et al. Improving efficiency and stability of perovskite solar cells with photocurable fluoropolymers. *Science* 2016; aah4046.
[32] Stoumpos CC, Malliakas CD, Kanatzidis MG. Semiconducting Tin and Lead Iodide Perovskites with Organic Cations: Phase Transitions, High Mobilities, and Near-Infrared Photoluminescent Properties. *Inorg Chem* 2013; 52: 9019–9038.
[33] Noh JH, Im SH, Heo JH, et al. Chemical Management for Colorful, Efficient, and Stable Inorganic–Organic Hybrid Nanostructured Solar Cells. *Nano Lett* 2013; 13: 1764–1769.
[34] Niu G, Li W, Meng F, et al. Study on the stability of $CH_3NH_3PbI_3$ films and the effect of post-modification by aluminum oxide in all-solid-state hybrid solar cells. *J Mater Chem A* 2013; 2: 705–710.
[35] Han Y, Meyer S, Dkhissi Y, et al. Degradation observations of encapsulated planar $CH_3NH_3PbI_3$ perovskite solar cells at high temperatures and humidity. *J Mater Chem A* 2015; 3: 8139–8147.
[36] Eperon GE, Habisreutinger SN, Leijtens T, et al. The Importance of Moisture in Hybrid Lead Halide Perovskite Thin Film Fabrication. *ACS Nano* 2015; 9: 9380–9393.
[37] You J, Yang Y (Michael), Hong Z, et al. Moisture assisted perovskite film growth for high performance solar cells. *Appl Phys Lett* 2014; 105: 183902.
[38] Dubey A, Kantack N, Adhikari N, et al. Room temperature, air crystallized perovskite film for high performance solar cells. *J Mater Chem A* 2016; 4: 10231–10240.

[39] Shirayama M, Kato M, Miyadera T, et al. Degradation mechanism of $CH_3NH_3PbI_3$ perovskite materials upon exposure to humid air. *J Appl Phys* 2016; 119: 115501.
[40] Christians JA, Miranda Herrera PA, Kamat PV. Transformation of the Excited State and Photovoltaic Efficiency of $CH_3NH_3PbI_3$ Perovskite upon Controlled Exposure to Humidified Air. *J Am Chem Soc* 2015; 137: 1530–1538.
[41] Yang J, Siempelkamp BD, Liu D, et al. Investigation of $CH_3NH_3PbI_3$ Degradation Rates and Mechanisms in Controlled Humidity Environments Using in Situ Techniques. *ACS Nano* 2015; 9: 1955–1963.
[42] Leguy AMA, Hu Y, Campoy-Quiles M, et al. Reversible Hydration of $CH_3NH_3PbI_3$ in Films, Single Crystals, and Solar Cells. *Chem Mater* 2015; 27: 3397–3407.
[43] Fang H-H, Adjokatse S, Wei H, et al. Ultrahigh sensitivity of methylammonium lead tribromide perovskite single crystals to environmental gases. *Sci Adv* 2016; 2: e1600534.
[44] Müller C, Glaser T, Plogmeyer M, et al. Water Infiltration in Methylammonium Lead Iodide Perovskite: Fast and Inconspicuous. *Chem Mater* 2015; 27: 7835–7841.
[45] Hall GN, Stuckelberger M, Nietzold T, et al. The Role of Water in the Reversible Optoelectronic Degradation of Hybrid Perovskites at Low Pressure. *J Phys Chem C* 2017; 121: 25659–25665.
[46] Ke JC-R, Walton AS, Lewis DJ, et al. In situ investigation of degradation at organometal halide perovskite surfaces by X-ray photoelectron spectroscopy at realistic water vapour pressure. *Chem Commun* 2017; 53: 5231–5234.
[47] Li Y, Xu X, Wang C, et al. Degradation by Exposure of Co-Evaporated $CH_3NH_3PbI_3$ Thin Films. *J Phys Chem C* 2015; 119: 23996–24002.
[48] Kittel C. *Introduction to Solid State Physics*. Wiley, 2004.
[49] Ashcroft NW, Mermin ND. *Solid State Physics*. Holt, Rinehart and Winston, 1976.
[50] Hubbell JH, Veigele WmJ, Briggs EA, et al. Atomic form factors, incoherent scattering functions, and photon scattering cross sections. *J Phys Chem Ref Data* 1975; 4: 471–538.
[51] Brown PJ, Fox AG, Maslen EN, et al. Intensity of diffracted intensities. In: Prince E (ed) *International Tables for Crystallography*. Chester, England: International Union of Crystallography, pp. 554–595.
[52] Ingo Salzmann. *Structural and energetic properties of pentacene derivatives and heterostructures*. PhD Thesis, Humboldt-Universität zu Berlin, 2008.
[53] Sebastian Bommel. *Unraveling nanoscale molecular processes in organic thin films*. PhD Thesis, Humboldt-Universität zu Berlin, 2015.
[54] Sze SM, Ng KK. *Physics of Semiconductor Devices*. John Wiley & Sons, 2006.
[55] Ziman JM. *Principles of the Theory of Solids*. Cambridge University Press, 1979.
[56] Kronig R de L, Penney WG. Quantum mechanics of electrons in crystal lattices. *Proc R Soc Lond A* 1931; 130: 499–513.
[57] YU P, Cardona M. *Fundamentals of Semiconductors: Physics and Materials Properties*. 4th ed. Berlin Heidelberg: Springer-Verlag, 2010.
[58] Phillips JC. Energy-Band Interpolation Scheme Based on a Pseudopotential. *Phys Rev* 1958; 112: 685–695.
[59] Ibach H, Lüth H. *Solid-State Physics: An Introduction to Theory and Experiment*. Berlin Heidelberg: Springer-Verlag, 1991.
[60] Ibach H, Lüth H. *Solid-State Physics: An Introduction to Principles of Materials Science*. 2nd ed. Berlin Heidelberg: Springer-Verlag, 1996.
[61] Ibach H, Lüth H. *Festkörperphysik: Einführung in die Grundlagen*. 7th ed. Berlin Heidelberg: Springer-Verlag, 2009.

[62] Jackson WB, Johnson NM, Biegelsen DK. Density of gap states of silicon grain boundaries determined by optical absorption. *Appl Phys Lett* 1983; 43: 195–197.
[63] Tiedje T, Cebulka JM, Morel DL, et al. Evidence for Exponential Band Tails in Amorphous Silicon Hydride. *Phys Rev Lett* 1981; 46: 1425–1428.
[64] Mott NF. Conduction in non-crystalline materials. *Philos Mag J Theor Exp Appl Phys* 1969; 19: 835–852.
[65] Conwell EM. Impurity Band Conduction in Germanium and Silicon. *Phys Rev* 1956; 103: 51–61.
[66] Ishii H, Sugiyama K, Ito E, et al. Energy Level Alignment and Interfacial Electronic Structures at Organic/Metal and Organic/Organic Interfaces. *Adv Mater*; 11: 605–625.
[67] Kahn A, Koch N, Gao W. Electronic structure and electrical properties of interfaces between metals and π-conjugated molecular films. *J Polym Sci Part B Polym Phys*; 41: 2529–2548.
[68] Romaner L, Heimel G, Brédas J-L, et al. Impact of Bidirectional Charge Transfer and Molecular Distortions on the Electronic Structure of a Metal-Organic Interface. *Phys Rev Lett* 2007; 99: 256801.
[69] Bröker B, Hofmann OT, Rangger GM, et al. Density-Dependent Reorientation and Rehybridization of Chemisorbed Conjugated Molecules for Controlling Interface Electronic Structure. *Phys Rev Lett* 2010; 104: 246805.
[70] Koch N, Gerlach A, Duhm S, et al. Adsorption-Induced Intramolecular Dipole: Correlating Molecular Conformation and Interface Electronic Structure. *J Am Chem Soc* 2008; 130: 7300–7304.
[71] Oehzelt M, Akaike K, Koch N, et al. Energy-level alignment at organic heterointerfaces. *Sci Adv* 2015; 1: e1501127.
[72] Oehzelt M, Koch N, Heimel G. Organic semiconductor density of states controls the energy level alignment at electrode interfaces. *Nat Commun* 2014; 5: 4174.
[73] Pierret RF. *Advanced Semiconductor Fundamentals*. Prentice Hall, 2003.
[74] Streetman BG, Banerjee S. *Solid State Electronic Devices*. Pearson, 2015.
[75] Kahn A. Fermi level, work function and vacuum level. *Mater Horiz* 2016; 3: 7–10.
[76] Koch N. Organic Electronic Devices and Their Functional Interfaces. *ChemPhysChem* 2007; 8: 1438–1455.
[77] Cahen D, Kahn A. Electron Energetics at Surfaces and Interfaces: Concepts and Experiments. *Adv Mater*; 15: 271–277.
[78] Lüth H. *Solid Surfaces, Interfaces and Thin Films*. 4th ed. Berlin Heidelberg: Springer-Verlag, 2001.
[79] Mönch W. *Semiconductor Surfaces and Interfaces*. 3rd ed. Berlin Heidelberg: Springer-Verlag, 2001.
[80] Heras JM, Albano EV. Interaction of water molecules with polycrystalline films of Fe, Co and Ni with different surface roughness: I. Water adsorption on clean films. *Appl Surf Sci* 1983; 17: 207–219.
[81] Benndorf C, Nöbl C, Rusenberg M, et al. H_2O interaction with clean and oxygen precovered Ni(110). *Surf Sci* 1981; 111: 87–101.
[82] Heras JM, Viscido L, Amorebieta V. Änderung des Austrittspotentials von Nickel-Filmen bei der Bildung einer Monoschicht adsorbierten Wassers. *Berichte Bunsenges Für Phys Chem*; 82: 1035–1041.
[83] Thiel PA, Madey TE. The interaction of water with solid surfaces: Fundamental aspects. *Surf Sci Rep* 1987; 7: 211–385.
[84] Romaner L, Heimel G, Ambrosch-Draxl C, et al. The Dielectric Constant of Self-Assembled Monolayers. *Adv Funct Mater* 2008; 18: 3999–4006.

[85] Heimel G, Rissner F, Zojer E. Modeling the Electronic Properties of π-Conjugated Self-Assembled Monolayers. *Adv Mater* 2010; 22: 2494–2513.
[86] Natan A, Kuritz N, Kronik L. Polarizability, Susceptibility, and Dielectric Constant of Nanometer-Scale Molecular Films: A Microscopic View. *Adv Funct Mater* 2010; 20: 2077–2084.
[87] Tengstedt C, Osikowicz W, Salaneck WR, et al. Fermi-level pinning at conjugated polymer interfaces. *Appl Phys Lett* 2006; 88: 053502.
[88] Hill IG, Kahn A. Energy level alignment at interfaces of organic semiconductor heterostructures. *J Appl Phys* 1998; 84: 5583–5586.
[89] Schottky W. Halbleitertheorie der Sperrschicht. *Naturwissenschaften* 1938; 26: 843–843.
[90] Mott NF. The theory of crystal rectifiers. *Proc R Soc Lond A* 1939; 171: 27–38.
[91] Schottky W. Zur Halbleitertheorie der Sperrschicht- und Spitzengleichrichter. *Z Für Phys* 1939; 113: 367–414.
[92] Rose G. Ueber einige neue Mineralien des Urals. *J Für Prakt Chem* 1840; 19: 459–468.
[93] Weber D. $CH_3NH_3PbX_3$, ein Pb(II)-System mit kubischer Perowskitstruktur / $CH_3NH_3PbX_33$, a Pb(II)-System with Cubic Perovskite Structure. *Z Für Naturforschung B* 2014; 33: 1443–1445.
[94] Weber D. $CH_3NH_3SnBr_xI_{3-x}$ (x = 0-3), ein Sn(II)-System mit kubischer Perowskitstruktur / $CH_3NH_3SnBr_xI_{3-x}$ (x = 0-3), a Sn(II)-System with Cubic Perovskite Structure. *Z Für Naturforschung B* 2014; 33: 862–865.
[95] Mitzi DB, Feild CA, Harrison WTA, et al. Conducting tin halides with a layered organic-based perovskite structure. *Nature* 1994; 369: 467–469.
[96] Lee MM, Teuscher J, Miyasaka T, et al. Efficient Hybrid Solar Cells Based on Meso-Superstructured Organometal Halide Perovskites. *Science* 2012; 338: 643–647.
[97] Kim H-S, Lee C-R, Im J-H, et al. Lead Iodide Perovskite Sensitized All-Solid-State Submicron Thin Film Mesoscopic Solar Cell with Efficiency Exceeding 9%. *Sci Rep* 2012; 2: 591.
[98] Yang WS, Park B-W, Jung EH, et al. Iodide management in formamidinium-lead-halide–based perovskite layers for efficient solar cells. *Science* 2017; 356: 1376–1379.
[99] Zhao D, Wang C, Song Z, et al. Four-Terminal All-Perovskite Tandem Solar Cells Achieving Power Conversion Efficiencies Exceeding 23%. *ACS Energy Lett* 2018; 3: 305–306.
[100] Walsh A. Principles of Chemical Bonding and Band Gap Engineering in Hybrid Organic–Inorganic Halide Perovskites. *J Phys Chem C Nanomater Interfaces* 2015; 119: 5755–5760.
[101] Goldschmidt VM. Die Gesetze der Krystallochemie. *Naturwissenschaften* 1926; 14: 477–485.
[102] Poglitsch A, Weber D. Dynamic disorder in methylammoniumtrihalogenoplumbates (II) observed by millimeter-wave spectroscopy. *J Chem Phys* 1987; 87: 6373–6378.
[103] Park N-G, Grätzel M, Miyasaka T. *Organic-Inorganic Halide Perovskite Photovoltaics: From Fundamentals to Device Architectures*. Springer, 2016.
[104] Onoda-Yamamuro N, Matsuo T, Suga H. Calorimetric and IR spectroscopic studies of phase transitions in methylammonium trihalogenoplumbates (II)†. *J Phys Chem Solids* 1990; 51: 1383–1395.
[105] Wasylishen RE, Knop O, Macdonald JB. Cation rotation in methylammonium lead halides. *Solid State Commun* 1985; 56: 581–582.

[106] T. Weller M, J. Weber O, F. Henry P, et al. Complete structure and cation orientation in the perovskite photovoltaic methylammonium lead iodide between 100 and 352 K. *Chem Commun* 2015; 51: 4180–4183.
[107] Schmidt-Mende L, Weickert J. *Organic and Hybrid Solar Cells, An Introduction*. 1st ed. Berlin ; Boston: De Gruyter, 2016.
[108] Saidaminov MI, Abdelhady AL, Murali B, et al. High-quality bulk hybrid perovskite single crystals within minutes by inverse temperature crystallization. *Nat Commun* 2015; 6: 7586.
[109] Shi D, Adinolfi V, Comin R, et al. Low trap-state density and long carrier diffusion in organolead trihalide perovskite single crystals. *Science* 2015; 347: 519–522.
[110] Schulz P, Edri E, Kirmayer S, et al. Interface energetics in organo-metal halide perovskite-based photovoltaic cells. *Energy Environ Sci* 2014; 7: 1377–1381.
[111] Shin D, Kang D, Jeong J, et al. Unraveling the Charge Extraction Mechanism of Perovskite Solar Cells Fabricated with Two-Step Spin Coating: Interfacial Energetics between Methylammonium Lead Iodide and C_{60}. *J Phys Chem Lett* 2017; 8: 5423–5429.
[112] Lin Q, Armin A, Nagiri RCR, et al. Electro-optics of perovskite solar cells. *Nat Photonics* 2015; 9: 106–112.
[113] Saba M, Cadelano M, Marongiu D, et al. Correlated electron–hole plasma in organometal perovskites. *Nat Commun* 2014; 5: 5049.
[114] D'Innocenzo V, Grancini G, Alcocer MJP, et al. Excitons versus free charges in organo-lead tri-halide perovskites. *Nat Commun* 2014; 5: 3586.
[115] Green MA, Ho-Baillie A, Snaith HJ. The emergence of perovskite solar cells. *Nat Photonics* 2014; 8: 506–514.
[116] Baikie T, Fang Y, Kadro JM, et al. Synthesis and crystal chemistry of the hybrid perovskite (CH_3NH_3) PbI_3 for solid-state sensitised solar cell applications. *J Mater Chem A* 2013; 1: 5628–5641.
[117] Hutter EM, Gélvez-Rueda MC, Osherov A, et al. Direct–indirect character of the bandgap in methylammonium lead iodide perovskite. *Nat Mater* 2017; 16: 115–120.
[118] Motta C, El-Mellouhi F, Kais S, et al. Revealing the role of organic cations in hybrid halide perovskite $CH_3NH_3PbI_3$. *Nat Commun* 2015; 6: 7026.
[119] Brivio F, Butler KT, Walsh A, et al. Relativistic quasiparticle self-consistent electronic structure of hybrid halide perovskite photovoltaic absorbers. *Phys Rev B* 2014; 89: 155204.
[120] Wang T, Daiber B, Frost JM, et al. Indirect to direct bandgap transition in methylammonium lead halide perovskite. *Energy Environ Sci* 2017; 10: 509–515.
[121] Zheng F, Tan LZ, Liu S, et al. Rashba Spin–Orbit Coupling Enhanced Carrier Lifetime in $CH_3NH_3PbI_3$. *Nano Lett* 2015; 15: 7794–7800.
[122] Herz LM. Charge-Carrier Mobilities in Metal Halide Perovskites: Fundamental Mechanisms and Limits. *ACS Energy Lett* 2017; 2: 1539–1548.
[123] Köhler A, Bässler H. *Electronic Processes in Organic Semiconductors: An Introduction*. John Wiley & Sons, 2015.
[124] Takahashi Y, Hasegawa H, Takahashi Y, et al. Hall mobility in tin iodide perovskite CH3NH3SnI3: Evidence for a doped semiconductor. *J Solid State Chem* 2013; 205: 39–43.
[125] Huang J, Yuan Y, Shao Y, et al. Understanding the physical properties of hybrid perovskites for photovoltaic applications. *Nat Rev Mater* 2017; 2: 17042.
[126] Xiao Z, Dong Q, Bi C, et al. Solvent annealing of perovskite-induced crystal growth for photovoltaic-device efficiency enhancement. *Adv Mater Deerfield Beach Fla* 2014; 26: 6503–6509.

[127] M. Ball J, M. Lee M, Hey A, et al. Low-temperature processed meso-superstructured to thin-film perovskite solar cells. *Energy Environ Sci* 2013; 6: 1739–1743.
[128] Giorgi G, Fujisawa J-I, Segawa H, et al. Small Photocarrier Effective Masses Featuring Ambipolar Transport in Methylammonium Lead Iodide Perovskite: A Density Functional Analysis. *J Phys Chem Lett* 2013; 4: 4213–4216.
[129] Heo JH, Im SH, Noh JH, et al. Efficient inorganic-organic hybrid heterojunction solar cells containing perovskite compound and polymeric hole conductors. *Nat Photonics* 2013; 7: 486–491.
[130] Juarez-Perez EJ, Wuβler M, Fabregat-Santiago F, et al. Role of the Selective Contacts in the Performance of Lead Halide Perovskite Solar Cells. *J Phys Chem Lett* 2014; 5: 680–685.
[131] Tress W, Marinova N, Inganäs O, et al. The role of the hole-transport layer in perovskite solar cells - reducing recombination and increasing absorption. In: *2014 IEEE 40th Photovoltaic Specialist Conference (PVSC)*. 2014, pp. 1563–1566.
[132] Ma Y, Wang S, Zheng L, et al. Recent Research Developments of Perovskite Solar Cells. *Chin J Chem* 2014; 32: 957–963.
[133] Burschka J, Pellet N, Moon S-J, et al. Sequential deposition as a route to high-performance perovskite-sensitized solar cells. *Nature* 2013; 499: 316–319.
[134] Liu M, Johnston MB, Snaith HJ. Efficient planar heterojunction perovskite solar cells by vapour deposition. *Nature* 2013; 501: 395–398.
[135] Chen Q, Zhou H, Hong Z, et al. Planar Heterojunction Perovskite Solar Cells via Vapor-Assisted Solution Process. *J Am Chem Soc* 2014; 136: 622–625.
[136] Sharenko A, Toney MF. Relationships between Lead Halide Perovskite Thin-Film Fabrication, Morphology, and Performance in Solar Cells. *J Am Chem Soc* 2016; 138: 463–470.
[137] Park N-G. Methodologies for high efficiency perovskite solar cells. *Nano Converg* 2016; 3: 15.
[138] Eperon GE, Burlakov VM, Docampo P, et al. Morphological Control for High Performance, Solution-Processed Planar Heterojunction Perovskite Solar Cells. *Adv Funct Mater* 2014; 24: 151–157.
[139] Xiao Z, Bi C, Shao Y, et al. Efficient, high yield perovskite photovoltaic devices grown by interdiffusion of solution-processed precursor stacking layers. *Energy Environ Sci* 2014; 7: 2619–2623.
[140] Yang WS, Noh JH, Jeon NJ, et al. High-performance photovoltaic perovskite layers fabricated through intramolecular exchange. *Science* 2015; 348: 1234–1237.
[141] Jeon NJ, Noh JH, Kim YC, et al. Solvent engineering for high-performance inorganic-organic hybrid perovskite solar cells. *Nat Mater* 2014; 13: 897–903.
[142] Niesner D, Wilhelm M, Levchuk I, et al. Giant Rashba Splitting in $CH_3NH_3PbBr_3$ Organic-Inorganic Perovskite. *Phys Rev Lett* 2016; 117: 126401.
[143] Wang C, Ecker BR, Wei H, et al. Valence band dispersion measurements of perovskite single crystals using angle-resolved photoemission spectroscopy. *Phys Chem Chem Phys PCCP* 2017; 19: 5361–5365.
[144] Lee M-I, Barragán A, Nair MN, et al. First determination of the valence band dispersion of $CH_3NH_3PbI_3$ hybrid organic–inorganic perovskite. *J Phys Appl Phys* 2017; 50: 26LT02.
[145] Yang J-P, Meissner M, Yamaguchi T, et al. Band Dispersion and Hole Effective Mass of Methylammonium Lead Iodide Perovskite (Solar RRL 10⁄2018). *Sol RRL* 2018; 2: 1870216.

[146] Chang YH, Park CH, Matsuishi K. First-principles study of the structural and the electronic properties of the lead-halide-based inorganic-organic perovskites ($(CH_3NH_3)PbX_3$ and $CsPbX_3$ (X = Cl, Br, I). *J Korean Phys Soc* 2004; 44: 889–893.
[147] Umebayashi T, Asai K, Kondo T, et al. Electronic structures of lead iodide based low-dimensional crystals. *Phys Rev B* 2003; 67: 155405.
[148] Brandt RE, Stevanović V, Ginley DS, et al. Identifying defect-tolerant semiconductors with high minority carrier lifetimes: Beyond hybrid lead halide perovskites. *MRS Commun* 2015; 5: 265–275.
[149] Kawai H, Giorgi G, Marini A, et al. The Mechanism of Slow Hot-Hole Cooling in Lead-Iodide Perovskite: First-Principles Calculation on Carrier Lifetime from Electron–Phonon Interaction. *Nano Lett* 2015; 15: 3103–3108.
[150] Endres J, Egger DA, Kulbak M, et al. Valence and Conduction Band Densities of States of Metal Halide Perovskites: A Combined Experimental–Theoretical Study. *J Phys Chem Lett* 2016; 7: 2722–2729.
[151] Yin W-J, Shi T, Yan Y. Unusual defect physics in $CH_3NH_3PbI_3$ perovskite solar cell absorber. *Appl Phys Lett* 2014; 104: 063903.
[152] Kulbak M, Cahen D, Hodes G. How Important Is the Organic Part of Lead Halide Perovskite Photovoltaic Cells? Efficient $CsPbBr_3$ Cells. *J Phys Chem Lett* 2015; 6: 2452–2456.
[153] Kot M, Wojciechowski K, Snaith H, et al. Evidence of Nitrogen Contribution to the Electronic Structure of the $CH_3NH_3PbI_3$ Perovskite. *Chem – Eur J* 2018; 24: 3539–3544.
[154] Frost JM, Butler KT, Brivio F, et al. Atomistic Origins of High-Performance in Hybrid Halide Perovskite Solar Cells. *Nano Lett* 2014; 14: 2584–2590.
[155] Egger DA, Bera A, Cahen D, et al. What Remains Unexplained about the Properties of Halide Perovskites? *Adv Mater* 2018; 30: 1800691.
[156] Amat A, Mosconi E, Ronca E, et al. Cation-Induced Band-Gap Tuning in Organohalide Perovskites: Interplay of Spin–Orbit Coupling and Octahedra Tilting. *Nano Lett* 2014; 14: 3608–3616.
[157] Yin W-J, Shi T, Yan Y. Superior Photovoltaic Properties of Lead Halide Perovskites: Insights from First-Principles Theory. *J Phys Chem C* 2015; 119: 5253–5264.
[158] Kim J, Lee S-H, Lee JH, et al. The Role of Intrinsic Defects in Methylammonium Lead Iodide Perovskite. *J Phys Chem Lett* 2014; 5: 1312–1317.
[159] Wang Q, Shao Y, Xie H, et al. Qualifying composition dependent p and n self-doping in $CH_3NH_3PbI_3$. *Appl Phys Lett* 2014; 105: 163508.
[160] Conings B, Baeten L, De Dobbelaere C, et al. Perovskite-Based Hybrid Solar Cells Exceeding 10% Efficiency with High Reproducibility Using a Thin Film Sandwich Approach. *Adv Mater* 2014; 26: 2041–2046.
[161] Emara J, Schnier T, Pourdavoud N, et al. Impact of Film Stoichiometry on the Ionization Energy and Electronic Structure of $CH_3NH_3PbI_3$ Perovskites. *Adv Mater* 2016; 28: 553–559.
[162] Haruyama J, Sodeyama K, Han L, et al. Termination Dependence of Tetragonal $CH_3NH_3PbI_3$ Surfaces for Perovskite Solar Cells. *J Phys Chem Lett* 2014; 5: 2903–2909.
[163] Quarti C, De Angelis F, Beljonne D. Influence of Surface Termination on the Energy Level Alignment at the $CH_3NH_3PbI_3$ Perovskite/C_{60} Interface. *Chem Mater* 2017; 29: 958–968.
[164] Mosconi E, Azpiroz JM, De Angelis F. Ab Initio Molecular Dynamics Simulations of Methylammonium Lead Iodide Perovskite Degradation by Water. *Chem Mater* 2015; 27: 4885–4892.

[165] Kulkarni SA, Baikie T, Boix PP, et al. Band-gap tuning of lead halide perovskites using a sequential deposition process. *J Mater Chem A* 2014; 2: 9221–9225.
[166] Li C, Wei J, Sato M, et al. Halide-Substituted Electronic Properties of Organometal Halide Perovskite Films: Direct and Inverse Photoemission Studies. *ACS Appl Mater Interfaces* 2016; 8: 11526–11531.
[167] Grancini G, Roldán-Carmona C, Zimmermann I, et al. One-Year stable perovskite solar cells by 2D/3D interface engineering. *Nat Commun* 2017; 8: 15684.
[168] Tress W, Marinova N, Moehl T, et al. Understanding the rate-dependent J–V hysteresis, slow time component, and aging in $CH_3NH_3PbI_3$ perovskite solar cells: the role of a compensated electric field. *Energy Environ Sci* 2015; 8: 995–1004.
[169] Babayigit A, Thanh DD, Ethirajan A, et al. Assessing the toxicity of Pb- and Sn-based perovskite solar cells in model organism *Danio rerio*. *Sci Rep* 2016; 6: 18721.
[170] Binek A, Petrus ML, Huber N, et al. Recycling Perovskite Solar Cells To Avoid Lead Waste. *ACS Appl Mater Interfaces* 2016; 8: 12881–12886.
[171] Boyd CC, Cheacharoen R, Leijtens T, et al. Understanding Degradation Mechanisms and Improving Stability of Perovskite Photovoltaics. *Chem Rev*. Epub ahead of print 16 November 2018. DOI: 10.1021/acs.chemrev.8b00336.
[172] Brunetti B, Cavallo C, Ciccioli A, et al. On the Thermal and Thermodynamic (In)Stability of Methylammonium Lead Halide Perovskites. *Sci Rep* 2016; 6: 31896.
[173] Akbulatov AF, Luchkin SYu, Frolova LA, et al. Probing the Intrinsic Thermal and Photochemical Stability of Hybrid and Inorganic Lead Halide Perovskites. *J Phys Chem Lett* 2017; 8: 1211–1218.
[174] Tang X, Brandl M, May B, et al. Photoinduced degradation of methylammonium lead triiodide perovskite semiconductors. *J Mater Chem A* 2016; 4: 15896–15903.
[175] Albrecht MG, Green M. The kinetics of the photolysis of thin films of lead iodide. *J Phys Chem Solids* 1977; 38: 297–306.
[176] Zu F-S, Amsalem P, Salzmann I, et al. Impact of White Light Illumination on the Electronic and Chemical Structures of Mixed Halide and Single Crystal Perovskites. *Adv Opt Mater* 2017; 5: 1700139.
[177] Aristidou N, Eames C, Sanchez-Molina I, et al. Fast oxygen diffusion and iodide defects mediate oxygen-induced degradation of perovskite solar cells. *Nat Commun* 2017; 8: ncomms15218.
[178] Aristidou N, Sanchez-Molina I, Chotchuangchutchaval T, et al. The Role of Oxygen in the Degradation of Methylammonium Lead Trihalide Perovskite Photoactive Layers. *Angew Chem Int Ed* 2015; 54: 8208–8212.
[179] Bryant D, Aristidou N, Pont S, et al. Light and oxygen induced degradation limits the operational stability of methylammonium lead triiodide perovskite solar cells. *Energy Environ Sci* 2016; 9: 1655–1660.
[180] Sun Q, Fassl P, Becker-Koch D, et al. Role of Microstructure in Oxygen Induced Photodegradation of Methylammonium Lead Triiodide Perovskite Films. *Adv Energy Mater* 2017; 7: 1700977.
[181] Tian Y, Merdasa A, Unger E, et al. Enhanced Organo-Metal Halide Perovskite Photoluminescence from Nanosized Defect-Free Crystallites and Emitting Sites. *J Phys Chem Lett* 2015; 6: 4171–4177.
[182] Wei L, Ma W, Lian C, et al. Benign Interfacial Iodine Vacancies in Perovskite Solar Cells. *J Phys Chem C* 2017; 121: 5905–5913.
[183] deQuilettes DW, Zhang W, Burlakov VM, et al. Photo-induced halide redistribution in organic-inorganic perovskite films. *Nat Commun* 2016; 7: 11683.

[184] Anaya M, Galisteo-López JF, Calvo ME, et al. Origin of Light-Induced Photophysical Effects in Organic Metal Halide Perovskites in the Presence of Oxygen. *J Phys Chem Lett* 2018; 9: 3891–3896.
[185] Ciccioli A, Latini A. Thermodynamics and the Intrinsic Stability of Lead Halide Perovskites $CH_3NH_3PbX_3$. *J Phys Chem Lett* 2018; 9: 3756–3765.
[186] Juarez-Perez EJ, Hawash Z, Raga SR, et al. Thermal degradation of $CH_3NH_3PbI_3$ perovskite into NH_3 and CH_3I gases observed by coupled thermogravimetry–mass spectrometry analysis. *Energy Environ Sci* 2016; 9: 3406–3410.
[187] Juarez-Perez EJ, Ono LK, Maeda M, et al. Photodecomposition and thermal decomposition in methylammonium halide lead perovskites and inferred design principles to increase photovoltaic device stability. *J Mater Chem A* 2018; 6: 9604–9612.
[188] Kim N-K, Min YH, Noh S, et al. Investigation of Thermally Induced Degradation in $CH_3NH_3PbI_3$ Perovskite Solar Cells using In-situ Synchrotron Radiation Analysis. *Sci Rep* 2017; 7: 4645.
[189] Koehl M, Heck M, Wiesmeier S, et al. Modeling of the nominal operating cell temperature based on outdoor weathering. *Sol Energy Mater Sol Cells* 2011; 95: 1638–1646.
[190] Chung I, Song J-H, Im J, et al. CsSnI3: Semiconductor or Metal? High Electrical Conductivity and Strong Near-Infrared Photoluminescence from a Single Material. High Hole Mobility and Phase-Transitions. *J Am Chem Soc* 2012; 134: 8579–8587.
[191] Tang KC, You P, Yan F. Highly Stable All-Inorganic Perovskite Solar Cells Processed at Low Temperature. *Sol RRL* 2018; 2: 1800075.
[192] Ruess R, Benfer F, Böcher F, et al. Stabilization of Organic–Inorganic Perovskite Layers by Partial Substitution of Iodide by Bromide in Methylammonium Lead Iodide. *ChemPhysChem* 2016; 17: 1505–1511.
[193] Kim H-S, Seo J-Y, Park N-G. Material and Device Stability in Perovskite Solar Cells. *ChemSusChem* 2016; 9: 2528–2540.
[194] Hoke ET, Slotcavage DJ, Dohner ER, et al. Reversible photo-induced trap formation in mixed-halide hybrid perovskites for photovoltaics. *Chem Sci* 2014; 6: 613–617.
[195] Jeon NJ, Noh JH, Yang WS, et al. Compositional engineering of perovskite materials for high-performance solar cells. *Nature* 2015; 517: 476–480.
[196] Bi D, Tress W, Dar MI, et al. Efficient luminescent solar cells based on tailored mixed-cation perovskites. *Sci Adv* 2016; 2: e1501170.
[197] Saliba M, Matsui T, Seo J-Y, et al. Cesium-containing triple cation perovskite solar cells: improved stability, reproducibility and high efficiency. *Energy Environ Sci* 2016; 9: 1989–1997.
[198] Reference Air Mass 1.5 Spectra | Grid Modernization | NREL, https://www.nrel.gov/grid/solar-resource/spectra-am1.5.html (accessed 1 December 2018).
[199] Voß B, Knobloch J, Goetzberger A. *Sonnenenergie: Photovoltaik: Physik und Technologie der Solarzelle*. 2., überarbeitete und erweiterte Aufl. 1997. Stuttgart: Teubner Verlag, 1997.
[200] Nelson J. *The Physics of Solar Cells*. World Scientific Publishing Company, 2003.
[201] Johannes Frisch. *Electronic properties of interfaces in polymer based organic photovoltaic cells*. PhD Thesis, Humboldt-Universität zu Berlin, 2015.
[202] Shaklee KL, Nahory RE. Valley-Orbit Splitting of Free Excitons? The Absorption Edge of Si. *Phys Rev Lett* 1970; 24: 942–945.
[203] Knupfer M. Exciton binding energies in organic semiconductors. *Appl Phys A* 2003; 77: 623–626.

[204] Miyata A, Mitioglu A, Plochocka P, et al. Direct measurement of the exciton binding energy and effective masses for charge carriers in organic–inorganic tri-halide perovskites. *Nat Phys* 2015; 11: 582–587.
[205] Riede M, Mueller T, Tress W, et al. Small-molecule solar cells—status and perspectives. *Nanotechnology* 2008; 19: 424001.
[206] Scharber MC, Mühlbacher D, Koppe M, et al. Design Rules for Donors in Bulk-Heterojunction Solar Cells—Towards 10 % Energy-Conversion Efficiency. *Adv Mater*; 18: 789–794.
[207] Snaith HJ, Abate A, Ball JM, et al. Anomalous Hysteresis in Perovskite Solar Cells. *J Phys Chem Lett* 2014; 5: 1511–1515.
[208] van Reenen S, Kemerink M, Snaith HJ. Modeling Anomalous Hysteresis in Perovskite Solar Cells. *J Phys Chem Lett* 2015; 6: 3808–3814.
[209] Hertz H. Ueber einen Einfluss des ultravioletten Lichtes auf die electrische Entladung. *Ann Phys* 1887; 267: 983–1000.
[210] Einstein A. Über einen die Erzeugung und Verwandlung des Lichtes betreffenden heuristischen Gesichtspunkt. *Ann Phys* 1905; 322: 132–148.
[211] Hüfner S. *Photoelectron Spectroscopy: Principles and Applications*. 3rd ed. Berlin Heidelberg: Springer-Verlag, 2003.
[212] Koch N. Energy levels at interfaces between metals and conjugated organic molecules. *J Phys Condens Matter* 2008; 20: 184008.
[213] Schattke W, Hove MAV. *Solid-State Photoemission and Related Methods: Theory and Experiment*. John Wiley & Sons, 2008.
[214] American society for testing and materials. Standard terminology relating to surface analysis (E673-90). *Surf Interface Anal* 1991; 17: 951–958.
[215] Seah MP, Dench WA. Quantitative electron spectroscopy of surfaces: A standard data base for electron inelastic mean free paths in solids. *Surf Interface Anal* 1979; 1: 2–11.
[216] Schlesinger R. *Energy-Level Control at Hybrid Inorganic/Organic Semiconductor Interfaces*. Springer International Publishing, 2017.
[217] Végh J. The Shirley background revised. *J Electron Spectrosc Relat Phenom* 2006; 151: 159–164.
[218] Krause MO, Oliver JH. Natural widths of atomic K and L levels, Kα X-ray lines and several KLL Auger lines. *J Phys Chem Ref Data* 1979; 8: 329–338.
[219] Koch N, Pop D, Weber RL, et al. Radiation induced degradation and surface charging of organic thin films in ultraviolet photoemission spectroscopy. *Thin Solid Films* 2001; 391: 81–87.
[220] Ibach H. *Electron Spectroscopy for Surface Analysis*. Springer Science & Business Media, 2012.
[221] Einstein TL. Changes in density of states caused by chemisorption. *Phys Rev B* 1975; 12: 1262–1274.
[222] Henrich VE. Ultraviolet photoemission studies of molecular adsorption on oxide surfaces. *Prog Surf Sci* 1979; 9: 143–164.
[223] Penn DR. Photoemission Spectroscopy in the Presence of Adsorbate-Covered Surfaces. *Phys Rev Lett* 1972; 28: 1041–1044.
[224] Moulder JF, Stickle WF, Sobol PE, et al. *Handbook of X-ray Photoelectron Spectroscopy*. 1995.
[225] Sakurai JJ. *Modern quantum mechanics*. Rev. ed., reprinted with corr. Reading, Mass. ; Bonn [u.a.]: Addison-Wesley, 1995.
[226] Seah MP. The quantitative analysis of surfaces by XPS: A review. *Surf Interface Anal* 1980; 2: 222–239.

[227] Benninghoven A. *Secondary ion mass spectrometry: basic concepts, instrumental aspects, applications and trends / A. Benninghoven ; F. G. Rüdenauer ; H. W. Werner*. New York u.a.: New York ua: Wiley, 1987.
[228] Benninghoven A. Chemical Analysis of Inorganic and Organic Surfaces and Thin Films by Static Time-of-Flight Secondary Ion Mass Spectrometry (TOF-SIMS). *Angew Chem Int Ed Engl* 1994; 33: 1023–1043.
[229] Harvey SP, Li Z, Christians JA, et al. Probing Perovskite Inhomogeneity beyond the Surface: TOF-SIMS Analysis of Halide Perovskite Photovoltaic Devices. *ACS Appl Mater Interfaces* 2018; 10: 28541–28552.
[230] Ralaiarisoa M, Busby Y, Frisch J, et al. Correlation of annealing time with crystal structure, composition, and electronic properties of $CH_3NH_3PbI_{3-x}Cl_x$ mixed-halide perovskite films. *Phys Chem Chem Phys* 2016; 19: 828–836.
[231] Pithan L. *On the role of external stimuli to tailor growth of organic thin films*. PhD Thesis, Humboldt-Universität zu Berlin, 2017.
[232] Vineyard GH. Grazing-incidence diffraction and the distorted-wave approximation for the study of surfaces. *Phys Rev B* 1982; 26: 4146–4159.
[233] Als-Nielsen J, McMorrow D. *Elements of Modern X-ray Physics*. John Wiley & Sons, 2011.
[234] Binnig G, Quate CF, Gerber Ch. Atomic Force Microscope. *Phys Rev Lett* 1986; 56: 930–933.
[235] Gadelmawla ES, Koura MM, Maksoud TMA, et al. Roughness parameters. *J Mater Process Technol* 2002; 123: 133–145.
[236] Honda M, Kanai K, Komatsu K, et al. Atmospheric effect of air, N_2, O_2, and water vapor on the ionization energy of titanyl phthalocyanine thin film studied by photoemission yield spectroscopy. *J Appl Phys* 2007; 102: 103704.
[237] Ballantyne JM. Effect of Phonon Energy Loss on Photoemissive Yield near Threshold. *Phys Rev B* 1972; 6: 1436–1455.
[238] Kochi M, Harada Y, Hirooka T, et al. Photoemission from Organic Crystal in Vacuum Ultraviolet Region. IV. *Bull Chem Soc Jpn* 1970; 43: 2690–2702.
[239] Meyerhofer D. Characteristics of resist films produced by spinning. *J Appl Phys* 1978; 49: 3993–3997.
[240] Greczynski G, Kugler T, Salaneck WR. Characterization of the PEDOT-PSS system by means of X-ray and ultraviolet photoelectron spectroscopy. *Thin Solid Films* 1999; 354: 129–135.
[241] Hwang J, Amy F, Kahn A. Spectroscopic study on sputtered PEDOT·PSS: Role of surface PSS layer. *Org Electron* 2006; 7: 387–396.
[242] Koch N, Kahn A, Ghijsen J, et al. Conjugated organic molecules on metal versus polymer electrodes: Demonstration of a key energy level alignment mechanism. *Appl Phys Lett* 2002; 82: 70–72.
[243] Jodlowski AD, Roldán-Carmona C, Grancini G, et al. Large guanidinium cation mixed with methylammonium in lead iodide perovskites for 19% efficient solar cells. *Nat Energy* 2017; 2: 972–979.
[244] Aron J. Huckaba, Saba Gharibzadeh, Maryline Ralaiarisoa, et al. Low cost TiS_2 as Hole Transport Material for Perovskite Solar Cells. *Small Methods* 2017; 1: 1700250.
[245] Jeong S, Yoo D, Jang J, et al. Well-Defined Colloidal 2-D Layered Transition-Metal Chalcogenide Nanocrystals via Generalized Synthetic Protocols. *J Am Chem Soc* 2012; 134: 18233–18236.
[246] Többens DM, Zander S. KMC-2: an X-ray beamline with dedicated diffraction and XAS endstations at BESSY II. *J Large-Scale Res Facil JLSRF* 2016; 2: 49.

[247] Philip Schulz EE. Interface energetics in organo-metal halide perovskite-based photovoltaic cells. *Energy Amp Environ Sci* 2014.
[248] Pool VL, Gold-Parker A, McGehee MD, et al. Chlorine in $PbCl_2$-Derived Hybrid-Perovskite Solar Absorbers. *Chem Mater* 2015; 27: 7240–7243.
[249] Matteocci F, Busby Y, Pireaux J-J, et al. Interface and Composition Analysis on Perovskite Solar Cells. *ACS Appl Mater Interfaces* 2015; 7: 26176–26183.
[250] Yang B, Keum J, Ovchinnikova OS, et al. Deciphering Halogen Competition in Organometallic Halide Perovskite Growth. *J Am Chem Soc* 2016; 138: 5028–5035.
[251] Simbrunner J, Simbrunner C, Schrode B, et al. Indexing of grazing-incidence X-ray diffraction patterns: the case of fibre-textured thin films. *Acta Crystallogr Sect Found Adv* 2018; 74: 373–387.
[252] Wang Q, Lyu M, Zhang M, et al. Transition from the Tetragonal to Cubic Phase of Organohalide Perovskite: The Role of Chlorine in Crystal Formation of $CH_3NH_3PbI_3$ on TiO_2 Substrates. *J Phys Chem Lett* 2015; 6: 4379–4384.
[253] Pistor P, Borchert J, Fränzel W, et al. Monitoring the Phase Formation of Coevaporated Lead Halide Perovskite Thin Films by in Situ X-ray Diffraction. *J Phys Chem Lett* 2014; 5: 3308–3312.
[254] Luo S, Daoud WA. Crystal Structure Formation of $CH_3NH_3PbI_{3-x}Cl_x$ Perovskite. *Materials* 2016; 9: 123.
[255] Soe CMM, Stoumpos CC, Harutyunyan B, et al. Room Temperature Phase Transition in Methylammonium Lead Iodide Perovskite Thin Films Induced by Hydrohalic Acid Additives. *ChemSusChem*; 9: 2656–2665.
[256] Huang Y-C, Tsao C-S, Cho Y-J, et al. Insight into Evolution, Processing and Performance of Multi-length-scale Structures in Planar Heterojunction Perovskite Solar Cells. *Sci Rep* 2015; 5: 13657.
[257] Yamamuro O, Matsuo T, Suga H, et al. Neutron diffraction and calorimetric studies of methylammonium iodide. *Acta Crystallogr B* 1992; 48: 329–336.
[258] Sass RL, Brackett EB, Brackett TE. THE CRYSTAL STRUCTURE OF LEAD CHLORIDE. *J Phys Chem* 1963; 67: 2863–2864.
[259] Chia H-C, Sheu H-S, Hsiao Y-Y, et al. Critical Intermediate Structure That Directs the Crystalline Texture and Surface Morphology of Organo-Lead Trihalide Perovskite. *ACS Appl Mater Interfaces* 2017; 9: 36897–36906.
[260] Zheng Z, Liu A, Wang S, et al. In situ growth of epitaxial lead iodide films composed of hexagonal single crystals. *J Mater Chem* 2005; 15: 4555–4559.
[261] Noël C, Houssiau L. Hybrid Organic/Inorganic Materials Depth Profiling Using Low Energy Cesium Ions. *J Am Soc Mass Spectrom* 2016; 27: 908–916.
[262] Wehbe N, Pireaux J-J, Houssiau L. XPS Evidence for Negative Ion Formation in SIMS Depth Profiling of Organic Material with Cesium. *J Phys Chem C* 2014; 118: 26613–26620.
[263] Busby Y, Nau S, Sax S, et al. Direct observation of conductive filament formation in Alq3 based organic resistive memories. *J Appl Phys* 2015; 118: 075501.
[264] Dualeh A, Tétreault N, Moehl T, et al. Effect of Annealing Temperature on Film Morphology of Organic-Inorganic Hybrid Pervoskite Solid-State Solar Cells. *Adv Funct Mater* 2014; 24: 3250–3258.
[265] Artyushkova K, Fulghum JE. Quantification of PVC–PMMA polymer blend compositions by XPS in the presence of x-ray degradation effects. *Surf Interface Anal* 2001; 31: 352–361.
[266] Calloni A, Abate A, Bussetti G, et al. Stability of Organic Cations in Solution-Processed $CH_3NH_3PbI_3$ Perovskites: Formation of Modified Surface Layers. *J Phys Chem C* 2015; 119: 21329–21335.

[267] Ralaiarisoa M, Salzmann I, Zu F-S, et al. Effect of Water, Oxygen, and Air Exposure on $CH_3NH_3PbI_{3-x}Cl_x$ Perovskite Surface Electronic Properties. *Adv Electron Mater* 2018; 0: 1800307.
[268] Ishii H, Sugiyama K, Ito E, et al. Energy Level Alignment and Interfacial Electronic Structures at Organic/Metal and Organic/Organic Interfaces. *Adv Mater* 1999; 11: 605–625.
[269] Koocher NZ, Saldana-Greco D, Wang F, et al. Polarization Dependence of Water Adsorption to $CH_3NH_3PbI_3$ (001) Surfaces. *J Phys Chem Lett* 2015; 6: 4371–4378.
[270] Winter B, Weber R, Widdra W, et al. Full Valence Band Photoemission from Liquid Water Using EUV Synchrotron Radiation. *J Phys Chem A* 2004; 108: 2625–2632.
[271] Zhu Z, Hadjiev VG, Rong Y, et al. Interaction of Organic Cation with Water Molecule in Perovskite $MAPbI_3$: From Dynamic Orientational Disorder to Hydrogen Bonding. *Chem Mater* 2016; 28: 7385–7393.
[272] Grancini G, D'Innocenzo V, Dohner ER, et al. $CH_3NH_3PbI_3$ perovskite single crystals: surface photophysics and their interaction with the environment. *Chem Sci* 2015; 6: 7305–7310.
[273] Sadoughi G, Starr DE, Handick E, et al. Observation and Mediation of the Presence of Metallic Lead in Organic–Inorganic Perovskite Films. *ACS Appl Mater Interfaces* 2015; 7: 13440–13444.
[274] Guo J-H, Luo Y, Augustsson A, et al. X-ray emission spectroscopy of hydrogen bonding and electronic structure of liquid water. *Phys Rev Lett* 2002; 89: 137402.
[275] Connor JA, Considine M, Hillier IH, et al. Low energy photoelectron spectroscopy of solids. Aspects of experimental methodology concerning metals and insulators. *J Electron Spectrosc Relat Phenom* 1977; 12: 143–159.
[276] Kim YD, Wei T, Stultz J, et al. Dissociation of Water on a Flat, Ordered Silica Surface. *Langmuir* 2003; 19: 1140–1142.
[277] Henderson MA. The interaction of water with solid surfaces: fundamental aspects revisited. *Surf Sci Rep* 2002; 46: 1–308.
[278] Zhang L, Sit PH-L. Ab initio static and dynamic study of $CH_3NH_3PbI_3$ degradation in the presence of water, hydroxyl radicals, and hydroxide ions. *RSC Adv* 2016; 6: 76938–76947.
[279] Zhang L, Sit PH-L. Ab Initio Study of Interaction of Water, Hydroxyl Radicals, and Hydroxide Ions with $CH_3NH_3PbI_3$ and $CH_3NH_3PbBr_3$ Surfaces. *J Phys Chem C* 2015; 119: 22370–22378.
[280] Hoffman D, Singh B, III JHT. *Handbook of Vacuum Science and Technology*. Academic Press, 1997.
[281] Frankel GS, Chen X-B, Gupta RK, et al. Effect of Vacuum System Base Pressure on Corrosion Resistance of Sputtered Al Thin Films. *J Electrochem Soc* 2014; 161: C195–C200.
[282] Kieslich G, Sun S, Cheetham AK. Solid-state principles applied to organic–inorganic perovskites: new tricks for an old dog. *Chem Sci* 2014; 5: 4712–4715.
[283] Szafrański M. Investigation of phase instabilities in guanidinium halogenoplumbates(II). *Thermochim Acta* 1997; 307: 177–183.
[284] Szafrański M, Katrusiak A. Phase transitions in the layered structure of diguanidinium tetraiodoplumbate. *Phys Rev B* 2000; 61: 1026–1035.
[285] Jodlowski AD, Yépez A, Luque R, et al. Benign-by-Design Solventless Mechanochemical Synthesis of Three-, Two-, and One-Dimensional Hybrid Perovskites. *Angew Chem Int Ed Engl* 2016; 55: 14972–14977.
[286] Gund P. Guanidine, trimethylenemethane, and 'Y-delocalization.' Can acyclic compounds have 'aromatic' stability? *J Chem Educ* 1972; 49: 100.

[287] Williams ML, Gready JE. Guanidinium-Type resonance stabilization and its biological implications. I. the guanidine and extended-guanidine series. *J Comput Chem* 1989; 10: 35–54.
[288] Olthof S, Meerholz K. Substrate-dependent electronic structure and film formation of $MAPbI_3$ perovskites. *Sci Rep* 2017; 7: 40267.
[289] Lindblad R, Bi D, Park B, et al. Electronic Structure of $TiO_2/CH_3NH_3PbI_3$ Perovskite Solar Cell Interfaces. *J Phys Chem Lett* 2014; 5: 648–653.
[290] Huang J, Xu P, Liu J, et al. Sequential Introduction of Cations Deriving Large-Grain $Cs_xFA_{1-x}PbI_3$ Thin Film for Planar Hybrid Solar Cells: Insight into Phase-Segregation and Thermal-Healing Behavior. *Small* 2017; 13: 1603225.
[291] Gholipour S, Ali AM, Correa-Baena J-P, et al. Globularity-Selected Large Molecules for a New Generation of Multication Perovskites. *Adv Mater* 2017; 29: 1702005.
[292] De Marco N, Zhou H, Chen Q, et al. Guanidinium: A Route to Enhanced Carrier Lifetime and Open-Circuit Voltage in Hybrid Perovskite Solar Cells. *Nano Lett* 2016; 16: 1009–1016.
[293] Soe CMM, Stoumpos CC, Kepenekian M, et al. New Type of 2D Perovskites with Alternating Cations in the Interlayer Space, $(C(NH_2)_3)(CH_3NH_3)nPb_nI_{3n+1}$: Structure, Properties, and Photovoltaic Performance. *J Am Chem Soc* 2017; 139: 16297–16309.
[294] Quan LN, Yuan M, Comin R, et al. Ligand-Stabilized Reduced-Dimensionality Perovskites. *J Am Chem Soc* 2016; 138: 2649–2655.
[295] Buin A, Comin R, Xu J, et al. Halide-Dependent Electronic Structure of Organolead Perovskite Materials. *Chem Mater* 2015; 27: 4405–4412.
[296] Nagabhushana GP, Shivaramaiah R, Navrotsky A. Direct calorimetric verification of thermodynamic instability of lead halide hybrid perovskites. *Proc Natl Acad Sci* 2016; 113: 7717–7721.
[297] Gratia P, Grancini G, Audinot J-N, et al. Intrinsic Halide Segregation at Nanometer Scale Determines the High Efficiency of Mixed Cation/Mixed Halide Perovskite Solar Cells. *J Am Chem Soc* 2016; 138: 15821–15824.
[298] Preda N, Mihut L, Baibarac M, et al. Raman and photoluminescence studies on intercalated lead iodide with pyridine and iodine. *J Optoelectron Adv Mater* 2008; 10: 319–322.
[299] Ono LK, Schulz P, Endres JJ, et al. Air-Exposure-Induced Gas-Molecule Incorporation into Spiro-MeOTAD Films. *J Phys Chem Lett* 2014; 5: 1374–1379.
[300] Hock R, Mayer T, Jaegermann W. p-Type Doping of Spiro-MeOTAD with WO_3 and the Spiro-MeOTAD/WO_3 Interface Investigated by Synchrotron-Induced Photoelectron Spectroscopy. *J Phys Chem C* 2012; 116: 18146–18154.
[301] Domanski K, Correa-Baena J-P, Mine N, et al. Not All That Glitters Is Gold: Metal-Migration-Induced Degradation in Perovskite Solar Cells. *ACS Nano* 2016; 10: 6306–6314.
[302] Yang G, Tao H, Qin P, et al. Recent progress in electron transport layers for efficient perovskite solar cells. *J Mater Chem A* 2016; 4: 3970–3990.
[303] Yu Z, Sun L. Recent Progress on Hole-Transporting Materials for Emerging Organometal Halide Perovskite Solar Cells. *Adv Energy Mater* 2015; 5: 1500213.
[304] Saliba M, Orlandi S, Matsui T, et al. A molecularly engineered hole-transporting material for efficient perovskite solar cells. *Nat Energy* 2016; 1: 15017.
[305] Saliba M, Matsui T, Seo J-Y, et al. Cesium-containing triple cation perovskite solar cells: improved stability, reproducibility and high efficiency. *Energy Environ Sci* 2016; 9: 1989–1997.

[306] Rakstys K, Saliba M, Gao P, et al. Highly Efficient Perovskite Solar Cells Employing an Easily Attainable Bifluorenylidene-Based Hole-Transporting Material. *Angew Chem* 2016; 128: 7590–7594.
[307] Saliba M, Orlandi S, Matsui T, et al. A molecularly engineered hole-transporting material for efficient perovskite solar cells. *Nat Energy* 2016; 1: 15017.
[308] Qin P, Tanaka S, Ito S, et al. Inorganic hole conductor-based lead halide perovskite solar cells with 12.4% conversion efficiency. *Nat Commun* 2014; 5: 3834.
[309] Christians JA, Fung RCM, Kamat PV. An Inorganic Hole Conductor for Organo-Lead Halide Perovskite Solar Cells. Improved Hole Conductivity with Copper Iodide. *J Am Chem Soc* 2014; 136: 758–764.
[310] Gharibzadeh S, Nejand BA, Moshaii A, et al. Two-Step Physical Deposition of a Compact CuI Hole-Transport Layer and the Formation of an Interfacial Species in Perovskite Solar Cells. *ChemSusChem* 2016; 9: 1929–1937.
[311] You J, Meng L, Song T-B, et al. Improved air stability of perovskite solar cells via solution-processed metal oxide transport layers. *Nat Nanotechnol* 2016; 11: 75–81.
[312] Zuo C, Ding L. Solution-Processed Cu_2O and CuO as Hole Transport Materials for Efficient Perovskite Solar Cells. *Small* 2015; 11: 5528–5532.
[313] Koo B, Jung H, Park M, et al. Pyrite-Based Bi-Functional Layer for Long-Term Stability and High-Performance of Organo-Lead Halide Perovskite Solar Cells. *Adv Funct Mater* 2016; 26: 5400–5407.
[314] Huckaba AJ, Sanghyun P, Grancini G, et al. Exceedingly Cheap Perovskite Solar Cells Using Iron Pyrite Hole Transport Materials. *ChemistrySelect* 2016; 1: 5316–5319.
[315] Whittingham MS. Electrical Energy Storage and Intercalation Chemistry. *Science* 1976; 192: 1126–1127.
[316] Gupta U, Rao BG, Maitra U, et al. Visible-Light-Induced Generation of H_2 by Nanocomposites of Few-Layer TiS_2 and TaS_2 with CdS Nanoparticles. *Chem – Asian J* 2014; 9: 1311–1315.
[317] Conroy LE, Park KC. Electrical properties of the Group IV disulfides, titanium disulfide, zirconium disulfide, hafnium disulfide and tin disulfide. *Inorg Chem* 1968; 7: 459–463.
[318] Xu Y, Schoonen MAA. The absolute energy positions of conduction and valence bands of selected semiconducting minerals. *Am Mineral* 2000; 85: 543–556.
[319] Let A, Mainwaring D, Rix C, et al. Synthesis and Optical Properties of TiS2 Nanoclusters. *Rev Roum Chim* 2007; 52: 235–241.
[320] Morasse RAL, Li T, Baum ZJ, et al. Rational Synthesis of Dimensionally Reduced TiS2 Phases. *Chem Mater* 2014; 26: 4776–4780.
[321] Coster D, L. Kronig RD. New type of auger effect and its influence on the x-ray spectrum. *Physica* 1935; 2: 13–24.
[322] Martinez H, Auriel C, Gonbeau D, et al. Studies of 1T TiS_2 by STM, AFM and XPS: the mechanism of hydrolysis in air. *Appl Surf Sci* 1996; 93: 231–235.
[323] Gonbeau D, Guimon C, Pfister-Guillouzo G, et al. XPS study of thin films of titanium oxysulfides. *Surf Sci Lett* 1991; 254: A476–A476.
[324] Kurmaev EZ, Ek J van, Ederer DL, et al. Experimental and theoretical investigation of the electronic structure of transition metal sulphides: CuS, FeS_2 and $FeCuS_2$. *J Phys Condens Matter* 1998; 10: 1687.
[325] Li J, Jiu T, Tao G-H, et al. Manipulating surface ligands of copper sulfide nanocrystals: synthesis, characterization, and application to organic solar cells. *J Colloid Interface Sci* 2014; 419: 142–147.

[326] Teich D, Lorenz T, Joswig J-O, et al. Structural and Electronic Properties of Helical TiS_2 Nanotubes Studied with Objective Molecular Dynamics. *J Phys Chem C* 2011; 115: 6392–6396.
[327] Ivanovskaya VV, Seifert G, Ivanovskii AL. Electronic structure of titanium disulfide nanostructures: Monolayers, nanostripes, and nanotubes. *Semiconductors* 2005; 39: 1058–1065.
[328] Liu Y-H, Porter SH, Goldberger JE. Dimensional Reduction of a Layered Metal Chalcogenide into a 1D Near-IR Direct Band Gap Semiconductor. *J Am Chem Soc* 2012; 134: 5044–5047.
[329] Fischer DW. X-Ray Band Spectra and Electronic Structure of TiS_2. *Phys Rev B* 1973; 8: 3576–3582.
[330] Ralaiarisoa M, Rodríguez Y, Salzmann I, et al. Impact of solvent exposure on the structure and electronic properties of $CH_3NH_3PbI_{3-x}Cl_x$ mixed halide perovskite films. *Appl Phys A* 2019; 125: 470.
[331] K. Ono L, R. Raga S, Remeika M, et al. Pinhole-free hole transport layers significantly improve the stability of $MAPbI_3$-based perovskite solar cells under operating conditions. *J Mater Chem A* 2015; 3: 15451–15456.
[332] Malinkiewicz O, Yella A, Lee YH, et al. Perovskite solar cells employing organic charge-transport layers. *Nat Photonics* 2014; 8: 128–132.
[333] Kaltenbrunner M, Adam G, Głowacki ED, et al. Flexible high power-per-weight perovskite solar cells with chromium oxide-metal contacts for improved stability in air. *Nat Mater* 2015; 14: 1032–1039.
[334] Zhou X, Li X, Liu Y, et al. Interface electronic properties of co-evaporated $MAPbI_3$ on ZnO(0001): In situ X-ray photoelectron spectroscopy and ultraviolet photoelectron spectroscopy study. *Appl Phys Lett* 2016; 108: 121601.
[335] Xiao M, Huang F, Huang W, et al. A Fast Deposition-Crystallization Procedure for Highly Efficient Lead Iodide Perovskite Thin-Film Solar Cells. *Angew Chem Int Ed* 2014; 53: 9898–9903.
[336] Huang L, Hu Z, Yue G, et al. $CH_3NH_3PbI_{3-x}Cl_x$ films with coverage approaching 100% and with highly oriented crystal domains for reproducible and efficient planar heterojunction perovskite solar cells. *Phys Chem Chem Phys* 2015; 17: 22015–22022.
[337] Hugenschmidt MB, Gamble L, Campbell CT. The interaction of H_2O with a TiO_2(110) surface. *Surf Sci* 1994; 302: 329–340.
[338] Peuckert M. A comparison of thermally and electrochemically prepared oxidation adlayers on rhodium: Chemical nature and thermal stability. *Surf Sci* 1984; 141: 500–514.
[339] Osedach TP, Andrew TL, Bulović V. Effect of synthetic accessibility on the commercial viability of organic photovoltaics. *Energy Environ Sci* 2013; 6: 711–718.

Appendix

Appendix A

He-discharge UV light and X-ray source parameters

Table A1 He-discharge UV light and X-ray source lines and respective intensities and satellites shifts.[224]

	Source	Relative Intensity (%)	Satellite shift (eV)
UV	**HeI α (21.22 eV)**	100	0
	HeI β	1.2 – 1.8	1.87
	HeI γ	0.5	2.52
	HeII α (40.81 eV)	100	0
	HeII β	<10	7.56
	HeII γ	n.a.	10.2
X-ray	**Al $K\alpha_{1,2}$ (1486.6 eV)**	100	0
	Al $K\alpha_3$	6.4	9.8
	Al $K\alpha_4$	3.2	11.8
	Mg $K\alpha_{1,2}$ **(1253.6 eV)**	100	0
	Al $K\alpha_3$	8.0	8.4
	Al $K\alpha_4$	4.1	10.1

Appendix B

Comparison of Valence band Spectra Plotted on a Linear and Logarithmic Scale for HOIP films investigated in the result chapter 5

Valence band spectra of $MAPbI_{3-x}Cl_x$ films annealed for 10 min and 100 min in section 5.1

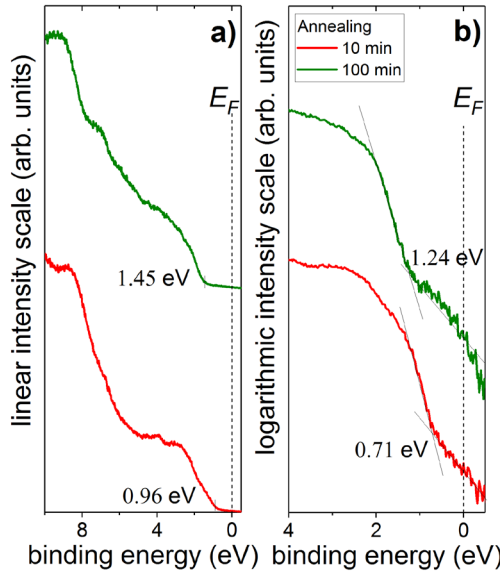

Figure B1 Valence band spectra corresponding to the data in Figure 5.10 plotted on **a)** a linear, and **b)** a logarithmic intensity scale for the determination of the VBM of $MAPbI_{3-x}Cl_x$ films annealed for different time.

Valence band spectra of $MAPbI_{3-x}Cl_x$ films exposed to different environment in section 5.2

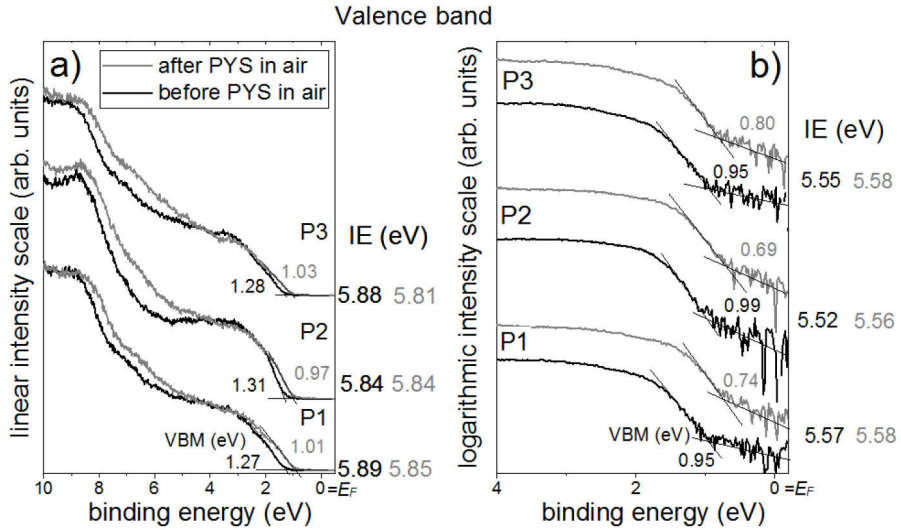

Figure B2 Valence band spectra corresponding to the data in Figure 5.13 plotted on **a)** a linear, and **b)** a logarithmic intensity scale for the determination of the VBM of $MAPbI_{3-x}Cl_x$ films before and after exposure to air for KP and PYS measurements.

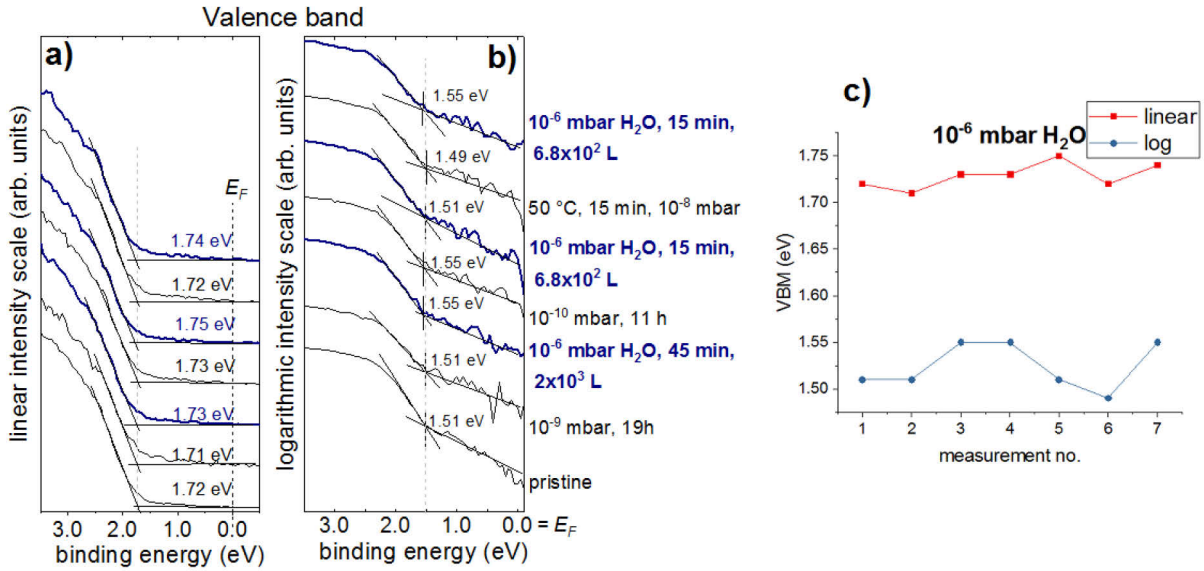

Figure B3 Valence band spectra corresponding to the data in Figure 5.15 plotted on **a)** a linear, and **b)** a logarithmic intensity scale for the determination of the VBM of $MAPbI_{3-x}Cl_x$ films exposed to $p_{H2O}=10^{-6}$ mbar. **c)** Comparison of the VBM values obtained from both intensity scales.

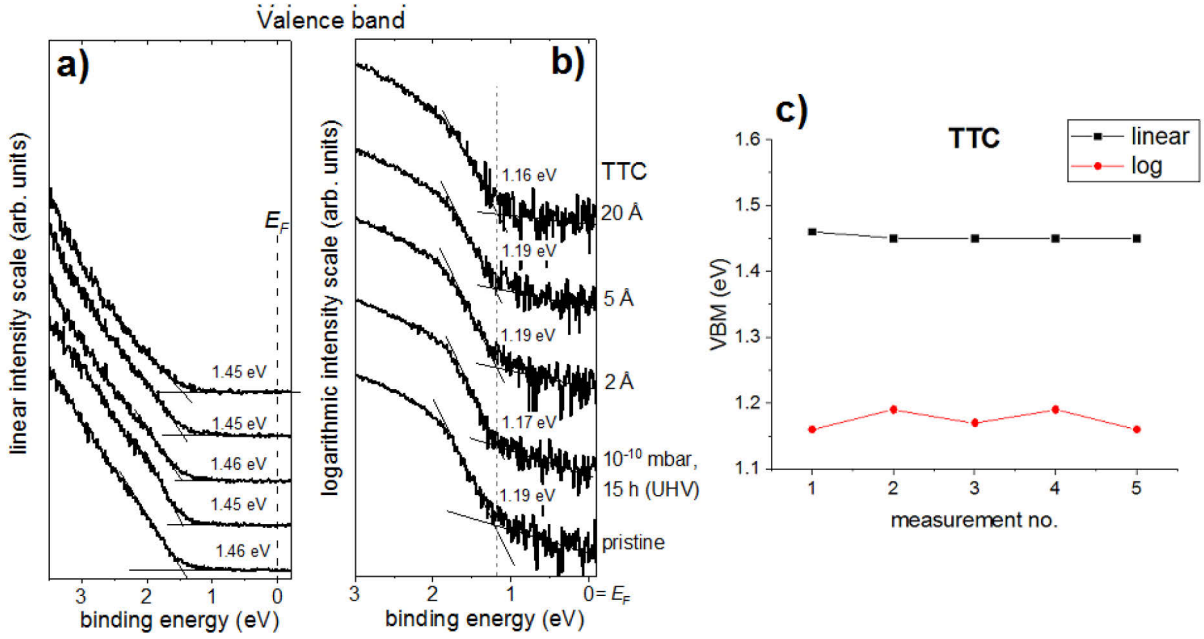

Figure B4 Valence band spectra corresponding to the data in Figure 5.16 plotted on **a)** a linear, and **b)** a logarithmic intensity scale for the determination of the VBM of $MAPbI_{3-x}Cl_x$ films with incremental deposition of TTC layers of nominal thicknesses: 2 Å, 5Å, 20 Å. **c)** Comparison of the VBM values obtained from both intensity scales.

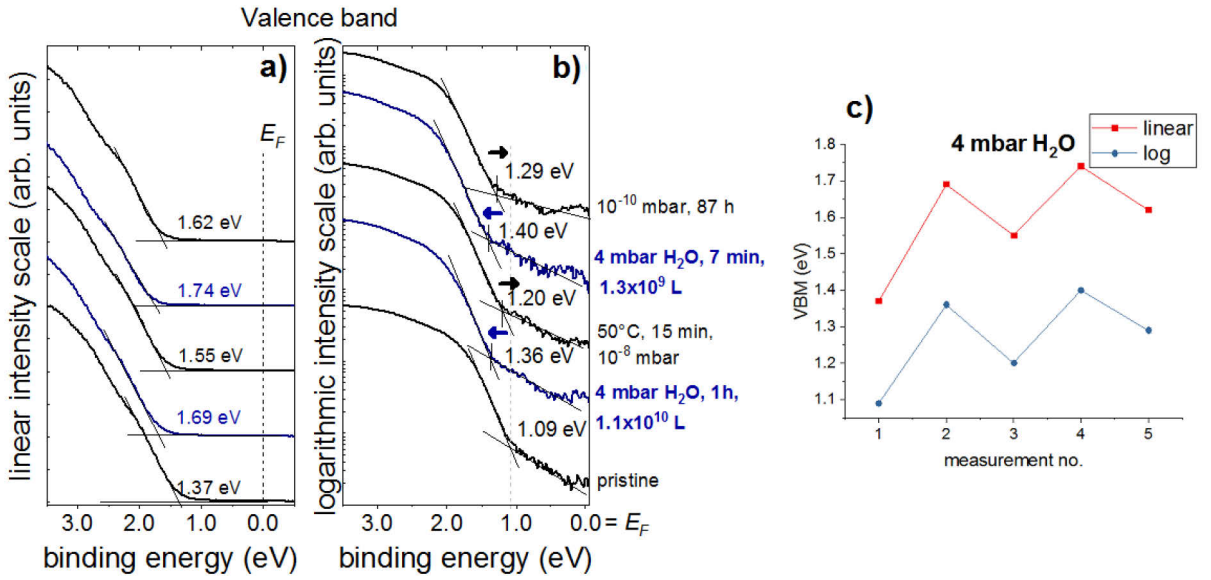

Figure B5 Valence band spectra corresponding to the data in Figure 5.17 plotted on **a)** a linear, and **b)** a logarithmic intensity scale for the determination of the VBM of $MAPbI_{3-x}Cl_x$ films exposed to p_{H2O}=4 mbar and subsequently heated at 50°C or vacuum-dried in UHV. **c)** Comparison of the VBM values obtained based on both intensity scales.

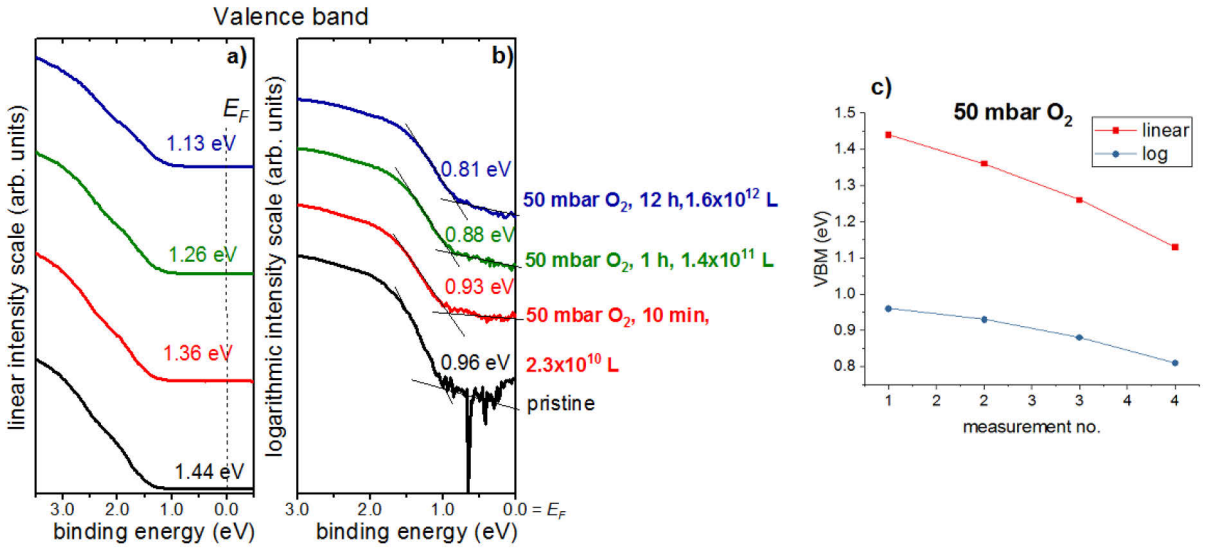

Figure B6 Valence band spectra corresponding to the data in Figure 5.18 plotted on **a)** a linear, and **b)** a logarithmic intensity scale for the determination of the VBM of $MAPbI_{3-x}Cl_x$ films exposed to 50 mbar oxygen. **c)** Comparison of the VBM values obtained from both intensity scales.

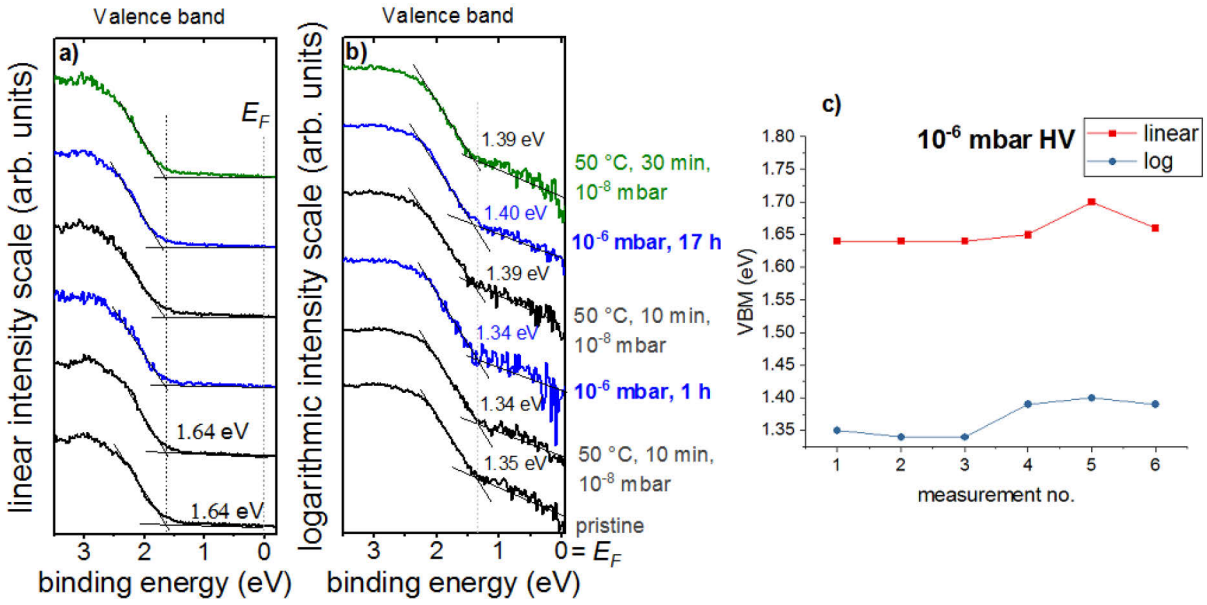

Figure B7 Valence band spectra corresponding to the data in Figure 5.20 plotted on **a)** a linear, and **b)** a logarithmic intensity scale for the determination of the VBM of of $MAPbI_{3-x}Cl_x$ films stored in HV condition (10^{-6} mbar) and mildly heated at 50°C. **c)** Comparison of the VBM values obtained from both intensity scales.

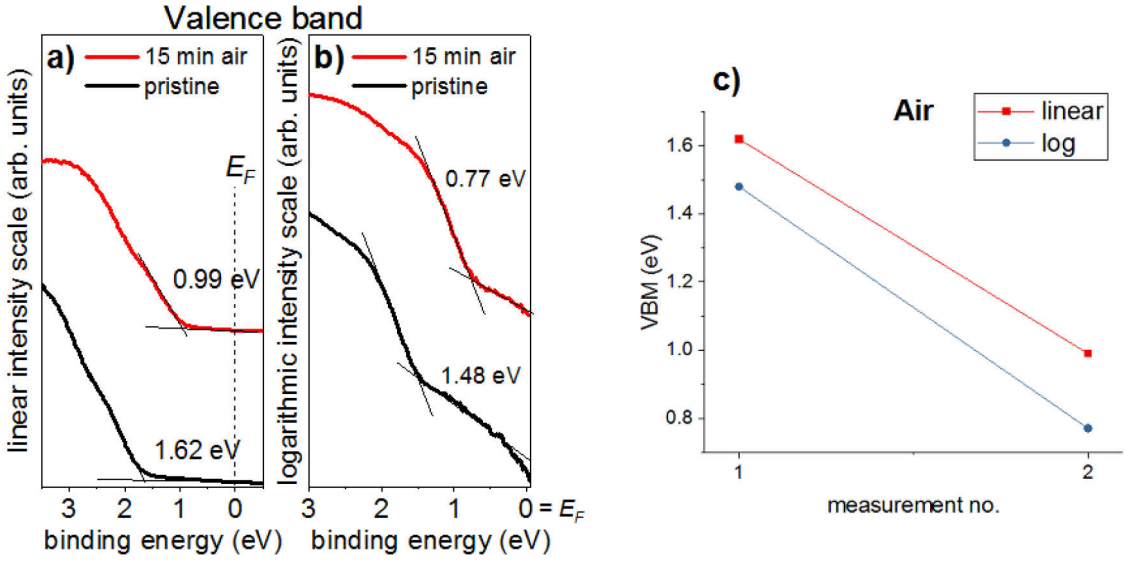

Figure B8 Valence band spectra corresponding to the data in Figure 5.21 plotted on **a)** a linear, and **b)** a logarithmic intensity scale for the determination of the VBM of $MAPbI_{3-x}Cl_x$ films exposed to air for 15 min. **c)** Comparison of the VBM values obtained from both intensity scales.

Valence band spectra of $MA_{1-x}Gua_xPbI_3$ films with different Gua content x (0<x<1) in subsection 5.3.1

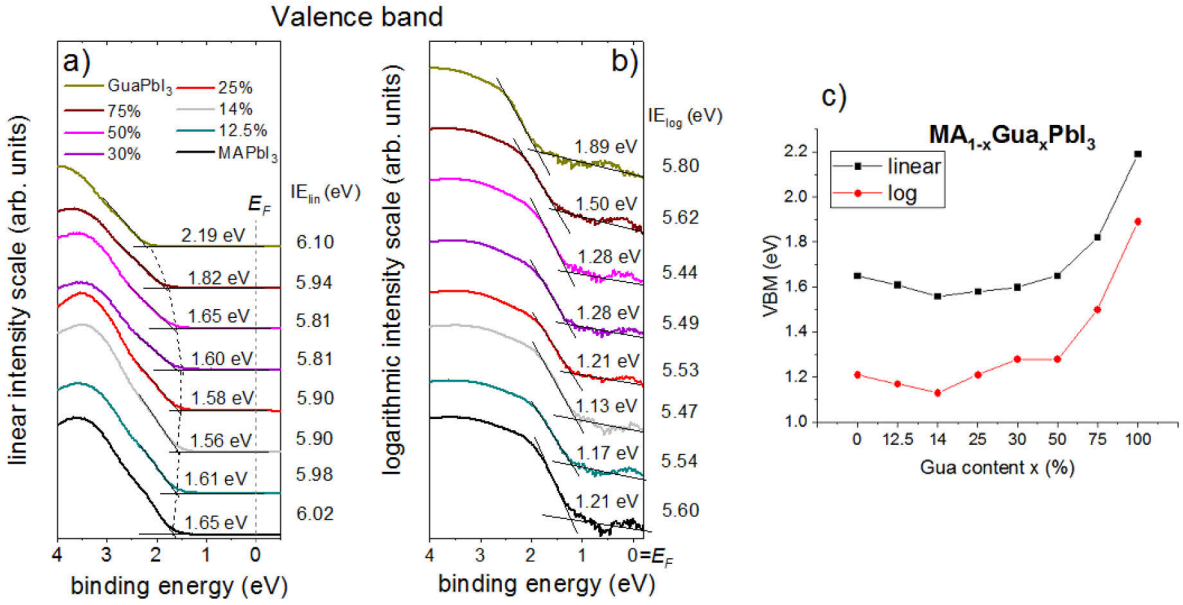

Figure B9 Valence band spectra corresponding to the data in Figure 5.25 plotted on **a)** a linear, and **b)** a logarithmic intensity scale for the determination of the VBM of $MA_{1-x}Gua_xPbI_3$ films with different percentages of Gua (x:1-x represents the Gua:MA ratio where x is the percentage in decimal form). **c)** Comparison of the VBM values obtained from both intensity scales.

Valence band spectra of the $(FAPbI_3)_{0.85}(MAPbBr_3)_{0.15}$ film shown in subsection 5.3.2

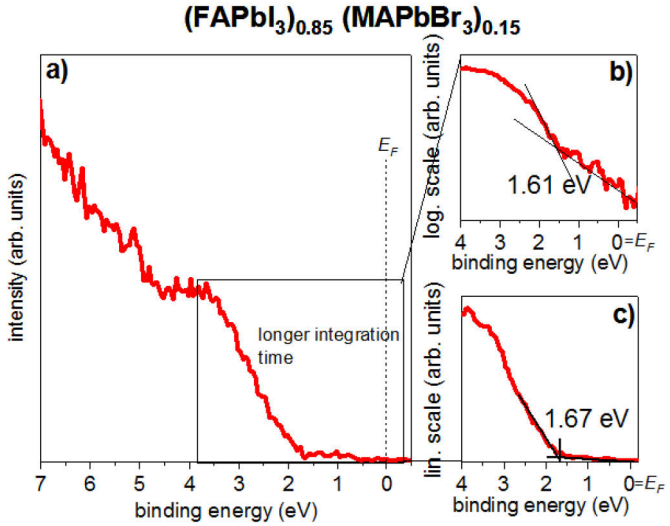

Figure B10 Valence band spectra corresponding to the data in Figure 5.31 plotted on **a)** a linear, and **b)** a logarithmic intensity scale for the determination of the VBM of a $(FAPbI_3)_{0.85}(MAPbBr_3)_{0.15}$ film.

Valence band spectra of $MAPbI_{3-x}Cl_x$ films exposed to solvents shown in subsection 5.4.1

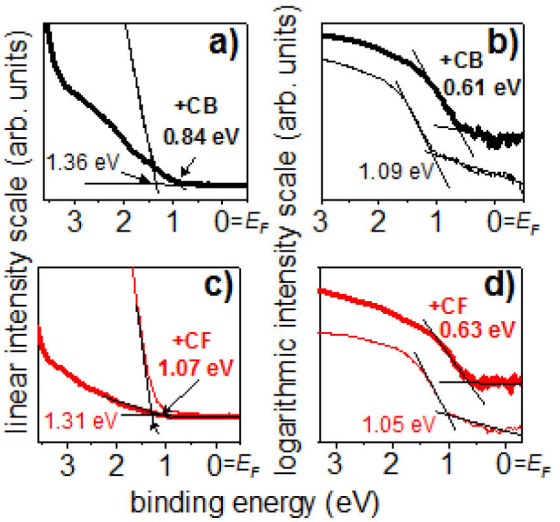

Figure B11 Valence band spectra corresponding to the data in Figure 5.37, plotted on **a)** and **c)** a linear, and **b)** and **d)** a logarithmic intensity scale for the determination of the VBM of $MAPbI_{3-c}Cl_x$ films before (normal) and after (bold) exposure to chlorobenzene (a and b), and chloroform (c and d).

Valence band spectra of $MAPbI_{3-x}Cl_x$ films exposed to solvents shown in subsection 5.4.2

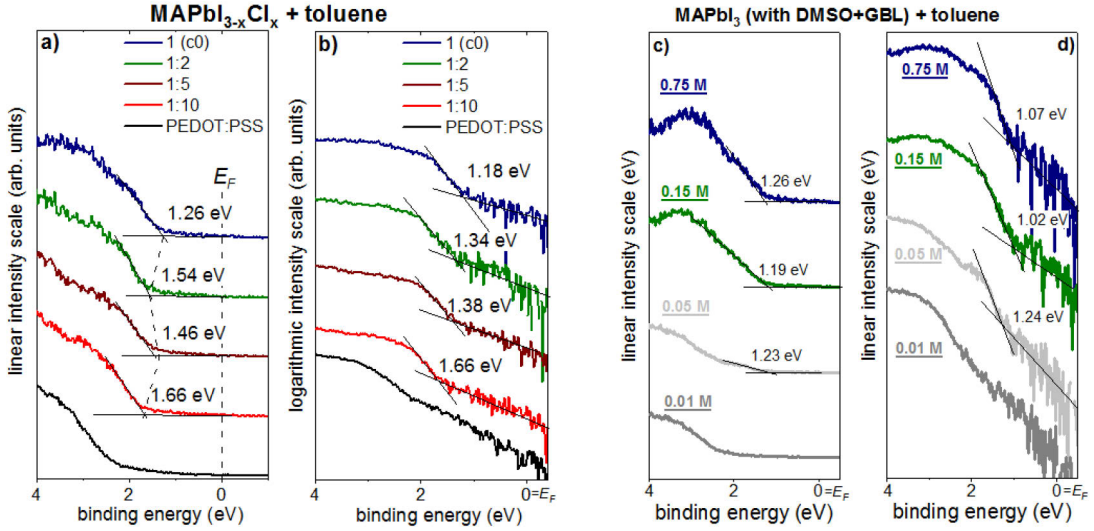

Figure B12 Valence band spectra plotted on **a)** a linear and **b)** logarithmic scale corresponding to the data in Figure 5.41 for $MAPbI_{3-c}Cl_x$ films prepared from different dilution and with the toluene-drip method. **c)-d)** Valence band spectra plotted on **c)** a linear and **d)** logarithmic scale corresponding to the data in Figure 5.42 for $MAPbI_3$ films prepared from different dilution and with the toluene-drip method.

Appendix C

Supporting results for the investigation of environmental effects in section 5.2

KP and PYS data: alternation of UPS measurements in UHV before and after KP and PYS measurements in air on 3 similarly prepared perovskite samples (P1, P2, and P3)

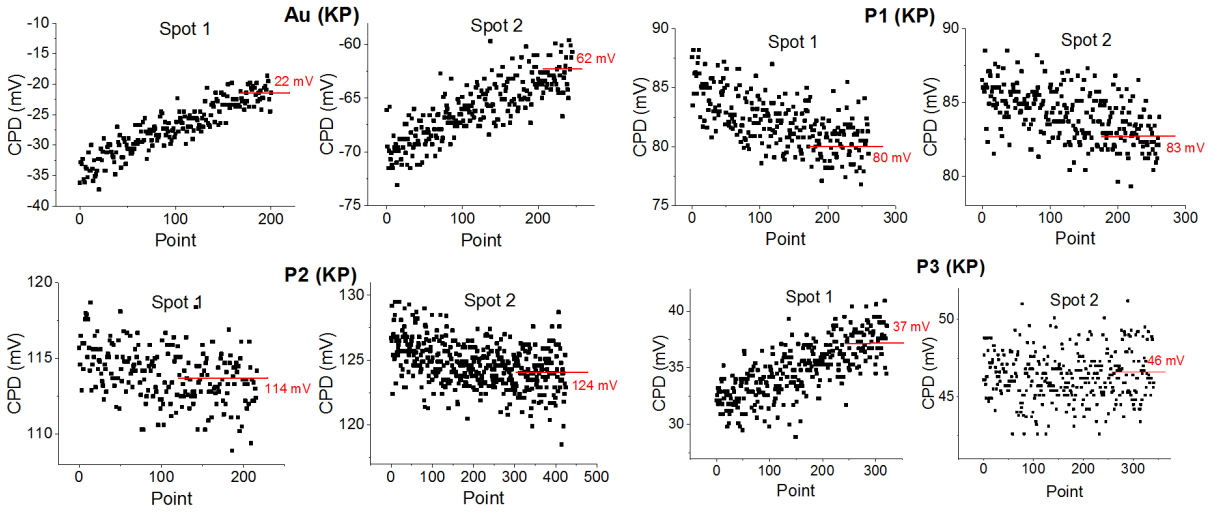

Figure C1 Kelvin Probe (KP) data from which the work function values listed in Table 5.1 were derived. For each $MAPbI_{3-x}Cl_x$ film (P1, P2, and P3, respectively) and Au sample, measurements were done on two spots and for each spot one CPD was extracted from a linear extrapolation of the data when the signal stabilized (red values). The average of the two CPDs was used to derive the work function of each sample by considering the KP and PYS data (see Figure C2 below) of the Au reference sample (see section 3.4).

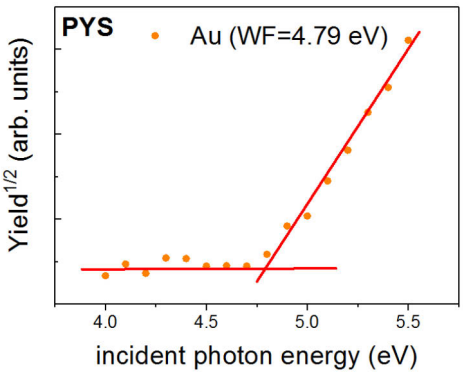

Figure C2 Photoelectron yield spectroscopy (PYS) data, from which the work function of the Au reference sample in Figure C1 were extracted.

UPS and XPS of a $MAPbI_{3-x}Cl_x$ film exposed to p_{H2O}=5 mbar for 13 h

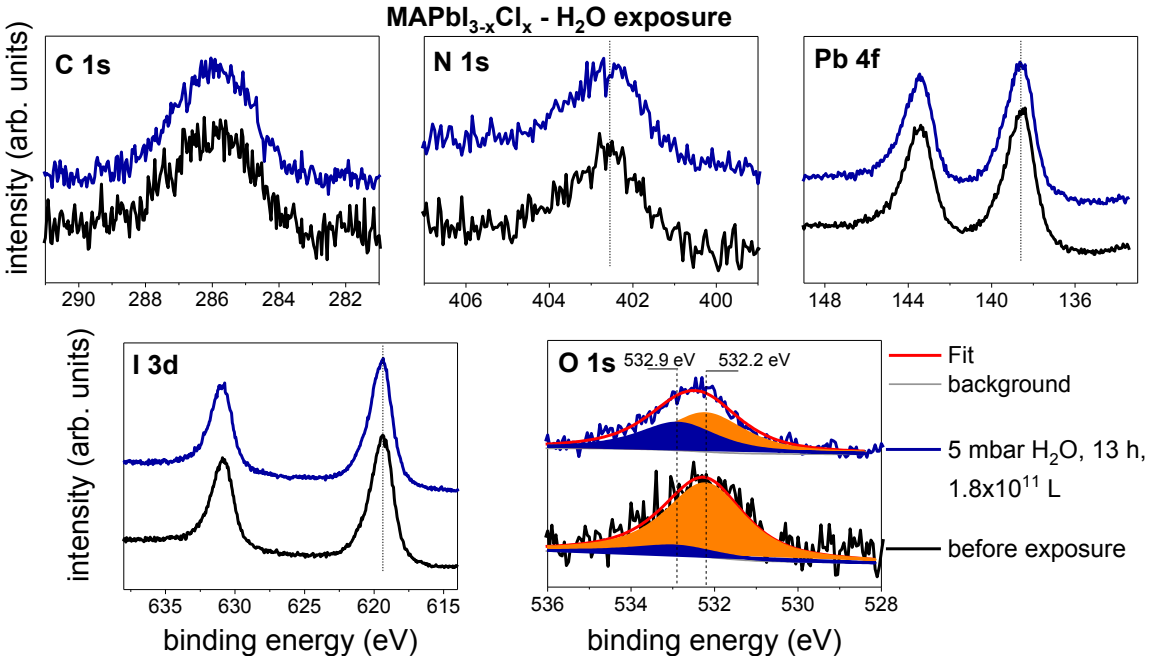

Figure C3 XPS spectra of the C 1s, N 1s, Pb 4f, I 3d, and O 1s of a $MAPbI_{3-x}Cl_x$ film prepared similarly to the samples in section 5.2, and exposed to p_{H2O}=5 mbar for 13 h. No shift of the core levels peak positions were observed, however an increase of the signal intensity from the O1s peak at higher BE, which can correspond to oxygen in H_2O,**[337, 338]** after water exposure is consistent with the presence of H_2O molecules on the surface. The corresponding UPS data are shown in Figure C4.

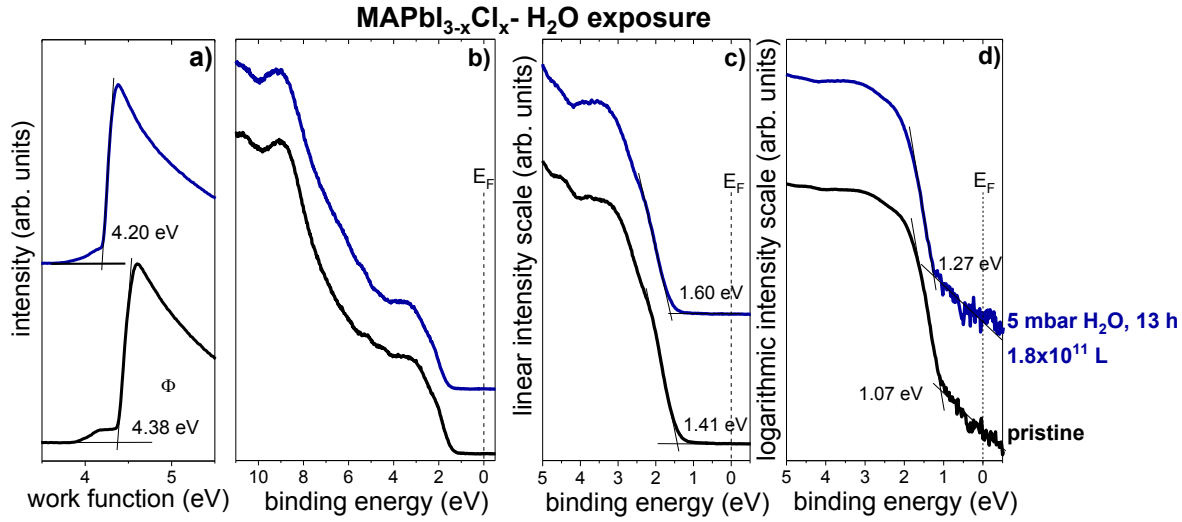

Figure C4 UPS spectra of the $MAPbI_{3-x}Cl_x$ film in Figure C3: **a)** SECO, **b)** wide range binding energy (BE) valence spectra, and narrow binding energy range valence band spectra with valence band maxima (VBM) determined from the onset of the spectra on **c)** linear and **d)** logarithmic intensity scale. The decrease and VBM shift to higher BE is consistent with the data in section 5.2.

Appendix D

Supporting results for the investigation of mixed methyl ammonium guanidinium lead iodide perovskite in subsection 5.3.1

Optical properties of $MA_{1-x}Gua_xPbI_3$ perovskite films

The absorption spectra of $MAPbI_3$ and five representative $MA_{1-x}Gua_xPbI_3$ perovskite films with $x \leq 0.5$ are shown in Figure D1a. A tiny but continuous shift in the absorption band edge is observed for $x < 0.2$, whereas a lowering of the absorption capacity and a larger blue shift of the band edge (~0.02 eV), implying a band gap widening, is recorded for $x > 0.2$. This band gap widening can be associated with the different organic-inorganic interactions mediated by the new additional hydrogen bonds, which result in local distortions of the Gua neighbouring positions, and ultimately, in the expansion of the unit cell. Additionally, for $x > 0.5$ features at ~500 nm and at 390 nm related to the band edge and the excitonic peak of 1D $GuaPbI_3$, respectively, as well as a feature corresponding to the absorption edge at ~775 nm of $MA_{0.75}Gua_{0-25}PbI_3$ are discerned (Figure D2a). These features evidence that both individual $GuaPbI_3$ and $MA_{0.75}Gua_{0-25}PbI_3$ phases are preserved in $MA_{1-x}Gua_xPbI_3$ for $x > 0.5$. In line with the absorption data, the photoluminescence (PL) spectra in Figure D1b and (Figure D2b-d exhibit a gradual shift towards higher energy for $x < 0.2$ and a more apparent shift for $x = 0.25$, which is preserved for higher x (Figure D2d), thus indicating a band gap widening.

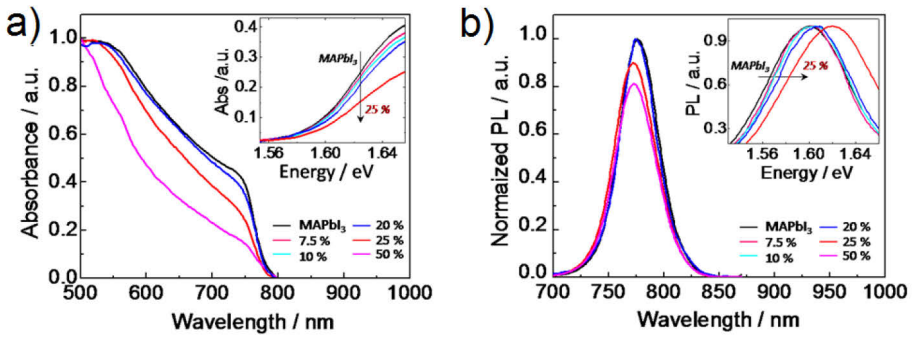

Figure D1 **a)** Ultraviolet-visible-near-infrared absorption spectra of the $MA_{1-x}Gua_xPbI_3$ films containing $x \leq 0.5$ shown in Figure 5.24. The optical band edge region is magnified in the inset for $MA_{1-x}Gua_xPbI_3$ films containing $x \leq 0.5$. **b)** Photoluminescence (PL) spectra of the $MA_{1-x}Gua_xPbI_3$ films in a). Absorption data from Gustavo de Miguel (Universidad de Córdoba), PL-data from Giulia Grancini (EPFL Sion), figures reproduced with permission from ref. **[243]**.

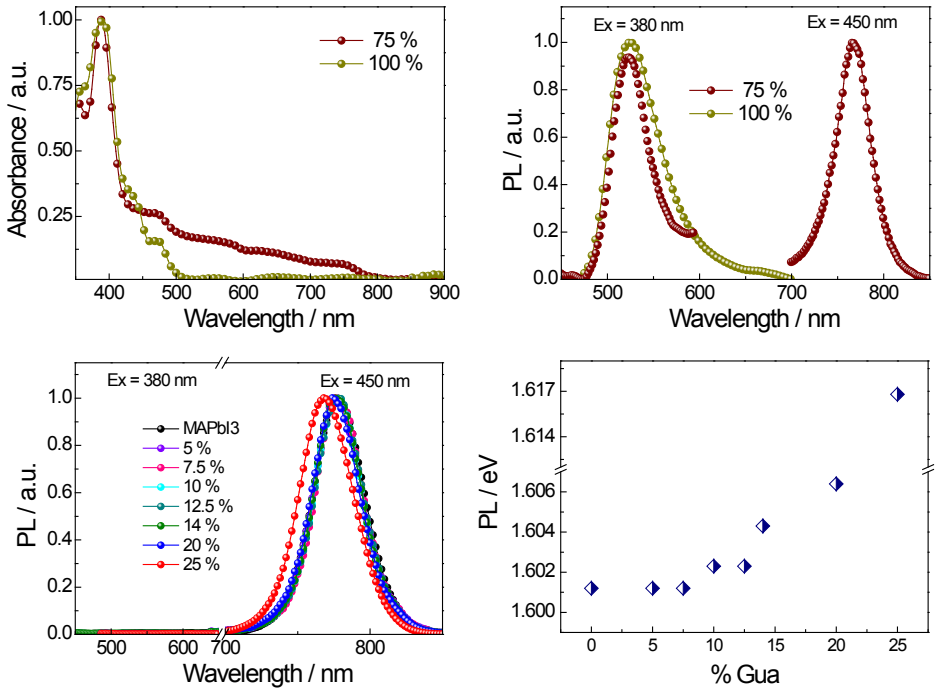

Figure D2 a) UV-visible absorption spectra for the 1D $GuaPbI_3$ perovskite and the mixed $MA_{0.25}Gua_{0.75}PbI_3$. **b)** Photoluminescence (PL) spectra recorded for the samples in a), excited at 380 nm and 450 nm. The $MA_{0.25}Gua_{0.75}PbI_3$ (75% Gua content) sample exhibits emissions which correspond to the two coexisting $GuaPbI_3$ and $MA_{1-x}Gua_xPbI_3$ phases. **c)** PL spectra recorded for $MA_{1-x}Gua_xPbI_3$ mixed perovskite with different $x \leq 0.25$. **d)** Evolution of PL peak maximum (in eV) with increasing percentage of Gua. PL data from Giulia Grancini (EPFL Sion), figures reproduced with permission from ref. [243].

Morphology and phase segregation of $MA_{1-x}Gua_xPbI_3$ perovskite films

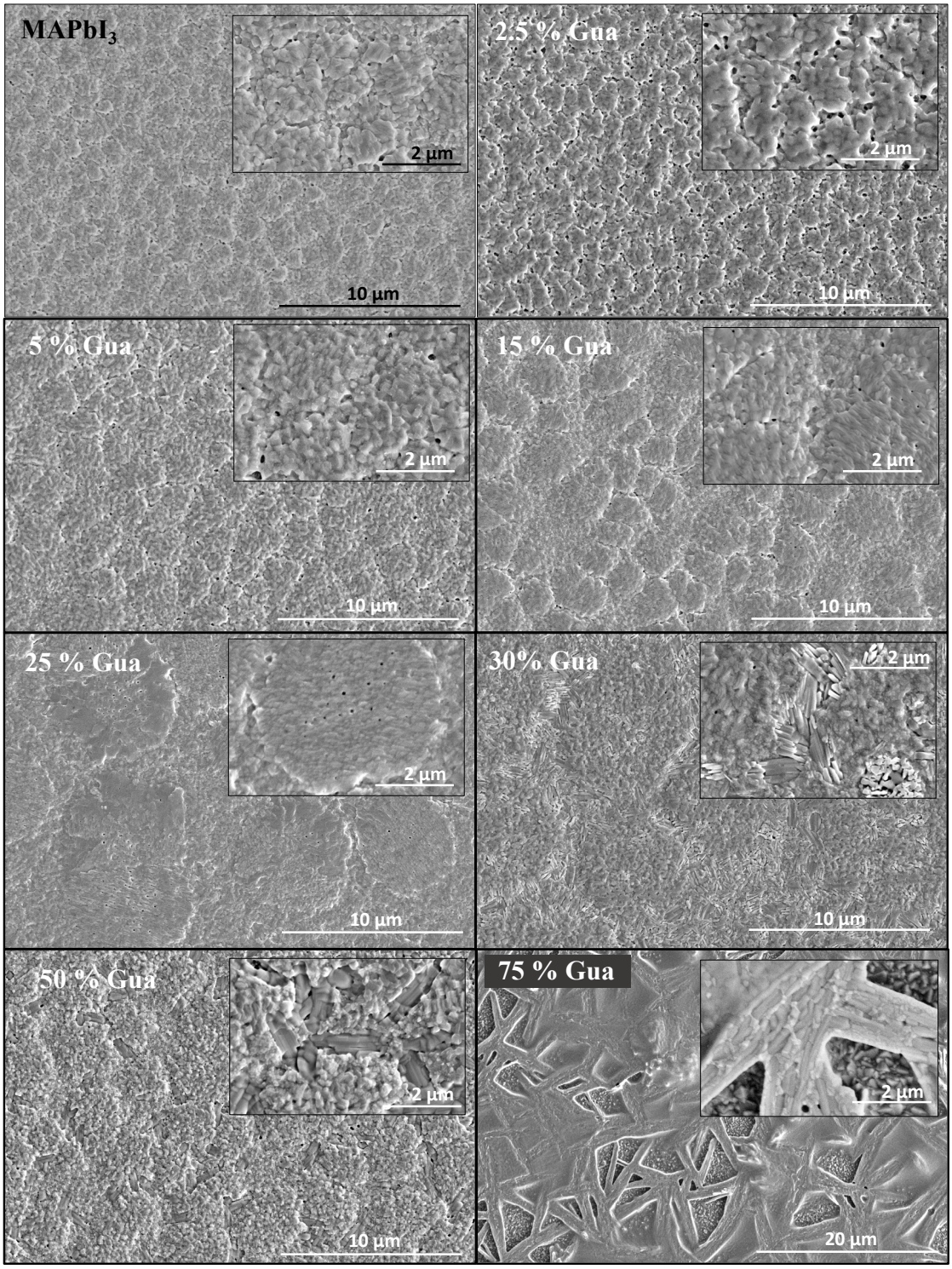

Figure D3 Top-view SEM images of $MAPbI_3$ and $MA_{1-x}Gua_xPbI_3$ mixed perovskites with different percentages of Gua content. SEM data from Cristina Roldán-Carmona (EPFL Sion), figures adapted and reproduced with permission from ref. [243].

The micro-PL and micro-Raman results in Figure D4a and Figure D4b, respectively, confirm the above observations. The micro-PL maps depicting the distribution of the PL peak positions in Figure D4a evidence that whereas no relevant change in the PL peak is observed in the wavelength emission range between 710 nm and 780 nm for $x < 0.25$, a distinctly contrasted PL map with regions extending to a few micrometres is observed for $x = 0.75$. Since the PL peak position is related to the material band gap, which changes with composition[297] and/or local disorder over microscopic sample areas, the results here points out a phase segregation in the material, related to a band gap distribution across the film. Micro-Raman spectra recorded on the same areas yield spectra similar to $MAPbI_3$ for x values up to 0.25 (Figure D4b). The gradual shift to lower wavenumber of the peak at ca. 250 cm^{-1}, associated with the vibrations of the organic cation, indicates the shrinking of the mode due to the insertion of Gua. The peak shift can be attributed to isolated Pb–I planes, similar to PbI_2 intercalated with large organic molecules,[298] and therefore, suggest the formation of low-dimensional perovskite as for the pure $GuaPbI_3$ in the 1D phase. For Gua > 0.25, the relative intensity of the peaks at 120 cm^{-1} and at 135 cm^{-1} increased significantly and the spectra became comparable to that acquired on area with rod-like morphology of the mixed perovskite sample with x=0.75. This further corroborates the phase homogeneity for $x < 0.25$ and the increasingly severe phase segregation into 3D/1D mixture for higher Gua amounts, while the individual features of the single constituents are still retained.

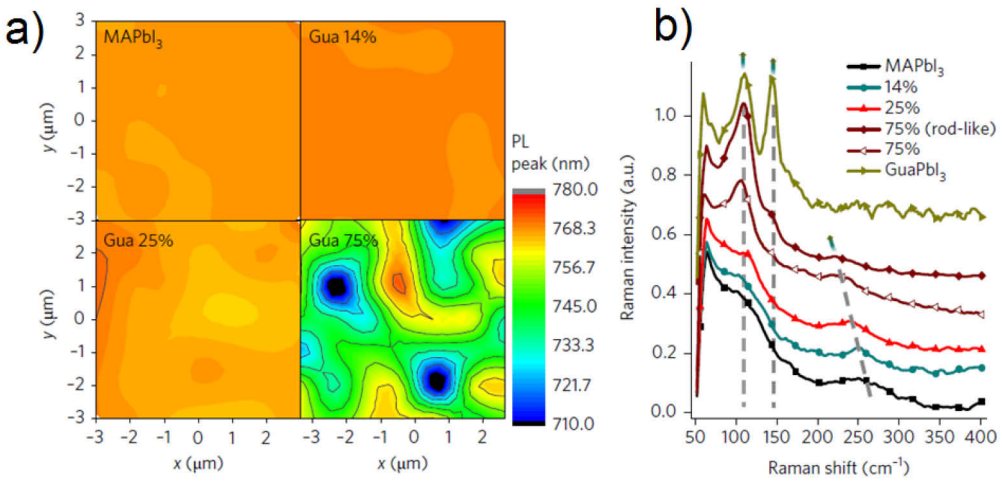

Figure D4 a) Maps over 6×6 μm^2 regions of the micro-PL wavelength peak shift for different Gua percentages. **b)** Micro-Raman spectra of the perovskite surfaces for different Gua percentages. Dashed lines highlight the shifts. PL and Raman data from Giulia Grancini (EPFL Sion), figures reproduced with permission from ref. **[243]**.

Appendix E

Supporting results for the investigation of titanium disulfide TiS_2 as hole transport material in subsection 5.3.2

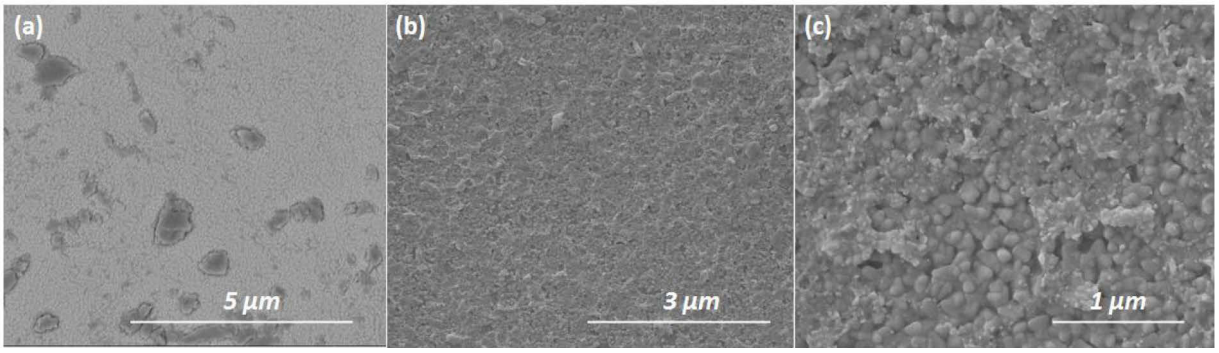

Figure E1 Top surface SEM images of TiS_2 films deposited on Si substrate **a)** at a spin speed of 2000 rpm showing particles with different sizes, and **b, c)** at a spin speed of 5000 rpm showing only small particles with a diameter below 100 nm. SEM data from Cristina Roldán-Carmona (EPFL Sion), figures reproduced with permission from ref.[244].

Table E1 Estimated chemical synthesis cost and waste streams for different HTMs.[a] Data calculated by Aron Huckaba (EPFL Sion), reproduced with permission from ref. **[244]**.

a, b: Taken from the literature.[339] c: Total estimated material cost for one gram of product. d: Total estimated chemical waste for the synthesis of one gram of product, and the waste of halogenated solvents given in parentheses.

Material	Steps[b]	Material Cost ($/g)[c]	Cost per m^2 ($/$m^2$)	Chemical Waste[d] (kg/g)	Commercial Price ($/g)
Spiro-OMeTAD[a]	6	92	39.46	3.6 (1.0)	170-425
Amorphous TiS_2	1	7.37	0.25	0.516(0.0)	n/a

Appendix F

Supporting results for the investigation of perovskite thin films and films obtained from different solution dilutions

$MAPbI_3$ films of different nominal thicknesses obtained by co-evaporation of MAI and PbI_2

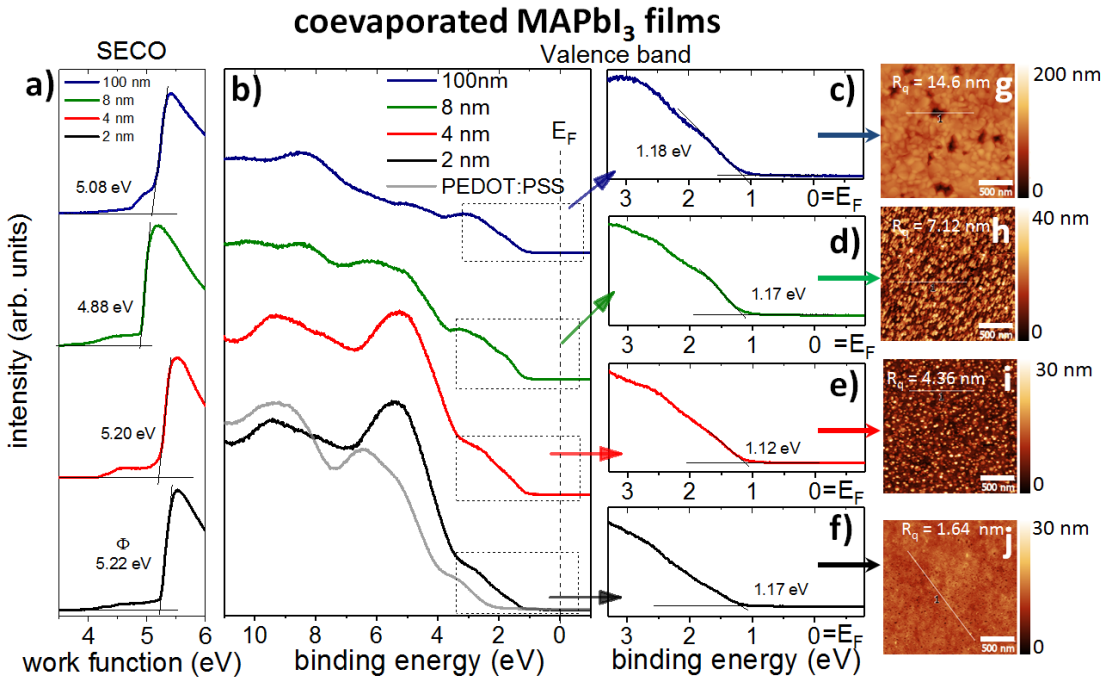

Figure F1 a) SECO, and **b)** wide binding energy range valence spectra of PEDOT:PSS, and $MAPbI_3$ films of different nominal thickness obtained by coevaporation of MAI and PbI_2. Narrow binding energy range valence region spectra of **c)** 100 nm, **d)** 8 nm, **e)** 4 nm, **f)** 2 nm nominally thick films in a, b) and their respective AFM micrographs in **g-j)**. Scale bar in micrographs is 500 nm; additionally, the respective rms roughness is given. For profiles corresponding to the drawn lines, see Figure F2. Samples prepared by Cristina Roldán-Carmona (EPFL Sion).

The UPS spectra of $MAPbI_3$ films of 2 nm, 4 nm, 8 nm, and 100 nm thicknesses, obtained by co-evaporation of MAI and PbI_2 on PEDOT:PSS substrates are shown in Figure F1 Sample preparation, i.e. thermal deposition for co-evaporation, was carried out by Cristina Roldán-Carmona from the GMF group at EPFL Sion, Switzerland. Although the 2 and 4 nm thick samples still exhibited features related to the PEDOT:PSS substrate, for instance around 9.6 eV, peaks related to perovskite, e.g. at ca. 5 and 3.7 eV were observed, which distinctly evolved to more pronounced features for the 8 nm thick sample (Figure F1b). The film roughness increased with the nominal film thickness (Figure F1g-j), which is correlated with

the expansion of the grains, as indicated by the corresponding profiles in Figure F2. No band bending could have been deduced from the UPS data, since all samples exhibited comparable VBM (Figure F1 c-f).

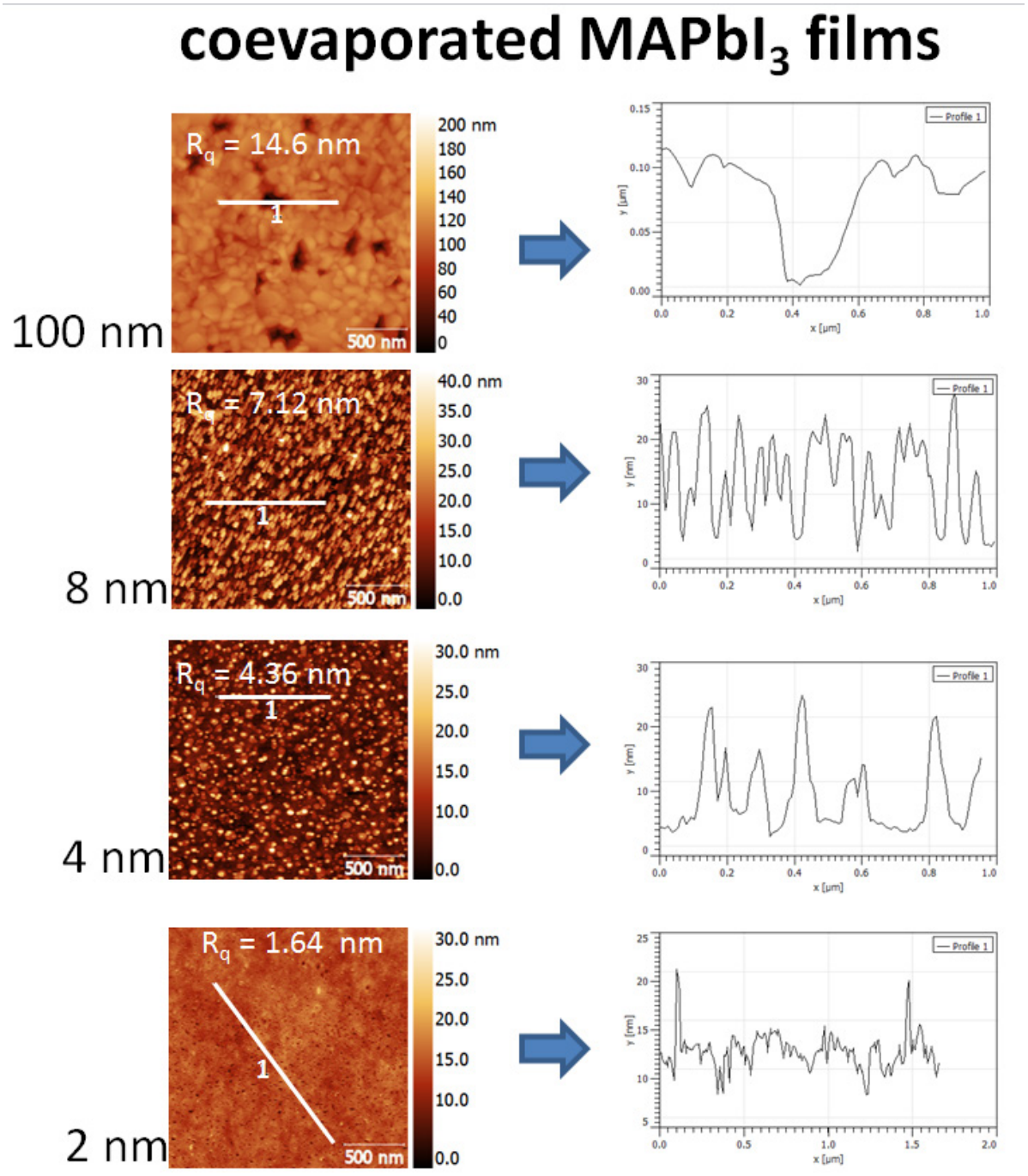

Figure F2 AFM micrographs of the $MAPbI_{3-x}Cl_x$ films in Figure F1 and selected line profiles.

$MAPbI_{3-x}Cl_x$ films obtained from precursor solutions with different concentrations precursor solutions

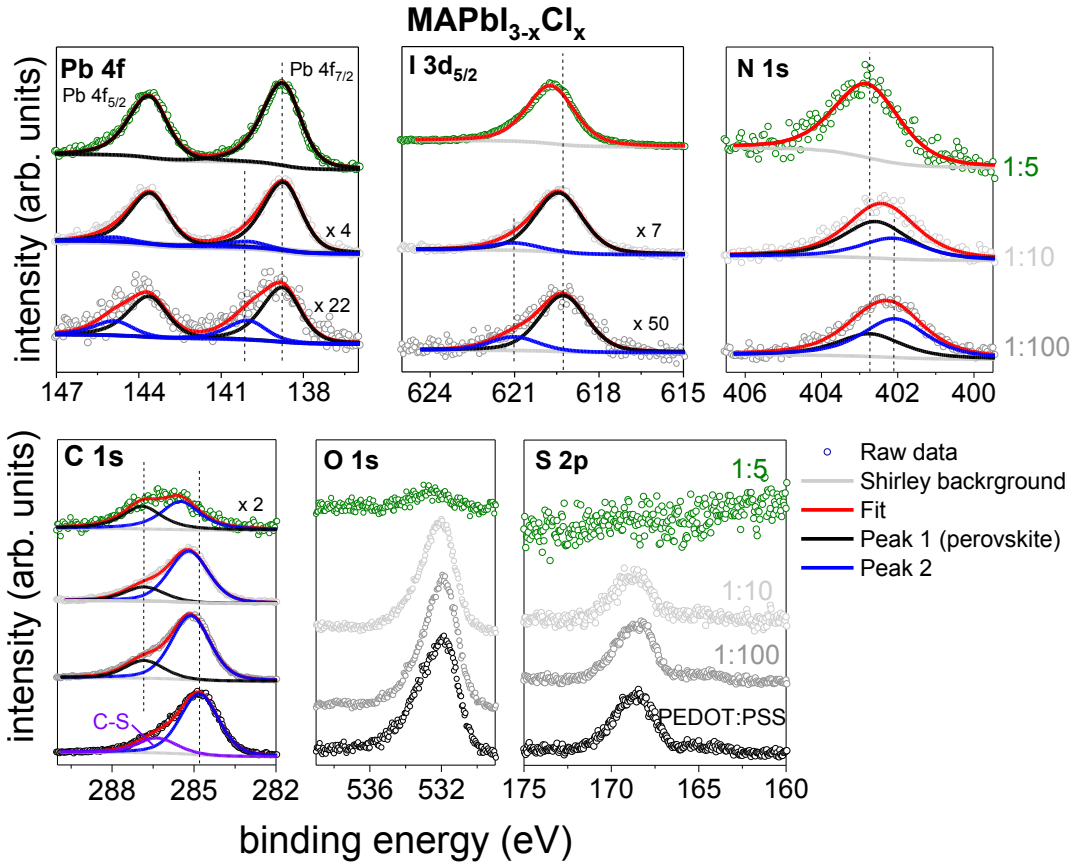

Figure F3 XPS spectra of Pb 4f, I $3d_{5/2}$, N 1s, C 1s, O 1s, and S 2p core levels for films obtained from 1:5, 1:10, and 1:100 dilution of a reference $MAPbI_{3-x}Cl_x$ precursor solution of concentration c0 (40 wt%), *cf.* Figure 5.40 for UPS spectra. For optimal representation, the signal intensity of some core levels is magnified; in such case, the respectice magnification factor is indicated. Dotted lines are drawn only as visual support in identifying related peaks.

AFM of perovskite films obtained from precursors solution of different concentration and by adopting different preparation

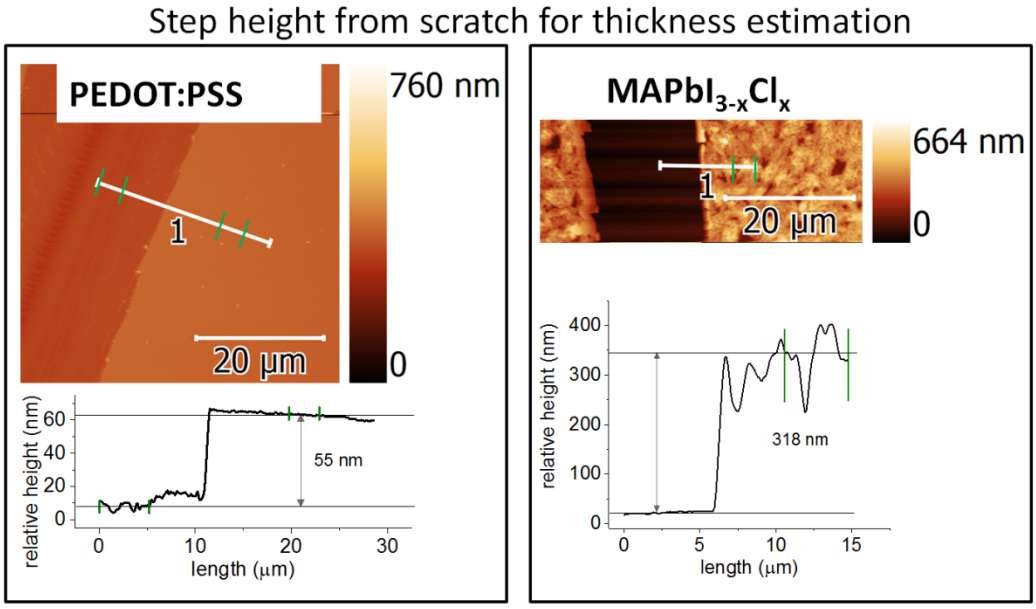

Figure F4 AFM micrographs showing the edge of a scratch on a PEDOT:PSS film on a ITO substrate **(left)** and a $MAPbI_{3-x}Cl_x$ film (from a c0 solution concentration) on ITO/PEDOT:PSS substrate **(right)**. The scratch was mechanically performed with a syringe needle but without applying pressure to not scratch the underlying ITO glass substrate. The height line profile at the scratch edge (white line) is represented in the respective bottom graph (black line). The thickness is determined by the difference between the ITO substrate height (closer to 0 nm) and the respective film height; both heights are an average of the region delimited by the green lines. The line profiles yield film thicknesses of ca. 55 nm for PEDOT:PSS and of ca. 260 nm for the perovskite layer (assuming a 55 nm thick PEDOT:PSS layer underneath).

Note for Figure F5: After the UPS measurements shown in Figure 5.40, a series of PES measurements (not shown here) involving white light illumination for 30 min has been carried out on the sample 1:5 of the $MAPbI_{3-x}Cl_x$ series before the corresponding AFM micrograph shown here in Figure F5 (top, right) was recorded. The light exposure resulted in generation of Pb^0 and it is not excluded that the morphology of this sample might have been affected. However, this 1:5 micrograph is just shown to evidence the formation of a thick layer of material with grain-like morphology in comparison to the 1:10 and 1:100 samples. For the samples obtained from $MAPbI_{3-x}Cl_x$ (top figures in Figure F5), 1:100 and 1:10 exhibit the same morphology as PEDOT:PSS (Figure 4.2). Randomly scattered bright spots (yellow circles) are displayed, which correspond to grains that aggregate into clusters of about 200 nm width with varying heights up to 30 nm are observed, which can be associated with perovskite. The morphology was improved for the same dilution 1:10 by applying the anti-

solvent method (toluene dripping 5 s before the end of the spin-coating step) for similar $MAPbI_{3-x}Cl_x$ dilution, as supported by the formation of larger grains (middle figures in Figure F5), in clear contrast with the disparate and small clusters observed with the same concentration but without toluene dripping. For both series (with and without toluene dripping), the micrographs of 1:5 indicate the formation of homogeneous films.

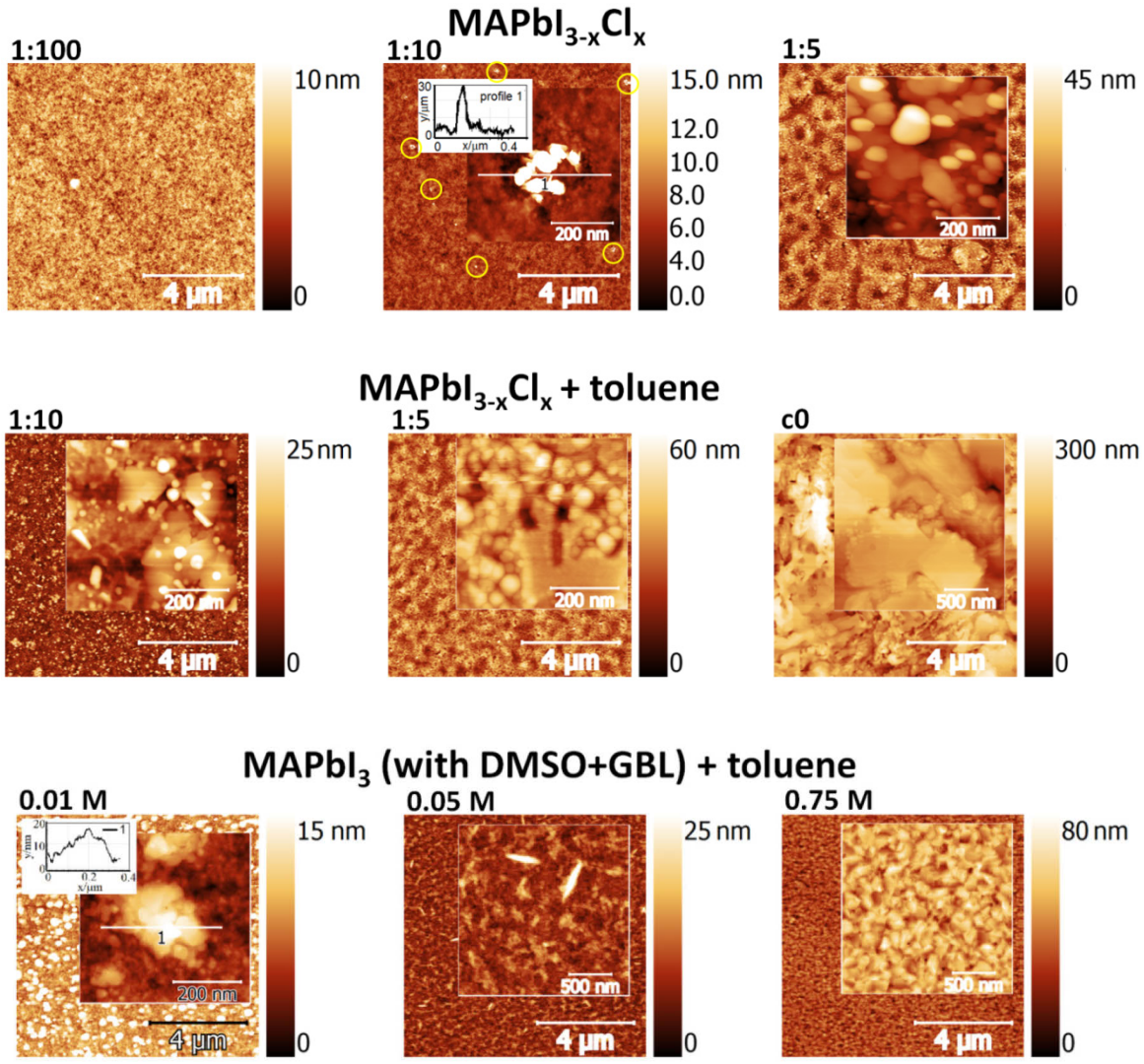

Figure F5 Top: AFM micrographs of films obtained from different dilution of $MAPbI_{3-x}Cl_x$ precursor solution c0 (40 wt%), which were investigated by UPS (*cf.* Figure 5.40). For 1:10, the inset shows a region corresponding to one of the white spots (yellow circles), which is a ca. 200 nm large aggregate of grains with widths up to 30 nm. **Middle**: $MAPbI_{3-x}Cl_x$ films obtained from different dilution of $MAPbI_{3-x}Cl_x$ precursor solution c0 (40 wt%) and by anti-solvent method using toluene. **Bottom**: $MAPbI_3$ films obtained from perovskite precursor solutions containing MAI and PbI_2 in a mixture of DMSO and GBL and with the anti-solvent method using toluene (bottom). The rms roughness of the respective sample is given in Table F1.

Table F1 Rms roughness of the perovskite samples in Figure F5, derived from the corresponding AFM images in Figure F5.

Rms roughness (nm)/concentration				
	Scanned area	**1:100**	**1:10**	**1:5**
$MAPbI_{3-x}Cl_x$	$10 \times 10\ \mu m^2$	1.61	1.35	6.79
	$500 \times 500\ nm^2$	-	5.31	7.38
		1:10	**1:5**	**c0 (40 wt%)**
$MAPbI_{3-x}Cl_x$ + toluene	$10 \times 10\ \mu m^2$	7.32	3.66	39.4
	$500 \times 500\ nm^2$	7.48	4.60	32.2
		0.01 M	**0.05 M**	**0.75 M**
$MAPbI_3$ **(w/ DMSO+GBL) + toluene**	$10 \times 10\ \mu m^2$	8.86	2.70	6.84
	$500 \times 500\ nm^2$	3.01	-	-
	$2 \times 2\ \mu m^2$	-	3.61	9.30

The samples obtained from $MAPbI_3$ solution in a mixture of DMSO and GBL and with toluene dripping during deposition exhibit different morphology (bottom figures in Figure F5) in comparison to the two $MAPbI_{3-x}Cl_x$ series. Grains also aggregate in clusters; however, in contrast to 1:10 of the first series for instance, the clusters are more densely spread. The terrace-like profile extracted for one of these clusters (Figure F5, bottom left, inset) indicates an island growth.

GIXRD of perovskite films obtained from precursor solutions of different concentration and by adopting different preparation

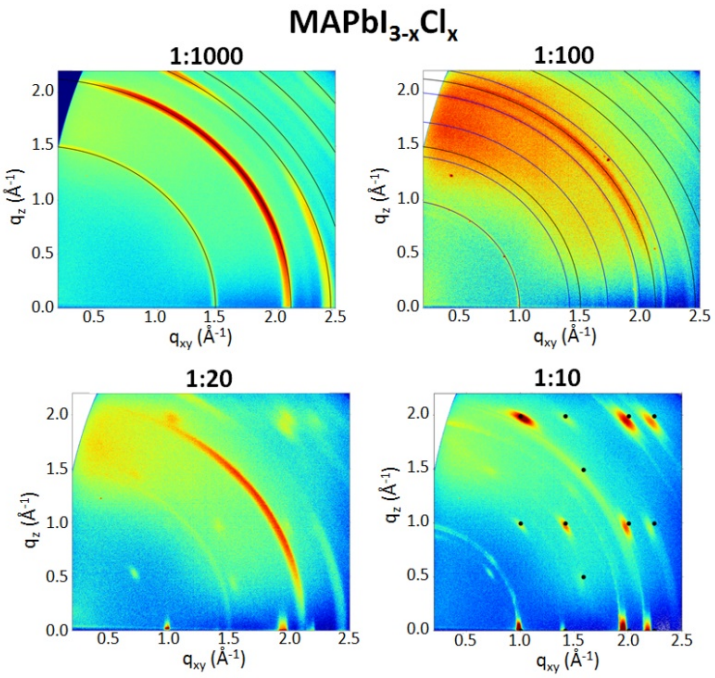

Figure F6 2D GIXRD patterns of $MAPbI_{3-x}Cl_x$ films (*cf.* Figure 5.40 for PES of similar samples) obtained from precursor solutions of different concentration prepared from the dilution of a reference concentration c0 (40 wt%) with the dilution factors 1000, 100, 20, and 10. The calculated diffraction rings for ITO (black) are shown in 1:1000 and 1:100, and those corresponding to cubic (blue) perovskite are shown in 1:10. The dots in 1:10 point out the fiber texture. Simulation performed by Ingo Salzmann, formerly HU Berlin.

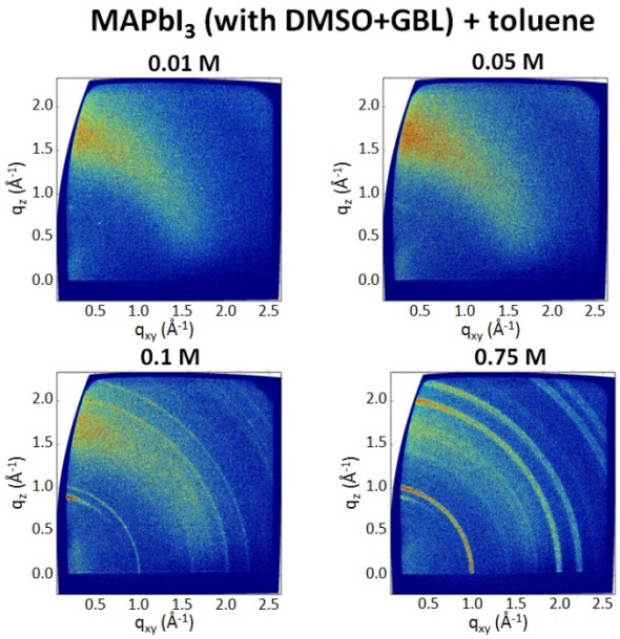

Figure F7 2D GIXRD patterns of $MAPbI_3$ films (*cf.* Figure 5.42 for PES of similar samples) obtained from precursor solutions (MAI and PbI_2 in DMSO and GBL) of different concentration 0.01 M, 0.05 M, 0.1 M, and 0.75 M. Perovskite features are detected starting at 0.05 M concentration, characterized by the diffraction at q=10 Å.

Acknowledgements

First of all, my special thanks go to Prof. Norbert Koch for giving me the opportunity to work on my thesis in his group on the topic of perovskites. Thank you for the trust in me, for the helpful discussions, the supervision, and the support over the years. You have set an example of excellence as a researcher and inspired me in sharpening my accurateness in my research.

I also want to thank for financial support through the graduate school hybrid4energy, the IMPRS, and the SFB951.

I would like to thank my thesis committee members for their availability and their time.

I want to thank all my colleagues in the research group Supramolecular Systems for their helpfulness, the many constructive discussions, the fun moments, and convivial atmosphere during this journey. Particularly, I want to thank Johannes Frisch, Moritz Futscher, Paul Beyer, Fengshuo Zu, Berthold Wegner, Patrick Amsalem, Thorsten Schultz, Raphael Schlesinger, Ingo Salzmann, and Ana Anselmo.

I would like to thank Prof. Jean-Jacques Pireaux for letting me conduct measurements in his laboratory at the University of Namur in Belgium. A big thank you goes to Yan Busby, who introduced me to ToF-SIMS, did the measurements with me, and patiently answered the many questions I had about the method.

I would also like to thank Prof. Mohammad Khaja Nazeeruddin from the Ecole Polytechnique de Lausanne in Switzerland for giving me the possibility to visit his laboratory and get an insight in the interesting world of perovskite solar cells fabrication. In this regard, my thanks also go to Cristina Roldán-Carmona who assisted me professionally and personally during my stay. Thank you also to the entire group of Prof. Nazeeruddin for the nice collaborative works.

I want to thank all my friends who supported me during these many years, thank you.

Finally, I want to thank my amazing family for the constant support and encouragement I have gotten over the years.

Selbstständigkeitserklärung

Hiermit erkläre ich, die Dissertation selbstständig und nur unter Verwendung der angegebenen Hilfen und Hilfsmittel angefertigt zu haben. Ich habe mich nicht anderwärts um einen Doktorgrad in dem Promotionsfach beworben und besitze keinen entsprechenden Doktorgrad. Die Promotionsordnung der Mathematisch-Naturwissenschaftlichen Fakultät, veröffentlicht im Amtlichen Mitteilungsblatt der Humboldt-Universität zu Berlin Nr. 42 am 11. Juli 2018, habe ich zur Kenntnis genommen.

Maryline Ralaiarisoa
Berlin, 12.12.2018